



**HAL**  
open science

# Enabling Techniques for IoT, mMTC, and URC in 5G and B5G Systems

Leila Nasraoui

► **To cite this version:**

Leila Nasraoui. Enabling Techniques for IoT, mMTC, and URC in 5G and B5G Systems. Networking and Internet Architecture [cs.NI]. Ecole Supérieure des Communications de Tunis (Tunisie), 2022. tel-03846096

**HAL Id: tel-03846096**

**<https://theses.hal.science/tel-03846096>**

Submitted on 9 Nov 2022

**HAL** is a multi-disciplinary open access archive for the deposit and dissemination of scientific research documents, whether they are published or not. The documents may come from teaching and research institutions in France or abroad, or from public or private research centers.

L'archive ouverte pluridisciplinaire **HAL**, est destinée au dépôt et à la diffusion de documents scientifiques de niveau recherche, publiés ou non, émanant des établissements d'enseignement et de recherche français ou étrangers, des laboratoires publics ou privés.

Ministry of Higher Education and Scientific Research  
Higher School of Communication of Tunis



University Accreditation in  
(Habilitation Universitaire)  
Information and Communication Technologies

# Enabling Techniques for IoT, mMTC, and URC in 5G and B5G Systems

By

Dr. Leïla NASRAOUI

National School of Computer Sciences (ENSI), University of Manouba

Defended on the 16<sup>th</sup> of September 2022, before the committee composed of:

Chair	Prof. Slim REKHIS	Professor at SUPCOM, Tunisia
Reviewers	Prof. Noura SELLAMI	Professor at ENIS, Tunisia
	Prof. Tijani CHAHED	Professor at Telecom SudParis, France
Examiner	Prof. Leïla SAIDANE	Professor at ENSI, Tunisia
	Prof. Hichem BESBES	Professor at SUPCOM, Tunisia

Academic year: 2021/2022

# Contents

<b>Contents</b>	<b>i</b>
<b>List of Figures</b>	<b>v</b>
<b>List of Tables</b>	<b>x</b>
<b>1 Introduction</b>	<b>1</b>
1.1 General Context . . . . .	1
1.2 Scope of the Research Works . . . . .	3
1.3 Contributions and Outline . . . . .	4
<b>2 Synchronization for WiFi and LTE Standards</b>	<b>9</b>
2.1 Introduction . . . . .	9
2.2 System Model . . . . .	10
2.2.1 OFDM Modulator/Demodulator . . . . .	10
2.2.2 MIMO-OFDM System . . . . .	11
2.3 Related Works . . . . .	12
2.4 Time and Frequency Synchronization for WiFi Standard . . . . .	13
2.4.1 IEEE 802.11n System Description . . . . .	14
2.4.2 Reduced-Complexity Synchronization . . . . .	16
2.4.3 Performance Evaluation . . . . .	18
2.5 Primary Synchronization for LTE Standard . . . . .	21
2.5.1 LTE System Description . . . . .	22
2.5.2 Simply-Differential Synchronization . . . . .	24
2.5.3 Doubly-Differential Synchronization . . . . .	26
2.5.4 Performance Evaluation . . . . .	28
2.6 Time Synchronization for MTC over LTE System . . . . .	32
2.6.1 Enhancement for MTC over LTE . . . . .	33

2.6.2	Simply-Differential Synchronization for MTC . . . . .	34
2.6.3	Performance Evaluation . . . . .	37
2.7	Conclusion . . . . .	39
<b>3</b>	<b>RS-based Neighbor Discovery</b>	<b>40</b>
3.1	Introduction . . . . .	40
3.2	Related Works . . . . .	41
3.3	System Architecture . . . . .	42
3.3.1	Signal Structure . . . . .	42
3.3.2	SideLink Communication . . . . .	43
3.3.3	Reference Signals . . . . .	45
3.3.4	Discovery Framework . . . . .	48
3.4	SRS-based Discovery . . . . .	49
3.4.1	Discovery Metric . . . . .	50
3.4.2	Complexity Evaluation . . . . .	51
3.4.3	Closed-Form Discovery Probability . . . . .	52
3.4.4	Performance Evaluation . . . . .	55
3.5	DMRS-based Discovery . . . . .	57
3.5.1	Discovery Metric . . . . .	58
3.5.2	Complexity Evaluation . . . . .	60
3.5.3	Closed-Form Discovery Probability . . . . .	61
3.5.4	Performance Evaluation . . . . .	65
3.6	Conclusion . . . . .	68
<b>4</b>	<b>Random Access-Like Neighbor Discovery</b>	<b>70</b>
4.1	Introduction . . . . .	70
4.2	Single Discovery Strategy . . . . .	71
4.2.1	System Architecture . . . . .	71
4.2.2	Discovery Framework . . . . .	73
4.2.3	Partial Contention-Free Discovery . . . . .	73
4.2.4	Performance Evaluation . . . . .	76
4.3	Group Discovery Strategies . . . . .	79
4.3.1	System Architecture . . . . .	79
4.3.2	Discovery Framework . . . . .	82
4.3.3	Distributed Discovery . . . . .	83

4.3.4	Network-Assisted Discovery . . . . .	84
4.3.5	Performance Evaluation . . . . .	85
4.4	Conclusion . . . . .	89
<b>5</b>	<b>UAV Positioning and UE Localization</b>	<b>90</b>
5.1	Introduction . . . . .	90
5.2	Related Works . . . . .	91
5.3	UAV Positioning . . . . .	93
5.3.1	System Model . . . . .	93
5.3.2	Height-dependent Coverage . . . . .	96
5.3.3	Height-dependent Spectral Efficiency . . . . .	97
5.3.4	Performance Evaluation . . . . .	99
5.4	UE Localization . . . . .	101
5.4.1	System Model . . . . .	101
5.4.2	Multi-stage Localization . . . . .	104
5.4.3	Beamforming and Position Estimation . . . . .	105
5.4.4	Performance Evaluation . . . . .	107
5.5	Conclusion . . . . .	112
<b>6</b>	<b>Energy and MCS Allocation for Ultra-Reliable Communication</b>	<b>114</b>
6.1	Introduction . . . . .	114
6.2	Related Works . . . . .	115
6.3	Performance of ARQ/HARQ . . . . .	116
6.3.1	Presentation of the ARQ Protocol . . . . .	117
6.3.2	ARQ Performance for BPSK Modulation . . . . .	119
6.3.3	ARQ/HARQ Performance for M-ary Modulation . . . . .	120
6.4	Impact of PC and AMC on ARQ Performance . . . . .	122
6.4.1	Energy Allocation for BPSK modulation . . . . .	122
6.4.2	Energy Allocation and MCS Selection for M-ary Modulation . . . . .	123
6.5	Optimized Performance through PC . . . . .	125
6.5.1	Problem Formulation . . . . .	125
6.5.2	GA-based Solution . . . . .	126
6.5.3	Performance Evaluation . . . . .	128
6.6	Optimized Performance through PC and AMC . . . . .	130
6.6.1	Problem Formulation . . . . .	130

6.6.2	GA-based Solution . . . . .	131
6.6.3	Performance Evaluation . . . . .	135
6.7	Conclusion . . . . .	139
<b>7</b>	<b>Resource Allocation in Energy Harvesting WBAN for E-Health Systems</b>	<b>140</b>
7.1	Introduction . . . . .	140
7.2	Related Works . . . . .	141
7.3	Network Lifetime Maximization using Heuristic Algorithm . . . . .	142
7.3.1	System Model . . . . .	142
7.3.2	Problem Statement . . . . .	144
7.3.3	Time Slot Allocation Algorithm . . . . .	145
7.3.4	Performance Evaluation . . . . .	147
7.4	Network Lifetime Maximization using Game Theory . . . . .	150
7.4.1	System Model . . . . .	151
7.4.2	First Price Sealed-Bid Auction Modeling . . . . .	152
7.4.3	Time Slot Allocation Algorithm . . . . .	155
7.4.4	Performance Evaluation . . . . .	156
7.5	Conclusion . . . . .	158
<b>8</b>	<b>Conclusion and Future Work</b>	<b>160</b>
8.1	Conclusion . . . . .	160
8.2	Ongoing and Future Works . . . . .	162
	<b>Bibliography</b>	<b>164</b>

# List of Figures

2.1	Differential Alamouti STBC block diagram. . . . .	11
2.2	IEEE 802.11a/g/n preamble structure. . . . .	15
2.3	Coarse metric under noiseless conditions using different subdivisions. . . . .	17
2.4	Coarse and Fine metrics under noiseless conditions. . . . .	17
2.5	CDR of the preamble start. . . . .	19
2.6	MSE of the FFO. . . . .	19
2.7	CDR of the preamble start. . . . .	21
2.8	MSE of the FFO. . . . .	21
2.9	LTE frame structure in the FDD mode: 7 OFDM symbols with normal CP [46].	23
2.10	The proposed coarse DD and SD metrics for time domain and frequency domain based ZC sequences under noiseless conditions. . . . .	25
2.11	PSS start CDR in the EPA channel for different FO values. . . . .	30
2.12	PSS start CDR in the ETU channel for different FO values. . . . .	30
2.13	FDR of the SID in the EPA channel for different FO values. . . . .	32
2.14	FDR of the SID in the ETU channel for different FO values. . . . .	32
2.15	The simply-differential metrics : (a) initial ZC sequence, (b) Mapped ZC sequence (LTE signal). . . . .	35
2.16	Probability of correct detection of the ZC sequence start: Theory and Simulation.	38
3.1	Enabled Sidelink for direct communication in LTE network [105]. . . . .	44
3.2	Sidelink synchronization subframe structure [105]. . . . .	45
3.3	Physical Resource Block. . . . .	46
3.4	SRS-based Discovery metric for active and inactive ProSe-enabled users [31]. . . . .	50
3.5	Receiver Operating Characteristic (ROC). . . . .	56
3.6	The neighbor discovery performance as a function of the SNR. . . . .	57
3.7	The neighbor discovery performance as a function of the user position. . . . .	57
3.8	Probability of Discovery of the SRS-based approach: Analytical vs Simulation.	58

3.9	DMRS-based Discovery metric for active and inactive ProSe-enabled users [32].	59
3.10	ROC of the PNC and the GLRT methods for SNR value 5dB. . . . .	66
3.11	Probability of Discovery of DMRS-based methods: PNC vs GLRT. . . . .	67
3.12	PD for single-user scenario in the AWGN channel. . . . .	67
3.13	PD for multi-user scenario in Rayleigh multipath fading channels. . . . .	68
4.1	System architecture: cellular user and D2D users. . . . .	72
4.2	Messages exchanged during the discovery process. . . . .	74
4.3	Network deployment with different UE densities. . . . .	76
4.4	Total number of uplink RBs allocated for Tx-UEs and Rx-UEs as a function of the number of UEs (density $\lambda$ ) for different discovery distance $D$ . . . . .	77
4.5	Collision probability as a function of the number of UEs (density $\lambda$ ) for different discovery distance $D$ . . . . .	77
4.6	Collision probability as a function of the number of slots reserved for the discovery process. . . . .	78
4.7	Link discovery probability as a function of the number of slots reserved for the discovery process. . . . .	78
4.8	The structure of the PSDCH resource pool. . . . .	80
4.9	Example of discoveries in a resource pool with $N_r = N_t \times N_f$ discrete resources organized into $N_f = 3$ blocks and $N_t = 4$ sub-frames. . . . .	81
4.10	An example of Markov chain of the discovery process for $N_u = 8$ and $N_r = 4$ ; the states of the chain show the number of discovered UEs which starts at $N_D(0) = 0$ and ends at $N_D(N_{DCT}) = 7$ . . . . .	83
4.11	An example of realization of a distributed discovery scenario. . . . .	84
4.12	An example of realization of a network-assisted discovery scenario. . . . .	85
4.13	$E(N_{DCT})$ as a function of $N_u$ for $N_r = 12$ resources in low-mobility conditions. . . . .	87
4.14	$E(N_{DCT})$ as a function of $N_u$ for $N_r = 12$ resources in high-mobility conditions. . . . .	87
4.15	Collision rate as a function of $N_u$ for $N_r = 12$ resources. . . . .	88
4.16	Collision rate as a function of $\theta$ for $N_r = 12$ resources and $N_u = 20$ users. . . . .	88
5.1	Example of a typical A-2-G communication system comprising a UAV and randomly distributed G-UEs over open areas with a rough surface. . . . .	93
5.2	$\beta$ shown in the link geometry context. . . . .	95
5.3	Variation of $K$ with the elevation angle for $h_2 = 1m$ : (a) different altitude values and a fixed $\beta_0 = 0.784$ , (b) different $\beta_0$ values and fixed altitude $h_1 = 100m$ . . . . .	96

5.4	The set of configuration space for pairs $(h_1, R_{h_1})$ showing the optimum configuration for $PD_{\text{target}} = 0.999$ : (a) $\beta_0 = 0.784$ and (b) $\beta_0 = 0.617$ . . . . .	100
5.5	The set of configuration space for pairs $(h_1, R_{h_1})$ showing the optimum configuration for $PC_{\text{target}} = 0.999$ over K-Model 1: (a) $\beta_0 = 0.784$ and (b) $\beta_0 = 0.617$ . . . . .	101
5.6	Typical structure of LTE 3-sector cells. . . . .	102
5.7	The proposed localization method block diagram. . . . .	104
5.8	Angle search using a rough step $\delta_\theta = \pi/100$ and a number of antennas $M = 4$ in the noiseless case. . . . .	106
5.9	RMSE of the angle estimate's $\hat{\theta}$ a function of the SNR for numbers of antennas $M = 4$ and $M = 100$ . . . . .	108
5.10	RMSE of the distance and coordinates as a function of SNR for numbers of antennas $M = 4$ and $M = 100$ . . . . .	109
5.11	Probability of sub-meter precision as a function of the SNR for numbers of antennas $M = 4$ and $M = 100$ . . . . .	109
5.12	RMSE of distance and coordinates as a function of the number of antennas at the BS for SNR=5 dB. . . . .	110
5.13	Probability of sub-meter precision as a function of the number of antennas at the BS for SNR=5 dB. . . . .	110
5.14	Probability of sub-meter precision of distance and coordinates estimates $\hat{d}$ , $\hat{c}_c$ , and $\hat{c}_f$ as a function of the SNR for carrier frequencies $f_c = 7GHz$ and $f_c = 30GHz$ . . . . .	111
5.15	RMSE of the angle estimates $\hat{\theta}_c$ and $\hat{\theta}_f$ as a function of the SNR for carrier frequencies $f_c = 7GHz$ and $f_c = 30GHz$ . . . . .	111
5.16	Probability of sub-meter precision of distance and coordinates estimates $\hat{d}$ , $\hat{c}_c$ , and $\hat{c}_f$ as a function of the SNR for channel estimation error variance $\sigma_{CH}^2 = 10^{-1}$ and $\sigma_{CH}^2 = 10^{-2}$ for carrier frequencies $f_c = 7GHz$ and $f_c = 30GHz$ . . . . .	112
5.17	RMSE of the angle estimates $\hat{\theta}_c$ and $\hat{\theta}_f$ a function of the SNR for perfect channel and erroneous channel estimation with error variance $\sigma_{CH}^2 = 10^{-1}$ and $\sigma_{CH}^2 = 10^{-2}$ for carrier frequencies $f_c = 7GHz$ and $f_c = 30GHz$ . . . . .	112
6.1	Setup for ARQ protocol. The transmitter sends the first packet and waits for the ACK from the receiver. Once ACK1 is received, the transmitter sends packet 2. If the receiver can not decode the packet, it discards the packet and sends back a NACK to the transmitter to ask for packet re-transmission. . . . .	117

6.2	The setup for HARQ protocol. The transmitter sends first packet 1 and waits for the ACK from the receiver. Then it sends packet 2. If the receiver can not decode the packet, it buffers the packet and asks for re-transmission. Then, when it receives packet 2 once more, it combines it with the buffered packet to extract the information. . . . .	118
6.3	Throughput efficiency as a function of the average SNR for conventional ARQ (initial and upper envelope). $N = 3, k = 90, n = 100$ . . . . .	123
6.4	Throughput efficiency as a function of the SNR $\gamma$ for conventional ARQ with different modulation and coding schemes. . . . .	124
6.5	ARQ throughput efficiency as a function of the average SNR for QPSK, 16-QAM and 64-QAM modulations, $N=3, Q=120$ symbols. . . . .	125
6.6	Throughput efficiency as a function of the average SNR for the optimized ARQ. $N = 3, k = 90, n = 100$ . . . . .	128
6.7	Number of retransmission attempts, $N = 3, k = 90, n = 100$ . . . . .	129
6.8	Probability of packet erasure, $N = 3, k = 90, n = 100$ . . . . .	129
6.9	Genetic Algorithm Based Diagram . . . . .	133
6.10	Average Throughput Efficiency for PC-AMC-ARQ of the proposed GA-based and the Lagrange-based [145] approaches, $Q=120$ , static and fading channels $N = 3$ . . . . .	136
6.11	Average Throughput Efficiency for PC-AMC-HARQ type I of the proposed GA-based and the Lagrange-based [146] approaches, $Q=120$ , static and fading channels, $N = 3$ . . . . .	136
6.12	Probability of packer erasure for PC-AMC-HARQ type I of the proposed GA-based approach, $Q=120$ , static and fading channels, $N = 3$ . . . . .	137
6.13	Examples of optimized energy budget allocation throughout (re)transmission attempts for different energy average in static channel. . . . .	138
7.1	Body Sensor Network in pervasive health monitoring system [177] . . . . .	143
7.2	Instantaneous residual energy variations during 100 frames of 5 time slots each. . . . .	149
7.3	Averaged instantaneous residual energy level variations during 100 frames of 5 time slots each. . . . .	149
7.4	Probability of packet loss due to energy run out. . . . .	150
7.5	Frame structure of WBAN based on the standard IEEE 805.15.4. . . . .	152
7.6	First price sealed-bid auction mechanism. . . . .	153

7.7	Strategy matrix for one sensor during all $N_f$ slices. . . . .	153
7.8	Example of the Matrix utility. . . . .	154
7.9	Variations of the mean instantaneous energy during 100 time slices. . . . .	158

# List of Tables

2.1	LTE tapped-delay channel models parameters. . . . .	29
3.1	Simulation parameters of the SRS-based approach. . . . .	55
3.2	Simulation parameters of the DMRS-based approach . . . . .	66
5.1	Maximum coverage radius $R_{h_1}$ , $PD_{\text{target}} = 0.999$ , $\beta_0 = 0.784$ . . . . .	100
5.2	List of SID interval limits . . . . .	102
6.1	Convolutionally Coded Modulation . . . . .	135
7.1	Uninterrupted lifetime . . . . .	148
7.2	Relationship between the source rate and the lifetime (in second) of one sensor	149
7.3	Example of time slot allocation. . . . .	152
7.4	Relationship between the source rate and the lifetime (in second) of one sensor	157

# Chapter 1

## Introduction

### 1.1 General Context

According to Cisco, the number of devices connected to IP networks will be more than three times the global population by 2023. There will be 3.6 networked devices per capita by 2023 (29.3 billion networked devices), up from 2.4 networked devices per capita in 2018 (18.4 billion networked devices). The share of Internet of Things (IoT) devices -also referred to as Machine-Type-Communication (MTC), Device-to-Device (D2D), or Machine-to-Machine (M2M)- will be 50% [1]. On the other hand, the global mobile connections will grow from 8.8 billion in 2018 to 13.1 billion by 2023 at a compound annual growth rate of 24%. Among them, 1.4 billion will be 5G capable [1]. The vision of more than 1.4 billion connected devices is going to implement profound changes in the way people, businesses and society interact, such as social networking, public safety services, and advertising. These trends are based on proximity communication that enables User Equipments (UE) to transmit and receive information without going through the evolved Node B (eNB).

The Long Term Evolution (LTE) network is considered as a promising technology for cellular IoT as it provides mobility and connectivity along wide coverage area [2, 3]. Consequently, cellular IoT has become a research concern to support the emerging growth of IoT applications and services aiming to bring billions of scattered connected devices [4]. However, as IoT defines a different set of requirements than the initial LTE system, namely low-rate, low-overhead, low-power consumption, and low-cost, the 3<sup>rd</sup> Generation Partnership Project (3GPP) has

been working on numerous LTE features such as power saving, signaling reduction, overload control, and complexity reduction to meet the new requirements. D2D communication was introduced in the LTE cellular network under the name of Proximity Services (ProSe) as a vital component to enable novel and significant opportunities requiring localized communications in which nearby users exchange data [5, 6].

In addition to MTC features, 5G and beyond 5G systems are expected to provide users with the experience of “unlimited” network performance i.e., instantaneous delivery of huge volume of multimedia data over a highly stable connection [7]. Therefore, higher throughput and energy efficiency, lower latencies, lower outage probability, and more reliable data transmission are all key considerations in the design of future mobile communication systems [7, 8]. Ultra-Reliable Communication (URC) is one of the novel features of 5G system to provide a certain level of communication service with very high requirements on availability and reliability (1ms end-to-end delay,  $10^{-5}$  packet loss probability) almost 100% of the time [9, 10]. We identify three variants of URC : 1) URC-L for Long-term URC that concerns how to guarantee (provide with high probability) certain rates to multiple users over longer periods, 2) URC-S for Short-term URC that concerns provisioning of moderate data rates with low latency and very high probability, e.g. latency less than 2ms with 99.999% guarantee, for a limited number of devices, and 3) URC-E for Emergency that is related to providing communications when the infrastructure becomes partially damaged or non-functional [9].

The use of Unmanned Aerial Vehicles (UAVs), also known as drones, has risen dramatically in recent years and has been introduced as part of 5G system. This was driven by UAVs’ promising potential to reduce risk, cost, and time deployment for many activities, such as buildings inspection, surveillance and monitoring, search and rescue missions, delivery of medical supplies, and several other use cases [11]- [14]. Owing to their autonomy, flexibility, and quick deployment, there has been a tremendous increase in research efforts of both academia and industry for several years. Most of UAV-centric research were robotics or military-oriented and had focused on issues of navigation, control, and autonomy. However, the communication challenges of UAVs used to be considered as part of the control and autonomy components, and only in very recent years that UAVs communication aspects were considered as a main issue in communication systems [14, 15].

The previously cited features hit the design of both new network architectures, e.g. ProSe-enabled and Unmanned Aerial Vehicles (UAV)-assisted networks, and improved PHYSical/Medium

Access Control (PHY/MAC) layers procedures, e.g. discovery methods and radio resource management algorithms. These aspects present the main concerns of our research works, which cover several techniques that enable IoT implementation, massive MTC, and URC in 5G and beyond 5G systems.

## 1.2 Scope of the Research Works

The findings of the research works presented in this dissertation deal with two main features, namely MTC and URC. In particular, we investigate improved and new techniques deployed to ensure the requirements set by these two pillars of 5G and beyond 5G networks.

The introduction of ProSe-enabled networks relied on multiple enhancements to existing LTE standards including new functional elements and a Sidelink (SL) air interface for direct connectivity between devices. Three functionalities are defined under ProSe paradigm: direct communication, direct discovery, and synchronization. Direct communication allows UEs to establish a communication link between them without routing data via the eNB. Direct discovery is the functionality by which UEs advertise and detect useful information provided by their peers in proximity without the need for establishing a communication link. Finally, synchronization is the process necessary to agree on common system information and to be able to decode SL transmissions. Both *Synchronization* and *Neighbor Discovery* have been studied through different scenarios and configurations while respecting the standard specifications.

Also, 5G ecosystem includes a myriad of new applications based on location awareness and other contextual information, which made accurate localization a key component of 5G systems. The Global Navigation Satellite System (GNSS) has been the most dominant technology to enable outdoor localization. However, the multitude of localization demands causes GNSS saturation due to its limited capacity and coverage. Other problems with GNSS localization are the too much power consumption and the Line-of-Sight (LoS) to satellites requirement which is not guaranteed in urban regions. This motivated us to address 5G assets with massive Multiple Input Multiple Output (MIMO) antennas and millimeter waves (mm-waves) for improved *Localization*.

Having the capabilities to fly above the ground level and the flexibility to be positioned in the air and avoid obstacles, UAVs experience an increased likelihood of direct unobstructed

path with both the serving ground communicating network parts and peer flying nodes in the same area. Consequently, if properly deployed, UAV-enabled networks are expected to offer a remarkable performance improvement over the traditional network in terms of reliability, operation range, applications use cases, and throughput. To exploit the potential of UAV in 5G and beyond networks, we study the optimization of the *Positioning* of Low-Altitude Platform (LAP) for enhanced performance.

Due to the challenging wireless propagation environment, many techniques have been developed and optimized to enhance transmission reliability. In particular, Automatic Repeat reQuest (ARQ) and Hybrid-ARQ (HARQ) techniques were proposed to improve data link layer robustness by retransmitting packets received in error [16]. HARQ techniques have been a fundamental part of several current communication systems and are expected to be used in future communication systems as well [17]. While the use of ARQ and HARQ increases the reliability of communication, re-transmission operations decrease the throughput efficiency resulting in an overall system performance degradation. To overcome this limitation, Power Control (PC) and Adaptive Modulation and Coding (AMC) were used either jointly or separately. In our research, we study *Energy Allocation* and *Modulation and Coding Scheme (MCS) Selection* for maximized throughput to cope with re-transmissions' impact.

Recent advances in sensors and low-power integrated circuits have enabled the design of miniature sensors implanted in the body to gather patient information (e.g. electrocardiography signal) that are used in e-Health systems [20]. Due to scarcity of energy supply and uninterrupted service requirements, energy harvesting techniques were proposed to provide the energy necessary for the functioning of the Wireless Body Area Network (WBAN) from the environment (e.g. body heat, foot strike, finger strokes). To ensure uninterrupted network lifetime, we study the optimization of dynamic *Time Resource Allocation* based on the energy budget of each sensor node.

### 1.3 Contributions and Outline

In this section, we highlight the contributions of the research works which cover several techniques proposed to enable meeting 5G and beyond 5G system requirements in terms of massive MTC and URC. Some of the following contributions involve works achieved by PhD and Master students, while others are conducted with collaborators.

To enable direct communication between UEs, synchronization has to first be performed. In OFDM systems, the main purpose of synchronization is to acquire time and frequency offset estimates, in addition to the Sector Identifier (SID) determination in the case of cellular networks. First, a Reduced-Complexity (RC) synchronization technique [23], initially proposed for single-antenna OFDM system and assessed in AWGN channel [22] and multipath fading channel [24], is applied to the IEEE 802.11n WLAN standard. We exploit the repetitive structure of the IEEE 802.11n preamble and the diversity offered by MIMO configuration to apply the RC approach to the standard and assess the performance in the IEEE 802.11 channel B. Second, we focus on primary synchronization in cellular networks exploiting the Primary Synchronization Signal (PSS). Particularly, we conduct a theoretical study to assess the effect of frequency offset on synchronization performance of the two RC Simply Differential (SD) and Doubly Differential (DD) approaches initially proposed in [26] and [27] for the case of perfect frequency synchronization and single antenna configuration. Furthermore, simulations are investigated in the case of multiple antenna configuration in the Extended Pedestrian A (EPA) and Extended Typical Urban (ETU) channel models to ensure the robustness of the approaches. Then, we focus on synchronization in the context of MTC by applying the SD approach to the standardized signal introduced in the 3GPP Rel. 12 to be used for direct communication. The performance of the studied approach is evaluated in terms of theoretical correct detection probability derived in its closed form, and compared to the experimental probability. The outcomes of the previously cited contributions are presented in chapter 2, and lead to three conference papers [29] and [28], and one journal paper [30]. These contributions present an extension of the PhD findings and involve the PhD supervisory team, professor Leïla Najjar (COSIM. Research Lab., SUP'COM) and professor Mohamed Siala (MEDIATRON Research Lab., SUP'COM).

The second step required to establish a direct communication is neighbor discovery, by which a UE knows about other UEs in its vicinity. We first investigate neighbor discovery based on SL transmissions, where a UE can discover his peers through simply listening to their transmissions, sensing the reference signals by performing correlation, and finally applying a binary hypothesis test to decide. We propose two approaches that use Sounding Reference Signal (SRS) with cross-correlation and Demodulation Reference Signal (DMRS) with power-normalized-correlation. Both approaches are evaluated through simulations and theoretical studies of the probability of correct discovery calculated in its closed form to ensure their effectiveness for any system parameters. The main advantage of these approaches is their com-

patibility with the LTE standardized signal structure without the requirement of any additional resources, in addition to the reduced complexity offered by recursive implementations. The findings of these research works are detailed in chapter 3 of this manuscript and appeared in the papers [31–34]. The previously cited contributions involve professor Leila Najjar (COSIM. Research Lab., SUP’COM) and Dr. Salama Ikki (Associate professor at the Electrical Engineering Department, Lakehead University, Ontario, Canada), and some of them received a fund from the Natural Sciences and Engineering Research Council of Canada (NSERC) through its Discovery Grant Program (DP).

Neighbor discovery is further investigated in chapter 4 from a MAC perspective for both ProSe and V2X services in single user and multiple user scenarios. Exploiting random-access like procedures, we first propose a partial-contention free discovery approach in which the ProSe-enabled UEs first select beacons that are forwarded to the eNB in charge of verifying collisions and enabling connections between contention-free ProSe-enabled neighbors. We evaluate the collision probability considering several scenarios, for which we study the impacts of the distance between transmitter and receiver devices, the density of connected users, and the time dedicated for the discovery process. Group discovery is then studied in distributed and centralized (network-assisted) communication modes defined for 5G communications. In the first case, we use a method inspired by Aloha protocol, while Polling-like protocol is used in the second one. The performance is evaluated in terms of the time required to complete the group discovery. Also, two different collision models are assumed for performance evaluation. The first model considers MAC collision, referred to as the L-2 model, in which when two or more UEs pick the same resource, the mutual interference will prevent any collided message from being received by other UEs. The second one considers a more practical assumption where some collided messages may be received if the signal strength is sufficiently high to provide a satisfactory Block Error Rate (BLER), and it is referred to as the L-1 model. The findings of these contributions lead to two publications [33, 35]. The work in [33] is investigated in collaboration with Dr. Salama Ikki and funded by the Natural Sciences and Engineering Research Council of Canada (NSERC)-Discovery Program.

Chapter 5 deals with techniques that enhance coverage and ensure connectivity for emergency situations. Particularly, we investigate the optimization of network performance through a judicious positioning of a UAV for free-space propagation. Exploiting a physics-based Rician channel model, we study the maximum coverage radius and show that there exists a unique optimum height at which the UAV should be located to maximize the deployment area. Besides,

we consider outdoor localization of a steady UE under Rician channel conditions. We propose a multi-stage approach that exploits the potential of both massive MIMO and mm-waves in 5G systems. The approach performs a search over a limited beam to reduce the complexity. An assessment of the reference signal strength is first achieved to estimate the distance to the target UE, followed by a two-stage beamforming carried out to determine the coarse and fine AoA estimates using large and thin steps, respectively. Lastly, both distance and AoA estimates are used to find the UE coordinates, and localization is assessed in terms of sub-meter accuracy probability. The works in these concerns appear in the publications [36, 39, 40], where [36] and [40] are the findings of the PhD of Ms. Amal Sellami (PhD student at COSIM Research Lab., SUP'COM) entitled "Localization for 5G and IoT Systems", that I co-supervise with professor Leïla Najjar. Besides, the work on UAV positioning [39] was conducted during my scholar visit at FUNLab in collaboration with professor Sumit Roy (University of Washington, Seattle, USA).

Then, in chapter 6, we study the performance optimization of ARQ/HARQ protocols to reduce the effect of re-transmissions on throughput efficiency. The proposed solution uses a combination of PC and AMC techniques exploiting Genetic Algorithm (GA) treatment to maximize the throughput while maintaining a constant energy budget. For a specific Signal to Noise Ratio (SNR) value, an adequate Modulation and Coding Scheme (MCS) is chosen and a vector of energy values corresponding to the energies used for each packet (re)-transmission attempt is determined. We assume a partial Channel State Information (CSI) knowledge, such as to perform optimization for an SNR value to enable offline treatment. We first investigate the simple case of Binary Phase Shift Keying (BPSK) with only optimized energy allocation. Then, we extend the optimization problem to the general case of combined use of AMC with PC. The findings of this research work are published in [41] and under review in [42]. This work is achieved in collaboration with professor Leïla Najjar and professor Mohamed Siala, and it also involves the work of a master of research project of Mr. Akram Dabbar (PhD student at ENSI).

The last part of the dissertation also concerns resource allocation, yet for energy harvesting WBAN in the context of e-health system. The aim is to maximize the uninterrupted network lifetime through a judicious time scheduling of sensor nodes transmissions. First, the energy harvesting process is modeled as a discrete-time Markov chain. Then, by minimizing the gap between consumed and harvested energies during each time slot, a sensor node maintains a sufficient energy level for a longer time. Two solutions are proposed based on the energy budget

of each sensor node : 1) a heuristic algorithm based, and 2) a game-theory based. The heuristic solution aims to minimize this gap for a general Time Division Multiple Access (TDMA) frame, while a first price sealed-bid auction-based is proposed using the frame structure of the IEEE 805.15.4 standard during which sensor nodes compete for slices. At the beginning of each super-frame, sensor nodes with a specific instantaneous energy level can bid and enter the auction. The findings of these two solutions are presented in chapter 7 of the manuscript and are published in [43,44]. This work is the finding of the PhD of Mrs. Nedra Badri (PhD student at CRISTAL Research Lab., ENSI) entitled “Resource Allocation for IoT Health Monitoring Applications with Energy Harvesting”, that I co-supervise with professor Leïla Azzouz Saidane.

Other research works that are not presented in the manuscript focuses on security aspects for IoT applications based on LoRa connectivity [45], which are conducted in collaboration with professor Adnane Cabani from the University of Rouen, France.

## Chapter 2

# Synchronization for WiFi and LTE Standards

### 2.1 Introduction

Orthogonal Frequency Division Multiplexing (OFDM) is a Multi-Carrier Modulation (MCM) technique used to reduce the Inter-Symbol Interference (ISI) of wireless systems. This technique has gained popularity in several applications, such as the LTE, WiMAX (IEEE 802.16e), and WiFi (IEEE 802.11n/ac and IEEE 802.22), and has shown promising potential for use in 5G standard. In addition to its robustness to multipath fading distortions and narrow-band interferences, the greatest benefit of using OFDM among MCM techniques is its high spectral efficiency due to the orthogonality between sub-carriers. However, both time and frequency errors destroy the orthogonality among the OFDM sub-carriers such that OFDM symbols can no longer be correctly demodulated. Hence, the start of OFDM symbols needs to be accurately determined and the Frequency Offset (FO) must be estimated and compensated before demodulation.

In this chapter, we focus on time and frequency synchronization in the standards LTE-A and WiFi based on the finding of the PhD. Initially, data-aided reduced complexity synchronization approaches were proposed for the case of single-antenna and multiple-antenna OFDM systems in [24] and [25], respectively. We here study the adaptation and application of [24, 25] to the case of WiFi networks exploiting both cyclic and space-time diversities. Further, during

the PhD, doubly and simply primary synchronization approaches were presented in [26, 27] for single-antenna LTE system under perfect frequency synchronization assumption. We here study the case of multiple antenna configuration under standardized channel models (EPA and ETU) and FO. The effect of the FO is also assessed theoretically to analyse its impact on time synchronization accuracy in both approaches [30]. Then, we conduct a theoretical study of the approach [27] and investigate its application to the newly introduced LTE interface for Machine Type Communication (MTC) [139]. It is worth to note that, although the baselines of this chapter are the findings of my PhD research works, none of the herein presented results was included in the PhD thesis [21], and all the studies were performed afterward.

## 2.2 System Model

### 2.2.1 OFDM Modulator/Demodulator

The OFDM technique allows to enhance the spectral efficiency and to reduce the ISI due to multi-path propagation through dividing a high-data rate stream of information units into several parallel lower-rate streams and modulating each stream on separate orthogonal carriers (sub-carriers) [46, 47].

In practice, the OFDM system is implemented through banks of modulators and demodulators that are deployed by Inverse Discrete Fourier Transform (IDFT)/Discrete Fourier Transform (DFT). At the transmitter, the  $k^{\text{th}}$  time-domain OFDM symbol is generated by applying an  $N_u$ -point IDFT to the complex data  $c(m)$  as

$$s(k) = 1/\sqrt{N_u} \sum_{m=0}^{N_u-1} c(m)e^{j2\pi \frac{km}{N_u}}. \quad (2.1)$$

Reciprocally, the receiver will apply an  $N_u$ -point DFT to recover the modulated data. The complete OFDM symbol has a length of  $N_s$  samples and is built up by its useful part generated as in equation (2.1) whose length is  $N_u$  to which a Cyclic Prefix (CP) of length  $N_g$  is prepended ( $N_s = N_u + N_g$ ) to mitigate the multipath effect. While OFDM technique solves most of the wideband mobile communication limitations, it introduces new problems itself. By using high numbers of narrow sub-carriers, the system becomes very sensitive to time and frequency offsets, which both cause ISI and Inter-Carrier Interference (ICI) to deteriorate the

orthogonality. In our work, we consider the received OFDM signal expressed as

$$r(k) = e^{j2\pi \frac{k\nu}{N_u}} \sum_{l=0}^{N_H-1} h(l)s(k + \tau_l) + \omega(k), \quad (2.2)$$

where  $h(l)$  is the  $l^{\text{th}}$  sampled complex channel impulse response,  $N_H$  is the channel memory length,  $\nu$  is the normalized carrier FO with respect to the sub-carriers spacing, and  $\omega(k)$  is a complex Additive White Gaussian Noise (AWGN).

## 2.2.2 MIMO-OFDM System

The combination of Multiple-Input Multiple-Output (MIMO) wireless technology with OFDM technique has been recognized as one of the most promising techniques to provide high data rate and robust reception through spatial diversity and spatial multiplexing [48–50]. Space Time Bloc Coding (STBC) is a technique implemented to extract the total available spatial diversity in a MIMO channel through appropriate construction of the space-time codewords. As we focus on non-coherent reception, we opt for the Differential Space Time Bloc Coding (D-STBC), which was first proposed by Tarokh *et al.* in [52] for two transmit antennas and  $N_r$  receive antennas configuration. The coding rule in (2.3) is applied to the codeword to be sent at time index  $2t$  and it involves the previously coded block as

$$\mathbf{s}_{2t} = (s_{2t} \ s_{2t+1}) = (c_{2t} \ c_{2t+1}) \begin{pmatrix} s_{2t-2} & s_{2t-1} \\ -s_{2t-1}^* & s_{2t-2}^* \end{pmatrix}. \quad (2.3)$$

As depicted in figure 2.1, once generating the codeword  $\mathbf{s}_{2t}$ , the transmitter applies the Alamouti's STBC to the differentially coded samples. Hence, at time index  $2t$ ,  $s_{2t}$  and  $s_{2t+1}$  are sent from antennas one and two respectively, while  $-s_{2t+1}^*$  and  $s_{2t}^*$  are sent at time index  $2t + 1$ .

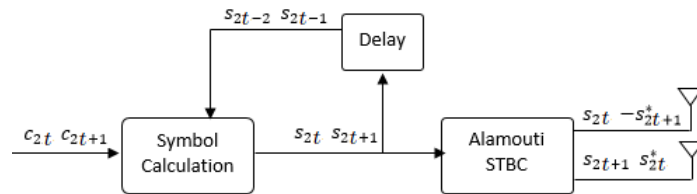


Figure 2.1: Differential Alamouti STBC block diagram.

Assuming a constant channel over two consecutive data symbols (fading conditions can be considered constant), the received signal in equation (2.6) can be rewritten as:

$$\mathbf{r} = \mathbf{s}\mathbf{H} + \eta, \quad \mathbf{H} = \begin{pmatrix} h_1 & -h_2^* \\ h_2 & h_1^* \end{pmatrix}, \quad (2.4)$$

where  $\mathbf{r} = (r_{2t} \ r_{2t+1}^*)$ ,  $\mathbf{s} = (s_{2t} \ s_{2t+1}^*)$ ,  $\eta = (\eta_{2t} \ \eta_{2t+1})$ ,  $\eta_{2t}$  and  $\eta_{2t+1}$  are independent AWGN. At the receiver, a non-coherent differential detection with low complexity, as proposed in [52], is carried to decode the source symbols sent from each transmit antenna ( $c_{2t} \ c_{2t+1}$ ) as  $\hat{c}_{2t} = \langle (r_{2t-2}, r_{2t-1}^*), (r_{2t}, r_{2t+1}^*) \rangle$  and  $\hat{c}_{2t+1} = \langle (r_{2t-1}, -r_{2t-2}^*), (r_{2t}, r_{2t+1}^*) \rangle$ .

It was shown in [52] that the differential MIMO system works 3 dB poorer than the coherent decoder [53] with perfect channel knowledge. Naturally, it is expected that the performance of this scheme degrades in frequency-selective channels. However, the combination of differential Alamouti STBC (as previously described) with the OFDM multi-carrier technique mitigates this effect [54]. This solution is adopted in the remaining of this chapter.

## 2.3 Related Works

Accurate synchronization is required in OFDM systems for correct demodulation [18]. Among existing synchronization techniques, some techniques exploit the redundancy in the CP [58]–[60], for blind synchronization, which is more suited to continuous flow transmissions. Other techniques use preambles with specific structures to which tailored metrics are designed [19, 22, 23, 61–63]. These approaches, known as data-aided synchronization methods, cost in terms of bandwidth but are generally more efficient than blind ones, especially for bursty packet traffic [22], [23]. The works in [61], [18], and [19] for example, use training symbols with repetitive structures (two identical halves in [61], [18], and [19], and 4 identical parts in [62]) and estimates the preamble start from the auto-correlation based metrics of the received signal. These methods are simple and have low implementation complexity. However, the estimation variance is very large due to the plateau in the timing metric, which becomes larger than the CP length when there are more than two repeated preamble sub-sequences. The works in [62]–[65] investigate time and frequency synchronization problem for MIMO-OFDM systems applied for the WiFi standards IEEE 802.11. The authors of [62] and [63] use a simple MIMO extension of Schmidl’s synchronization algorithm [61]. Further, in [64, 65], three-step synchronization

schemes are proposed. For coarse timing synchronization, the algorithms use a sliding window differentiator after a conventional auto-correlation metric so that the timing ambiguity caused by the auto-correlation metric plateau can be removed. For fine timing synchronization, a metric called signal-to-interference ratio (SIR) is derived based on the cross-correlation output in a small search window, which is around the estimated coarse timing position. Thus, a more precise timing estimation is acquired based on this metric. In the third step, the frame timing is refined in a small window around the estimation from the second step, based on a threshold operation whose aim is to distinguish the first path from the fake paths caused by noise.

Data-aided synchronization approaches are also used in LTE standards, that initially provide specifically designed synchronization signals, known as Primary Synchronization Signal (PSS) and Secondary Synchronization Signal (SSS) [21]. We here focus on the primary synchronization process that includes time synchronization and Sector Identifier (S-ID) recovery, which involves the PSS generated from ZC sequences. Several research works have been done on this issue. Some approaches propose new synchronization signals which are not compliant with the LTE signal [66, 67], while others exploit dedicated synchronization signals and tailor specific metrics to them [69]- [71]. The approaches in [69]- [71] exploit the redundancy in the CP to accomplish symbol start detection in a blind manner. Then, the S-ID is determined through cross-correlating the three local known PSS sequence candidates to the frequency-domain extracted OFDM symbols. In [69], non-differential correlation and differential correlation are used for long and short channel delay spreads respectively, while only differential correlation is used in [70] and [71].

## 2.4 Time and Frequency Synchronization for WiFi Standard

In this section, we focus on synchronization for the standard IEEE 802.11n. In particular, we study the application of the two-stage Reduced-Complexity (RC) method proposed in [24, 25], which exploits a preamble with repetitive structure and different sequence types [51]. The RC method showed a good trade-off between complexity and detection accuracy in single antenna OFDM systems and is here applied to the WiFi standard considering single antenna configuration in [68], and multiple antenna configuration in [29] based on the work in [28].

### 2.4.1 IEEE 802.11n System Description

Wireless LANs (WLANs) based on the IEEE 802.11n standard is high performance successor to the older 802.11a/g standards whose initial aim was to achieve 600 Mbps reached through several physical (PHY) layer digital communication techniques and Medium Access Control (MAC) layer protocols [72], [68]. We consider a MIMO-OFDM system with  $N_t$  transmit antennas and  $N_r$  receive antennas which respects the IEEE 802.11n standard that incorporates three mechanisms to exploit the spatial diversity available in multiple configurations, namely, STBC [53], Spatial Division Multiplexing (SDM) [73], and Cyclic Delay Diversity (CDD) [74]. Whilst SDM increases the throughput by sending independent data streams through the different transmit antennas, STBC and CDD are used to improve the reception reliability and hence the system performance. To help the receiver accomplish synchronization, the standard uses a preamble that has the same structure as in the IEEE 802.11a/g standards [75] for compatibility with old devices.

#### 2.4.1.1 Preamble Structure

The 802.11n standard defines the High Throughput (HT) Mixed Format (MF) preamble, which is divided into two parts: (1) the first part is legacy compatible with devices that implement the 802.11a/g amendments; (2) the second part contains the HT fields. The MF mode is mandatory for 802.11n devices for compatibility with IEEE 802.11a/g amendments [68]. The HT-MF preamble, on which we focus, is presented in figure 2.2. The legacy preamble contains the legacy short training field (L-STF), the Legacy Long Training Field (L-LTF), and the Legacy Signal Field (L-SIG). The first one is composed of ten identical short symbols denoted by  $t_1$  to  $t_{10}$ , each of length 16 samples ( $0.8\mu s$ ), and used for packet detection, automatic gain control, and gross time and frequency synchronization. The L-LTF is composed of two identical long symbols  $T_1$  and  $T_2$ , of length 64 samples each ( $3.2\mu s$ ), extended with a 32-sample CP ( $1.6\mu s$ ). These symbols are generally used for fine time and frequency synchronization and channel estimation. The total preamble length is 320 samples ( $16\mu s$ ) [76].

In addition to synchronization, the preamble is exploited for multiple processing in the receiver including automatic gain control level setting and channel estimation. The training preamble is followed by the signal field and data.

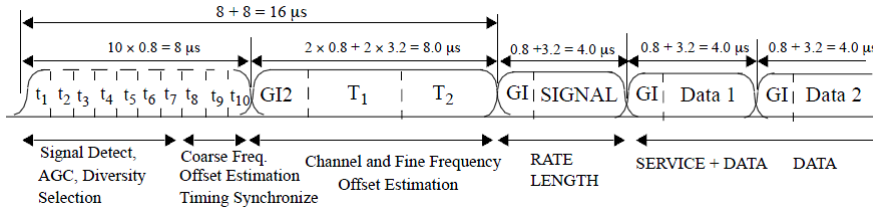


Figure 2.2: IEEE 802.11a/g/n preamble structure.

Thanks to the IEEE 802.11n preamble repetitive structure, several synchronization techniques, initially proposed for the OFDM systems, can be applied to it [29]. In the remaining of this chapter, we assess the suitability of the RC technique [24] to achieve synchronization exploiting the L-STF composed of ten identical parts. The choice of the L-STF provides an early time synchronization to allow the processing of the other tasks (carrier frequency offset estimation, channel estimation) that use the other preamble parts.

#### 2.4.1.2 Cyclic Delay Diversity

In IEEE 802.11n systems, the HT device supports spatial multiplexing and the preamble is a single stream signal. To transmit the legacy preamble using all available antennas without undesirable effects (power loss, undesirable beamforming effects), the solution is to use a CDD scheme to decorrelate the signal transmitted at different antennas. In other words, CDD is used to avoid the unintentional beamforming effect which arises when multiple copies of the same signal are transmitted through different antennas [55]. The use of a CDD scheme creates pseudo-path in the received signal which can cause further degradation in the synchronization accuracy [74].

In this case, the OFDM signal  $s_i$  transmitted from the  $i^{\text{th}}$  antenna is a cyclic delay shifted version of the original modulated signal with a delay  $d_i$ . The shift of the signal transmitted from the first antenna is generally set to 0. The transmitted signal then becomes

$$s_i(k) = s_0(\text{mod}(k + d_i, N_u)), \quad (2.5)$$

where  $N_u$  denotes the number of sub-carriers and  $\text{mod}$  denotes the modulo function. The received signal at the  $j^{\text{th}}$  receive antenna after multipath channel propagation results from the

summation of the  $N_t$  transmitted signals and is expressed as

$$r_j(k) = e^{j2\pi\nu k/N} \sum_{i=1}^{N_t} \sum_{l=0}^{N_H-1} h_{i,j}(l)s_i(k-l) + \omega_j(k), \quad (2.6)$$

where  $h_{i,j}(l)$  is the  $l^{\text{th}}$  sampled complex channel impulse response between the  $i^{\text{th}}$  transmit antenna and the  $j^{\text{th}}$  receive antenna.

In the IEEE 802.11n systems, STBC is an optional functionality used to map Spatial Streams (SS) to space-time streams (STS), while CDD is necessary to decorrelate the signals transmitted at each STS to mitigate the undesirable beamforming effects [76]. The number of SS and STS are denoted by  $N_{SS}$  and  $N_{STS}$ , respectively. In this work, we investigate the STBC scheme with  $N_{SS} = 1$  and  $N_{STS} = 2$ . Although it is not explicitly specified, the considered standard opts for the Alamouti STBC scheme [53], [28].

## 2.4.2 Reduced-Complexity Synchronization

The RC technique aims to provide a high detection accuracy while reducing the computational load by combining the sliding and differential correlations and splitting the synchronization processing into two stages [24], [25].

### 2.4.2.1 Coarse stage

Coarse time acquisition consists on finding the preamble start over an approximate range of samples [28]. To this aim, a two identical part preamble is required. Exploiting the L-STF preamble, two ways to split it into two parts are possible: (1) two parts of five short symbols; (2) two parts of four short symbols extended with a CP composed of two short symbols as in [57].

The coarse synchronization is achieved by auto-correlating the received signal using a shift equal to the preamble repetitive part length ( $N_u/2$ ), respecting the algorithm in [61] as

$$M_c^j(k) = \sum_{m=0}^{N_u/2-1} r_j(k+m)r_j^*(k+m+N_u/2), \quad (2.7)$$

The coarse time estimate is chosen as the argument that maximizes  $|M_c^j|$  and is denoted by  $\hat{\tau}_c$ . This metric can be implemented in a recursive way to reduce the computational complexity as explained in [61]. When using more than one receive antenna, the correlation outputs of different antennas are combined to improve the performance in a way similar to Maximum Ratio Combining (MRC) as below

$$M_c(k) = \sum_{j=1}^{N_r} M_c^j(k). \quad (2.8)$$

The coarse metric is drawn in figure 2.3 using the two introduced subdivisions of the L-STF. It is shown that using five short symbols as the preamble repetitive part leads to a wide shape metric with a single peak that corresponds to the start of the preamble. On the other hand, when considering a CP in the preamble, we note that the coarse metric exhibits a plateau whose length is equal to that of the CP length. The plateau effect makes the estimation error very large leading to uncertainty in the preamble start detection, especially in noisy environments. To overcome this limitation, we here opt for the first subdivision (five short symbols in each preamble half).

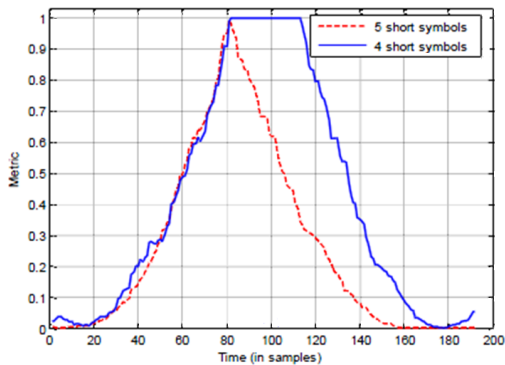


Figure 2.3: Coarse metric under noiseless conditions using different subdivisions.

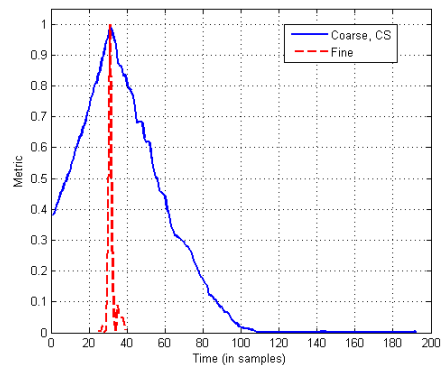


Figure 2.4: Coarse and Fine metrics under noiseless conditions.

### 2.4.2.2 Fine stage

The fine time synchronization aims to detect the exact preamble start position around the coarse time estimate [28]. To this aim, a differential correlation-based metric with a correlation shift  $q$  different from the preamble repetitive part length is processed over a reduced interval

centered on  $\hat{\tau}_c$ , which we refer to as the uncertainty interval  $\Delta\tau$  as in [56] and [57]. The fine metric is given by

$$M_f^j(k) = \sum_{m=0}^{N_u/2-1} r_j(k+m)r_j^*(k+m+q)p(m)p^*(m+q), \quad q \in [1, \dots, N_u/2-1], \quad (2.9)$$

where  $p(m)$  stands for the  $m^{\text{th}}$  preamble sample. The preamble fine start estimate  $\hat{\tau}_f$  is chosen as the argument that maximizes the metric amplitude  $|M_f^j|$ . A judicious choice of the correlation shift  $q$  such to be equal to the delay  $d_i$  allows avoiding the pseudo-path problem caused by the CDD scheme.

The fine timing metric is drawn in figure 2.4, for an uncertainty interval  $\Delta\tau$  equal to a short symbol length. We note that it provides an extremely high sharp peak compared to the coarse one, which greatly enhances the detection accuracy.

### 2.4.2.3 Fractional Frequency Offset Estimation

The FFO estimation is here based on the algorithms in [29] which is deduced from the timing metric phase at the preamble start estimate that had already proved its accuracy under different scenarios [56], [57]. We recall that the FO causes a shift of the information signal leading to a phase rotation. It then follows that all summed terms have a constant phase within the two preamble parts. Hence, we can estimate the FFO by determining the actual phase of the coarse timing metric at the estimated preamble start as

$$\hat{\nu} = \frac{1}{\pi} \angle M_f(\hat{\tau}_f). \quad (2.10)$$

As the estimation range of the phase is limited to  $[-\pi, \pi]$ , the FO estimation range provided in equation (2.10) is limited as well to its fractional part only, which we denote by  $\hat{\nu}$ .

### 2.4.3 Performance Evaluation

We use Matlab simulations ( $10^4$  Monte Carlo trials) to evaluate the synchronization technique, showing the Correct Detection Rate (CDR) of the preamble start and the Mean Squared Error

(MSE) of the FFO estimate. The CDR is evaluated as the rate of trials where  $\hat{\tau}_f$  coincides with the correct preamble start. The obtained results are compared with the three-stage algorithm proposed by Wang *et al.* in [64].

The system parameters are fixed respecting the standard IEEE 802.11n [76] for the 20MHz bandwidth using QPSK modulation:  $N_u=64$ ,  $N_g = 16$ ,  $CDD=[0, 8]$ . The normalized frequency offset  $\nu$  is set to 0.4 sub-carrier spacing. The simulations are carried out for different SNR values and under the multipath Rayleigh standardized  $2 \times 2$  MIMO channel B [77] in section 2.4.3.1, while Rayleigh-fading  $2 \times 1$  and  $2 \times 2$  MIMO channel models are considered in section 2.4.3.2.

### 2.4.3.1 Performance with CDD

Figure 2.5 illustrates the CDR of the coarse and fine estimators of the RC technique and Wang's estimator. As in the general case of OFDM system [24], the considered RC approach provides satisfactory detection accuracy and it outperforms the considered benchmark. Indeed, the detection is good for most of practical SNR values and it becomes perfect (CDR=100%) above an SNR of 6 dB. The approach of Wang provides a lower detection rate for all SNR ranges, and it exhibits a loss of about 5 dB for a target CDR equal to 90%. The coarse synchronization provides the lowest CDR, which is expected due to the metric shape. The obtained performance ensures the suitability of the RC approach for time synchronization in the IEEE 802.11n system.

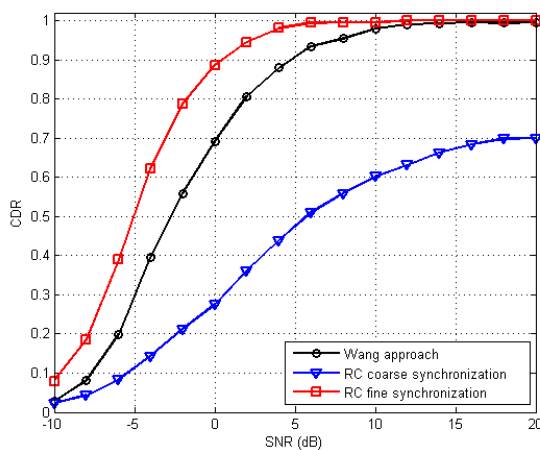


Figure 2.5: CDR of the preamble start.

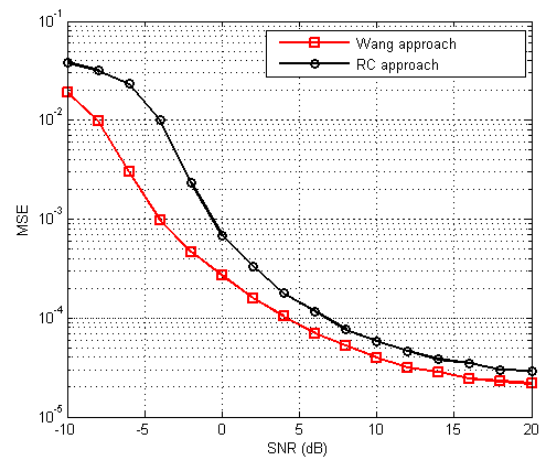


Figure 2.6: MSE of the FFO.

Figure 2.6 presents the mean squared error of the fractional frequency offset estimate. We

note that Wang's technique also allows the estimation of the FFO through the evaluation of the metric phase at the preamble start estimate respecting the algorithm of Schmidl and Cox [61] recalled in (2.10). Figure 2.8 shows that the RC estimator provides lower MSE which decreases to  $2 \cdot 10^{-5}$  sub-carrier spacing for high SNR values and realizes a gain of about 5 dB compared to the estimator of Wang. It is worth to mention that, even if the same estimator is used in both of the compared techniques, the RC technique outperforms the considered benchmark. This is due to a more accurate time estimation provided by the RC approach. We also observe that, consistently with the previous results, the low estimation error of the FFO ensures the suitability of the RC approach for frequency synchronization in the IEEE 802.n standard [29], which was also confirmed for any OFDM system [56].

#### 2.4.3.2 Performance with STBC

Figure 2.7 draws the CDR of the compared synchronization techniques. As expected, it is obvious that the synchronization becomes significantly more robust if full-spatial diversity is exploited through the use of space time coding in the proposed scheme. Moreover, exploiting differential STBC avoids any channel estimation requirements. Figure 2.7 shows that at very low SNR values, the compared schemes provide close detection performance. At higher SNR values, the proposed technique outperforms Wang's scheme and realizes a gain of about 4 dB for a target CDR of 90% in both MIMO configurations ( $2 \times 2$  and  $2 \times 1$ ). We also note that the use of a second receive antenna enhances the detection accuracy, and offers a gain of about 2 dB in the proposed scheme as well as the considered benchmark. Furthermore, at high SNR values, both compared schemes provide perfect detection with CDR equal to 100%.

Figure 2.8 presents the mean squared error of the fractional frequency offset estimate. Wang's technique also allows the estimation of the FFO through the evaluation of the metric phase at the preamble start estimate respecting the algorithm of Cox and Schmidl [61] recalled in (2.10). Even if the same estimator is used in both of the compared techniques, the proposed one outperforms the considered benchmark, due to a more accurate time estimate. It is shown in figure 2.8 that the proposed estimator provides the lowest MSE for  $2 \times 2$  configuration, which reduces to  $2 \cdot 10^{-5}$  sub-carrier spacing for high SNR values and realizes a gain of about 5 dB compared to the other estimator. Using a  $2 \times 1$  configuration, the proposed estimator provides almost the same performance as Wang's estimator for  $2 \times 2$  configuration. Wang's estimator has the highest error using a single receive antenna.

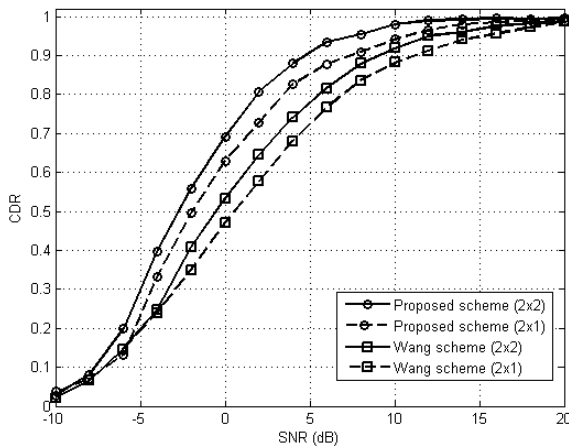


Figure 2.7: CDR of the preamble start.

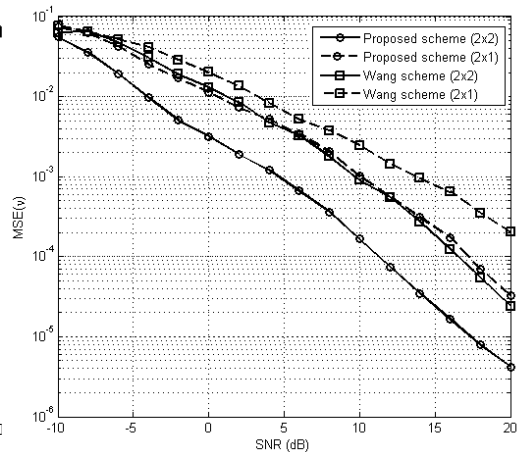


Figure 2.8: MSE of the FFO.

## 2.5 Primary Synchronization for LTE Standard

LTE is a broadband wireless communication standard that supports both Frequency Division Duplexing (FDD) and Time Division Duplexing (TDD) modes [86]. The combination of OFDM and MIMO techniques allows high data rate in a harsh propagation environment [46]. To access the LTE network, a User Equipment (UE) has to follow the access procedures that mainly consist in time and frequency synchronization, cell search, and acquisition of other useful system parameters (cyclic prefix length, access mode...). To this aim, the UE exploits the Primary Synchronization Signal (PSS) and the Secondary Synchronization Signal (SSS) broadcasted regularly in each cell.

In this section, we study the performance of the primary Synchronization approaches initially proposed in [27] and [26]. In particular, we explicitly take into account the effect of the FO on time synchronization performance to assess the FO-combatting capabilities of the studied approaches. To this aim, theoretical analysis as well as simulations are carried out and compared to validate the obtained results. Moreover, we evaluate the two approaches in LTE system parameters with multiple antenna configuration and under standardized channel models (EPA and ETU).

### 2.5.1 LTE System Description

The LTE as defined by the 3GPP is an innovative wireless communication standard that provides peak rates of at least 100 Mbps and 50 Mbps for DL and UL respectively and it supports scalable bandwidth from 1.4 MHz to 20 MHz. By offering a highly flexible radio interface, LTE suits the needs of different network operators that have different bandwidth allocations. Thanks to its robustness to frequency-selective channels, the OFDM technique is used for the DL transmission [46]. For the UL, where the available transmission power is significantly lower than that for the DL, single-carrier transmission based on DFT-precoded OFDM, also referred to as single-carrier frequency-division multiple access (SC-FDMA) [78].

Before a UE can communicate through an LTE network it has to acquire synchronization to a cell within the network. Precisely, it should accomplish primary synchronization which consists in detecting the PSS start and determining the S-ID. There are 504 different physical-layer cell-ID which are grouped into 168 groups identified by a number  $N_{ID}^{(1)}$  (ranging from 0 to 167), where each group consists in three identities specified by a number  $N_{ID}^{(2)}$  (ranging from 0 to 2). The cell-ID is determined as

$$C_{ID} = 3N_{ID}^{(1)} + N_{ID}^{(2)}. \quad (2.11)$$

The parameter  $N_{ID}^{(2)}$  represents the sector identifier (S-ID) of each cell, which is strongly related to the PSS, whereas the parameter  $N_{ID}^{(1)}$  represents the physical-layer group identifier and is sent on the SSS.

#### 2.5.1.1 Downlink Frame Structure

In LTE systems, the transmitted signal is organized into radio frames of  $10ms$  duration, each consisting of 10 sub-frames of length  $1ms$  which are further divided into two slots of  $0.5ms$  each as shown in figure 2.9. We note that depending on whether normal or extended CP is used, a slot contains 7 or 6 OFDM symbols of duration equal to  $66.7\mu s$  each among them two symbols for the PSS and the SSS sent regularly in the last two OFDM symbols of slot 0 and slot 10. Transmitted data are mapped on a time-frequency resource grid consisting of elementary units, called resource blocks, defined as 12 consecutive 15kHz sub-carriers over one slot. The first symbol in each frame has a longer CP with a length denoted by  $N_{g1}$  [46].

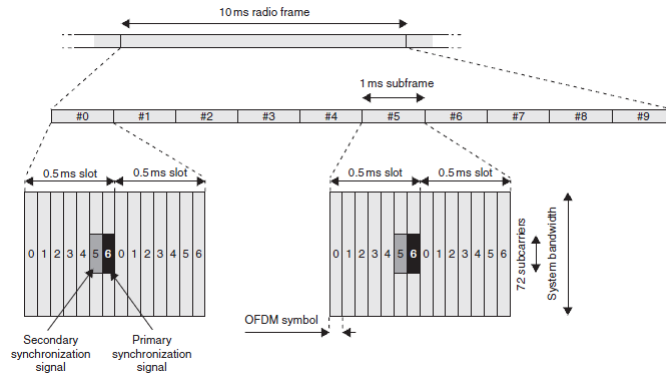


Figure 2.9: LTE frame structure in the FDD mode: 7 OFDM symbols with normal CP [46].

### 2.5.1.2 Primary Synchronization Signal (PSS)

In one cell, the two PSSs within a frame are identical. The PSS is generated from one of three known ZC sequences with length  $N_{zc} = 63$  and root index  $u \in \{25, 29, 34\}$ , which corresponds to the S-ID  $N_{ID}^{(2)} \in \{0, 1, 2\}$  [87]. ZC sequences that we here denote by  $d_u(n)$  are complex exponential sequences generated respecting the equation below

$$d_u(n) = e^{-j \frac{\pi u n(n+1)}{N_{zc}}}, 0 \leq n \leq N_{zc} - 1. \quad (2.12)$$

During resource mapping, the 32<sup>nd</sup> sample is omitted to avoid modulating the DC sub-carrier and only 62 samples of the ZC sequence are mapped on the 62 centered sub-carriers in the transmission bandwidth. The PSS is then generated in time domain using an IFFT of size  $N_u$ . The size of the IFFT, as well as the number of sub-carriers set to zero in both sides of the ZC sequence depend on the system bandwidth [79]. Furthermore, the PSS occupies 6 resource blocks which makes 72 sub-carriers for it (five resource elements at each side of the synchronization sequence are set to zero) [46]. The corresponding time-domain signal can be generated using an IFFT of size  $N_u$ . The size of the IFFT depends on the system bandwidth. In our work, we exploit the duality between ZC sequences in time and frequency domains, which states that the IFFT of a ZC sequence remains a ZC sequence [84] that allows applying the SD approach to LTE signal.

## 2.5.2 Simply-Differential Synchronization

The SD approach, initially proposed in [27], achieves time synchronization by locating the ZC sequence position within the received signal. When applied to LTE systems, the SD metric fulfills both coarse PSS start detection and sector search in a sole stage. The joint detection is a particularity in the SD approach when compared to several existing primary synchronization approaches.

### 2.5.2.1 Simply-Differential Metric

The SD metric is based on differential correlation carried out onto the received signal. Observing the correlation outcome of the  $l^{\text{th}}$  received sample with its  $q$ -shifted counterpart, which we denote by  $M_{SD}(l) = r(l)r^*(l - q)$ , along the received signal. For independent samples, the correlation outcome is very low. However, when the received samples fall within the ZC sequence, and under noiseless conditions and ideal channel, the correlation output is given by

$$M_{SD}(l) = e^{-j\frac{\pi u l(l+1)}{N_{zc}}} e^{j\frac{\pi u(l-q)(l+1-q)}{N_{zc}}} = e^{-j\frac{\pi u(2ql-q^2+q)}{N_{zc}}} = e^{-j\frac{\pi u(2ql)}{N_{zc}}}. \quad (2.13)$$

In this case, when compensating  $M_{SD}(l)$  with its complex conjugate  $e^{j\frac{\pi u(2ql)}{N_{zc}}}$ , the resulting output turns into a constant value. Hence, the addition of differentially correlated and compensated elements sums constructively and allows the localization of the ZC sequence position within the received signal. We, then, define the SD metric  $M_{SD}^u$ , that sums the adjusted elements along  $N_{zc}$  adjacent samples as

$$M_{SD}^u(k) = \left| \sum_{l=0}^{N_{zc}-1} M_{SD}(k+l) e^{j\frac{\pi u(2q(l+k))}{N_{zc}}} \right|, \quad (2.14)$$

This metric was shown to provide high accuracy with low complexity achieved through a recursive implementation that reduces the number of complex multiplication required to evaluate the metric  $M_{SD}^u(k)$  from  $2N_{zc}$  to only 4 with additional 2 complex addition operations whose computational load is trifling compared to multiplication operations [27].

When applied to the LTE signal, the SD metric exhibits a plateau due to the CP insertion. To mitigate this effect, the approach proceeds to a second stage, in which the PSS located in

the received signal is cross-correlated with the local known ZC sequence  $D_u = \text{IFFT}(d_u)$  as

$$M_F^u(k) = \left| \sum_{l=0}^{N_u-1} r(k+l)D_u^*(l) \right|. \quad (2.15)$$

The fine metric  $M_F^u$  is here calculated over a short interval  $I$  centered on the coarse estimate and the fine PSS start estimate is selected as the argument that maximizes (2.15) as

$$\hat{\tau} = \underset{k \in I}{\operatorname{argmax}} \{M_F^u(k)\}. \quad (2.16)$$

Figure 2.10 presents the SD and DD coarse metrics drawn for LTE signal parameters ( $N_u = 2048$ ,  $N_g = 144$ ). It is shown that the metrics keep their triangular shapes, yet with an aperture wider than that of the time-domain based metrics. The DD metric localizes the PSS start regardless of the ZC training sequence, while the SD metric localizes the PSS start for the effectively transmitted ZC sequence. Indeed, only one among the three SD calculated metrics clearly shows the PSS position, which here corresponds to the sequence generated using the root  $u = 25$ . We also note that, due to the CP extension, the metrics exhibit a plateau, whose effect is mitigated by opting for the second stage in both approaches, which enhances the detection accuracy.

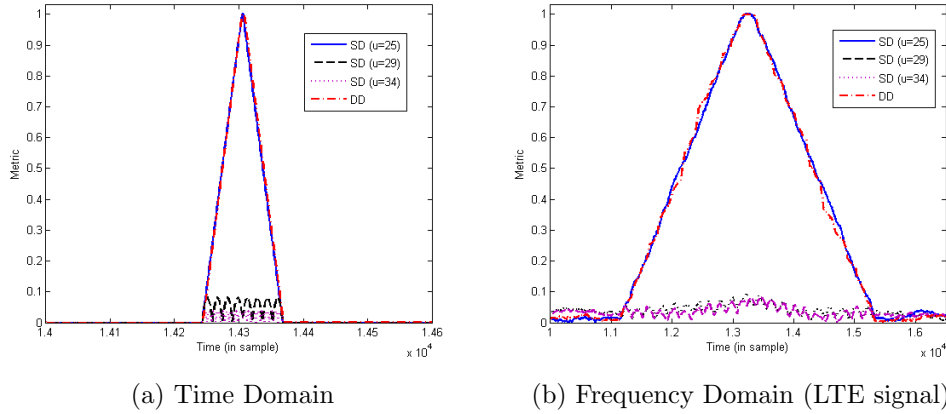


Figure 2.10: The proposed coarse DD and SD metrics for time domain and frequency domain based ZC sequences under noiseless conditions.

### 2.5.2.2 Impact of the Frequency Offset on the Metric

Now, to assess the impact of a frequency offset on the SD timing metric, we consider that the received signal is affected by a frequency offset  $\nu$ , and analyze its effect. In this case, the expression of  $M_{SD}$  in equation (2.13), for time index  $l$  belonging to the ZC sequence, turns into

$$\begin{aligned} M_{SD}(l) &= e^{-j\frac{\pi ul(l+1)}{N_{zc}}} e^{j\frac{2\pi \nu l}{N_{zc}}} e^{j\frac{\pi u(l-q)(l+1-q)}{N_{zc}}} e^{-j\frac{2\pi \nu(l-q)}{N_{zc}}} = e^{-j\frac{\pi u(2ql-q^2+q)}{N_{zc}}} e^{j\frac{2\pi \nu q}{N_{zc}}} \\ &= e^{-j\frac{\pi u(2ql)}{N_{zc}}} e^{j\frac{2\pi \nu q}{N_{zc}}}. \end{aligned} \quad (2.17)$$

We note that, at the correlator output, the same expression obtained in (2.13) appears here, yet with an additional term including the frequency offset  $\nu$ . Hence, the timing metric  $M_{SD}^u$  in (2.14), that compensates  $M_{SD}(l)$  with the adjustment term  $e^{j\frac{\pi u(2ql)}{N_{zc}}}$  leads to a constant value multiplied by the factor  $e^{j\frac{2\pi \nu q}{N_{zc}}}$  that also encompasses  $\nu$ . The residual term in the timing metric demonstrates the sensitivity of the SD metric to the FO, which leads to performance degradation.

### 2.5.3 Doubly-Differential Synchronization

The DD approach, initially proposed in [26], locates a ZC sequence pattern within the received signal regardless of the root used to generate the ZC training sequence. The calculated metric correlates consecutive samples and it allows the compensation of any frequency offset, which is a main feature in this approach. When applied to the LTE signal, the DD approach requires two stages to achieve primary synchronization. The first stage aims to roughly detect the PSS start while the second stage provides the S-ID using conventional cross-correlation based metric. Detecting the PSS start from the first step allows performing the sector search processing over only one symbol instead of being carried over all symbols as done in conventional approaches.

#### 2.5.3.1 Doubly-Differential Metric

The DD metric is also based on differential correlation. Let us define the sequence  $M_{DD}$  resulting from doubly-differential correlation of the received samples as

$$M_{DD}(l) = [r(l)r^*(l-q)][r(l-1)r^*(l-1-q)]^*, \quad (2.18)$$

where  $q$  stands for the correlation shift that is arbitrarily chosen in the range of  $[1, N_{zc} - 1]$ . For independent samples, the differential correlation output has low value. Whereas, for samples falling within a ZC sequence, and under noiseless conditions and ideal channel,  $M_{DD}(l)$  turns into

$$M_{DD}(l) = d_u(l)d_u^*(l-q)d_u^*(l-1)d_u(l-1-q) = e^{-j\frac{2\pi ul}{N_{zc}}} e^{j\frac{2\pi u(l-q)}{N_{zc}}} = e^{-j\frac{2\pi uq}{N_{zc}}}. \quad (2.19)$$

We note that the DD correlated terms  $M_{DD}(l)$  are independent of  $l$  and they are all equal to the constant value  $e^{-j\frac{2\pi uq}{N_{zc}}}$  for samples belonging to a ZC sequence. Hence, we define the timing metric  $M_{DD}$  as the sum of the correlation output along the ZC sequence length as

$$M_{DD}(k) = \left| \sum_{l=0}^{N_{zc}-1} M_{DD}(k+l) \right|. \quad (2.20)$$

The metric  $M_{DD}$  sums constructively and, as shown in figure 2.10, its amplitude exhibits a triangular shape that reaches its maximum at the ZC sequence start where it sums over all ZC sequence elements. Note that  $u$  is unknown in practice. This metric was also implemented through a recursive formula to lower its complexity, which was reduced from  $3N_{zc}$  complex multiplication operations to only 6.

When applied to the LTE signal, the DD in 2.20 only localizes the arrival time of a ZC sequence within the received signal. Hence a second stage is required to provide the exact PSS start and the S-ID. A cross-correlation metric respecting (2.15) is calculated three times involving the three local PSS candidates  $D_u$ . The sequence  $D_u$  that provides the highest peak identifies the S-ID by the root  $u$  while the time index that maximizes the selected metric indicates the PSS start estimate as

$$\{\hat{u}, \hat{\tau}\} = \underset{u, k \in I}{\operatorname{argmax}} \{M_F^u(k)\}. \quad (2.21)$$

As in the SD approach, the fine stage is here carried over a short interval centered on the coarse PSS start estimate.

### 2.5.3.2 Impact of the Frequency Offset on the Metric

To analyze the impact of the frequency offset on the DD metric, we hereafter consider the received signal in equation (2.6) affected by the frequency offset  $\nu$ . Similarly to the noiseless case, the correlation of data symbols here leads to very low values. When correlating samples belonging to a ZC sequence, the correlation output  $M_{DD}$  of the  $l^{\text{th}}$  sample is given by

$$\begin{aligned}
 M_{DD}(l) &= \left[ d_u(l) e^{j \frac{2\pi\nu l}{N_{zc}}} d_u^*(l-q) e^{-j \frac{2\pi\nu(l-q)}{N_{zc}}} \right] \left[ d_u^*(l-1) e^{-j \frac{2\pi\nu(l-1)}{N_{zc}}} d_u(l-1-q) e^{j \frac{2\pi\nu(l-1-q)}{N_{zc}}} \right] \\
 &= e^{-j \frac{2\pi\nu l}{N_{zc}}} e^{j \frac{2\pi\nu(l-q)}{N_{zc}}} e^{j \frac{2\pi\nu(2l-1-q)}{N_{zc}}} e^{-j \frac{2\pi\nu(2l-1-q)}{N_{zc}}} \\
 &= e^{-j \frac{2\pi\nu q}{N_{zc}}}.
 \end{aligned} \tag{2.22}$$

We here note that, although the received signal is affected by a frequency offset, the correlation output  $M_{DD}$  reduces to its expression in the case where no FO is present as in equation (2.19). This latter corresponds to the constant  $e^{-j \frac{2\pi\nu q}{N_{zc}}}$ , which is independent of the time index  $l$ . As a result, the effect of the frequency offset is totally eliminated without additional processing.

The analysis of the frequency offset impact on the DD metric proves its immunity to any frequency offset when the correlated samples fall within the ZC sequence. This would greatly enhance the time detection accuracy.

### 2.5.4 Performance Evaluation

In this section, we evaluate the performance of the presented primary synchronization approaches for PSS start detection and S-ID recovery through Monte Carlo simulation carried over  $10^4$  trials. Time synchronization is evaluated in terms of PSS start Correct Detection Rate (CDR), defined as the percentage of realizations where the estimated time index coincides with the correct PSS start ( $\hat{\tau} = \tau$ ). Sector search is evaluated in terms of S-ID Failure Detection Rate (FDR), defined as the percentage of realizations for which an isolated sector is recovered. The erroneous detection corresponds to the case where one of the other correlation terms generates a peak higher than the peak corresponding to the actual sector.

### 2.5.4.1 Simulation Parameters

We consider the 20 MHz LTE communication system with 2 antennas at the transmitter and 2 antennas at the receiver with normal CP transmission mode. For the chosen sampling rate 30.72 MHz, each OFDM symbol is composed of  $N_u = 2048$  samples, modulated from a set of QPSK constellation, and is extended with a CP of length  $N_g = 144$  samples. The first symbol of each slot has larger CP of length  $N_{g_1} = 160$  samples. The correlation shift  $q$  used to evaluate the DD approach is set to 1, while three different shifts used in the SD approach are set to  $\{32, 162, 162\}$  and the adjustment frequency  $\delta = \frac{u'q}{N_u}$  to  $\{5, 2, 2046\}$ . The fine stage is calculated over a short interval around the coarse PSS start estimate of length equal to the CP length  $N_g$ . To assess the effect of the FO on synchronization performance, we consider an error  $\nu = 0.4$  sub-carrier spacing and compare the detection accuracy provided for the indicated  $\nu$  value and a zero-valued one.

Table 2.1: LTE tapped-delay channel models parameters.

Tap no.	EPA Channel		ETU Channel	
	$\tau$ (ns)	SMR (dB)	$\tau$ (ns)	SMR (dB)
1	0	0.0	0	-1.0
2	30	-1.0	50	-1.0
3	70	-2.0	120	-1.0
4	90	-3.0	200	0.0
5	110	-8.0	230	0.0
6	190	-17.2	500	0.0
7	410	-20.8	1600	-3
8			2300	-5
9			5000	-7

To demonstrate the capability of the investigated synchronization approaches in challenging scenarios, we adopt standardized channel models. The LTE specifications defines an extension of the 3GPP and ITU models [88], resulting in the Extended Pedestrian A (EPA), Extended Vehicular A (EVA) and Extended Typical Urban (ETU) channel models to characterize three basic environments having low, medium and large delay spread, respectively. We consider the EPA and ETU channel models specified in TS 36.101 [89] and TS 36.104 [90] and summarized in table I.

### 2.5.4.2 PSS Detection Performance

Figure 2.11 displays the PSS start CDR in the case of EPA channel. We note that, overall, the compared approaches provide good time detection accuracy that becomes almost perfect at SNR values above 4 dB and 8 dB for the DD and the SD approaches, respectively. At very low SNR values (lower than -2 dB), we note that the SD estimator outperforms the DD one and, for a target CDR equal to 0.5, it realizes a gain of 5 dB that lessens as the SNR rises. For high SNR values, the CDR of the DD estimator increases fast and becomes higher than that provided by the SD approach. This latter is more advantageous in harsh propagation environment with low SNR. However, the DD approach is penalized by doubling the number of samples involved in the metric calculation, which doubles the noise energy resulting in poor detection at low SNR.

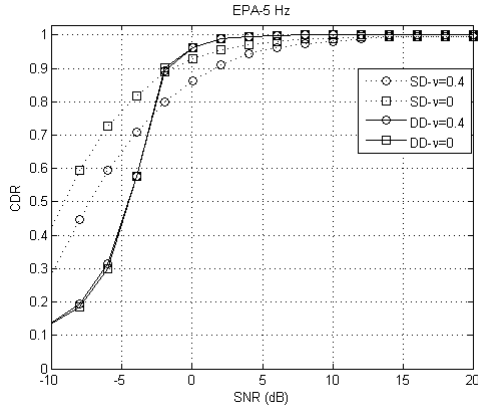


Figure 2.11: PSS start CDR in the EPA channel for different FO values.

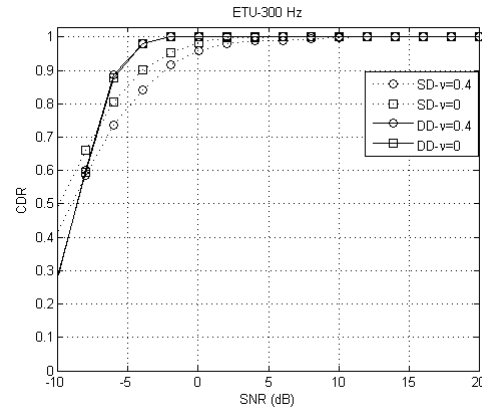


Figure 2.12: PSS start CDR in the ETU channel for different FO values.

The curves are drawn in figure 2.11 shed light on the impact of a FO on synchronization performance for each approach. On one hand, we record that the SD approach exhibits a loss of about 2 dB when the received signal is affected by a FO, whose value is here set to 0.4 sub-carrier spacing. On the other hand, the DD approach provides almost the same CDR at all considered SNR range regardless of the FO value. These results concord well with the analytical study carried for both approaches in sections 2.5.2.2 and 2.5.3.2, which shows the sensitivity of the SD metric and the immunity of the DD metric to frequency offsets.

To ensure the efficiency of the presented approaches, we now assess their performance in the ETU channel and depict the CDR in figure 2.12. We note that both approaches provide satisfactory detection accuracy which becomes near-perfect at SNR values about 4 dB and -2

dB for the SD and DD detectors, respectively. Consistently with the previous results provided for short channel delay spread, the SD detector here outperforms the DD detector for very low SNR values (lower than  $-4$  dB), due to high noise value in the DD metric. For higher SNR values, the detectors' behavior is switched and the DD one provides better detection accuracy thanks to its insensitivity to the FO effects. This property is ensured through the CDR curves that concord well along all the considered SNR range. However, the SD detector, whose metric is sensitive to the FO, provides worse CDR with a gap of about 1.5 dB when the offset  $\nu \neq 0$ .

In both of the considered channel models, the time synchronization performance provided by the presented approaches is globally good. Although the second fine stage is the same in both approaches, the performance results show a noteworthy gap in the detection accuracy. This gap is due to the coarse synchronization stages which carry different timing metrics with different features. Comparing the previously presented results depicted in figures 2.11 and 2.12, we observe that the SD approach and the DD approach are well suited for large delay spread channels. For example, we record gains of about 3 dB and 2 dB for a target CDR of 0.8 realized by the DD and the SD approaches respectively, between EPA and ETU channels.

### 2.5.4.3 Sector ID Search Performance

The performance is here provided in terms of FDR and is illustrated in figures 2.13 and 2.14 for the EPA and ETU channel models. In the first case, the recorded error is about 0.05, at very low SNR values, and it declines continuously to reach  $10^{-4}$  and  $10^{-5}$  for the SD and DD approaches, respectively. Along the considered SNR range, the SD detector outperforms the DD detector and it realizes a gain that increases as the SNR value becomes higher. It is worth to note that the effect of the FO on the sector detection is trifling. Indeed, the FDR is almost the same for the simulation scenarios where  $\nu = 0$  and  $\nu = 0.4$  sub-carrier spacing in both approaches.

The case of ETU channel model, depicted in figure 2.14, shows a similar trend in the S-ID acquisition performance when compared to the previous case (EPA channel model). Indeed, at very low SNR values, the SD approach performs better and achieves a gain of about 4 dB for an error equal to 0.05. For higher SNR values, the DD approach improves its S-ID detection that becomes perfect (FDR=0) at -4 dB, while the FDR provided by the SD approach vanishes at 0 dB. Once again, we note that the SD and DD sector recovery schemes are not sensitive

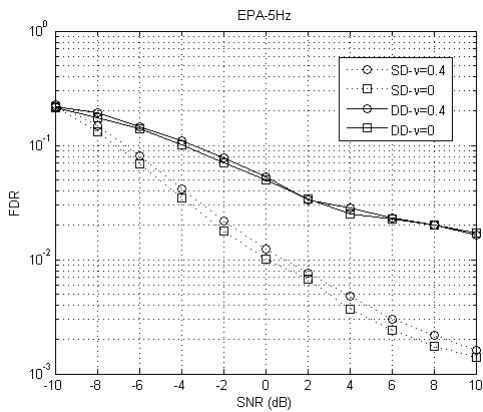


Figure 2.13: FDR of the SID in the EPA channel for different FO values.

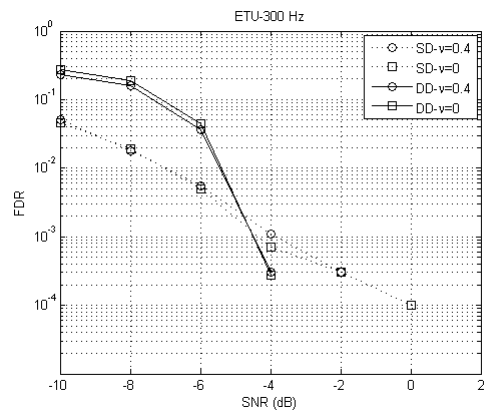


Figure 2.14: FDR of the SID in the ETU channel for different FO values.

to the FO as the FDR provided for different values of  $\nu$  are almost equal in both approaches.

The results presented in this section show the robustness of the DD and SD approaches in both channel models. However, they are well suited for channels with high mobility like the considered example of ETU channel, for which the FDR of the sector ID vanishes at very low SNR values. The DD detector is based on conventional algorithms [69]- [71] that consist in cross-correlating the received signal with the local known PSS candidates in either time or frequency domains, which provided poorer S-ID recovery performance [26]. The improvement recorded in the DD approach is due to the robustness of the DD coarse stage, which offers accurate PSS localization. Hence, the timing synchronization errors have a great impact on the DD S-ID recovery. However, the SD detector allows the S-ID recovery from the first stage which makes it independent from timing synchronization errors.

## 2.6 Time Synchronization for MTC over LTE System

Recently, there have been several works in extending the cellular systems with Machine MTC to support the emerging growth of IoT applications and services aiming to bring about billions of scattered connected devices [4]. The LTE is considered as a promising technology for cellular MTC as it provides mobility and connectivity along a wide coverage area [2,3]. As MTC defines a different set of requirements than the initial LTE system, namely low-rate, low-overhead, low-power consumption, and low-cost, the 3GPP has been working on numerous LTE features such as power saving, signaling reduction, overload control and complexity reduction to meet

new requirements [81]. These features hit the design of discovery methods, physical layer procedures, and radio resource management algorithms.

We here investigate the low-complexity SD synchronization approach proposed in [27] and described earlier. The contribution of this work is to assess the performance of the SD metric and ensure its synchronization capabilities for narrow-band LTE systems. Our study here exclusively concerns the coarse SD metric, and it is carried out through simulation and theoretical analysis to validate the obtained results. To this aim, the metric is first approximated by a Gaussian distribution, to which we have determined the mean and variance. Then, we derive the expression of the Probability of Correct Detection (PCD) in its closed-form expression.

### 2.6.1 Enhancement for MTC over LTE

In this section, we summarize features that are relevant to MTC, which have been standardized in different 3GPP releases, with the main focus on synchronization issues.

#### 2.6.1.1 LTE Cat-0 and Cat-M

Recently, the 3GPP achieved a major milestone to enhance network capabilities for cellular IoT over LTE [3]. These improvements address the issues of overload control, support of a massive number of low-throughput devices, device cost reduction, low-power consumption, signaling overhead, and coverage enhancement. Key functionalities of new LTE UE with the maximum throughput of 1 Mbps are defined in the most two recent LTE releases.

In LTE Release 12, new UE category was developed, referred to as LTE Category 0, or simply LTE Cat-0. This was the first device category specifically targeting reduced complexity and, thus, reduced cost for the IoT. It has the following reduced capabilities : 1) Single receive antenna and associated receiver chain, 2) Reduced peak data rates of 1 Mbps in both downlink and uplink, and 3) Optional half-duplex FDD operation. LTE Category M (for Machine-Type Communication) is a key theme in LTE Release 13 with significantly reducing complexity, further cost saving and improving battery lifetime. The main altered issues compared to Cat-0 device are : 1) Reduced device RF bandwidth of 1.4 MHz in both downlink and uplink, and 2) Reduced maximum transmit power to allow for an integrated power amplifier implementation, e.g. 20 dBm compared to 23 dBm for the baseline LTE device. Whilst the new categories Cat-0

and Cat-M offer a reduced specification, they still comply with the LTE system requirements.

### 2.6.1.2 Synchronization Aspects

Synchronization is required in both eNB coverage area and outside eNB coverage area and it is assisted by the transmission of the known synchronization or reference signals. A UE assumes that synchronization signals are transmitted by either an eNB or a peer UE. The synchronization signals are exemplified by the PSS and the SSS in the LTE system [79, 80]. Outside eNB coverage areas, Primary and Secondary Sidelink Synchronization Signals (PSSS and SSSS) are prescribed as signals for synchronization between MTC devices. The PSSS is transmitted on the 2<sup>nd</sup> and 3<sup>rd</sup> OFDM symbols in the slot of the sub-frame assigned for synchronization signal transmission, while the SSSS is transmitted on the 5<sup>th</sup> and 6<sup>th</sup> OFDM symbols. Instead of carrying the physical Cell ID, the PSSS and SSSS carry a Sidelink Identifier (SID). The SID value also indicates whether the UE transmitting the sidelink synchronization signals has derived its synchronization from the network or a peer device.

The synchronization between two devices depends on the scenario and coverage situation in a hierarchical way. First of all, the device needs to determine if it is located in the coverage area or not, based on the signal quality measurement using the Reference Signal Received Power (RSRP) measurement performed on the downlink signal [82]. If the measured RSRP values are above a specific threshold, the device considers itself in the coverage area and uses LTE Rel-8 downlink signals (PSS, SSS) for synchronization. Otherwise, the device cannot detect an eNB and is assumed out of the coverage area. The device, then, starts looking for PSSS and SSSS, which are transmitted once every 40 *ms*, from other devices.

## 2.6.2 Simply-Differential Synchronization for MTC

In this section, we study the application of the SD synchronization metric to MTC underlying LTE-A network [139]. We also derive the probability of correct detection in its closed form to ensure the effectiveness of our analysis. The SD approach can be used in all systems that exploit ZC sequences as a training sequence for synchronization purposes. It achieves time synchronization by locating the ZC sequence within the received signal. The SD metric exploits the differential correlation outcome of the  $n^{\text{th}}$  received sample with its  $q$ -shifted counterpart as described in section 2.5.2.

Figure 2.15 depicts the SD metric presented for ZC sequence in the frequency domain (a) and in the time domain after mapping on the OFDM symbol (b). The metric is here drawn for 1.4 MHz LTE communication system having useful OFDM symbol length  $N_u = 128$ , Cyclic Prefix (CP) length  $N_g = 10$ , ZC sequence length  $N_{zc} = 63$  and a root  $u = 25$ . We note that both metrics exhibit a triangular shape that reaches its maximum at the ZC sequence start, where the sum in (2.14) spans the whole ZC sequence. The gap of the metric in Figure 2.15.b is wider due to oversampling the ZC sequence used in LTE signal. We also highlight that the metrics are drawn for the three possible ZC sequences specified in the LTE standard, and only the correct sequence provides a high magnitude. This allows the detection of the sector identifier which is a part of the Cell ID/Sidelink ID.

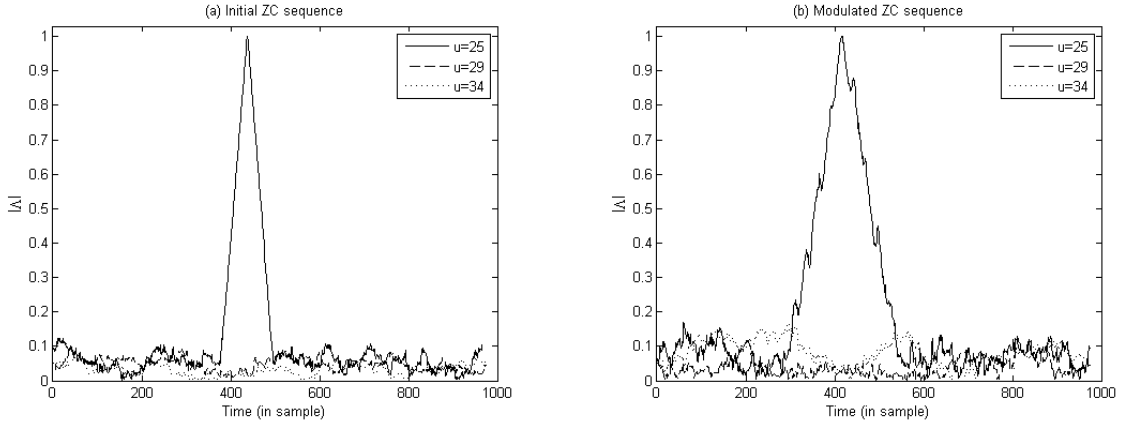


Figure 2.15: The simply-differential metrics : (a) initial ZC sequence, (b) Mapped ZC sequence (LTE signal).

### 2.6.2.1 Distribution of the SD Metric

The SD timing metric expressed in (2.14) sums up  $N_{zc}$  random variables [139]. Assuming the independence between the summed terms of  $M_{SD}$  in (2.14) and for  $N_{zc}$  sufficiently large, the central limit theorem enables to approximate  $M_{SD}(n)$  by a Gaussian distribution [85] with mean  $\mu_n$  and variance  $\sigma_n^2$ . To calculate the mean  $\mu_n = E[M_{SD}(n)]$  and variance  $\sigma_n^2 = E[|M_{SD}(n)|^2] - \mu_n^2$  values, we first split the received sample to signal and noise components as  $r_n = s_n + \omega_n$ . The metric can then be rewritten as

$$M_{SD}(n) = \sum_{k=0}^{N_{zc}-1} (s_{n+k} + \omega_{n+k})^* (s_{n+k+q} + \omega_{n+k+q}) e^{\frac{j\pi u}{N_{zc}} 2q(n+k)}. \quad (2.23)$$

Since  $s_n$  and  $\omega_n$  are independent and  $\omega_n$  is centered, the expected value of  $M_{SD}$  turns into

$$\mathbb{E}[M_{SD}(n)] = \sum_{k=0}^{N_{zc}-1} \mathbb{E} \left[ (s_{n+k}^* s_{n+k+q}) e^{\frac{j\pi u}{N_{zc}} 2q(n+k)} \right]. \quad (2.24)$$

As the correlation shift  $q \neq 0$ ,  $M_{SD}(n)$  is then zero mean unless for  $n$  falling within the ZC sequence, where it becomes

$$\mu_n = \sum_{k=n}^{N_{zc}-1} e^{-\frac{j\pi u}{N_{zc}} 2q(n+k)} e^{\frac{j\pi u}{N_{zc}} 2q(n+k)} = N_{zc} - 1 - n. \quad (2.25)$$

To find the variance of the SD metric, look at its square value  $|M_{SD}(n)|^2$  expressed as

$$\begin{aligned} |M_{SD}(n)|^2 = & \sum_{k,l=0}^{N_{zc}-1} \left[ s_{n+k} s_{n+l}^* s_{n+k+q}^* s_{n+l+q} + s_{n+k} s_{n+l}^* \omega_{n+k+q}^* \omega_{n+l+q} + \omega_{n+k} \omega_{n+l}^* s_{n+k+q}^* s_{n+l+q} \right. \\ & \left. + \omega_{n+k} \omega_{n+l}^* \omega_{n+k+q}^* \omega_{n+l+q} \right] e^{\frac{-j\pi u}{N_{zc}} 2q(k-l)}. \end{aligned} \quad (2.26)$$

For samples belonging to a ZC sequence, it turns into

$$|M_{SD}(n)|^2 = N_{zc} E_s^2 + 2N_{zc} E_s E_\omega + N_{zc} E_\omega^2 + (N_{zc} - 1 - n)^2 - (N_{zc} - 1 - n), \quad (2.27)$$

were  $E_s$  and  $E_\omega$  stand respectively for the symbol and noise energies. However, for randomly generated samples, the squared metric in (2.26) reduces to

$$|M_{SD}(n)|^2 = N_{zc} E_s^2 + 2N_{zc} E_s E_\omega + N_{zc} E_\omega^2. \quad (2.28)$$

As  $|M_{SD}(n)|^2$  is constant, the value of its expectation is  $\mathbb{E}[|M_{SD}(n)|^2] = |M_{SD}(n)|^2$ . The variance  $\sigma_n^2$  of the metric for time indexes out of the ZC sequence corresponds to the root square of the metric in (2.28), due to their zero mean value. However, along the ZC sequence, the variance value becomes

$$\sigma_n^2 = N_{zc} E_s^2 + 2N_{zc} E_s E_\omega + N_{zc} E_\omega^2 - (N_{zc} - 1 - n). \quad (2.29)$$

### 2.6.2.2 Probability of Correct Detection

The estimated correct time denoted as  $n_c$  is the argument that maximizes the metric  $|M_{SD}(n)|$ . The PCD is defined as the probability that, for all values of time index  $n$ , the magnitude of  $|M_{SD}(n)|$  is less than that of  $|M_{SD}(n_c)|$ . The time index  $n_c$  corresponds to the first received sample of the ZC sequence [139]. For notational convenience, we denote  $|M_{SD}(n_c)|$  by  $\zeta$  and introduce the random discrete variable  $X$  to refer  $|M_{SD}(n)|$ . Assuming the independence between the different values of  $X$  and  $\zeta$ , the PCD is expressed in its closed form as

$$\text{PCD} = \int_0^{+\infty} \prod_{n \neq n_c} F_n(\zeta) P_{n_c}(\zeta) d\zeta, \quad (2.30)$$

where  $F_n(\zeta)$  is the cumulative distribution function of the SD metric modeled by the Gaussian random variable  $X$ , which is determined as

$$\begin{aligned} F_{|X|}(\zeta) &= P(|X| < \zeta) = \frac{1}{\sqrt{2\pi\sigma_n^2}} \int_{-\zeta}^{\zeta} e^{-\frac{(x-\mu_n)^2}{2\sigma_n^2}} dx = \frac{1}{\sqrt{\pi}} \int_{\frac{-\zeta-\mu}{\sqrt{2\sigma^2}}}^{+\infty} e^{-x'^2} dx' - \frac{1}{\sqrt{\pi}} \int_{\frac{\zeta-\mu}{\sqrt{2\sigma^2}}}^{+\infty} e^{-x'^2} dx' \\ &= \frac{1}{2} \operatorname{erfc} \left( \frac{-\zeta - \mu_n}{\sqrt{2\sigma_n^2}} \right) - \frac{1}{2} \operatorname{erfc} \left( \frac{\zeta - \mu_n}{\sqrt{2\sigma_n^2}} \right), \end{aligned} \quad (2.31)$$

In the PCD closed form expression (2.30),  $P_{n_c}(\zeta)$  stands for the probability density function of the SD metric for the correct ZC sequence start position  $n_c$ , expressed as follows

$$P_{n_c}(\zeta) = \frac{1}{\sqrt{2\pi\sigma_{n_c}^2}} \left( e^{-\frac{-(\zeta-\mu_{n_c})^2}{2\sigma_{n_c}^2}} + e^{-\frac{-(-\zeta-\mu_{n_c})^2}{2\sigma_{n_c}^2}} \right). \quad (2.32)$$

### 2.6.3 Performance Evaluation

The performance of the SD synchronization approach is here assessed in terms of ZC sequence start probability of correct detection. Monte Carlo simulation is carried out for  $10^4$  trials to evaluate the experimental PCD, which is compared to the theoretical probability derived in (2.30). The simulated PCD is defined as the number of trials for which the estimated ZC sequence start corresponds to the exact one. We highlight that the study derived here concerns the coarse SD metric and further detection accuracy could be reached through the fine metric, which is based on cross-correlation, as explained in [27]. We consider the 1.4 MHz

LTE communication system with single antenna configuration and peak data rate of 1 Mbps, which is the configuration introduced in Rel-13 of the 3GPP standards. We also assume that the terminal is located within the coverage area. The considered OFDM system parameters are as follows : useful data symbol length  $N_u = 128$ , cyclic prefix length  $N_g = 10$  and the ZC sequence has a length  $N_{zc} = 63$ . The correlation shift  $q$  in (2.14) is set to 1. The evaluation is here carried out in the AWGN channel and over practical SNR range.

Figure 2.16 illustrates the PCD in two scenarios: in the first one, we consider the exact point as a reference point, while in the second one we tolerate an error of 2 samples around the exact point. Globally, the provided detection accuracy is satisfactory. Indeed, the PCD reaches a target of about 90% from an SNR value equal to 5 dB, which is quite good for coarse synchronization performance. This accuracy helps to reduce the time interval around which the fine metric may be calculated for further detection accuracy. The figure also shows that the analytical probability exhibits a good match with the experimental one in the first scenario, up to a very slight gap of about 0.5 dB for an SNR range between 0 dB and 10 dB. In the second scenario, we note that the probabilities concord perfectly. Overall, the experimental results ensure the theoretical analysis and validate the synchronization capabilities of the studied metric in the considered system.

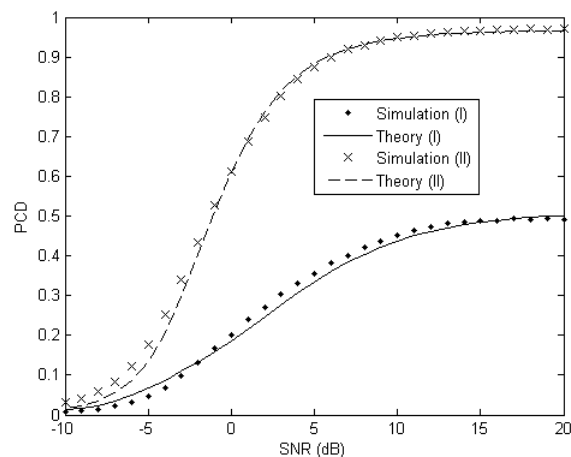


Figure 2.16: Probability of correct detection of the ZC sequence start: Theory and Simulation.

## 2.7 Conclusion

In this chapter, reduced complexity synchronization techniques for OFDM systems were presented and applied to the standards IEEE 802.11n WLAN and LTE in the context of cellular and machine-type communications that are adapted for IoT applications. We exploited the repetitive structure of the IEEE 802.11n preamble and applied a two-stage processing to it. To first provide a coarse preamble start estimation, the approach uses sliding correlation. Then, for more accurate estimation, differential correlation is carried out over a short interval centered on the coarse time estimate. The combined use of sliding and differential correlations and the designed metric provide satisfactory performance in terms of detection accuracy and computational load. The performance was evaluated respecting the parameters of the WLAN standard IEEE 802.11n and exploiting both cyclic and space time diversities. Simulation results showed the robustness of the reduced-complexity approach under the IEEE 802.11 channel B and thus its suitability for the considered standard.

Then, we studied reduced-complexity timing synchronization and sector search approaches for the LTE system. The first approach calculates a Simply-Differential correlation based metric and allows joint time synchronization and S-ID recovery using the same metric. The second approach carries out Doubly-Differential correlation based metric to detect a ZC sequence pattern within the received signal, then recovers the S-ID during the second stage. The performance evaluation investigated in the EPA and ETU channel models showed the robustness of the approaches even at very low SNR values. The DD approach has a computational load higher than that of the SD approach and provides better detection performance for medium and high SNR values. We also analyzed the effect of a FO on time synchronization performance and approved the immunity of the DD approach and the sensitivity of the SD approach to FO.

The reduced complexity of these approaches makes them suitable for MTC over cellular LTE networks. Hence, we investigated the application of the simply differential approach to machine type communication to jointly provide time synchronization and sector identifier. The performance of the studied approach was evaluated in terms of theoretical correct detection probability, which was derived in its closed form, and compared to the experimental probability. The obtained results showed that, when applied to the LTE signal specified for MTC, the studied approach provided good detection accuracy. Moreover, the simulated probability perfectly agrees with the theoretical one, which validates the analysis carried out.

## Chapter 3

# RS-based Neighbor Discovery

### 3.1 Introduction

In its latest releases, the LTE standard was defined to support new paradigms for LTE to improve network capacity and efficiency. Among them, Device-to-Device (D2D) communication was proposed as a vital component to enable novel and significant opportunities requiring localized communications and IoT applications. From Rel. 12, D2D communication was introduced in the LTE cellular network under the name of Proximity Services (ProSe) [5]. The standard enables a User Equipment (UE) to communicate directly with other UEs in its vicinity using a portion of the channel known as SideLink (SL) through the new interface PC5. Later on, Rel. 14 and Rel. 15 included the cellular Vehicle-to-Everything (V2X) standard with further enhancements to the Vehicle-to-Vehicle (V2V) standard that was defined as a part of ProSe communications. In particular, short-range V2X was added to the features of LTE and 5G to allow vehicles, roadside devices, and vulnerable users to directly exchange information using the same chipset used in traditional long-range connections [108, 109].

To establish a direct link, a UE has to first perform neighbor discovery, which is defined as the process by which it advertises and detects useful information provided by its peers using a specific set of time and frequency resources contained in the Physical Sidelink Discovery Channel (PSDCH) [5]. The announcement and monitoring of discovery messages are authorized by the upper layers. In the radio network, discovery procedures involve only the Media Access Control (MAC) and Physical (PHY) layers. The MAC layer builds a MAC protocol data

unit carrying a discovery message from the upper layer and determines the radio resource for announcing the discovery message.

In this chapter, we address the problem of neighbor discovery in LTE networks exploiting direct radio links between ProSe-enabled users. In particular, we use Reference Signals (RS), i.e. Sounding Reference Signal (SRS) [31] and the Demodulation Reference Signal (DMRS) [32], which are sent periodically within the UL/SL frame to sense the presence of neighboring UEs in the vicinity. The SRS-based discovery performs simple cross-correlation, while the DMRS-based discovery performs a power normalized correlation between the received signal and the local known reference sequences. Both approaches exploit a hypothesis binary test to decide about the activity of a neighboring user. The performance is evaluated through a theoretical study of the probability of discovery and simulation.

## 3.2 Related Works

The discovery procedure can use conventional wireless localization methods such as time-of-arrival (TOA), angle-of-arrival (AOA), time-difference-of-arrival (TDOA), and global positioning system (GPS) to track the location of each UE [93]. However, these methods can not provide the required accuracy for the proximity-based service. To overcome this limitation, beacon-based D2D discovery schemes, in which D2D users find their nearby peers using pre-defined proximity beacons can be used. Depending on the level of network involvement, the discovery process can be assorted into centralized and direct [94]. In direct discovery methods, discovery is distributed and does not involve the base station. Wireless ad hoc networks including Bluetooth and WiFi-direct, which work on unlicensed band are examples of fully-distributed networks. Centralized discovery can further be assorted into fully-controlled (centralized) in which the base station manages the whole discovery and link establishment process and loosely controlled (semi-centralized) in which the task is performed based on information exchange between D2D users and the base station.

The proximity beacon-based discovery scheme has been studied in several research works [95]- [101]. In [95,96], FlashLinQ, which is the neighbor discovery scheme proposed by Qualcomm, provides a synchronous and distributed device discovery solution for wireless ad hoc networks, yet on the licensed band. This architecture is completely flat as there are no centralized masters that control the operations of other devices. In [97] and [98], adaptive peer

discovery schemes were considered in which the probing rate of peer discovery is varied according to social domain information or the wakeup schedule of D2D users is changed according to predicted inter-contact time of users. In [100], peer discovery based on the LTE beacon structure was considered. It exploited primary and secondary synchronization signals followed by information bits as beacons. However, the use of such a beacon for the D2D discovery can lead to underutilization of resource blocks and a high collision probability. To overcome this limitation, a random access procedure like scheme was proposed in [101], which uses the preamble dedicated for random access phase as beacons to identify in a centralized way. The work in [102] focused on neighbor discovery utilizing SRS channel, which can be accessed by peer UEs that are LTE-compliant. Under the constraint of unknown channel statistics during uplink hearing, neighbor detection is achieved through the conventional Constant False Alarm Rate (CFAR) detector. Then, in [103], the authors used DMRS signal to which a Generalized Likelihood Ratio Test (GLRT) estimator is applied, followed by a hypothesis test to detect neighboring users.

### 3.3 System Architecture

We consider an LTE cellular network that supports direct user communications, in which UEs might access the eNB for regular cellular communications or establish D2D pairwise links for both ProSe and V2X application cases. In this case, active users can be potentially captured during UL/SL periods for which a UE is not transmitting to the eNB.

#### 3.3.1 Signal Structure

To reduce hardware requirements on UE, it was agreed that the SL uses the UL resources as well as Single-Carrier Orthogonal Frequency Division Multiple Access (SC-FDMA) transmission keeping almost the same signals and channels [104]. Resources assigned to the SL are taken from the UL, i.e. from the subframes on the UL frequency in frequency division duplex mode and from the subframes assigned to UL in time division duplex mode. This choice is justified by the lower UL subframes occupation compared to the DL subframes [105]. The sub-frame is in this case made of two 0.5ms slots, each made of 7 SC-FDMA symbols.

Each ProSe-enabled user  $i$  (UE- $i$ ) interested in creating a D2D link, transmits his signal

which is received with a delay  $\tau_i$ . The signal received at the listener ProSe-enabled user  $j$  (UE- $j$ ), which aims to discover the presence of his peers in his neighborhood is written as

$$\mathbf{r}_j = \sum_{i=1; i \neq j}^U \mathbf{h}_i \mathbf{y}_i(\tau_i) + \boldsymbol{\omega}_j, \quad (3.1)$$

where  $h_i$  denotes the channel coefficient,  $\mathbf{y}_i(\tau_i)$  stands for the delayed received version of the signal  $\mathbf{y}_i$  that is transmitted from the neighbor UE- $i$ . The parameter  $\boldsymbol{\omega}_j$  is the AWGN assigned to the UE- $j$ . As some users might not be involved in the D2D communication, the channel coefficient  $h_i$  is then set to 0 for inactive users ( $\text{UE-}i \in \mathcal{U}_0$ ). We introduce the variable  $\sigma_s^2$  and  $\sigma_\omega^2$  corresponding to the symbol energy, and the noise energy at the discoverer UE- $j$ , respectively. Note that the symbol energy is the invariant for all UEs and  $\sigma_s^2$  is used hereafter to design the symbol energy for a specific UE- $i$ .

### 3.3.2 SideLink Communication

The SL is an LTE feature initially introduced in 3GPP Rel.12 to enable D2D communication underlying cellular LTE radio access networks [5]. In Rel.13, SL functionalities have been enriched to be applicable to public safety and commercial communication use cases, and recently (Rel.14 and Rel.15) to Vehicle-to-Everything (V2X) scenarios.

#### 3.3.2.1 Sidelink Channels

In conventional cellular traffic over Uu interface, the eNB communicates with the UE via the UL and DL for both signaling and data. In contrasting fashion, as shown in figure 3.1, SL enables the direct communication between proximal UEs, often called ProSe-enabled UEs, using the newly defined PC5 interface and data does not need to go through the eNB. The first definitions of D2D communications used the term SL to distinguish it from downlink (eNB-to-UE) and uplink (UE-to-eNB). The interface defined for this scope is named PC5 and the newly defined physical layer channels are:

- PSBCH: Physical SideLink Broadcast CHannel, which carries system information and synchronization signals;
- PSCCH: Physical SideLink Control CHannel, which carries UE-to-UE control plane data;

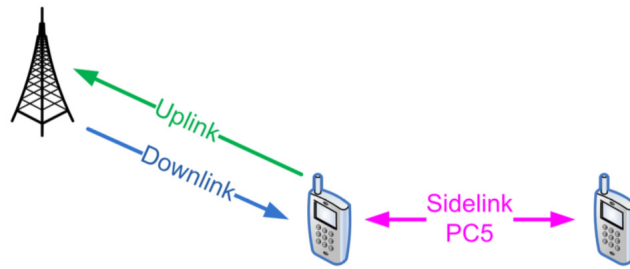


Figure 3.1: Enabled Sidelink for direct communication in LTE network [105].

- PSDCH: Physical SideLink Discovery CHannel, which supports UE direct discovery transmissions;
- PSSCH: Physical SideLink Shared CHannel, which is used for user plane data transmission.

The design of SL revolves around three functionalities for enabling direct UE communications: synchronization, discovery, and communication. Primary and Secondary Synchronization signals share the PSBCH using broadcast signals; discovery messages use the dedicated PSDCH, and control messages and data transmissions employ PSCCH and PSSCH respectively. During synchronization, UEs come to a consensus over timing to ensure the subsequent transmission of data and control packets. During the discovery procedure, UEs announce their presence and discover other UEs in the vicinity. This information is used to determine the subsequent communications phase, where actual data transport occurs.

### 3.3.2.2 Sidelink Frame Structure

The LTE signal is organized in frames of  $10ms$  composed of 10 subframes having each a length of  $1ms$ . Each subframe is structured in two slots that comprise 7 and 6 SC-FDMA symbols for normal and extended CP respectively. The SL subframe is depicted in figure 3.2. Similar to synchronization design in LTE conventional downlink, two synchronization signals, primary sidelink synchronization signal (PSSS) and secondary sidelink synchronization signal (SSSS), are defined for sidelink, where each occupies the center 62 sub-carriers and two SC-FDMA symbols within the  $1ms$  subframe. PSSS is transmitted in the 2<sup>nd</sup> and 3<sup>rd</sup> symbols of the first time slot (half of the subframe) while SSSS is transmitted in the 5<sup>th</sup> and 6<sup>th</sup> symbols of the second time slot.

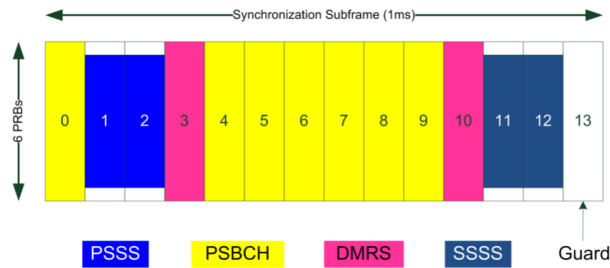


Figure 3.2: Sidelink synchronization subframe structure [105].

These signals are used by listener UEs to synchronize with broadcasting UE, which is willing to initiate direct D2D communication. Along with the subframe, two Demodulation Reference Signals (DMRS) are mapped in the 4<sup>th</sup> symbol of each slot and is intended to be used for coherent channel demodulation. The DMRS structure will be explained separately in more detail in the next section. The last symbol in a sub-carrier is punctured to serve as guard period.

### 3.3.2.3 Resource Block

In the LTE network, the radio resources are allocated in units of time-frequency physical Resource Block (RB). Each RB spans one time slot in the time domain and 12 sub-carriers in the frequency domain as shown in figure 3.3. Each time slot further consists of 7 or 6 OFDM symbols, depending on whether a normal or an extended cyclic prefix is used [46].

The allocation of SL resources is based on resource pools, which are formed by a subframe pool in the time domain and a Resource Block (RB) pool in the frequency domain. The bandwidths that can be allocated to SL differ based on the following rule: up to 20 MHz can be reserved for discovery, whereas 10 MHz is the maximum for communication and control.

### 3.3.3 Reference Signals

In addition to the physical channel, the LTE standard defines two reference signals in its UL: Demodulation Reference Signals (DMRS) and Sounding Reference Signals (SRS). The DMRS is intended to be used by the eNB for channel estimation for coherent demodulation of the UL physical channels (PUSCH and PUCCH). In contrast, the SRS is used to support UL channel-

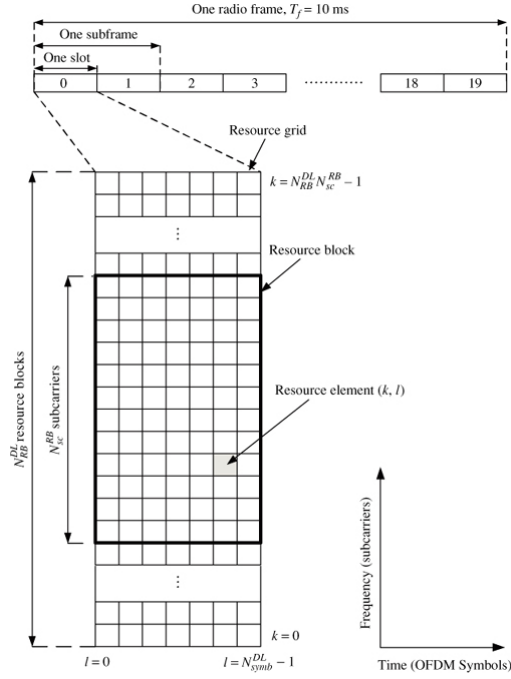


Figure 3.3: Physical Resource Block.

dependent scheduling and link adaptation and to estimate the DL channel-state assuming sufficient UL/DL reciprocity. It can also be used in cases when UL transmission is needed, although there is no data to transmit [46]. To support a large number of UEs, RS sequences are defined by cyclically shifting a base sequence  $\bar{r}$  as

$$r^{(\delta_i)}(n) = e^{j\delta_i n} \bar{r}(n), \quad 0 \leq n < M, \quad (3.2)$$

where  $\delta_i$  is the shift,  $M = mN_{RB}$  is the length of RS sequences,  $m$  is the number of RBs and  $N_{RB}$  is the size, in sub-carriers, of each RB. As the sub-carrier bandwidth is set to 15kHz, each RB contains 12 sub-carriers, i.e.  $N_{RB} = 12$  [110]. Multiple RS sequences can be derived from a single base sequence through different values of  $\delta_i$  and each sequence is attributed to one user. The definition of the base sequence  $\bar{r}$  depends on the sequence length. For  $M \geq 3N_{RB}$ , the base sequence  $\bar{r}$  is chosen as the cyclic extension of a Zadoff-Chu (ZC) sequence  $x_u$  of root  $u$  and is expressed as

$$\bar{r}(n) = x_u(n \bmod N_{zc}), \quad 0 \leq n < M, \quad (3.3)$$

where  $N_{zc}$  is the length of the ZC sequence  $x_u$ . This is given by the largest prime number such that  $N_{zc} < M$  [83]

$$x_u(n) = e^{-j\frac{\pi un(n+1)}{N_{zc}}}, \quad 0 \leq n \leq N_{zc} - 1. \quad (3.4)$$

As the number of available ZC sequences of a certain length  $N_{zc}$ , i.e. the number of possible values of  $u$ , equals the number of integers that are relatively prime to  $N_{zc}$ , a cyclic extension of prime-length sequences would be preferred to maximize the number of available reference signals. Before transmission, an  $N$ -point IFFT is applied to  $r^{(\delta_i)}$  in (3.2) to generate the RS sequence to be mapped into the frame. Thanks to their good correlation properties, this type of sequences is well suited for detection and synchronization purposes. Moreover, they have the advantage of remaining invariant under several operations such as the FFT and IFFT, which are applied to generate the RS signal in the LTE system [84]. Since the resulting sequences are all mutually orthogonal, they can serve as unique identifiers for UEs that are willing to set up a direct link with their neighbors.

### 3.3.3.1 Sounding Reference Signal

There are two types of SRS transmission defined for the LTE UL: periodic SRS transmission, which has been available from the first release of LTE (release 8); and aperiodic SRS transmission, introduced in LTE release 10. Periodic SRS transmission from a UE occurs at regular time intervals, from as often as once every 2ms (every 2 sub-frames) to as infrequently as once every 160ms (every 16 sub-frames). When the SRS is transmitted within a sub-frame, it occupies the last SC-FDMA symbol of the sub-frame.

Authorized UEs are scheduled to transmit by the eNB and they can be multiplexed in the same SRS symbol in a combination of FDM or CDM. In a given sub-frame, all UEs within the same cell and sharing the same SRS bandwidth are generated from the same ZC sequence. The system offers a multiplexing capacity of 8 users. The sequence mapping reflects the Single Carrier Interleaved Frequency Division Multiple Access (SC-IFDMA) transmission scheme of the SRS: within its allocated bandwidth, a UE's SRS sequence is mapped to every second subcarrier, creating a comb-like spectrum. As a result, the total SRS multiplexing capacity for a given SRS bandwidth is 16 users [46].

### 3.3.3.2 Demodulation Reference Signal

The DMRS signals are intended to be used by the base station for channel estimation for coherent demodulation of the uplink physical channels (PUSCH and PUCCH). They are thus only transmitted together with PUSCH or PUCCH and are then transmitted with the same

bandwidth as the corresponding physical channel. Likewise, in Rel. 12 and beyond, DMRS is associated with physical SL channels (PSSCH, PSCCH, PSDCH, and PSBCH) for coherent demodulation. The DMRS is mapped on the 4<sup>th</sup> symbol of each slot for ProSe in Rel. 12 [110] and on the 3<sup>rd</sup> and 6<sup>th</sup> symbols of each slot for V2X communication [111].

### 3.3.4 Discovery Framework

In the studied system, ProSe-enabled UEs can be aware of potential partners in the vicinity through their RS and hence initiate direct communication between each other. Unlike conventional discovery approaches which may not be compliant with the LTE specifications [98], require additional physical resources [99] or detect the presence of a neighbor only [102], the proposed framework exploits the standardized UL/SL signal structure to accomplish the detection of active users and the identification of their beacons.

To set up D2D communication links, each active UE should first learn about his neighbors, which are the set of UEs within a limited range. The set of neighbors is denoted by  $\mathcal{U}$  and is partitioned into two sets: 1) a set of target users  $\mathcal{U}_1$ , which are ProSe-enabled users located within a limited area interested in D2D communication, and 2) a set of inactive users  $\mathcal{U}_0$ , which are not involved in the D2D communication. Assuming synchronization between ProSe-enabled UEs, the RS transmitter is designed in such a way to assign a unique beacon to each UE which is derived from the extended and cyclically shifted ZC sequence as explained in section 3.3.3. As the generated beacons sharing the same duration are orthogonal, they can be used as beacons to identify ProSe-enabled UEs. The received signal at each ProSe-enabled UE resulting from the summation of neighboring signals in (3.1) becomes

$$\mathbf{r}_j = \sum_{i=1; i \neq j}^{N_u} \mathbf{h}_i \mathbf{s}_i + \boldsymbol{\omega}_j, \quad (3.5)$$

where  $N_u$  is the number of ProSe-enabled UEs ( $\mathcal{U}_1$ ) in the network,  $j$  and  $i$  stand for the indexes of the listener and the sender UEs, respectively. As we assume synchronization between ProSe-enabled users, the transmitted signal  $\mathbf{y}_i$  in (3.1) is here replaced by the RS sequence  $\mathbf{s}_i$  of the UE- $i$ . It is worth noting that both DMRS and SRS signals provide specific information related to each UE and thus can serve as discovery beacons to identify UEs and to establish D2D links.

Upon receiving a signal, the listener UE performs a correlation-based metric followed by a

binary hypothesis test to detect the active UEs. The binary hypothesis test with two hypotheses  $\mathcal{H}_0$  and  $\mathcal{H}_1$ . First,  $\mathcal{H}_1$  denotes the hypothesis corresponding to the case that a UE is a true active neighbor from the set of target D2D users. On the other hand,  $\mathcal{H}_0$  stands for the hypothesis corresponding to the case that a UE is not an active neighbor. The hypothesis test that corresponds to UE- $i$  discovery task can then be modeled as

$$\begin{cases} \mathcal{H}_0 : & \text{UE-}i \in \mathcal{U}_0 \\ \mathcal{H}_1 : & \text{UE-}i \in \mathcal{U}_1. \end{cases} \quad (3.6)$$

It is worthy to note that according to UEs activity,  $\mathcal{U}_0$  and  $\mathcal{U}_1$  components can vary through time. The false alarm probability  $P_F$  and the detection probability  $P_D$  of the detector are defined as

$$P_D = P(\mathcal{H}_1|\mathcal{H}_1) \quad \text{and} \quad P_F = P(\mathcal{H}_1|\mathcal{H}_0), \quad (3.7)$$

where  $P(\mathcal{H}_i|\mathcal{H}_j)$  denotes the probability that  $\mathcal{H}_i$  is claimed under  $\mathcal{H}_j$  and is useful to set the threshold  $\eta$  according to the requirements on false and correct detection probabilities.

Note that depending on the position of the discoverer UE, we can denote UE-0, RS sequences that can be communicated through the eNB using RRC signaling, e.g. via system information blocks (SIBs), if the UE is located in the coverage area. For a partial coverage scenario, the configuration can be forwarded to UE-0 by one or multiple UEs that are in-coverage, or others that are outside the coverage area. For an out-of-coverage scenario, the configuration can be predefined or broadcasted by a centralized D2D device. Alternatively, the configuration can be associated with and signaled by an independent synchronization source, with the configuration further forwarded by other synchronization sources [113].

### 3.4 SRS-based Discovery

In this section, we address the problem of neighbor discovery in LTE networks exploiting direct radio links between ProSe-enabled users, which have been allowed for data transmission in Rel. 12 [82]. In particular, we exploit the SRS sent periodically within the UL frame as a D2D neighbor discovery beacon [31, 34]. Based on the SRS structure, which is known for all UEs, we perform a correlation between the received signal and the local known SRS candidates at each searching UE. Hence, the discovery is enabled by exploiting the orthogonality between

different SRS sequences. To the best of our knowledge, such properties, have not been exploited to this purpose in the literature.

### 3.4.1 Discovery Metric

Exploiting the orthogonality between beacons of all ProSe-enabled UEs, we define the discovery metric that cross-correlates the received signal at the  $j^{\text{th}}$  user with the local known SRS candidates to identify active neighbor

$$\Gamma_j(i, n) = \left| \frac{1}{N} \sum_{l=0}^{N-1} r_j^*(n+l) s_i(l) \right|, \quad i \in \mathcal{U} \quad (3.8)$$

Note that  $n$  is the time index spanning the observing window of  $N$  samples, positioned at the start of the SRS symbol (last SC-FDMA symbol of the sub-frame) [31]. The discovery metric in figure 3.4 depicts the cases for one active UE and one inactive UE in the vicinity of the listener UE in the noiseless case. For the active neighbor, we note that the metric exhibits high magnitude when it performs the cross-correlation with the SRS candidate that corresponds to the one sent from the active transmitter. However, a trifling magnitude is exhibited if no UE in the vicinity is using an SRS sequence corresponding to the candidate that the listener uses for correlation, which corresponds to an inactive user.

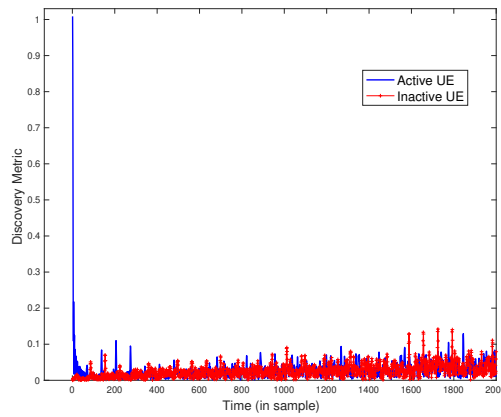


Figure 3.4: SRS-based Discovery metric for active and inactive ProSe-enabled users [31].

Let us analyze the correlation output in the discovery metric  $\Gamma_j$  for any active UE of index  $i$  based on the ZC sequence expression in (3.4). Respecting [84], the IFFT of a ZC sequence preserves the initial properties of ZC sequences and can be considered as a ZC sequence, yet

with new root and length that are here denoted as  $u'$  and  $N'_{zc}$  respectively. In the noiseless case, and when correlating the received signal with the correct local SRS sequence  $i$ , which is a ZC sequence [84],  $\Gamma_j$  turns into

$$\Gamma_j(i, n) = e^{-j \frac{\pi u n(n+1)}{N'_{zc}}} e^{j \frac{\pi u' n(n+1)}{N'_{zc}}} = 1. \quad (3.9)$$

Hence the sum in (3.22) adds constructively in such a way to provide high metric magnitude when the output sums up the ZC sequence length  $N'_{zc}$  ( $N'_{zc} = N$  in this case). However, if the received signal is correlated with a different SRS sequence that is not used by any of the active users, the correlation output becomes

$$\Gamma_j(i, n) = e^{-j \frac{\pi u' n(n+1)}{N'_{zc}}} e^{j \alpha n} e^{j \frac{\pi u' n(n+1)}{N'_{zc}}} = e^{j \alpha n}. \quad (3.10)$$

In this case, the sum in (3.22) adds randomly which results in low metric magnitude.

The addition of correlated elements along the beacon length sums constructively for active users and allows their detection based on the test in (3.11). Since the shared SRS sequence set is known to all UEs within the network, each D2D receiver can detect all present sequences as part of the neighbor discovery process. To identify active D2D users, the receiving UE  $j$  applies the following detection rule onto each  $i^{\text{th}}$  line of the decision metric  $\Gamma_j$  as

$$\max_n \left\{ \Gamma_j(i, n) \right\} \underset{\mathcal{H}_0}{\overset{\mathcal{H}_1}{\geq}} \eta, \quad (3.11)$$

where  $\eta$  is a preset threshold and  $\mathcal{H}_0$  and  $\mathcal{H}_1$  are the two hypothesis of the binary test.  $\mathcal{H}_1$  denotes the hypothesis corresponding to the case that a UE is a true active neighbor, while  $\mathcal{H}_0$ , stands for the hypothesis corresponding to the case that a UE is not an active neighbor. Hypothesis  $\mathcal{H}_1$  holds for UE- $i$  in the set of active ProSe-enabled neighbors ( $\Gamma_j(i, n_{\max}) > \eta$ ). Otherwise, hypothesis  $\mathcal{H}_0$  detains to indicate that the UE- $i$  is not an active UE.

### 3.4.2 Complexity Evaluation

In (3.22), the detection metric should be calculated  $U$  times to ensure the discovery of the whole set of active users  $\mathcal{U}_1$ , which may result in a huge computational load. To overcome this

limit, we suggest a reduced complexity recursive implementation as

$$\Gamma_j(i, n+1) = \Gamma_j(i, n) - \frac{1}{N} \left| r^*(n) x_i(0) \right| + \frac{1}{N} \left| r^*(n+N-1) x_i(N-1) \right|. \quad (3.12)$$

In the initial metric (3.22), the computation of each element  $\Gamma_j(n)$  requires  $N$  complex multiplication operations. However, the proposed recursive implementation expressed in (3.12) reduces this number to only 2 with additional 2 complex addition operations whose computational load is trifling compared to multiplication operations. Thus,  $N-2$  complex multiplication operations are saved using (3.12) rather than (3.22). For the whole discovery process, which involves the set of D2D users, the recursive implementation saves  $U \times (N-2)$  complex multiplication operations per metric evaluation.

### 3.4.3 Closed-Form Discovery Probability

To determine the probability of discovery in its closed form, we first study the statistical properties of the discovery metric [34]. We assume that we have two ProSe-enabled UEs; a listener UE- $j$  and a sender UE- $i$  and suppose that the channel coefficient  $h$  is perfectly known. The received signal at the listener side can be reduced to  $\mathbf{r}_j = \mathbf{s}_i + \boldsymbol{\omega}$ . The discovery metric in (3.8) sums up  $N$  variables. Assuming the independence between the summed terms in  $\mathbf{\Gamma}_j$  and for  $N$  sufficiently large, by the Central Limit Theorem  $\mathbf{\Gamma}_j$  is Gaussian and is characterized by its mean  $\mu_{\mathbf{\Gamma}_j}$  and variance  $\sigma_{\mathbf{\Gamma}_j}^2$ . Recall that to decide whether a neighbor is active or not, the metric is evaluated at its maximum value as in (3.27). Hence, it is necessary to study the statistics of the metric in the cases of active and inactive neighbors [34].

#### 3.4.3.1 Case of Active Neighbor

We here focus on deriving the mean and variance of the magnitude of  $\mathbf{\Gamma}_j$  at its maximum value for an effective ProSe-enabled UE- $i$  [34]. Substituting the simplified received signal expression in the equation (3.8), the metric yields

$$\Gamma_j(i, n) = \frac{1}{N} \sum_{l=n}^{N+n-1} |s_i(l)|^2 + \omega^*(l) s_i(l). \quad (3.13)$$

For notational convenience, we introduce the Gaussian random variable  $X$  that corresponds

to the maximum of  $\Gamma_j(i, n_{\max})$ . Referring to the analysis of the metric in section 3.4.1, the mean of  $X$  is  $\mu_X = \sigma_s^2$ , since each of the  $N$  elements belonging to the SRS sequence has an expected value of  $\sigma_s^2$  and all the other terms have an expected value of zero.

To determine the variance of the metric, we need to first evaluate the expectation of the squared metric which can be expressed as:

$$\begin{aligned} \mathbb{E}\left(|\Gamma_j(i, n)|^2\right) &= \frac{1}{N} \times \mathbb{E}\left(\sum_{l,k=n}^{N+n-1} [|s_i(l)|^2 + \omega_j^*(l)s_i(l)] [|s_i(k)|^2 + \omega_j(k)s_i^*(k)]\right) \\ &= \frac{1}{N} \mathbb{E}\left(\sum_{l,k=n}^{N+n-1} |s_i(l)|^2 |s_i(k)|^2 + \sum_{l=k=n}^{N+n-1} |s_i(l)|^2 |\omega_j(l)|^2\right) \\ &= N\sigma_s^4 + \sigma_s^2 \sigma_\omega^2, \end{aligned} \quad (3.14)$$

The variance is then evaluated as

$$\sigma_\Gamma^2 = \mathbb{E}(|\Gamma_j|^2) - |\mu_{\Gamma_j}|^2 = N\sigma_s^4 + \sigma_s^2 \sigma_\omega^2 - \sigma_s^4 = (N-1)\sigma_s^4 + \sigma_s^2 \sigma_\omega^2, \quad (3.15)$$

### 3.4.3.2 Case of Inactive Neighbor

We now focus on the statistical characterization of the discovery metric in the case of any inactive user, for which the metric correlates between the received signal with the SRS sequence of the inactive user that we denote as UE- $g$  and the local sequence candidate  $s_i$  ( $i \neq g$ ) [34].

The metric can then be written as

$$\Gamma_j(n) = \frac{1}{N} \sum_{l=n}^{N+n-1} s_i(l)s_g(l) + \omega^*(l)s_g(l). \quad (3.16)$$

In this case, the metric sums randomly and the output has an insignificant value as demonstrated in section 3.4.1. The expected value of the metric output for all inactive UEs is then null leading to a mean  $\mu = 0$ . Consequently, the variance will be equal to the expected value

of the square of the discovery metric determined as

$$\begin{aligned}
\mathbb{E}(|\Gamma_j(i, n)|^2) &= \frac{1}{N} \mathbb{E} \left( \sum_{l,k=n}^{N+n-1} [s_i^*(l)s_g(k) + \omega^*(l)s_g(k)] \times [s_i(l)s_g^*(k) + \omega(l)s_g^*(k)] \right) \\
&= \frac{1}{N} \mathbb{E} \left( \sum_{l=k=n}^{N+n-1} |s_i(l)|^2 |s_g(k)|^2 + |\omega(l)|^2 |s_g(k)|^2 \right) \\
&= \sigma_s^4 + \sigma_\omega^2 \sigma_s^2.
\end{aligned} \tag{3.17}$$

### 3.4.3.3 Discovery Probability

We have shown in the previous section that the decision metric can be approximated with a Gaussian random variable with mean  $\mu_\gamma = \sigma_s^2$  and variance  $\sigma_\gamma^2 = (N-1)\sigma_s^4 + \sigma_s^2\sigma_\omega^2$  for active neighbor and zero mean with variance  $\sigma_\gamma = \sigma_s^4 + \sigma_\omega^2\sigma_s^2$  for an inactive neighbor. We here exploit these results to derive the Discovery Probability (DP) in its closed form. The discovery probability can be defined as the probability that the magnitude of  $X$  is higher than a preset threshold  $\eta$  for the active user UE- $i$  and that of  $Y$  is less than the threshold. Therefore, assuming the independence between the metric values calculated for each UE, this probability can be expressed as

$$PD = P(\gamma_i > \eta)P(\gamma_j \leq \eta) = [1 - F_{\gamma_i}(\eta)]F_{\gamma_j}(\eta), \tag{3.18}$$

where  $F_X(\eta)$  stands for the Cumulative Distribution Function (CDF) of the random variable  $X$  evaluated at  $\eta$ , which can be determined as

$$F_{|X|}(x) = P(X \leq \eta) + P(-X \leq \eta) = \int_{-\eta}^{\eta} \frac{1}{\sqrt{2\pi\sigma_X^2}} e^{-\frac{(x-\mu_X)^2}{2\sigma_X^2}} dx \tag{3.19}$$

for the studied metric  $\gamma$  modeled by the random Gaussian variable  $X$ . For notational convenience we consider  $X \in \{\gamma_i, \gamma_j\}$ ,  $\mu_X \in \{\mu_{\gamma_i}, \mu_{\gamma_j}\}$  and  $\sigma_X^2 \in \{\sigma_{\gamma_i}^2, \sigma_{\gamma_j}^2\}$ . The CDF of the Gaussian random variable expressed in (6.2) can, after applying a variable change of  $x$  by

$x' = \frac{x - \mu_X}{\sigma_X}$ , be determined as

$$\begin{aligned} F_{|X|}(\eta) &= \frac{1}{\sqrt{\pi}} \int_{\frac{-\eta - \mu_X}{\sqrt{2\sigma_X^2}}}^{\frac{\eta - \mu_X}{\sqrt{2\sigma_X^2}}} e^{-x'^2} dx' = \frac{1}{\sqrt{\pi}} \int_{-\infty}^{+\infty} e^{-x'^2} dx' - \frac{1}{\sqrt{\pi}} \int_{\frac{\eta - \mu_X}{\sqrt{2\sigma_X^2}}}^{+\infty} e^{-x'^2} dx' \\ &= \frac{1}{2} \operatorname{erfc} \left( \frac{-\eta - \mu_X}{\sqrt{2\sigma_X^2}} \right) - \frac{1}{2} \operatorname{erfc} \left( \frac{\eta - \mu_X}{\sqrt{2\sigma_X^2}} \right), \end{aligned} \quad (3.20)$$

where  $\operatorname{erfc}(x)$  is the complementary error function of  $x$  defined as

$$\operatorname{erfc}(x) = \frac{2}{\sqrt{\pi}} \int_x^{\infty} e^{-t^2} dt. \quad (3.21)$$

### 3.4.4 Performance Evaluation

The performance of the correlation-based neighbor discovery approach is here assessed in terms of analytical and simulated Probability of Discovery (PD) as a function of the SNR. Monte Carlo simulation is carried out for  $10^4$  trials to evaluate the simulated PD, which is defined as the number of trials for which the detected UE corresponds to the active ProSe-enabled UE. The parameters of the simulation setting are summarized in table 3.1 respecting LTE standard specifications.

Table 3.1: Simulation parameters of the SRS-based approach.

Parameter	Value
System bandwidth	20 MHz
FFT size $N$	2048 sub-carriers
CP size $N_g$	140 sub-carriers
SRS bandwidth	96 RB (1152 sub-carriers)
ZC sequence length $N_{zc}$	571 sub-carriers
E-ZC sequence length $M$	576 sub-carriers
D2D pathloss	$148 + 40 \log_{10}(d[\text{Km}])$
Transmission power	0 (dBm)

The considered system involves  $N_c = 2$  SRS combs and hence a total of  $U = 16$  possible SRS transmitters. Due to Interleaved FDMA, each SRS comb is composed of 576 sub-carriers, which is half of the SRS bandwidth. We consider the neighbor discovery process in which 12 out of 16 possible SRS transmitters are actively transmitting by sharing the same SRS symbol and

with fixed transmission power. For each observation, one among the 12 active users is chosen as searching D2D users around which are distributed the target D2D users. A random choice of the active users is done in each iteration. At the searching user, the discovery metric in (3.11) is first calculated for each user  $UE-i \in \mathcal{U}$ , then the decision rule in (3.11) is applied to identify active users among the 16 possible candidates. Given a target value of false alarm probability  $P_F$ , the detection threshold  $\eta$  is set empirically from  $10^3$  independent channel realizations.

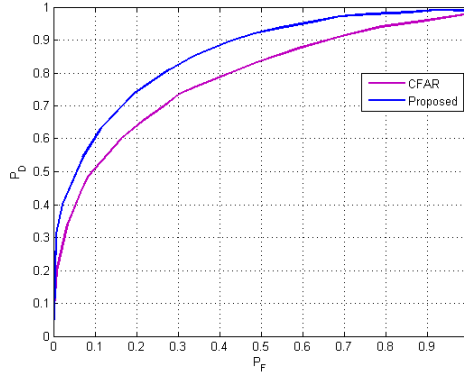


Figure 3.5: Receiver Operating Characteristic (ROC).

Figure 3.5 presents the ROC curves of the proposed discovery scheme and the constant false alarm rate (CFAR) detector developed in [102] and here considered as a benchmark. The ROC of both schemes is evaluated for an SNR value of 10dB. Overall, the proposed scheme performs better than the CFAR with approximately 0.1 higher detection probability for all target false alarm values. In the following results, the detection threshold is set by fixing  $P_F = 0.01$ .

Figures 5.1 and 3.7 depicts the experimental ProSe-enabled user Discovery rate, defined as the number of trials for which the searching user succeeds to detect transmitting ones. The figures depict two scenarios: the first one evaluates the performance for steady users while the second one assumes a pedestrian profile with low speed. In the latter scenario, we opt for the Evolved Pedestrian-A (EPA) channel, which exhibits 7 taps with delays  $\{0,30,70,90,110,190,410\}$  (ns) and relative power  $\{0,-1,-2,-3,-8,-17.2\}$ (dB). The EPA channel is defined for 5Hz maximum Doppler frequency, which translates to UE velocity of 2.7Km/h.

In figure 5.1, which depicts the discovery rate as a function of the SNR, we note a good discovery accuracy, which becomes perfect for steady users from an SNR value of 13dB, while it stagnates at a probability of 0.9 for pedestrian users. Naturally, higher SNR leads to better performance of the system. Figure 3.7 shows the discovery rate when varying the distance

between searching and transmitting D2D users. As the transmission power is fixed, it is expected that the discovery accuracy lessens as the distance between neighbors increases. The detection remains satisfactory up to distances of 50m and 40m respectively for steady and pedestrian users. We also note that in the pedestrian profile, no neighbors can be detected farther than 80m.

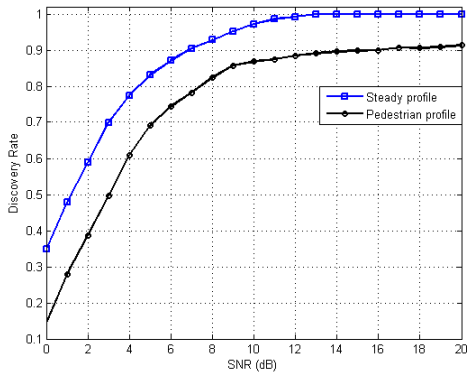


Figure 3.6: The neighbor discovery performance as a function of the SNR.

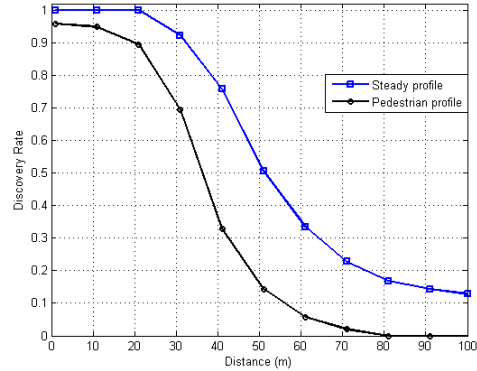


Figure 3.7: The neighbor discovery performance as a function of the user position.

Figure 3.8 illustrates the comparison of the analytical and simulated probability of discovery determined in section 3.4.3.3. It is worth noting that the studied SRS-based provides a satisfactory discovery accuracy that becomes perfect from an SNR value equal to 10 dB and approved through both simulation and analysis. Indeed, the figure shows that the analytical probability exhibits a very good match with the simulated one, up to a very slight gap less than 0.1 dB for an SNR range between 5 dB and 9 dB. Elsewhere, we note that the probabilities concord perfectly. The obtained results prove that the assumptions made in the analysis are valid and the simulation results validate the theoretical analysis.

### 3.5 DMRS-based Discovery

This section explores DMRS signals which are sent regularly through the UL/SL for coherent demodulation to fulfill neighbor discovery [32]. Within the SL, DMRS sequences have the same properties and structure as in the UL and are useful in assisting link setup. By simply listening to DMRS signals from nearby transmitters, a ProSe-enabled UE can be aware of potential partners in its vicinity and hence initiate direct communication with its peers. A robust method that carries out power-normalized correlation between locally known DMRS

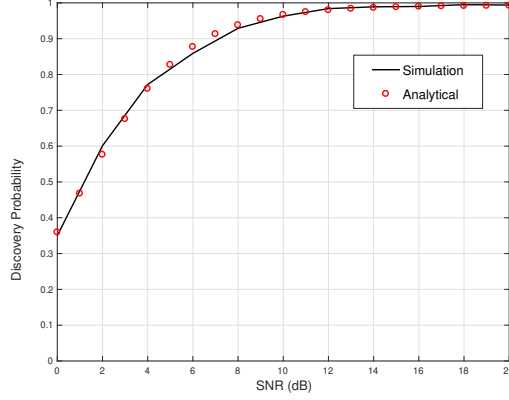


Figure 3.8: Probability of Discovery of the SRS-based approach: Analytical vs Simulation.

candidates and the signal received from neighbor devices is here investigated. To decide about neighbor detection success, a binary hypothesis test is used to design the discoverer UE under a preset false alarm rate constraint. ation of SRS signals [?] without any additional resources.

### 3.5.1 Discovery Metric

To distinguish users interested in establishing a direct link for ProSe communication from inactive or disabled users, the listener UE-0 performs a power normalized cross-correlation of the received signal to the local known DMRS sequence candidates. Assuming synchronization between UE-0 and UE- $i$ , the discovery metric carried out to identify a UE- $i$  willing to establish direct communication with UE-0 is then expressed as

$$\Gamma(i, n) = \left( \frac{|\gamma(i, n)|}{\rho(n)} \right)^2, \quad i \in \mathcal{U}, \quad (3.22)$$

where  $n$  refers to the time index ( with reference to the DMRS sequence start:  $0 \leq n \leq N-1$ ),  $\gamma(i, n)$  is the correlation of the received signal to the local known DMRS sequence candidate  $\mathbf{s}_i$  which is expressed as

$$\gamma(i, n) = \sum_{l=0}^{N-1} r^*(n+l)s_i(l), \quad (3.23)$$

and  $\rho(n)$  is the instantaneous power of the received signal at the time index  $n$  which is given by

$$\rho(n) = \sum_{l=n}^{n+N-1} |r(l)|^2. \quad (3.24)$$

Discovery metrics drawn for active and inactive neighbor UEs are depicted in figure 3.9 in the noiseless case. The figure shows a high magnitude exhibited at the start of the DMRS sequence for the active neighbor while trifling magnitudes are exhibited by inactive users with several side-peaks distributed at different positions. The highest magnitude of the metric associated with the active user corresponds to the first sample of the DMRS sequence, for which the metric sums up the  $N$  samples. Let us analyze the correlation output in the denominator

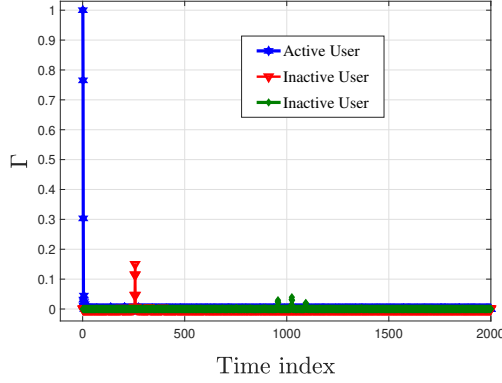


Figure 3.9: DMRS-based Discovery metric for active and inactive ProSe-enabled users [32].

of the discovery metric  $\gamma$  for any active UE of index  $i$  based on the ZC sequence expression in (3.4). Respecting [84], the IFFT of a ZC sequence preserves the initial properties of ZC sequences and can be considered as a ZC sequence, yet with new root and length that are here denoted as  $u'$  and  $N'_{zc}$  respectively. In the noiseless case, and when correlating the received signal with the correct local DMRS sequence  $i$ , which is a ZC sequence [84],  $\gamma$  turns into

$$\gamma(i, n) = e^{-j \frac{\pi u' n(n+1)}{N'_{zc}}} e^{j \frac{\pi u' n(n+1)}{N'_{zc}}} = 1. \quad (3.25)$$

Hence the sum in (3.23) adds constructively in such a way to provide high metric magnitude when the output sums up the ZC sequence length  $N'_{zc}$  ( $N'_{zc} = N$  in this case). However, if the received signal is correlated with a different DMRS sequence corresponding to an inactive UE,

the correlation output becomes

$$\gamma(i, n) = e^{-j\frac{\pi u' n(n+1)}{Nz_c}} e^{j\alpha n} e^{j\frac{\pi u' n(n+1)}{Nz_c}} = e^{j\alpha n}. \quad (3.26)$$

In this case, the sum in (3.23) adds randomly resulting in low metric magnitude.

Consequently, to determine whether the UE- $i$  is active and in the neighborhood of UE-0, the maximum of metrics related to different users are first picked and are compared to a preset threshold  $\eta$ . Then, a binary hypothesis test with two hypotheses  $\mathcal{H}_0$  and  $\mathcal{H}_1$ , where  $\mathcal{H}_1$  denotes the hypothesis that the UE- $i$  is a true active neighbor from the set of ProSe-enabled users, and  $\mathcal{H}_0$  corresponds to the case that the UE- $i$  is not an active neighbor, is applied. This test can be expressed as follows

$$\max_n \left\{ \Gamma(i, n) \right\} \underset{\mathcal{H}_0}{\overset{\mathcal{H}_1}{\gtrless}} \eta, \quad i \in \mathcal{U}, \quad (3.27)$$

Hypothesis  $\mathcal{H}_1$  holds if  $\max_n \left\{ \Gamma(i, n) \right\}$  for UE- $i$  is higher than the threshold  $\eta$ . Otherwise, hypothesis  $\mathcal{H}_0$  detains.

### 3.5.2 Complexity Evaluation

The computational complexity of the discovery method is defined as the number of real floating-point operations (flops) needed to identify active neighbors [32]. One complex multiplication is counted as six flops, whereas a complex addition is two flops [107]. Implementing the discovery metric  $\Gamma$  as expressed in (3.22) results in a huge computational load. Hence, a recursive implementation is proposed to reduce the load due to multiplication operations. To simplify the notation, let us denote by  $\gamma(n)$  the correlation related to any  $i^{\text{th}}$  UE. The evaluation of  $\gamma$  for the  $(i+1)^{\text{th}}$  index can be deduced from the  $i^{\text{th}}$  one as

$$\gamma(n+1) = \gamma(n) - r^*(n)s_i(0) + r^*(n+N-1)s_i(N-1). \quad (3.28)$$

Note that  $n=0$  is the time index corresponding to the start of the DMRS sequence within the received signal, which also represents the first sample of the correlation window of  $N$  samples. This window slides along in time as UE-0 attempting to discover UE- $i$ . The expression in (3.28) reduces the number of flops required per each evaluation to 16 flops in addition to the

number required for the initial term ( $n = 0$ ) which is equal to  $6N + 2(N - 1)$  flops. Hence, a total of  $6N + 18(N - 1)$  flops is consumed to calculate each output sample  $\gamma(n)$ . Identically, the power  $\rho$  in (3.24) can be calculated recursively and has the same cost as  $\gamma$ . The overall complexity cost required to discover a neighbor UE is then  $12N[1 + (N + 3(N - 1))]$  for a correlation window of size  $N$ .

### 3.5.3 Closed-Form Discovery Probability

The analysis presented here considers the case where UE- $i$  is an active neighbor of UE-0, assuming that  $h_i$  is perfectly known at UE-0 and that both UEs are synchronized ( $\tau_i = 0$ ) [32]. A similar assumption of perfect synchronization is also made in [114, 115]. Consequently, the received signal that is considered to compute the discovery metric turns into  $\mathbf{r} = \mathbf{s}_i + \boldsymbol{\omega}$ .

#### 3.5.3.1 Distribution of $\gamma(i, n)$

Substituting the new expression for  $\mathbf{r}$  in the correlation metric (3.23) yields  $\gamma(i, n) = \sum_{l=1}^N s_i^*(l+n)s_i(l) + \boldsymbol{\omega}^*(l+n)s_i(l)$ . When correlated with the correct DMRS sequence,  $\gamma(i, n)$  can be broken into an in-phase part and a quadrature part respecting the term  $s_i^*(l+n)s_i(l)$  product which has a phase  $\phi$ .

For usable SNR values and if the magnitude of  $\gamma(i, n)$  is considered, the quadrature part of it will be insignificant compared to the in-phase part and can therefore be omitted. The magnitude of  $\gamma(i, n)$  hence becomes

$$|\gamma(i, n)| \approx e^{-j\phi} \sum_{l=0}^{N-1} s_i^*(n+l)s_i(l) + \sum_{l=0}^{N-1} \mathbf{I}_\phi\{\boldsymbol{\omega}^*(n+l)s_i(l)\}, \quad (3.29)$$

where  $\mathbf{I}_\phi\{x\}$  stands for the component in the same direction of the phase  $\phi$ . The quadrature part is neglected because the Rician distribution can be approximated by a Gaussian random variable when taking the envelope of a dominant signal with Gaussian noise [116].

In (3.29), the first term is dominant since  $s_i^*(n+l)s_i(l)$  products have the same phase  $\phi$  and add constructively, while the second term can be neglected because its elements can sum with random phases. According to the Central Limit Theorem (CLT),  $|\gamma(i, n)|$  is Gaussian with mean  $\mu_{\gamma_i}$  and variance  $\sigma_{\gamma_i}^2$ . The mean is  $\mu_{\gamma_i} = N\sigma_s^2$  since each of the  $N$  elements  $s_i^*(n+l)s_i(l)$

has an expected value  $\sigma_s^2$ . To determine the variance of the metric, we first calculate the expectation of its square  $E(|\gamma(i, n)|^2)$ , which can be written as

$$\begin{aligned}
E(|\gamma(i, n)|^2) &= E \left[ \sum_{l,k=n}^{N+n-1} [|s_i(l)|^2 + \omega^*(l)s_i(l)] [|s_i(k)|^2 + \omega(k)s_i^*(k)] \right] \\
&= E \left[ \sum_{l,k=n}^{N+n-1} |s_i(l)|^2 |s_i(k)|^2 + \sum_{l=k=n}^{N+n-1} |s_i(l)|^2 |\omega(l)|^2 \right] \\
&= N^2 \sigma_s^4 + N \sigma_s^2 \sigma_\omega^2.
\end{aligned} \tag{3.30}$$

Then the variance can be evaluated as

$$\begin{aligned}
\sigma_{\gamma_i}^2 &= E(|\gamma(i, n)|^2) - (\mu_{\gamma_i})^2 \\
&= N^2 \sigma_s^4 + N \sigma_s^2 \sigma_\omega^2 - (N \sigma_s^2)^2 = N \sigma_s^2 \sigma_\omega^2.
\end{aligned} \tag{3.31}$$

### 3.5.3.2 Distribution of $\rho(n)$

By substituting the new expression of  $\mathbf{r}$  into (3.24), the power turns to

$$\rho(n) = \sum_{l=n}^{n+N-1} \left[ |s_i(l)|^2 + s_i^*(l)\omega(l) + s_i(l)\omega^*(l) + |\omega(l)|^2 \right]. \tag{3.32}$$

The expression of the power in (3.32) adds up to  $N$  variables. Assuming independence between the summed terms in  $\rho(n)$  and for  $N$  sufficiently large, the CLT enables us to approximate  $\rho(n)$  using a Gaussian distribution that is characterized by its mean  $\mu_\rho$  and variance  $\sigma_\rho^2$ . Furthermore, since  $s_i(l)$  and  $\omega(l)$  are mutually uncorrelated, the second and third terms of equation (3.32) have a zero mean. Only the first and the fourth terms are involved in its expected value, ultimately resulting in a mean  $\mu_\rho = N(\sigma_s^2 + \sigma_\omega^2)$ .

To calculate the variance of  $\rho(n)$ , we first evaluate the expected value of its square  $E(|\rho(n)|^2)$ ,

which can be written as

$$\begin{aligned}
E(|\rho(n)|^2) &= E \left[ \sum_{l=n}^{n+N-1} (r^*(l)r(l)) \sum_{k=n}^{n+N-1} (r(k)r^*(k)) \right] \\
&= E \left[ \sum_{l=n}^{n+N-1} (|s_i(l)|^2 + s_i^*(l)\omega(l) + s_i(l)\omega^*(l) + |\omega(l)|^2) \right. \\
&\quad \left. \times \sum_{k=n}^{n+N-1} (|s_i(k)|^2 + s_i(k)\omega^*(k) + s_i^*(k)\omega(k) + |\omega(k)|^2) \right]. \tag{3.33}
\end{aligned}$$

Exploiting the lack of correlation between the signal  $\mathbf{s}$  and the noise  $\boldsymbol{\omega}$  allows us to omit the terms including both variables, and so the expected value of  $|\rho(n)|^2$  can be written as

$$\begin{aligned}
E(|\rho(n)|^2) &= E \left[ \sum_{l,k=n}^{n+N-1} |s_i(l)|^2 |s_i(k)|^2 + 2 \sum_{l=k=n}^{n+N-1} |s_i(l)|^2 \right. \\
&\quad \left. |\omega(k)|^2 + 2 \sum_{l,k=n}^{n+N-1} |s_i(l)|^2 |\omega(k)|^2 + \sum_{l,k=n}^{n+N-1} |\omega(l)|^2 |\omega(k)|^2 \right] \\
&= N^2 \sigma_s^4 + 2N^2 \sigma_s^2 \sigma_\omega^2 + 2N \sigma_s^2 \sigma_\omega^2 + N^2 \sigma_\omega^4. \tag{3.34}
\end{aligned}$$

The variance of  $\rho(n)$  is then given by

$$\begin{aligned}
\sigma_\rho^2 &= E(|\rho(n)|^2) - (\mu_\rho)^2 = N^2 \sigma_s^4 + 2N^2 \sigma_s^2 \sigma_\omega^2 + 2N \sigma_s^2 \sigma_\omega^2 + N^2 \sigma_\omega^4 - (N(\sigma_s^2 + \sigma_\omega^2))^2 \\
&= 2N \sigma_s^2 \sigma_\omega^2. \tag{3.35}
\end{aligned}$$

### 3.5.3.3 Distribution of $\Gamma_{i,\max}$

In order to determine the distribution of the metric at  $\Gamma_{i,\max}$ , let its square root be defined as  $\alpha_i = |\gamma_{i,\max}|/\rho_{\max}$ , where  $|\gamma_{i,\max}|$  and  $\rho_{\max}$  stand respectively for the values of the correlation metric in (3.23) and the power in (3.24) at the PNC metric maximum. To simplify the notation, we use  $\mu_{\gamma_i}$  and  $\sigma_{\gamma_i}^2$  to refer to the mean and variance of  $|\gamma_{i,\max}|$ , while  $\mu_\rho$  and  $\sigma_\rho^2$  are used to refer to the mean and variance of  $\rho_{\max}$ .

Since  $\alpha_i$  has Gaussian random variables in the numerator and the denominator, and because the standard deviations of both the numerator and denominator ( $\sigma_{\gamma_i} = \sqrt{N\sigma_s^2\sigma_\omega^2}$  and  $\sigma_\rho = \sqrt{2N\sigma_s^2\sigma_\omega^2}$ ) are much smaller than their means ( $\mu_{\gamma_i} = N\sigma_s^2$  and  $\mu_\rho = N(\sigma_s^2 + \sigma_\omega^2)$ ), the ratio

$\alpha_i$  can be approximated by a single Gaussian random variable [117]. The mean of  $\alpha_i$  is

$$\mu_{\alpha_i} = \frac{\sigma_{\gamma_i}^2}{\sigma_{\gamma_i}^2 + \sigma_{\rho}^2}, \quad (3.36)$$

and its variance is

$$\sigma_{\alpha_i}^2 = \frac{\mu_{\gamma_i}^2 \sigma_{\rho}^2 + \mu_{\rho}^2 \sigma_{\gamma_i}^2}{\mu_{\rho}^4}. \quad (3.37)$$

The decision metric value  $\Gamma_{i,\max}$  corresponds to  $\alpha_i^2$  and follows the square of a Gaussian distribution with a variance  $\sigma_{\alpha_i}^2$  much smaller than its mean  $\mu_{\alpha_i}$ . Hence,  $\Gamma_{i,\max}$  can also be approximated by a Gaussian random variable expressed as

$$\begin{aligned} \Gamma_{i,\max} &\rightarrow (\mu_{\alpha_i} + z(0, \sigma_{\alpha_i}^2))^2 = \mu_{\alpha_i}^2 + 2\mu_{\alpha_i}z(0, \sigma_{\alpha_i}^2) + (z(0, \sigma_{\alpha_i}^2))^2 \\ &\approx \mu_{\alpha_i}^2 + 2\mu_{\alpha_i}z(0, \sigma_{\alpha_i}^2), \end{aligned} \quad (3.38)$$

where  $z(\mu, \sigma^2)$  is a Gaussian random variable with mean  $\mu$  and variance  $\sigma^2$ . The mean of  $\Gamma_{i,\max}$  is consequently expressed as

$$\mu_{\Gamma_{i,\max}} = E(\Gamma_{i,\max}) = \frac{\sigma_s^4}{(\sigma_s^2 + \sigma_{\omega}^2)^2}, \quad (3.39)$$

and the variance is

$$\begin{aligned} \sigma_{\Gamma_{i,\max}}^2 &= 4\mu_{\alpha_i}^2 \sigma_{\alpha_i}^2 \\ &= \frac{2\sigma_s^4[(1 + \mu_{\Gamma_{i,\max}})\sigma_s^2\sigma_{\omega}^2 + (1 + 2\mu_{\Gamma_{i,\max}})\sigma_{\omega}^4]}{N(\sigma_s^2 + \sigma_{\omega}^2)^4}. \end{aligned} \quad (3.40)$$

### 3.5.3.4 Discovery Probability

The probability of neighbor discovery is defined as the probability that the estimated maximum value of the metric in (3.22), which is denoted by  $\Gamma_{i,\max}$ , is higher than the threshold  $\eta$ , and can be expressed as [33]

$$PD_i = \Pr(\Gamma_{i,\max} > \eta) = \bar{F}_{\eta}(\Gamma_{i,\max}), \quad (3.41)$$

where  $\bar{F}$  is the complementary cumulative distribution function. Referring to the previous statistical analysis, which allowed for the approximation of  $\Gamma_{i,\max}$  through the use of a Gaussian random variable of mean  $\mu_{\Gamma_{i,\max}}$  and variance  $\sigma_{\Gamma_{i,\max}}^2$ , the discovery probability can be derived in its closed-form as

$$PD_i = 1 - \left[ \frac{1}{2} \left( 1 + \operatorname{erf} \left( \frac{\eta - \mu_{\Gamma_{i,\max}}}{\sqrt{2\sigma_{\Gamma_{i,\max}}^2}} \right) \right) \right] = Q \left( \frac{\eta - \mu_{\Gamma_{i,\max}}}{\sigma_{\Gamma_{i,\max}}} \right),$$

where  $\operatorname{erf}(\cdot)$  is the error function and  $Q(\cdot)$  is the Q-function.

At high SNR values, the mean in (3.39) approximately equals 1 and the variance in (3.40) is approximately  $2\sigma_s^4[(1+1)\sigma_s^2\sigma_\omega^2]/[N(\sigma_s^2)^4] \approx 4/(NSNR)$ . In this case,  $PD$  can be rewritten as a function of the SNR as follows

$$PD_i = Q \left( \frac{\eta - 1}{2\sqrt{\frac{1}{NSNR}}} \right). \quad (3.42)$$

### 3.5.4 Performance Evaluation

In this section, we evaluate the accuracy of the PNC approach in terms of Probability of Discovery (PD) through both simulation and theoretical results using the closed-form expression derived in (6.2). We also compare it to the GLRT-based approach [103]. The considered benchmark also exploits the DMRS sequence sent within the SL to which GLRT is performed to first estimate the channel gain. Then, a hypothesis test is applied to decide whether or not an estimated gain corresponds to an active ProSe-enabled neighbor. Simulations are performed using  $10^4$  Monte Carlo realization for which the distance between ProSe-enabled UEs is chosen randomly within a circle of 150-meter diameter. Unless otherwise indicated, the number of ProSe-enabled UEs  $N_u$  is here set to 10 users.

The parameters of the simulation setting are summarized in table 3.2 respecting LTE standard specifications.

To evaluate the performance of the PNC method proposed, we first present ROC in figure 3.10 for an SNR value equal to 5 dB. The GLRT explores the block structure of the channel vector while our method relies on the maximum magnitude of the discovery metric as expressed in (3.27). Compared to the GLRT, the proposed PNC method is optimal in the sense that

Table 3.2: Simulation parameters of the DMRS-based approach

Parameter	Value
System bandwidth	20 MHz
UE transmission power	0 dBm
FFT size	$N = 2048$ sub-carriers
CP size	$N_{cp} = 140$ sub-carriers
DMRS bandwidth	50 RB
ZC sequence length	$N_{zc} = 571$ sub-carriers
Extended ZC sequence length	$M = 578$ sub-carriers
D2D pathloss	$148 + 40 \log_{10}(d[\text{Km}])$

it provides the highest detection probability for a fixed false alarm rate, especially for low values. This is due to the good correlation properties of ZC sequences used to generate DMRS sequences that provide high peak for active users. In the following results, the detection threshold  $\eta$  is set by fixing  $P_F = 0.01$  among the  $10^4$  independent channel realizations.

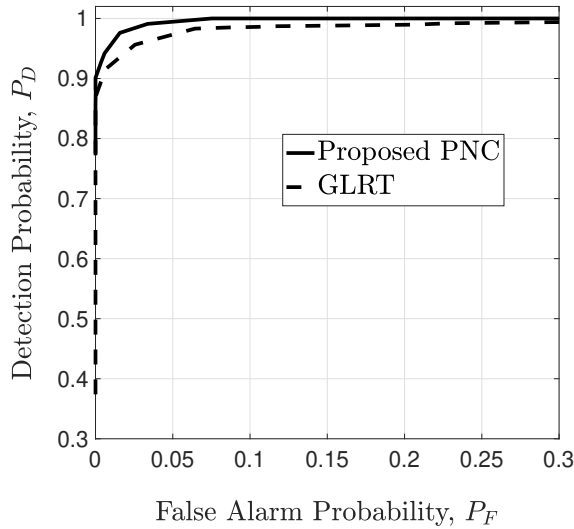


Figure 3.10: ROC of the PNC and the GLRT methods for SNR value 5dB.

The performance of the proposed method is depicted in terms of detection probability as a function of the SNR in figure 3.11. For each SNR value, the distance  $d$  between the listening device UE-0 and the sender UE-i is chosen randomly for each realization within a range of 150 meters. The result shows that the proposed PNC method is more immune to noise and it achieves almost perfect discovery from an SNR value equal to 2 dB. For a target detection probability of 0.9, the proposed method realizes a gain of 3 dB compared to the considered

benchmark, which is based on the application of the GLRT to the DMRS sequence [103].

Figure 3.12 depicts the theoretical and simulated PD of the PNC and the GLRT-based approaches in the case of AWGN channel. Globally, the provided discovery accuracy is satisfactory and outperforms the considered benchmark. Indeed, the PD becomes perfect from an SNR value less than 1 dB, which solidifies the robustness of the proposed approach and guarantees quality service, especially for Public Safety-critical scenarios.

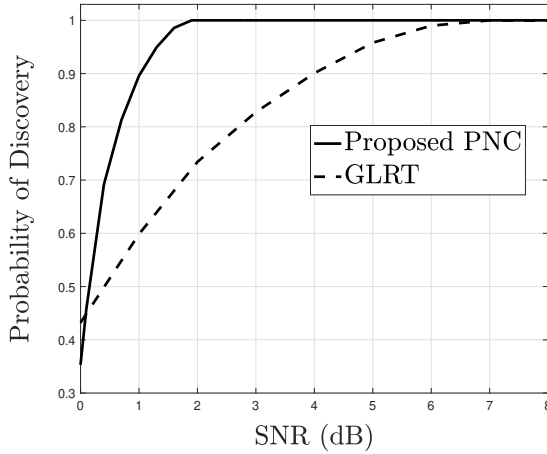


Figure 3.11: Probability of Discovery of DMRS-based methods: PNC vs GLRT.

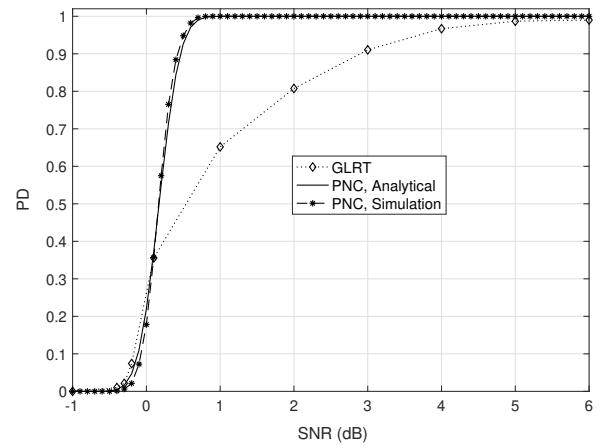


Figure 3.12: PD for single-user scenario in the AWGN channel.

It is worth noting that detection performance depends on the value of  $\eta$ . In fact, the lower the threshold value, the higher the possibility to detect an active user satisfying  $\mathcal{H}_1$  in (3.27) for a specific DMRS sequence candidate  $\mathbf{s}_i$ . This observation implies that UE- $i$  is an active neighbor. However, very low values of  $\eta$  may result in a false discovery.

To highlight the impact of interfering signals on the discovery probability, figure 3.13 depicts the PD in the multi-user case using the received signal expressed in (3.5) and considering more realistic multi-path fading channels for unsynchronized UEs in low and high mobility scenarios. It is shown that despite the accumulation in interference due to the increasing number of users transmitting their DMRS signals, the performance of both schemes only degrades a little, and remains satisfactory for the considered SNR range. Indeed, the probability reaches about 0.98 starting from SNR values of 8dB and 11dB for the PNC and GLRT methods, respectively. The minor effect of interfering signals can be explained by the orthogonality of DMRS sequences sent by different UEs; such orthogonality helps to prevent adjacent channel interference. On

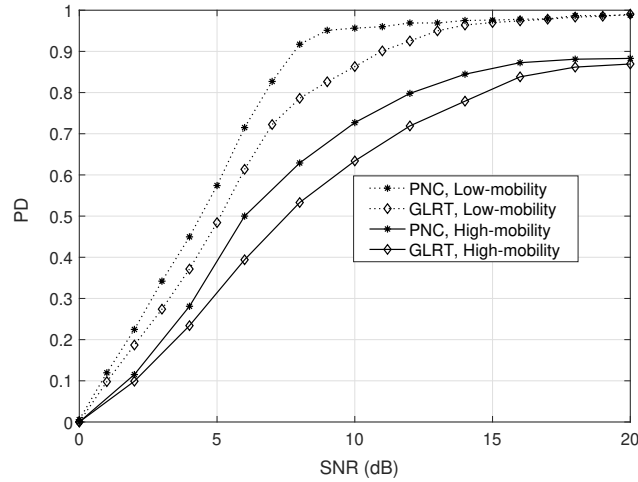


Figure 3.13: PD for multi-user scenario in Rayleigh multipath fading channels.

the other hand, however, the multi-path fading affects the detection performance, capping it at a maximum PD value of about 0.87 in both methods.

### 3.6 Conclusion

In this chapter, distributed neighbor discovery for proximity services in LTE networks is investigated based on reference signals. Indeed, due to the orthogonality between RS sequences, the approaches enable the discovery and the identification of the potential users willing to establish direct links with their peers. The proposed methods are fully compatible with the existing LTE architecture and can be used for both SL and UL liaisons without requiring any additional resources. The proposed approaches perform correlation on the RS signal assigned to ProSe-enabled UEs and sent through the UL/SL, followed by a binary hypothesis test. To reduce the computational load due to correlation with all available RS sequences, we suggested recursive implementations. Further, theoretical studies were carried out to determine the discovery probability in its closed-form of the SRS-based and the DMRS-based metric.

The SRS-based approach exploits cross-correlation while the DMRS-based approach uses a power-normalized-correlation metric. Simulation results showed the capability of the proposed methods to ensure an accurate discovery, with higher robustness offered by the DMRS-based approach at low SNR values. In the case of multi-user scenario, the discovery probability exhibited a minor effect of interfering signals, which can be explained by the orthogonality

of reference sequences sent by different UEs; such orthogonality helps to prevent adjacent channel interference. On the other hand, however, the multi-path fading affects the detection performance.

Furthermore, the obtained results demonstrate that, when applied to the LTE signal, the simulated probability agrees perfectly with the theoretical one, validating the analysis carried out in the two approaches and the approximated closed-form for any functional system setting.

## Chapter 4

# Random Access-Like Neighbor Discovery

### 4.1 Introduction

This chapter also focuses on neighbor discovery to enable D2D communication over cellular networks exploiting random access-like procedures for both centralized and distributed strategies. To achieve neighbor discovery, the first proposed scheme suggests partial contention-free beacon assignment. During the first stage, a D2D transmitter randomly selects a beacon among a predefined set of beacons and sends it to the D2D receiver, with whom it is willing to initiate a D2D link. The selected beacon will be used by the D2D receiver as a temporary beacon to switch from the idle mode to the connected mode during which the BS will assign a beacon from the contention-free part. Then, the eNB will allocate resources to each respective beacon so that the transmitter UE exploits it to pursue its communication. If two or more UEs select the same beacon at the first stage, a collision happens at the network side during the connection of the corresponding receiver UEs resulting in a connection failure. The proposed scheme helps to reduce the underutilization of resources through the random access procedure and it guarantees low collision probability thanks to the partial contention-free concept. Then, based on more recent 5G system specifications, we investigate network-assisted as well as distributed group discovery strategies for the available D2D communication modes: supervised and unsupervised. The studied strategies are inspired by the Aloha and Polling protocols, and are

evaluated in terms of time required to complete the group discovery. Two different collision models are assumed for performance evaluation. The first model considers MAC collision, referred to as the L-2 model, in which when two or more UEs pick the same resource, the mutual interference will prevent any collided message from being received by other UEs. The second one considers a more practical assumption where some collided messages may be received if the signal strength is sufficiently high to provide a satisfactory Block Error Rate (BLER), and it is referred to as the L-1 model.

Throughout the presented results, we cover both low-mobility for ProSe scenarios and high-mobility for public safety V2X scenarios. In both cases, multi-path Rayleigh fading channels are used with low and high Doppler shift values. Unlike most of the previously described approaches, this work uses the current standard specifications without the need for any additional signaling messages, making it fully compatible with the standard and applicable to real-life scenarios.

## 4.2 Single Discovery Strategy

In this section, we study neighbor discovery for a single user scenario. In particular, we investigate partial contention-free beacons' assignment to enable neighboring UEs to establish direct links by simply listening to their UL channels with the assistance of the eNB [35].

### 4.2.1 System Architecture

We consider an LTE-A cellular network that supports direct user communications through uplink for proximity-based services simultaneously with conventional cellular communications as depicted in figure 4.1. A UE in the network has access to the eNB for conventional cellular communications and can also establish direct D2D links with his neighbors if permitted by the network. We here briefly introduce the main elements of the LTE-A uplink channel that are involved in our scheme.

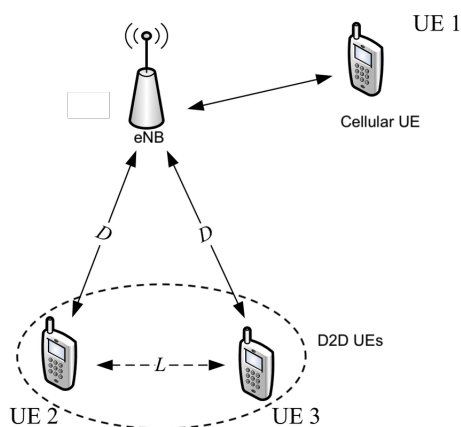


Figure 4.1: System architecture: cellular user and D2D users.

#### 4.2.1.1 Uplink Channels and Random Access Procedure

The LTE UL transmission comprises three physical channels: Physical Uplink Shared Channel (PUSCH), Physical Uplink Control Channel (PUCCH), and Physical Random Access Channel (PRACH). The PUSCH and PUCCH are dedicated channels, which are modulated using UE-specific information and exploited for the transport of data and control signaling, respectively. The eNB assigns different resources to different UEs such that their signal can be separated easily during uplink reception. The PRACH allows UEs to initiate a connection with the eNB during its identification within a cell or for reconnection. When a UE intends to establish a connection to the eNB, he first initiates a random access procedure by sending a preamble to the eNB via the PRACH. The RBs for PRACH are semi-statistically allocated within the PUSCH region and are repeated periodically. On a PRACH, a UE can transmit a preamble, on which a ZC sequence is mapped to allows multiple orthogonal sequences to be generated from the same ZC sequence.

During each PRACH time slot, a transmitting UE may randomly select a preamble from a predefined set of 64 orthogonal preambles to allow eNB to distinguish different UE transmissions. Since the preamble set is known to all UEs within the network, a UE that aims to establish a D2D link can detect different preamble sequences as part of the neighbor discovery process. Given this feature, we identify PRACH as a potential neighbor discovery opportunity.

### 4.2.2 Discovery Framework

We consider a single cell-centered by an eNB that presents the discovery entity, within which we define the set of the indices of all UEs involved in the D2D discovery by  $\mathcal{U}$  [35]. A user belonging to  $U$  is indexed by its identifier  $u$  and located by its two-dimensional coordinate  $\mathbf{c}_u$ . Each UE has a set of target users UEs  $\mathcal{T}$  within a discovery distance  $D$ . An unidirectional link from a UE  $i$  to UE  $j$  implied that UE  $i$  is willing to discover UE  $j$  in its proximity within the distance  $D$ . A link  $(i, j)$  is established if and only if UE  $j$  is in the proximity of UE  $i$  (i.e.,  $|\mathbf{c}_i - \mathbf{c}_j| \leq D$ ) and UE  $j$  belongs to the set of target users of UE  $i$  (i.e.,  $j \in \mathcal{T}_i$ ). The set of all available links is denoted by  $\mathcal{L}$ .

To be able to access to the network, the transmitter Tx-UE and the receiver Rx-UE must have identifiers, which are beacons selected from a predefined set that we here denote by  $\mathcal{B}$ . This latter is partitioned to two groups; the contention-based part ( $\mathcal{B}_{CB}$ ) and contention-free ( $\mathcal{B}_{CF}$ ) part of sizes  $N_{CB}$  and  $N_{CF}$  respectively. The first group is dedicated to being used by the Tx-UEs and by Rx-UEs temporary. The second group is reserved by the eNB for contention-free final beacon assignment. As the proposed scheme is based on the random access procedure of LTE-A system, beacons here are generated from ZC sequences. Hence, during each PRACH time slot, a Tx-UE will randomly select a beacon out of the  $64 \cdot N_{CF}$  orthogonal beacons made from the same ZC sequence.

### 4.2.3 Partial Contention-Free Discovery

The discovery procedure, depicted in figure 4.2 is designed in three steps. During the first step, the Tx-UE randomly selects a beacon from the contention-based sub-set. Then, the same beacon is used by the Rx-UE to connect to the eNB and obtain a new contention-free beacon, to which the eNB assigns uplink RBs. Finally, the Tx-UE is allocated the UL RB by the eNB corresponding to its initial beacon [35].

#### 4.2.3.1 Preamble Selection and Forward

Each Tx-UE selects a beacon out of the set of the possible  $64 \cdot N_{CF}$  available beacons. Let  $b_{TX}$  denotes the beacon index that is selected by Tx-UE  $i$  and  $\mathcal{T}^i$  denotes the set of target Rx-UE of

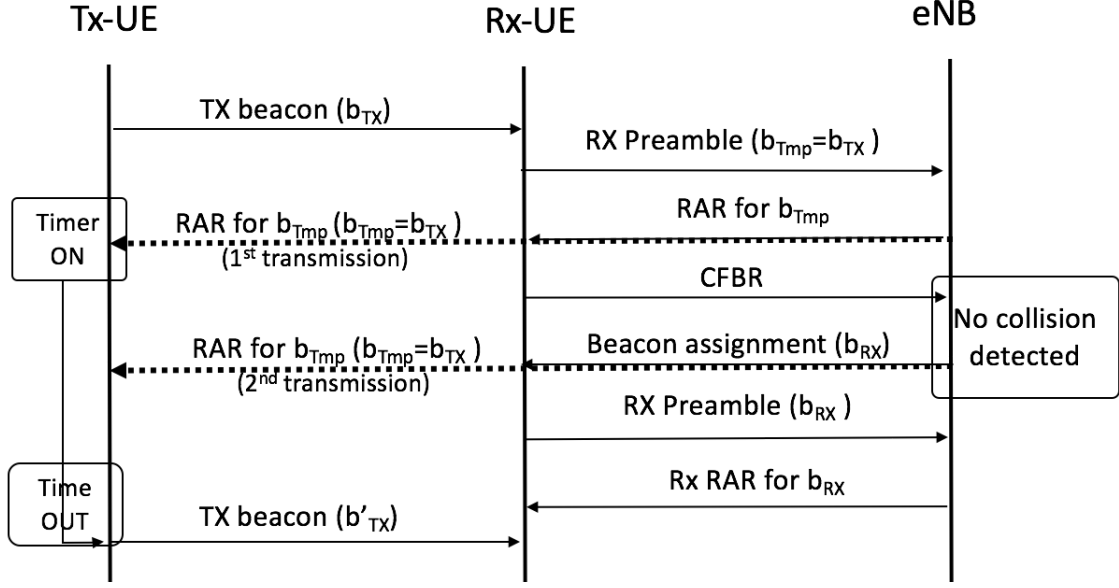


Figure 4.2: Messages exchanged during the discovery process.

*i.* Tx-UE  $i$  randomly selects its beacon  $b_{TX}$  out of  $\mathcal{B}_{CB}$  with an equal probability. The selected beacon is sent to the target Rx-UE through the uplink PRACH [35]. The transmission power of the beacon from the Tx-UE is set so that the target Rx-UEs within the discovery distance  $D$  can receive but the other Rx-UEs outside the set of target users  $\mathcal{T}_i$  cannot. Hence, the beacon from the Tx-UE  $i$  can be heard by any Rx-UE  $j$  for which  $|\mathbf{c}_i - \mathbf{c}_j| \leq D$ .

Any Rx-UE that is listening to the Uplink within his neighborhood for hearing beacons from any nearby Tx-UE, tries to receive beacons assigned to the discovery sub-set to which it belongs. Note that if more than one nearby Tx-UE sending the same beacon simultaneously, the Rx-UE can not distinguish how many Tx-UEs send the beacon but only knows there is at least one nearby Tx-UE that sends the beacon. Upon receiving at least one beacon, Rx-UE is activated. Next, we explain the second phase of the proposed scheme, which is the Rx-UE reporting phase.

#### 4.2.3.2 Receiver Connection Phase

In this phase, all activated Rx-UEs will report the received beacons to the eNB by using a method similar to the standard random access procedure. To this aim, the same beacon received during the previous step is used to temporary identify the Rx-UE. Let  $b_{tmp}$  denotes the

beacon index received at the activated Rx-UE  $j$ . The eNB receives all the beacons transmitted by all the activated Rx-UEs. Upon receiving the beacons from different Rx-UE, the eNB allocates a number of  $N_{\text{RB}}$  uplink RBs for each beacon which has been initially chosen by at least one activated Tx-UE and used to identify the Rx-UE during its connection to the eNB. The eNB sends a random access response (RAR) message for each received beacon, in which it specifies the uplink RB grant that maps each UE.

When receiving the RAR message, activated Rx-UE  $j$  finds the RBs corresponding to its temporary beacon  $b_{\text{tmp}}$  and sends a Contention-Free Beacon Request (CFBR) on those RBs. The CFBR message is introduced in our scheme to enable the Rx-UE to recover a new beacon. If more than one activated Rx-UEs forwarded the same beacon, a collision happens since more than one Rx-UEs send their CFBR messages on the same RBs. In this case, the eNB fails to decode the CFBR message and will not answer the request. The eNB can decode the CFBR messages transmitted on RBs without collision and answer the request by allocating a dedicated beacon for each successful Rx-UEs.

#### 4.2.3.3 Transmitter Connection Phase

Once the dedicated beacon is assigned to the Rx-UE, this latter will answer with a random access beacon with its new beacon, as in the contention-free random access procedure for the LTE-A standard. The eNB keeps the initial successful Rx-UE temporary beacon ( $b_{\text{tmp}}$ ) and sends a second RAR message corresponding to the uplink RBs for each beacon. As the Rx-UE have used the same beacon as temporary identifier to connect to the eNB, the connection request related to colliding beacons are failed from the previous step. This means that the Tx-UE who have initially chosen the same beacons are not involved during this step, which greatly reduces the time to process the connection procedure.

It is worth noting that using the same beacon to identify the Tx-UE and the Rx-UE in our scheme will induce ambiguity at the transmitter side which will normally answer the RAR message sent from the eNB corresponding to the beacon he selected. To solve this ambiguity, we suppose that the Tx-UE will not answer the first RAR message received from the eNB and set a timer starting from the first RAR message reception. If the Tx-UE does not receive a second RAR message after a timeout, a collision is assumed to happen for the selected beacon. The Tx-UE will then restart the random access procedure by selecting a new beacon as in the first

step. Another solution to solve this issue might be to add one bit in the RAR message which indicates the state 0 if the RAR message is destined to the Rx-UE (first RAR transmission) and the state 1 if the RAR message is destined to the Tx-UE (second RAR transmission). In this case, each UE will first check the state of the bit in the RAR message before using the RBs allocated to it.

#### 4.2.4 Performance Evaluation

In this section, we present the performance evaluation of the proposed neighbor discovery scheme by using matlab simulation. We consider a single cell with radius  $R=500\text{m}$  where the number of UEs (Tx and Rx) follows the Poisson point process with density  $\lambda$ . The density in what follows is given in the unit of the number of UEs per  $\text{m}^2$ . Among the users involved here, half of them is considered as Tx-UE while the other half is considered as Rx-UE. The total number of available beacons in the PRACH is fixed to 64 beacons, where half of them is reserved for contention-free allocation. Figure 4.3 presents two configurations of the UEs location in the considered network with different density values  $\lambda$ .

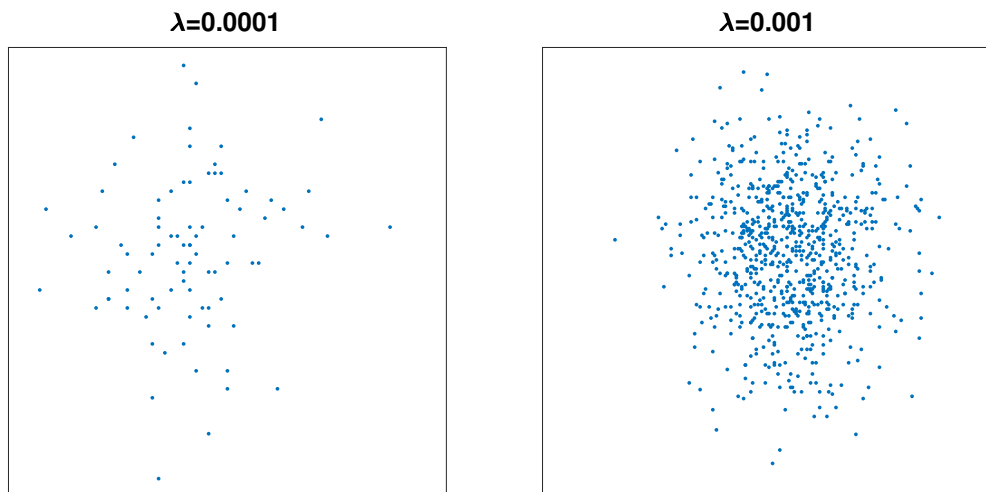


Figure 4.3: Network deployment with different UE densities.

We define the variable  $\tau$  corresponding to the number of slots for the discovery procedure. The maximum round-trip distance is here set to 100m between a Tx-UE and an Rx-UE. The duration of a beacon sequence is here considered equal to the length of one slot (0.5ms), and

the maximum round-trip time corresponding to 100m is then  $0.66\mu\text{s}$ . Therefore, it is possible to have more than 700 beacons in one slot for the proposed discovery scheme. Considering the cyclic prefix and the guard time, we estimate that 400 beacons are available in one slot resulting in a total number of available preambles  $400\tau$ . In the following, we set  $\tau$  to 2 time slots which results in a total number of 800 beacons.

In figure 4.4, we present the total number allocated RBs as a function of the density of UEs  $\lambda$ , and we also vary the discovery distance  $D$ . The plotted curves depict the sum of the numbers of uplink RBs allocated for both the Tx-UEs and the Rx-UEs. The figure shows that the number of allocated uplink RBs increases as the density of connected UEs increases. We also note that as the discovery distance increases, more uplink RBs are allocated. This result shows that the proposed scheme can adaptively allocate uplink RBs in response to the number of required links.

Figure 4.5 depicts the collision probability of beacons selected by Tx-UEs as a function of the total number of users and different discovery distances. Consistently with the previous results, the collision probability rises as the number of connected users increases. Also, for higher discovery ranges the collision probability rises as the number of users involved within the discovery group becomes high.

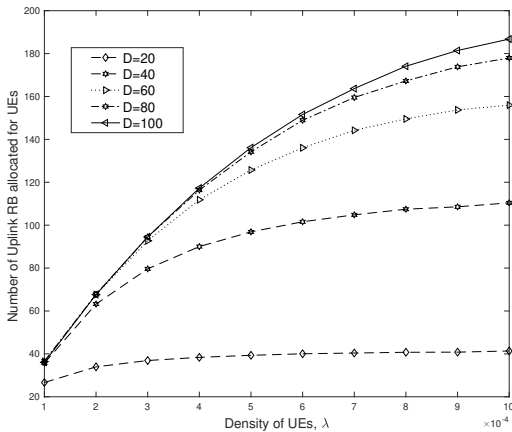


Figure 4.4: Total number of uplink RBs allocated for Tx-UEs and Rx-UEs as a function of the number of UEs (density  $\lambda$ ) for different discovery distance  $D$ .

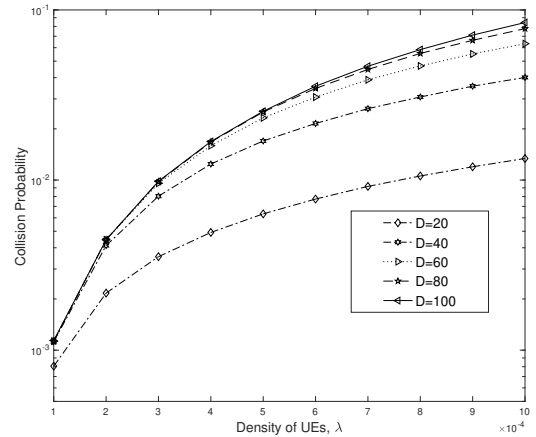


Figure 4.5: Collision probability as a function of the number of UEs (density  $\lambda$ ) for different discovery distance  $D$ .

In the following, we assess the impact of the number of slot dedicated for neighbor discovery

on the performance of the proposed scheme. Figure 4.6 illustrates the collision probability as a function of the number of slots ( $\tau$ ) reserved for the discovery procedure and for different UE density. We here observe that the collision probability can be decreased by increasing the number of slots reserved for discovery which increases the number of available beacons.

Another important measurement to evaluate the proposed scheme is the link discovery probability, which is defined as the number of the discovered links over the number of all available links. In figure 4.7, we can see that it is possible to achieve a target link discovery probability by adjusting the number of preambles. For example, to achieve the link discovery probability of 0.8 given that the density is  $\lambda = 0.007$ , there should be at least 5 slots for the discovery procedure, which means we need 2000 available beacons.

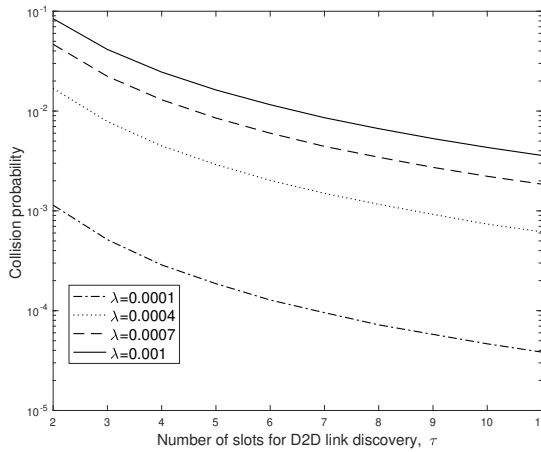


Figure 4.6: Collision probability as a function of the number of slots reserved for the discovery process.

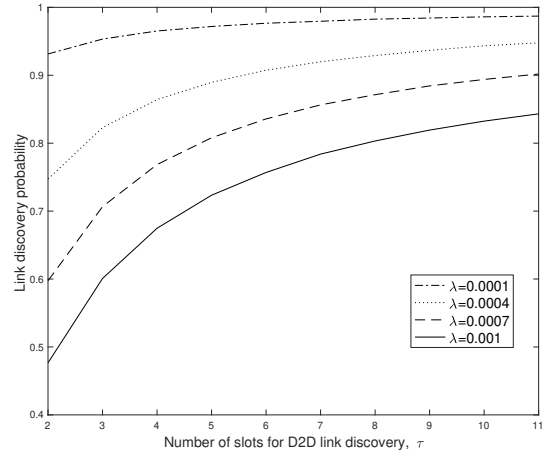


Figure 4.7: Link discovery probability as a function of the number of slots reserved for the discovery process.

The advantages of the proposed D2D discovery scheme can be summarized in three points: First, the proposed scheme can effectively prevent underutilization of available resources through the use of the random access procedure. Second, contention-free beacon assignment for the receiver UE greatly reduces the potential collision resulting from the random multiple selection of the same beacon. Third, the use of temporary beacons reduces the multiple message exchange between the D2D transmitter/D2D receiver and the BS, which can further reduce the time required to establish a D2D link.

### 4.3 Group Discovery Strategies

In this section, we explore the recent LTE D2D radio resource management specifications to evaluate the potential of neighbor discovery for safety-critical V2X communication. In particular, we investigate multiple-round discovery for a group of users through network-assisted and distributed strategies for the proposed D2D communication modes specified in the 5G system specification : supervised and unsupervised. The studied strategies are inspired by the Aloha and Polling protocols, and are evaluated in terms of time required to complete the group discovery [33].

#### 4.3.1 System Architecture

We consider the SL signal of an LTE radio access network using SC-FDMA transmission and an SL resource element grid in the frequency division duplex mode. The system supports direct communication modes in which UEs can establish direct pairwise links for both ProSe and V2X application cases.

##### 4.3.1.1 Discovery Message Transmission

The PSDCH resource pool repeats periodically in the time domain; the period is given by the parameter  $P$ , which is set by the Information Element (IE) *DiscPeriod*. The period takes a value in binary multiples of  $0.32s$  (i.e. a permissible set includes  $0.32s$ ,  $0.64s$ ,  $1.28s$ ,  $2.56s$ ,  $5.12s$ , and  $10.24s$ ). In each period, the PSDCH configuration variables  $prb - Start$ ,  $prb - End$ , and  $prb - Num$  determine the range of sub-bands that the PSDCH occupies, as depicted in Figure 4.8. The *SL - OffsetIndicator* IE provides the displacement of the pool from the first subframe, while the *SL - TF - ResourceConfig* IE contains these IEs [33].

An RB with index  $m$  is part of the PSDCH if  $prb - Start \leq m \leq prb - Start + prb - Num$  or  $prb - End - prb - Num \leq m \leq prb - End$ . The set of subframes that forms the PSDCH is encoded in a bitmap defined by the IE *subframeBitmap*, where bit 1 indicates that the corresponding subframe is part of the PSDCH. The bitmap is repeated for *numRepetition* times. The *subframeBitmap* IE is located in the *SL - DiscResourcePool*. A UE with a discovery message to send generates a uniformly distributed random value  $p \in (0, 1]$ . The

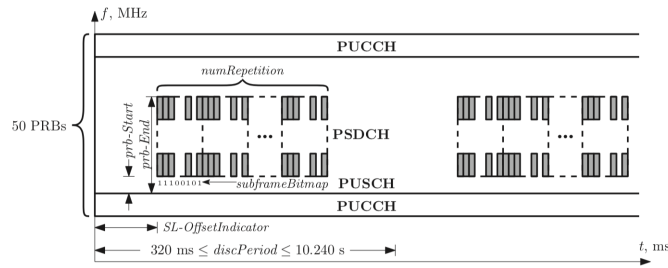


Figure 4.8: The structure of the PSDCH resource pool.

UE sends its message if  $p$  is less than a threshold value  $txProbability$ , which can take one of the four thresholds values:  $\{0.25, 0.50, 0.75, 1\}$ . Figure 4.8 shows the PSDCH structure and periodicity and illustrates the role of the various IEs.

#### 4.3.1.2 Control and Data Transmission

Direct communication over the LTE air interface supports two types of allocation schemes for the resources dedicated to the transmission of control and data traffic. The first type, known as mode 1 in Rel. 12 and mode 3 in Rel. 14, is dedicated to scheduled transmissions. Here, the UEs are assisted by the eNB and use dedicated radio resources for data transmission. The second one, known as mode 2 in Rel. 12 and mode 4 in Rel. 14, is dedicated to autonomous transmissions where UEs randomly select radio resources from a resource pool preconfigured by the eNB. In Rel. 12, data transmission is scheduled within the PSCCH period, during which a set of subframes is determined for the PSCCH transmission and a different set of subframes are determined for the PSSCH. Rel. 12 also contains the SideLink Control Information (SCI), also known as the Scheduling Assignment (SA), which is used by the receiver UE to determine the occupation of the PSSCH radio resources.

In Rel. 14, however, modes 3 and 4 do not provide a PSCCH period for the transmission of both physical channels into different temporal periods. Instead, the PSCCH and PSSCH are separated in the frequency domain. The resource grid is divided into sub-channels, in which the first RBs of these sub-bands compose the PSCCH pool while the others form the PSSCH pool. Control messages and data transmissions repeat periodically with periods  $40ms$ ,  $80ms$ ,  $160ms$ , or  $320ms$  [112]. The number of RBs devoted to each transmission type is defined before off-network SL transmission begins.

### 4.3.1.3 Resource Structure

The discovery pool here is modeled as a matrix of  $N_t$  effective subframes (mapped to 1) of  $1ms$  each and  $N_f$  physical RBs. This results in an overall  $N_r = N_t \times N_f$  resources available to be used for discovery during one discovery period. Resource pool sizes are preconfigured. At the beginning of each period, a UE determines whether or not to transmit with an independent trial with success probability of  $p$ . All active UEs then choose one of the available  $N_r$  resources to randomly transmit the message once per discovery period or round. During one subframe, a UE is either listening to his neighbors' transmissions or sending its discovery message. Figure 4.9 illustrates an example of resource selection by a set of 10 users shown in the chosen box. Numbers show the identifier for each UE that selects the resource while the color of the box

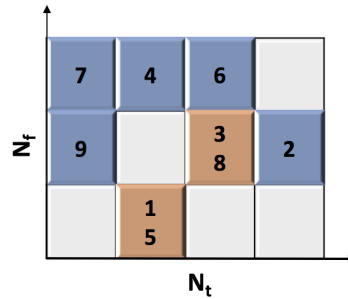


Figure 4.9: Example of discoveries in a resource pool with  $N_r = N_t \times N_f$  discrete resources organized into  $N_f = 3$  blocks and  $N_t = 4$  sub-frames.

indicates whether an RB is selected by one user or more for message transmissions. We assume that, in the L-2 collision model, if more than one discovery message occupy the same resource, all the co-located messages will be lost due to mutual interference, as is the case for UE-1 and UE-5.

In the L-1 collision model, however, an evaluation of the received colliding signals is required to verify the possibility of decoding one of the discovery messages. Hence, it might be possible to identify one of the two previously seen UEs if its signal strength is sufficiently high. Moreover, a half-duplex UE cannot transmit and receive at the same time, and thus misses any discovery messages that other UEs send in the subframe during which it is transmitting. For example, UE-7 and UE-9 are not able to discover each other during the first discovery period because they are broadcasting their discovery messages during the same frame.

### 4.3.2 Discovery Framework

We study the capability of a UE to discover the set of all UEs within its vicinity along multiple rounds. To this aim, we consider the set of all  $N_u$  UEs that are placed randomly following a uniform distribution in an area that represents a single collision domain. We focus on the discovery process for one randomly chosen UE, which we denote to be UE-0. We also assume that the area occupied by the  $N_u$  UEs is small enough that every UE in the set can receive transmissions from every other UE [33].

If a UE picks a resource that no other UE picks, its message will be received by all other UEs. From a MAC perspective, when two or more UEs pick the same resource, the mutual interference will prevent any collided message from being received by other UEs. In practice, channel effects will introduce a message loss probability for users with harsh channels. Consequently, some collided messages may be received by some UEs if the signal at the receiver is sufficiently strong. Depending on the BLER for a specific Signal to Interference Noise Ratio (SINR) value, UE-0 can decide to correctly decode the discovery messages.

The discovery process consists of individual discovery rounds, and during each of them all UEs contend to transmit using the available discovery pool. As stated in section 4.3.1.1, if a UE has a discovery message to send, it generates the discovery transmission probability  $p$ , which is then compared to the threshold indicated in the variable *txProbability* denoted by  $\theta$ . Afterwards, it decides whether or not the discovery message will be transmitted.

The time (in terms of number of discovery periods) to discover all other UEs is referred to as the discovery completion time  $N_{DCT}$ . We also define the variable  $N_D(t)$  as the number of UEs that have been discovered by UE-0 at the end of the  $t^{\text{th}}$  PSDCH period as having the number  $t$ . The range of possible values for  $N_D(t)$  is  $0 \leq N_D(t) \leq N_u - 1$ . The process of discovery can then be modeled as a discrete-time Markov chain with a single state variable  $N_D(t)$  that indicates the number of discoveries at the round number  $t$ .

The chain starts at the state  $N_D(0) = 0$  as UE-0 has not yet discovered any of the other  $N_u - 1$  UEs in its group. The ending state of the chain is  $N_D(t) = N_u - 1$ , which is reached at  $t = N_{DCT}$ . Figure 4.10 shows an example of a Markov chain describing the discovery process of the UE-0 for a resource pool of size  $N_r = 4$  and a set of  $N_u = 8$  users. During each round, UE-0 can discover  $nb$  neighbor UEs at a time, where  $0 \leq nb \leq \min(N_r, N_u)$ . In the example,

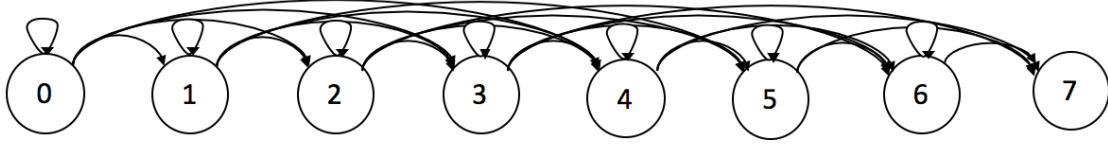


Figure 4.10: An example of Markov chain of the discovery process for  $N_u = 8$  and  $N_r = 4$ ; the states of the chain show the number of discovered UEs which starts at  $N_D(0) = 0$  and ends at  $N_D(N_{DCT}) = 7$ .

UE-0 can discover up to 4 UEs during one discovery round even though none of these 4 UEs, who selected the same sub-frame to transmit, can decode other users' discovery messages due to the half-duplex mode.

### 4.3.3 Distributed Discovery

Distributed discovery is well adapted to autonomous communication modes 2 and 4 [33]. During each discovery period, all UEs contend to transmit using the pre-configured shared resource pool via an Aloha-like protocol. According to the Aloha access protocol, collision information is immediately available upon transmission and is followed by a back-off process that controls subsequent channel access for nodes that have previously collided. Unlike what is seen in the wired network, wireless UEs are unable to detect collisions and so no mechanism exists to modify subsequent behavior based on collision detection. As a preemptive mechanism of collision avoidance, UEs contend to access the channel with the probability  $p < \theta$  to reduce the number of UEs attempting to transmit at one discovery period .

Figure 4.11 presents an example of potential discoveries based on a distributed strategy, in which both the discovered UEs (e.g. UE-7) and collided UEs (e.g. UE-2 and UE-8) continue advertising regardless of any previous discoveries. A discovery round is conducted as follows: Each UE generates a uniform random variable  $p$  that is first compared to the threshold  $\theta$ . If the randomly generated number is less than  $\theta$ , the UE is considered active in this period, meaning that it seeks to transmit its discovery message. Each active UE uniformly selects one of the  $N_r$  available resources, through which it can transmit its discovery message. UE-0, which is not ready to transmit, scans the  $N_r$  resources in the pool to decode the discovery messages. After each discovery period, the discoverer UE-0 logs all new UEs discovered in that period

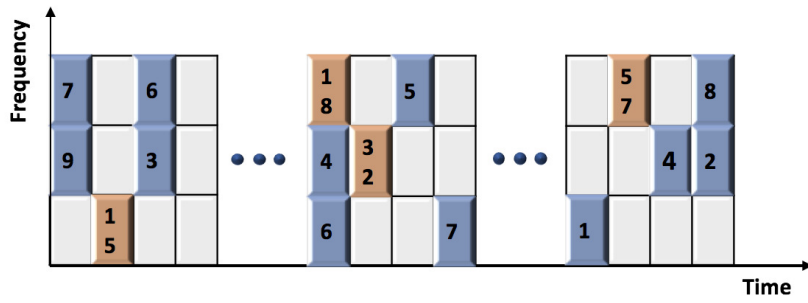


Figure 4.11: An example of realization of a distributed discovery scenario.

and updates its cumulative list of discoveries.

However, due to the memory-less character of the discovery process in distributed modes, none of the discovered UEs is notified and they will all continue sending their discovery messages indefinitely. This will keep the number of contending UEs relatively high at any period, leading to a high number of collisions.

#### 4.3.4 Network-Assisted Discovery

Network-Assisted (NA) discovery can be applied to modes 1 and 3 (i.e. for supervised communications) using a Polling-like access scheme. The basic feature of a polling network is evident when a central node, which serves as a controller, polls each of the nodes sharing the resource in a pre-specified cyclic order to provide access to the communication channel [33]. Applied to the cellular scenario, polling can be assigned to either the eNB or a relay node that possesses all discovery information within its coverage area. In this way, discovered UEs are notified and cease sending their discovery messages.

Indeed, after each round, a discoverer UE reports its discoveries to the eNB accumulating all the discoveries. The eNB then logs all new UEs discovered in that period and updates its cumulative list. When a UE is discovered by all his neighbors, the eNB notifies the concerned UE to stop sending its discovery messages during the following rounds. On the other hand, undiscovered UEs will continue advertising their discovery messages until receiving a notification of completed discovery. Consequently, the number of discovery messages will either remain constant or decrease during the phase of discovery. Figure 4.12 presents an example of potential discoveries based on an NA strategy, in which the discovered UEs (e.g. UE-7 and UE-9) cease advertising their presence. On the other hand, UEs that experience collisions (e.g.

UE-1 and UE-5) continue announcing their discovery messages in the following rounds. This greatly reduces the collision probability in the next round and consequently improves discovery reliability.

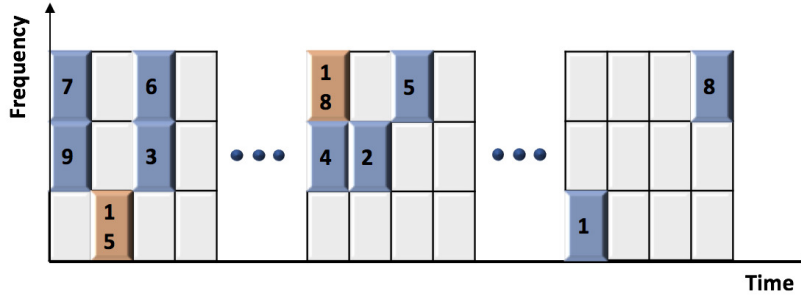


Figure 4.12: An example of realization of a network-assisted discovery scenario.

A discovery round is conducted in a way slightly similar to the distributed strategy. At the beginning, the same processing is performed to transmit the discovery messages. Then, if the resource selected by an active UE is not selected by another UE, the discovery of the sender UE is successful and it will be logged in the controller. At the end of each round, the controller accumulates all new discoveries and announces those that have been completed to the corresponding sender UEs. Discovered UEs continue listening to other SL transmissions while collided UEs are implicitly polled to proceed for discovery message transmission until discovery completion.

It is worth noting that in both distributed and NA discovery strategies, if a collision takes place during a discovery round, one discovery message among colliding ones can potentially be decoded. This can lead to a successful discovery for a receiving UE with sufficiently low BLER in the physical collision model.

### 4.3.5 Performance Evaluation

In this section, we present the performance results for neighbor discovery where several scenarios are run to capture all the essential angles of SL transmission [33]. The evaluation is performed in two Rayleigh channel models and Monte Carlo simulations are run for  $10^4$  trials. The two multi-path fading Rayleigh channels are used to cover low-mobility and high-mobility conditions of both ProSe and V2X application use cases. For low-mobility, we use a 4-tap channel with delays  $\{0,70,110,410\}$  ns, path gains  $\{0,-2,-8,-20\}$  dB and a Doppler shift equal

to 5Hz for all taps. The high-mobility channel is also modeled with a 4-tap channel having delays of  $\{0,200,433,700\}$  ns, path gains  $\{0,-2,-5,-7\}$  dB and different Doppler shifts set as  $\{0,689,-492,886\}$  Hz for Highway NLOS channel [119]. In both models, the first path is static and serves as a normalization for the other taps. The other taps are uniformly defined as Rayleigh taps.

We consider a 20 MHz LTE system with SC-FDMA symbol of size  $N = 2048$  sub-carriers appended to a CP of length  $N_{cp} = 140$  sub-carriers. The DMRS bandwidth is fixed to 50 RBs. The initial ZC sequence length is  $N_{zc} = 571$  sub-carriers, and its extended version has the length  $M = 578$  sub-carriers. We use *discPeriod* equal to 0.32s as specified in the standard for resource pool sizes with a number of sub-frames  $N_t < 320$ . The transmission probability threshold  $\theta$  is randomly chosen for each Monte-Carlo trial from the preset values  $\{0.25,0.5,0.75,1\}$ . Unless otherwise mentioned, the number of UEs is set to  $N_u = 20$  users that are placed randomly (i.e. distributed uniformly) on a disk of radius 500m. All UEs transmits at a power  $P_t = 0$ dBm.

#### 4.3.5.1 Discovery Time Performance

This section provides an evaluation of the multiple-round discovery presented through the mean of total discovery completion time  $E(N_{DCT})$  as a function of the number of UEs within the neighborhood of UE-0. The L-1 collision is modeled using the BLER vs SINR curves obtained in [118], assuming that a message is decodable so long as its BLER is less than  $10^{-2}$ .

Figures 4.13 and 4.14 depict  $E(N_{DCT})$  as a function of the total number of UEs  $N_u$ , in the low and high-mobility Rayleigh channel models, respectively. In the two channels and collision models, distributed strategies require more time to complete the discovery of all UEs due to the continuous discovery message transmissions along all rounds. This occurrence is more prominent, however, in the L-2 collision model. This model spends 34 rounds to discover 31 UEs, whereas only 10 rounds are needed in the L-1 collision model to discover the same number of UEs. The L-1 collision is modeled using the BLER vs SINR curves obtained in [118], assuming that a message is decodable so long as its BLER is less than  $10^{-2}$ .

It is also key to note that as  $N_u$  increases  $E(N_{DCT})$  increases, but for large values of  $N_u$ , the L-1 collision model illustrates that the discovery process takes significantly less time to complete. For example, figure 4.13 shows that for  $N_u = 36$  UEs and assuming a 0.32s

discovery period, the process takes about 5 rounds or 1.6s and 6 rounds or 1.92s for the NA and distributed strategies, respectively. For the physical L-1 collision model, the two strategies provide very close performance with no more than 2 additional rounds required to accomplish the discovery of all UEs for the  $N_u$  values.

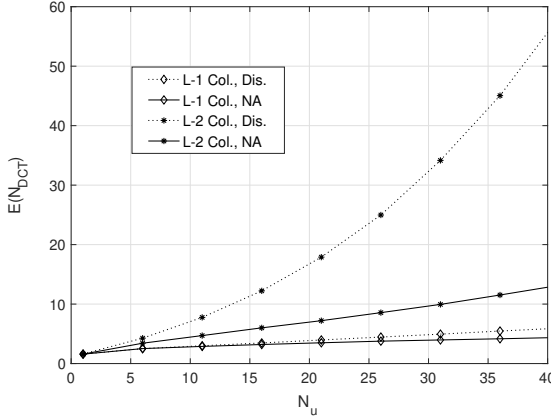


Figure 4.13:  $E(N_{DCT})$  as a function of  $N_u$  for  $N_r = 12$  resources in low-mobility conditions.

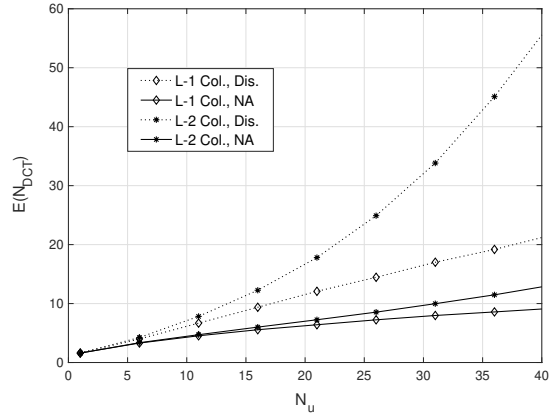


Figure 4.14:  $E(N_{DCT})$  as a function of  $N_u$  for  $N_r = 12$  resources in high-mobility conditions.

Compared with the results in figure 4.13, figure 4.14 shows that the time required to complete the discovery of all UEs remains invariant for the L-2 collision model because it is independent of any physical aspects. However, L-1 collision model showcases a prominent behavior change with increasing time demand as the number of users  $N_u$  increases. Indeed, distributed discovery requires 19 rounds to discover 31 UEs in high-mobility conditions, which corresponds to 6.09s while only 1.92s are spent in the low-mobility channel. The degradation is mainly due to the harsh multi-path effect and the high Doppler shift that weaken the signal and result in a higher BLER. Consequently, the discoverer UEs are incapable of decoding any of the discovery messages transmitted through the same resource.

#### 4.3.5.2 Collision Performance

In this section, we provide an evaluation of the multiple-round discovery in terms of collision rate for both L-1 and L-2 collision models as a function of the number of UEs within the neighborhood of UE-0 in figure 4.15, and as a function of the transmission probability  $\theta$  in figure 4.16.

Figure 4.15 presents the collision rate of both distributed and NA strategies for L-1 and L-2 collision models. Consistent with the previous results, as the number of UEs increases, collision increases mainly in distributed strategies because all UEs continue transmitting their discovery messages “infinitely”. The rate, in this case, reaches 83% when  $N_u = 20$  UEs for L-2 model, 35% for L-1 model in high-mobility channel, and 25% for L-1 model in low-mobility channel.

The same sequencing is perceived in NA strategies, but lower collision rates are exhibited. The surge in collision for high values of  $N_u$  justifies the extended period of time required to complete the discovery process for all UEs shown in figures 4.13 and 4.14. In the L-1 collision model, it is natural that the low-mobility channel provides better performance in terms of collision rate as the possibility to decode discovery messages sent through the same resource is higher than the case of high-mobility channel.

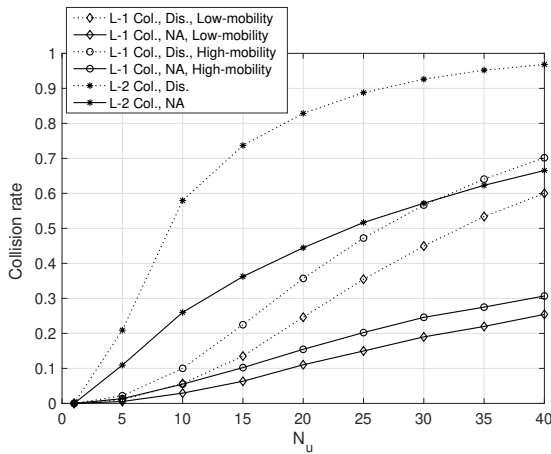


Figure 4.15: Collision rate as a function of  $N_u$  for  $N_r = 12$  resources.

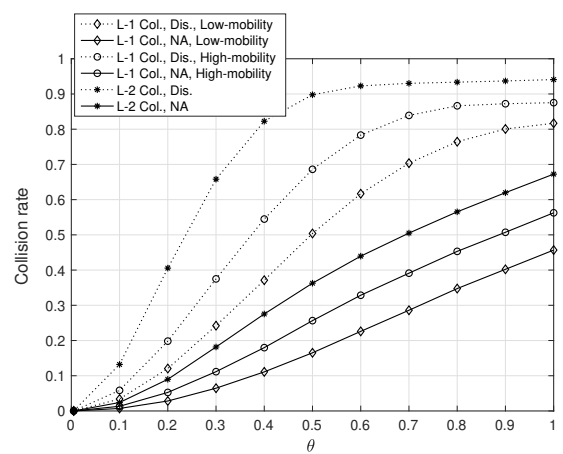


Figure 4.16: Collision rate as a function of  $\theta$  for  $N_r = 12$  resources and  $N_u = 20$  users.

Figure 4.16 presents the collision rate as a function of the transmission probability  $\theta$  for  $N_u = 20$  users. In all the envisaged scenarios, we note that the collision rate evolves proportionally to the value of  $\theta$ . Indeed, the higher the value of  $\theta$ , the more collisions occur, and the number of UEs with transmission probability lower than  $\theta$  increases.

Furthermore, as in figure 4.15, distributed strategies experience more collisions due to the continuous transmissions of discovery messages. For  $\theta$  values close to 1, the collision rate stagnates at rates greater than 80% because almost all the users are transmitting their discovery messages. In the L-1 collision model, as expected, the collision rate is lower for UEs with reduced speed since the BLER is better than in the high-speed scenario.

## 4.4 Conclusion

In this chapter, neighbor discovery for ProSe and V2X communications underlying cellular networks was investigated by utilizing random access-like procedures. First, we studied a beacon-based partial contention-free single discovery, in which a contention-based random access procedure-like is initially achieved to connect the receiver UE to the eNB. During this stage, the transmitter starts the selection of a beacon and forwards it to the receiver. Upon success of the first connection (no colliding beacons), the eNB carries out a contention-free random access procedure-like to allocate radio resource blocks to the receiver UE. Finally, the eNB specifies the resource blocks dedicated for the transmitter UE using the initial randomly selected beacon to allow data transmission between nearby user through uplink resource blocks. Performance evaluation of the proposed discovery scheme, assessed for different link distances, showed its ability to adaptively allocate resource blocks for the D2D neighbor discovery to prevent underutilization of radio resources. We also evaluated the collision probability considering several scenarios, for which we studied the impacts of the distance between transmitter and receiver devices, the density of the connected users, and the time dedicated for the discovery process. Overall, the collision probability showed low values thanks to the partial contention-free access that limited collisions for only transmitter UEs.

Then, multiple-round discovery was considered to assess the performance of distributed and network-assisted discovery strategies. In the distributed strategy, users continue to transmit their discovery messages, which results in a high collision rate that delays the completion of the discovery process of all users in the vicinity. In the network-assisted strategy, however, discovered users are notified to cease sending their discovery messages, which leads to enhanced performance. To present a realistic assessment of collision, we opted for a physical model in addition to the typical legacy MAC model. Throughout the performance evaluation, both low and high-mobility channel models were considered to cover both ProSe and vehicular use case applications. Simulation results showed a noticeable improvement in the physical collision model in all the considered scenarios.

## Chapter 5

# UAV Positioning and UE Localization

### 5.1 Introduction

UAVs admit several key potential applications in wireless systems and can be used as aerial base stations to enhance coverage, capacity, and reliability. The performance of the network in this case strongly depends on the UAV position, as it has a direct impact on the communication channel. Also, due to the increase of location awareness applications for mobile users and the use of UE as relays, accurate localization has become crucial. In this chapter, we focus on two techniques that help to extend the coverage in assisted networks. The first part of this chapter focuses on the positioning of UAVs that could serve as flying eBN or relay UE to extend the network coverage for terrestrial users (LTE ProSe mode 2). In particular, we study the optimization of a Low Altitude Platform (LAP) relay node positioning to maximize the detection range and the averaged connectivity of terrestrial UEs. Unlike the previously cited works, we investigate a *physics-based* Rician channel model, whose  $K$ -factor is dependent on the ground roughness, and we assess the impact of this latter on the network performance [39].

The second part deal with the localization of UEs communicating through millimeter-waves (mm-wave) in a massive MIMO context. We propose a multi-stage localization method that reduces the search space and then deduces the UE location. To achieve this, a processing center collects power measurements from all BSs and compares them to identify the hosting

BS and estimate the range. Once the hosting cell is identified, a downlink signal is used to identify the sector to which the user belongs. In a second step, multi-stage beamforming is carried out in the estimated sector to determine the AoA and deduce the coordinates of the UE. An extensive evaluation of the impact of several parameters on the localization accuracy is presented to highlight the asset of using MIMO and mm-waves techniques [36], [40].

## 5.2 Related Works

In this section, we review research works in both positioning aerial devices to ensure high-quality connection to ground users and performance, and localization of ground devices within a terrestrial network.

The work in [15] suggested a classification of UAVs based on their altitudes, into high altitude platforms (HAPs) and low altitude platform (LAPs). HAPs have altitudes above 17km and are typically quasi-stationary, while LAPs, on the other hand, can fly at altitudes of tens of meters up to a few kilometers, can quickly move, and are more flexible [120,121]. In an aerial context, flexibility vis-a-vis aerial positioning facilitates obstacle avoidance and the prospect of serving ground users with requisite performance in terms of reliability, throughput, and operation range [122]. Some recent research has focused on UAV positioning to optimize network performance with different objectives, such as a) maximizing the coverage area, b) aggregate downlink rates or c) ensuring connectivity of a set of drones with minimum cost. A variety of air-to-ground (A-2-G) channel models have been used in these formulations, some only use deterministic path loss of the channel without any consideration of random effects [124]- [125], while others have considered both long term and small scale variations [126]- [128] in the received signal. In [124], the authors optimized the position of a UAV relay node to improve the network connectivity through a free space Line Of Site (LOS) channel. The work in [125] studied the energy-efficient 3D placement of a UAV-BS that aims to maximize the number of covered ground nodes while keeping a minimum required transmit power based on a pure path loss model. The work in [126] presented an analytical approach to optimize the altitude of a LAP platform based on the finding of [123] to provide maximum radio coverage on the ground, yet it does not consider the small-scale fluctuations caused by the rapid changes in the propagation environment. Later, a Rician fading model with  $K$  factor depending on the elevation angle was introduced by [127, 128] who studied the outage probability and showed

that there exists an optimum height for the UAV node which maximizes the coverage area.

To determine the exact position of ground users, the Global Navigation Satellite System (GNSS) has been the most dominant technology to enable outdoor localization [129, 130]. The multitude of localization demands causes GNSS saturation due to its limited capacity and coverage. To tackle the problems with GNSS, many researchers have developed a series of localization schemes that rely on the estimated distance and can be obtained through measuring methods like Angle-of-Arrival (AoA), Time-of-Arrival (ToA), Time-Difference-of-Arrival (TDoA), or propagation model generated from RSSI value [131]. Several works have dealt with the problems above-mentioned.

Direct Localization for Massive MIMO (DiSouL) method [132] has solved the problem of localization under NLoS conditions by exploiting the high angular resolution of massive arrays. First, at each BS, the ToAs are roughly estimated via an adapted filter with an offset version of the reference signal. Second, the position is searched on a grid by solving a convex optimization problem (adjustment between observations from the positions and outputs of the adapted filter) relying on tools from compressive sensing. This technique has achieved sub-meter localization with high probability in dense multiple-path environments with narrow-band signals and has proven robustness against synchronization errors but this significant gain in accuracy is accompanied by a higher computational complexity compared to existing techniques.

Further, based on the Beam-RSRP and the Extended Kalman Filter (EKF), the work in [133] has exploited the 3D-beamforming features of multiantenna equipment employed in 5G networks. The position is estimated using a two-stage EKF that is based on reference signal received power (RSRP) measurements. During the first EKF phase, the Directions-of-Departure (DoDs) are estimated at each BS. These estimates are then merged into a central entity and using a second angle-based EKF phase, the 3D UE position estimate is obtained. The performance evaluation of this work in a 5G deployment shows that a sub-metric 3D positioning accuracy is achievable in future 5G millimeter wave (mmW) networks without taking into consideration the uncertainties in the orientation of the BS in the beamforming step.

## 5.3 UAV Positioning

Recent advances in UAV technology has enabled their increasing use as airborne elements within a wireless network that supports connectivity to ground users. In this section, we revisit the positioning of a low altitude UAV functioning as a relay node to provide connectivity and communication services to ground users who are out of coverage [39]. A *new* altitude dependant Rician distribution for the air-to-ground channel - derived from propagation physics - is used and its impact on the optimum altitude for network coverage is explored via numerical results.

### 5.3.1 System Model

In this work, we focus on low altitude UAVs operating over a largely open environment with a rough (ground) surface, as illustrated in Fig. 5.1, where the relay R-UAV is located at height  $h_1$  and an elevation angle  $\phi$  with respect to the ground nodes (G-UEs) located at height  $h_2$  and distance  $r$  from the projection of the R-UAV onto the ground plane  $O$ .

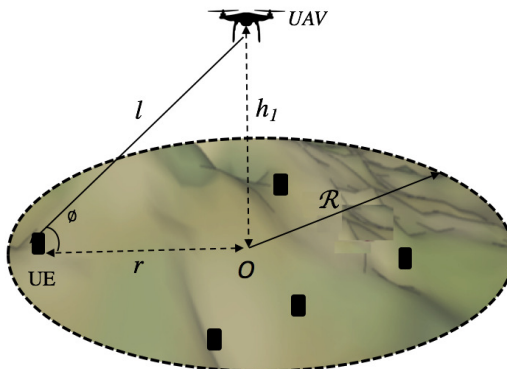


Figure 5.1: Example of a typical A-2-G communication system comprising a UAV and randomly distributed G-UEs over open areas with a rough surface.

Our primary objective in this work is to use physics-inspired Rician model for the received signal and compare its impact on the R-UAV positioning problem as compared to previous studies. *We demonstrate that not only does such physics-based modeling provide significantly different results, it also allows for more insightful interpretations as a function of the operational geometry.*

### 5.3.1.1 Channel Model

The net received signal at a ground node consists of a) direct LOS and b) diffuse or ground-scattered NLOS components. Consider that the R-UAV transmits at a power  $P_t$ , then the received mean signal power at the G-UE receiver corresponding to the LOS component is calculated according to the Friis propagation loss formula. For noise power  $\sigma_n^2$  in the signal band, the mean received SNR can then be written as

$$SNR = \frac{P_t \left(\frac{\lambda}{4\pi l}\right)^2}{\sigma_n^2} \Omega, \quad (5.1)$$

where  $\lambda$  is the signal wavelength corresponding to the center frequency of the band,  $l$  is the slant distance between the R-UAV and the G-UE given by  $l = \sqrt{r^2 + (h_1 - h_2)^2}$ , and  $\Omega \in [0, \infty]$  is the channel powerloss/gain factor.

We use the Rician distribution to model the (random) power loss/gain for a scenario that represents a combination of LOS path and diffuse multi-path due to nearby rough surface scattering [185]. The distribution of  $\Omega$  follows a non-central chi-square probability density function given by [134], for  $\omega > 0$

$$f_{\Omega}(\omega) = \frac{(K+1)e^{-K}}{\bar{\Omega}} e^{-\frac{(K+1)\omega}{\bar{\Omega}}} I_0\left(2\sqrt{\frac{K(K+1)\omega}{\bar{\Omega}}}\right) \quad (5.2)$$

where  $I_0(\cdot)$  is the zeroth-order modified Bessel function of the first kind,  $K = \frac{P_{LOS}}{P_{NLOS}}$  is the ratio of the powers in the LOS to the NLOS components and mean  $\bar{\Omega} = 1$  for normalization.

### 5.3.1.2 Rician Factor Model

For a UAV at a given height, the  $K$  value in the Rician model changes depending on the horizontal displacement of the UAV relative to the ground node (or equivalently, the elevation angle). For a reference  $P_{LOS} = 1$  (unity power LOS component), we can express using [135]

$$K = \frac{1}{\langle |\rho^2| \rangle}, \quad (5.3)$$

where  $\langle |\rho^2| \rangle$  is the mean square power from the scattered components, expressed as

$$\langle |\rho^2| \rangle = \int_{h_2 \cot 2\beta_0}^{h_1 \cot 2\beta_0} \frac{l^2 \cot^2 \beta_0}{\left( \pi (h_2^2 + x^2) (h_1^2 + (r-x)^2) \cos^4 \beta \right)} \times \exp\left( -\frac{\tan^2 \beta}{\tan^2 \beta_0} \right) dx. \quad (5.4)$$

As shown in Fig. 5.2,  $\beta$  presents the angle made by the bisector of the incident and scattered rays with the z-axis, and  $\beta_0$  is the area contributing to the diffused component of the reflected ray, given by

$$\tan(\beta_0) = \frac{2\sigma}{T}, \quad (5.5)$$

where  $\sigma$  is the standard deviation of normally distributed height variations and  $T$  is the horizontal auto-correlation distance.

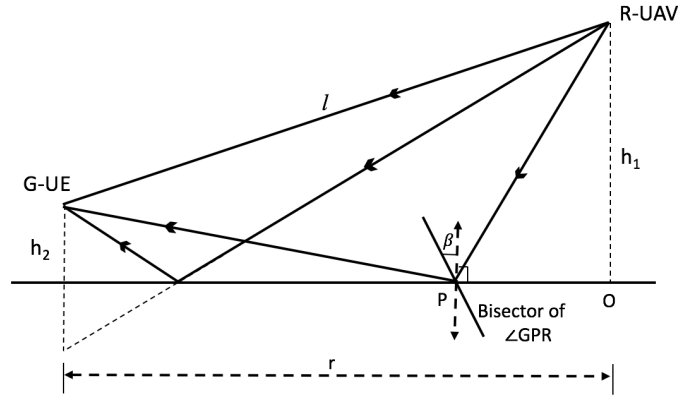


Figure 5.2:  $\beta$  shown in the link geometry context.

Fig. 5.3 shows the variation of  $K$  as a function of the elevation angle  $\phi$  which depends on the horizontal distance as  $\phi = \tan^{-1}\left(\frac{\Delta h}{r}\right)$ , where  $\Delta h = h_1 - h_2$ . We note in Fig. 5.3(a) that for a fixed UAV height,  $K$  initially decreases for small angles and then increases monotonically with the elevation angle. At low elevation angles,  $K$  is larger due to the strong specular component resulting from the ground behaving closer to an optical reflecting plane. This phenomenon is more evident in Fig. 5.3(b) for lower  $\beta_0$  values, where the area contributing to the diffused component of the reflected ray is smaller [185]. Also note that for a fixed elevation angle,  $K$  is higher for smoother surfaces (low  $\beta_0$  value) and more distant G-UE location, and higher for rougher surfaces and closer G-UE.

In the following, we study the problem of finding the best altitude of the R-UAV for opti-

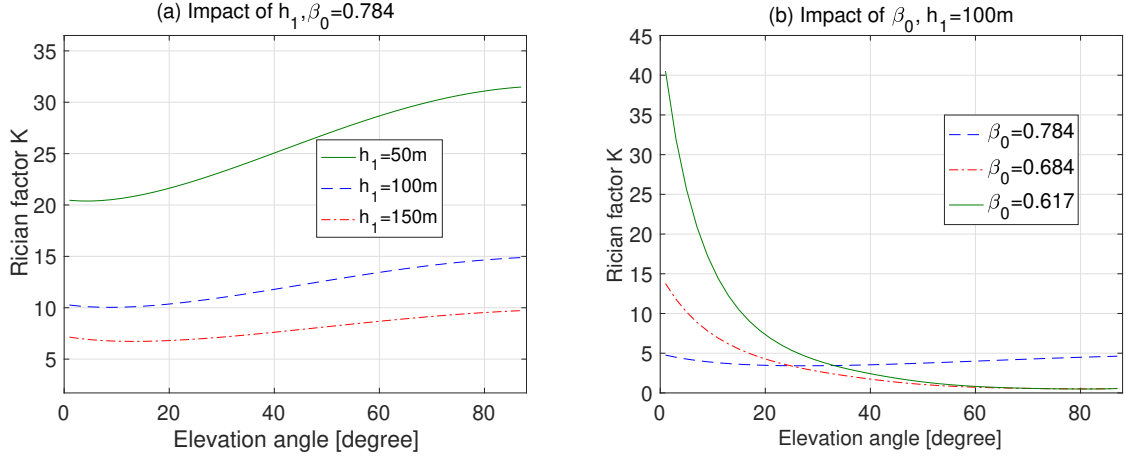


Figure 5.3: Variation of  $K$  with the elevation angle for  $h_2 = 1m$ : (a) different altitude values and a fixed  $\beta_0 = 0.784$ , (b) different  $\beta_0$  values and fixed altitude  $h_1 = 100m$ .

mizing the link reliability and explore its impact on the R-UAV coverage area. As a function of height, an A-2-G channel at greater height benefits from a lower path loss exponent (i.e. stronger LOS component). On the other hand, the link distance increases which increases the LOS path loss [39]. These two opposing features can be judiciously balanced by optimizing the UAV height to optimize the ground user detection performance (i.e. A-2-G link reliability) [185].

### 5.3.2 Height-dependent Coverage

We consider the worst-case which corresponds to a G-UE located at the edge of the coverage area at a distance  $r = R$ . We define the (minimum acceptable) probability of successful detection (PD) as one corresponding to SNR level greater than the minimum SNR required for the G-UE to detect the R-UAV signal. Denoting this SNR threshold by  $\xi$ , we can write PD as follows

$$PD = \bar{F}_\xi(SNR) = \Pr\left(\frac{P_t \left(\frac{\lambda}{4\pi l}\right)^2}{\sigma_n^2} \Omega > \xi\right), \quad (5.6)$$

where  $\bar{F}$  is the complementary cumulative density function. Substituting (5.2) in (5.6), the computation of PD leads to

$$PD = \int_{\sqrt{y}}^{\infty} x \exp\left(-\frac{x^2 + 2K}{2}\right) I_0(\sqrt{2K}x) dx, \quad (5.7)$$

where  $y = 2\xi[1 + K] \frac{l^2}{P_t} \left(\frac{4\pi\sigma_n}{\lambda}\right)^2$ . The probability of detection can then be rewritten as [134]

$$PD = Q\left(\sqrt{2K}, \sqrt{2\xi[1 + K]l^2B/P_t}\right), \quad (5.8)$$

where  $Q(.,.)$  is the first order Marcum Q-function and  $B = \left(\frac{4\pi\sigma_n}{\lambda}\right)^2$  is introduced to simplify the notation. For the considered Rician-K model, we study the impact of the R-UAV height on the maximum coverage area delimited by the SNR threshold  $\xi$  which is defined by a target probability of detection  $PD_{\text{target}}$  above which the link is deemed to be reliable. To this aim, we evaluate the radius of the coverage area  $R_{h_1}$  for a given R-UAV height  $h_1$ , which consists in solving the implicit equation

$$PD(h_1, R_{h_1}) = PD_{\text{target}}, \quad (5.9)$$

The set of all possible pairs  $(h_1, R_{h_1})$  presents a configuration space of the studied network among which there exist potential solutions of (5.9) that satisfy (5.6) and hence optimize the R-UAV position for maximum coverage with  $SNR > \xi$ . To determine the optimal configuration, we used an iterative computation of the inverse Marcum Q-function in (5.9).

### 5.3.3 Height-dependent Spectral Efficiency

We now consider the optimization of a different metric - the average spectral efficiency (ASE) at which information can be reliably transmitted to the UEs in the coverage area. From the Shannon capacity for AWGN, the spectral efficiency (SE)  $C$  is given by

$$C = \log_2(1 + SNR). \quad (5.10)$$

where the SNR is the signal-to-noise ratio at the ground UE receiver input. The SE is implicitly dependent on the height of the R-UAV, the distance of the G-UE to the center, and the physical propagation environment through the SNR defined in (5.1). Hence, the PDF  $g_C(c)$  for the SE expressed in equation (5.10) is obtained from the PDF of the SNR in (5.1) using the transformation of random variables as

$$g_C(c) = 2^c \ln(2) l^\alpha \frac{B}{P_t} f_C\left((2^c - 1) l^\alpha \frac{B}{P_t}\right), \quad c > 0, \quad (5.11)$$

where  $\alpha$  stands for the path loss exponent, which is set to 2 in the case of Friis propagation environment.

The A-2-G link between the R-UAV and a specific G-UE is considered reliable if the achievable ASE is higher than a preset threshold  $C_0$  defined by the desired QoS. This can be evaluated using the Probability of Connectivity  $PC$  which we define as the probability that the SE (5.10) is greater than a minimum acceptable  $C_0$ , expressed as

$$PC = \Pr\left(\log_2(1 + SNR) > C_0\right) = \int_{C_0}^{\infty} g_C(c) dc. \quad (5.12)$$

By replacing (5.11) in (5.12) and applying a variable substitution, the expression above turns into

$$PC = \int_{\sqrt{y}}^{\infty} x \exp\left(-\frac{x^2 + 2K}{2}\right) I_0\left(\sqrt{2K}x\right) dx, \quad (5.13)$$

where  $y = 2[1 + K][2^{C_0} - 1]l^\alpha B/P_t$ . Similar to the probability of detection, the probability of connectivity can be rewritten using the first-order Marcum function as

$$PC = Q\left(\sqrt{2K}, \sqrt{2[1 + K][2^{C_0} - 1]l^\alpha B/P_t}\right). \quad (5.14)$$

Our purpose here is to find the best altitude  $h_1$  for the R-UAV to maximize the connectivity area for a target  $PC_{\text{target}}$  that ensures the minimum ASE  $C_0$ . We consider the optimization of the ASE for the set of all served G-UEs within the boundary of the coverage area. The served G-UEs are first placed at different distances from the center  $O$  following a uniform distribution. Then, the ASE which is denoted by  $\bar{C}$  is obtained averaging  $C$  in (5.10) over the coverage area of ray  $R_{h_1}$ . The optimal altitude  $h_1$  for the averaged rate can then be found by numerically solving the following equation

$$PC(h_1, R_{h_1}) = PC_{\text{target}}. \quad (5.15)$$

The set of all possible pairs  $(h_1, R_{h_1})$  here stands for the potential solutions satisfying (5.12) for an ASE  $\bar{C} > C_0$ .

### 5.3.4 Performance Evaluation

Numerical evaluations were conducted for the results presented in the previous section for R-UAV height  $h_1$  varying from 0 to 500m and compared to the benchmark study in [127] that used a  $K$  factor model that increases exponentially with height. We performed the optimization for two different ground roughness values  $\beta_0 \in \{0.784, 0.617\}$ . It is assumed that  $B/P_t = 70\text{dB}$  and the QoS is defined by a  $PD_{\text{target}} = 0.999$  and  $PC_{\text{target}} = 0.999$ . The average Spectral Efficiency (SE)  $\bar{C}$  is obtained over 100 uniformly distributed G-UEs in the relevant region [39].

Fig. 5.4 shows the set of all pairs  $(h_1, R_{h_1})$  that satisfy the condition in (5.6) for our model (K-Model 1) and the considered benchmark (K-Model 2) for three different SNR threshold values. It is shown that as the R-UAV altitude  $h_1$  increases, the coverage radius  $R_{h_1}$  increases up to a maximum value and thereafter decreases. This implies that for lower altitudes the reduction of the multi-path effect provided by the increase of height is beneficial. However, for high altitudes, the path loss dominates and further height increase is detrimental for coverage. Between these two regimes, the depicted curves exhibit a unique sharp optimal altitude. It is worth noting that, at the maximum coverage radius, the elevation angle  $\phi$  is invariant for all threshold values showing that  $\phi$  is independent of the SNR threshold. Although different  $K$  values are used in Fig. 5.4(a), our result confirms the benchmark [127]’s conclusion that for all examined SNR threshold  $\xi$ , the optimal elevation angle is the same. Compared to the results in [127], our physics-based model, however, predicts a *higher maximum coverage radius* of 1620 m while the benchmark suggests 1350 m. On the other hand, the benchmark ensures connectivity for higher altitude that reaches 2500 m, for a very limited coverage radius.

The impact of the surface roughness on the optimal performance in our physics-based model is depicted in Fig. 5.4(b), where the optimal solution of the R-UAV altitude for  $\beta_0 = 0.617$  is shown. We note that the lower value of  $\beta_0$  results in a larger coverage radius in all cases (compared to Fig. 5.4(a)) albeit at lower altitudes. This can be explained by the relation between  $\beta_0$  and the Rician  $K$ -factor depicted in Fig. 5.2, which shows that a lower  $\beta_0$  value results in a higher  $K$  value for small elevation angles (i.e. larger ray  $r$ ). Indeed, it can be shown that for very low values of  $K$ , the Rician distribution reduces to a Rayleigh fading one, which represents a predominance of the multipath component. However, for higher values, the Rician model tends to an additive white Gaussian noise channel corresponding to a strong LoS between the transmitter and receiver.

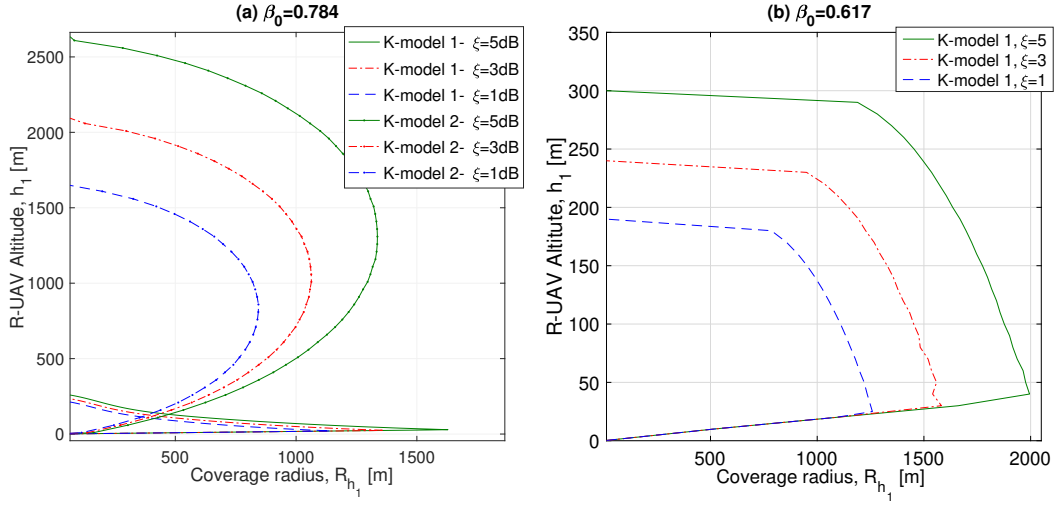


Figure 5.4: The set of configuration space for pairs  $(h_1, R_{h_1})$  showing the optimum configuration for  $PD_{\text{target}} = 0.999$ : (a)  $\beta_0 = 0.784$  and (b)  $\beta_0 = 0.617$ .

The maximum coverage radius of the two compared  $K$  factor models is depicted in Table 5.1 for different values of the SNR threshold  $\xi$ . It is shown that the coverage radius diminishes with the SNR threshold  $\xi$ , which is an expected behavior. Indeed, as presented in Fig. 5.4, increasing  $\xi$  decreases the detection probability which results in a smaller coverage area for the same detection target  $PD_{\text{target}}$  constraint. The results also depict that, for the same QoS, our Rician-K model provides a wider coverage radius compared with the model studied in [127].

Table 5.1: Maximum coverage radius  $R_{h_1}$ ,  $PD_{\text{target}} = 0.999$ ,  $\beta_0 = 0.784$ .

Threshold $\xi$ (dB)	0	4	8	12	16	20
$R_{h_1}$ , Model 1(m)	1883	1354	917	630	394	245
$R_{h_1}$ , Model 2(m)	1705	1078	680	429	270	170

Fig. 5.5 depicts the set of all configuration pairs  $(h_1, R_{h_1})$  that satisfy the constraint (5.12) in our physics-based K-Model 1. Similarly to the previous results, we note that there again exist two regimes and a unique (sharp) optimum at altitude  $h_1$  that maximizes the radius of the connectivity disc for an average SE  $\bar{C} > C_0$  of ground UEs within the area of radius  $R_{h_1}$  in the two different scenarios of  $\beta_0$  values. Observing the optimum pairs  $(h_1, R_{h_1})$  for each threshold  $C_0$ , we note that the optimization of the average SE leads to an invariant altitude value  $h_1$  independent of the threshold  $C_0$ . Interestingly, the maximum radius of the connectivity area is larger than the maximum radius of the coverage area presented in Fig. 5.4. Indeed, based on the average SE criteria, the connectivity radius can reach 2400 m while it is about 1620

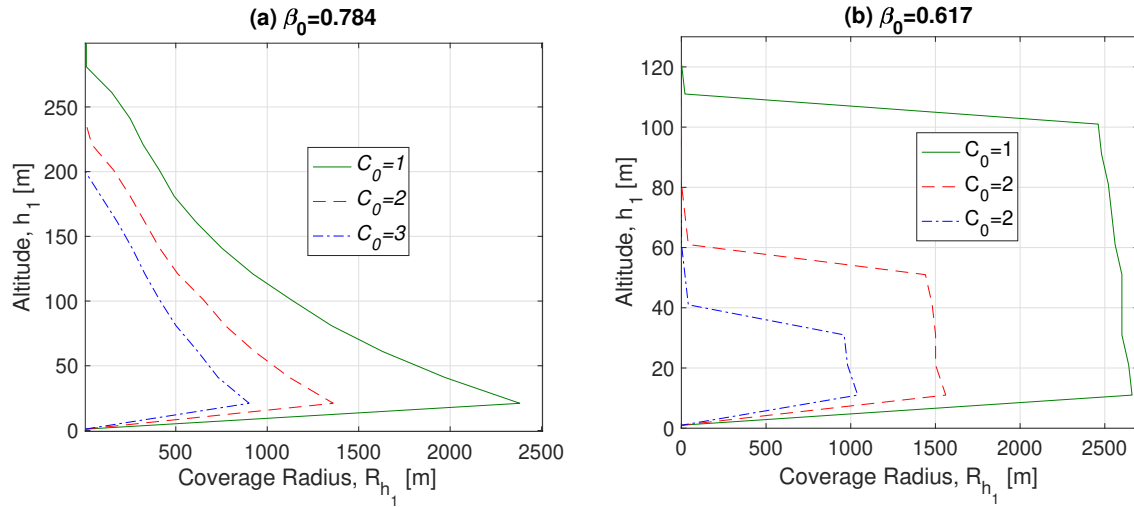


Figure 5.5: The set of configuration space for pairs  $(h_1, R_{h_1})$  showing the optimum configuration for  $PC_{\text{target}} = 0.999$  over K-Model 1: (a)  $\beta_0 = 0.784$  and (b)  $\beta_0 = 0.617$ .

$m$  when optimized based on the received SNR for an edge G-UE. We also observe that the optimal R-UAV height for the average SE connectivity metric depicted in Fig. 5.5(b) shows larger coverage that reaches 2650 m for low  $\beta_0$ , while it is about 2400 m for a high value of  $\beta_0$  which is concordant to the impact of  $\beta_0$  on the maximum coverage radius presented in Fig. 5.4.

## 5.4 UE Localization

The position of a UE in a wireless network can be estimated directly. However, it has been shown that two-step positioning approaches that first determines a set of parameters such as the ToA, the AoA, the TDoA, or the Received Signal Strength Indicator (RSSI), which are then used to estimate the accurate position of a UE [131], [140]. In this section, we propose a multi-stage processing that allows providing accurate coordinates estimation while keeping the complexity low through reducing the search space.

### 5.4.1 System Model

Our system includes one stationary UE located at the coordinate  $c = (x, y)$ , three neighboring massive MIMO BSs with  $M$  antennas each positioned at  $c_{BS} = (x_{BS}, y_{BS})$  as presented in figure

5.6, and one processing center. We suppose that these elements are perfectly synchronized.

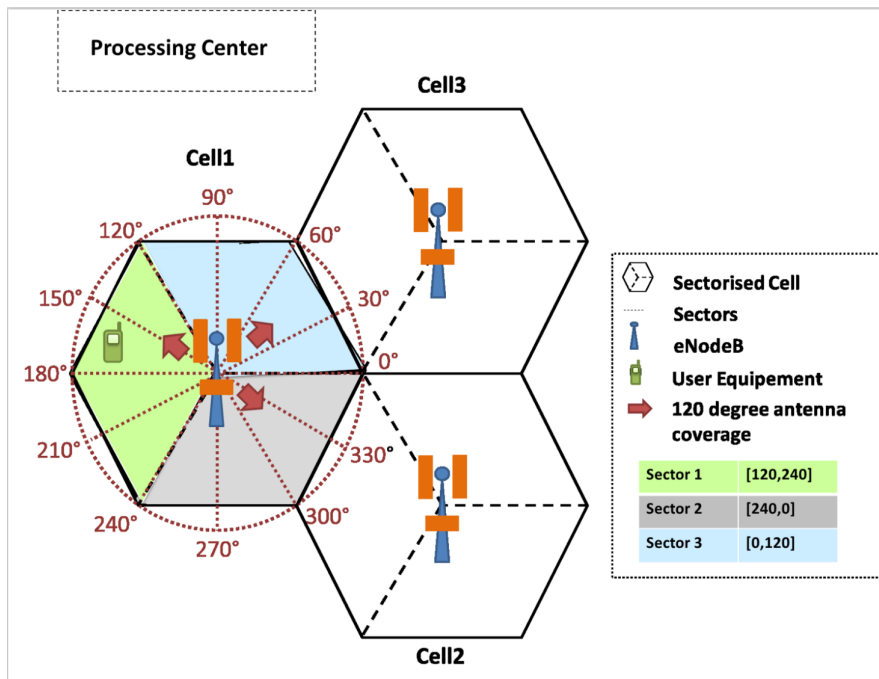


Figure 5.6: Typical structure of LTE 3-sector cells.

The synchronization phase will be treated in future work. The considered BSs are three sector antenna stations, each serving a hexagonal cell with three sectors each covering a specific interval as detailed in table 5.2.

Table 5.2: List of SID interval limits

Sector ID (SID)	Interval
0	[120, 240]
1	[240, 0]
2	[0, 120]

We denote by  $\mathbf{a}(\theta)$  the array response vector at the BS for a ray impinging from angle  $\theta$ , which is defined in the case of a uniform linear antenna (ULA) with half-wavelength spacing

as

$$\mathbf{a}(\theta) = \begin{pmatrix} 1 \\ e^{j\pi \sin \theta} \\ \cdot \\ \cdot \\ \cdot \\ e^{j\pi(M-2) \sin \theta} \\ e^{j\pi(M-1) \sin \theta} \end{pmatrix}. \quad (5.16)$$

The UE transmits a reference signal  $s(t)$  which propagates through the multipath environment, resulting in a received amplitude at the  $m^{\text{th}}$  BS and direction  $\theta$  given by

$$P_m(\theta) = |\mathbf{a}(\theta)^h \mathbf{s}_m(t)|, \quad (5.17)$$

where  $\mathbf{s}_m(t)$  concatenates the signals received at  $m^{\text{th}}$  BS.

The radio channels between a given UE and BSs are modelled according to Rice Channel model. Hence, NLoS components between the UE and BSs are taken into account. Considering that the UE transmits at a power  $P_t$ , the received signal power  $P_r$  at the BS side is calculated according to the Friis propagation loss:

$$P_r = P_t \left( \frac{\lambda}{4\pi d} \right)^2 \Omega, \quad (5.18)$$

where  $\lambda$  is the wavelength of the signal,  $d$  is the actual distance between the UE and the  $m^{\text{th}}$  BS and is given by

$$d = \sqrt{(x - x_{BS})^2 + (y - y_{BS})^2}, \quad (5.19)$$

$\Omega \in [0, \infty]$  is the Rician distributed channel gain corresponding to the effect of the small-scale fading such that  $\bar{\Omega} = 1$ .

Using this model, the distribution of  $\Omega$  follows a noncentral Chi-square probability density function given by [134]:

$$f_{\Omega}(\omega) = \frac{(K+1)e^{-K}}{\bar{\Omega}} e^{-\frac{(K+1)\omega}{\bar{\Omega}}} I_0 \left( 2\sqrt{\frac{K(K+1)\omega}{\bar{\Omega}}} \right), \quad (5.20)$$

where  $\omega \geq 0$ ,  $I_0(\cdot)$  is the zero-order modified Bessel function of the first kind, and  $K$  is the

Rician factor.

The parameters specifying the environment of the test are considered known and fixed during the measurements acquisition phase (K-Factor, carrier frequency, locations of the BSs). Given the above system model and the discussed assumptions, we aim to estimate the UE position situated in one of three BSs covering three hexagonal cells.

## 5.4.2 Multi-stage Localization

The proposed method exploits 5G potentials for communication [136] such as the high angular resolution of massive arrays. In this section, we propose a multi-stage processing to address the problem of localization.

### 5.4.2.1 Principle

The procedure of the method is as follows. First, each BS calculates the power received from the UE and transmits the power measurement to a processing center which estimates the ranges and decides what is the hosting cell. Second, the UE estimates the sector ID to which it belongs. Third, a multi-stage beamforming [140] is carried out to estimate the AoA. Both the range and the angle estimated serve to determine the UE coordinates. The entire process that we have just described is summarized in Fig. 5.7. In the following, we will detail the steps listed in the block diagram.

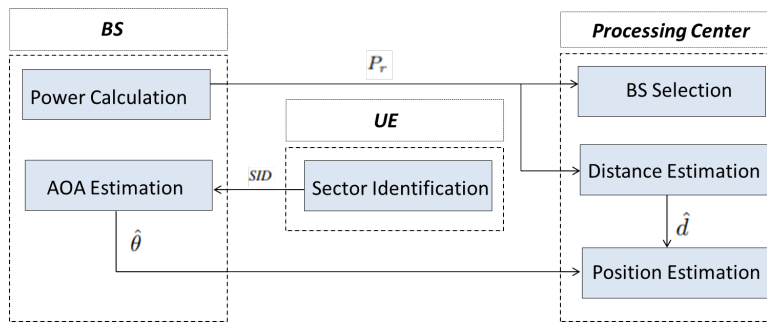


Figure 5.7: The proposed localization method block diagram.

### 5.4.2.2 Pre-treatment: Range estimation

The proposed method requires a preliminary step which consists in determining the cell to which the UE belongs. To do so, the UE broadcasts a known signal. Once received, each BS calculates the power received using the signal model (3) and transmits this value to a processing center which compares all the values received and decides which is the nearest BS to the UE. The value of the maximum power received allows the processing unit also to estimate the distance between the UE and the BS serving it by following the given formula:

$$\hat{d} = \sqrt{\frac{P_t \Omega}{P_r}} \frac{\lambda}{4\pi}, \quad (5.21)$$

where  $\lambda$  is the wavelength of the signal,  $P_t$  is the power transmitted by the UE,  $P_r$  is the power received at the BS side and  $\Omega$  is the Rician channel gain, which we assume to be known.

### 5.4.2.3 SID Determination

The sector search is usually performed as part of the identification of the Cell to which a UE aims to connect. We here exploit the SID to reduce the search space of the angle  $\theta$  within a limited interval of angles respecting table 5.2. In cellular networks, the SID is sent through the PSS broadcasted regularly by the BS to maintain the connection of the UE [137]. Three different PSS are used to identify the corresponding sector in the BS  $\in \{0, 1, 2\}$ . At the UE side, several SID determination approaches can be used to fulfill this task [?]- [?]. In our work, we used the approach presented in [?] which allows a robust sector identification.

## 5.4.3 Beamforming and Position Estimation

Once the new search space is determined, the AoA can be estimated using a two-stage beamforming.

### 5.4.3.1 Coarse stage

In the first time, the UE emits a reference signal to the BS and since the sector is known, the BS performs a scan in only the  $120^\circ$  of uncertainty instead of the entire cell range of  $360^\circ$ .

The search is performed respecting the model in equation (5.17) with a slightly large search angle  $\delta_\theta$ . The angle that provides the highest amplitude of (5.17) is considered as the coarse estimate of  $\theta$  that we denote by  $\hat{\theta}_c$ . The coarse search result is illustrated in Fig. 5.8 for a number of antennas  $M = 4$  and a search step  $\delta_\theta = \pi/100$  which shows a maximum at the AoA estimate.

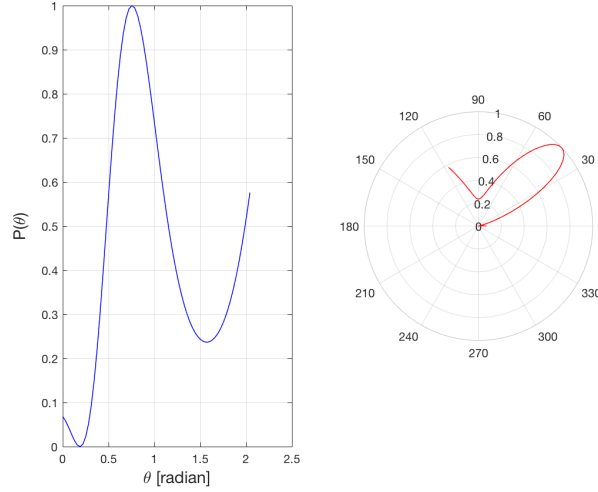


Figure 5.8: Angle search using a rough step  $\delta_\theta = \pi/100$  and a number of antennas  $M = 4$  in the noiseless case.

### 5.4.3.2 Fine stage

At this point, we have the smallest possible search space. We reproduce the coarse stage treatment but the BS performs a scan throughout a reduced interval equal to  $2\hat{\theta}_c^\circ$  centered on the coarse estimate  $\hat{\theta}_c$  using a new thinner step  $\delta_\theta$ . At the end of this stage, we obtain a more accurate estimation of the AoA, which we denote as  $\hat{\theta}_f$  to be used later during the localization step. It is to be noticed here that the multi-stage beamforming can also be envisaged by augmenting the used antenna size between the two stages: using a sub-antenna in the coarse stage and larger one in the fine stage.

### 5.4.3.3 Location estimation

At the end of the process, the value of the estimated distance  $\hat{d}$  obtained during the pre-treatment phase and the value of the angle obtained from the second stage of the beamforming  $\hat{\theta}$  are used to identify the coordinates  $(x, y)$  of the UE respecting the geometry rules for angles as

$$\begin{cases} \hat{x} = x_{BS} + \hat{d}\cos(\hat{\theta}), \\ \hat{y} = y_{BS} + \hat{d}\sin(\hat{\theta}). \end{cases} \quad (5.22)$$

where  $\hat{x}$  and  $\hat{y}$  are the UE  $x$  and  $y$  coordinates' estimates,  $x_{BS}$  and  $y_{BS}$  are the coordinates of the BS and  $\hat{\theta}$  is the AoA estimate.

## 5.4.4 Performance Evaluation

In this section, we provide the performance evaluation of the proposed localization method using centimeter waves with typical 5G parameters. We first describe the simulation setup, then present the result analysis and discussion.

### 5.4.4.1 Simulation Setup

All numerical results are run over  $10^4$  Monte-Carlo trials using the following parameters. We set the carrier frequency at  $f_c = 7\text{GHz}$ , the Rician K-factor at  $K=5$  and the three BS located at fixed coordinates  $[100,190]$ ,  $[250,103]$ , and  $[250.344,276.404]$  and one UE positioned randomly within an area of size  $500\text{ m} \times 500\text{ m}$ . Unless otherwise mentioned, the number of receive antennas is set to  $M = 4$  and  $M = 100$  antennas while the SNR is set to 5 dB. Performance is measured in terms of Root Mean Square Error (RMSE) of the AoA estimate  $\hat{\theta}$ , the distance to the UE estimate  $\hat{d}$ , and the coordinate estimates  $\hat{c} = (\hat{x}, \hat{y})$ . We also depict the probability of sub-meter precision of  $\hat{d}$  and  $\hat{c}$ . To assess the impact of the multi-stage beamforming, we present the estimate of the coordinate  $c$  in the coarse stage, where we use a large search step  $\delta_\theta = 10^2$  and the fine stage during which we use a very small step  $\delta_\theta = 10^4$  which is expected to greatly enhance the estimate. We denote the coarse and fine estimates of  $c$  by  $\hat{c}_c$  and  $\hat{c}_f$ , respectively.

### 5.4.4.2 Results and Discussion

Based on the described scenario, we now present the performance of the proposed method in terms of sub-meter location accuracy and RMSE. Let us see first the performance plots versus SNR. To do so, we have added a zero-mean Gaussian noise to the transmitted signal. The SNR value varies from -10 dB to 30 dB.

Fig. 5.9 depicts the AoA RMSE obtained using 4 and 100 antennas as a function of the SNR and for both the coarse stage and the fine stage results. As shown, the RMSE of  $\hat{\theta}$  decreases with the increase of SNR regardless of the number of antennas, and increasing the number of antennas further reduces the error in the estimation. It is also clear that the performance of the proposed estimator has been improved with the addition of the fine stage. Indeed, comparing  $\hat{\theta}_c$  estimate for  $M = 4$  and  $\hat{\theta}_f$  estimate for  $M = 100$  shows the gain by both changing antennas' number and search step between the coarse and fine stages. It is worth noting the effect of antennas' number when comparing coarse estimates (resp. fine estimates) for  $M = 4$  and  $M = 100$ , where we can reach the accuracy of the fine stage by increasing the number of antennas at the same SNR level.

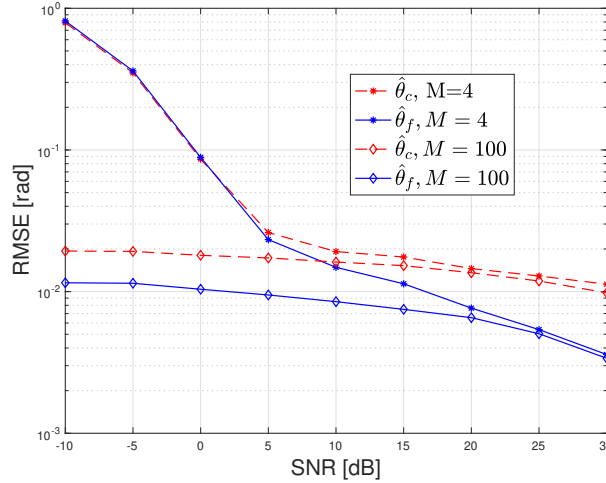


Figure 5.9: RMSE of the angle estimate's  $\hat{\theta}$  a function of the SNR for numbers of antennas  $M = 4$  and  $M = 100$ .

Fig. 5.10 and Fig. 5.11 present the RMSE and the probability of sub-meter accuracy of the distance and UE coarse and fine coordinates estimates in the case of coarse and fine estimate and for different antennas' number as a function of the SNR. Fig. 5.10 shows that

for all results, the RMSE decreases with the increase of the SNR value. The augmentation of the antennas' number further improves the estimation accuracy. Furthermore, thanks to the multi-stage processing, the probability of having an error less than 1m in the estimated location doubles. Compared to the distance estimate, we note that the UE location estimate exhibits a plateau starting from an SNR value of about 10 dB. This plateau is related to the error in the AoA estimate that depicts the same phenomena.

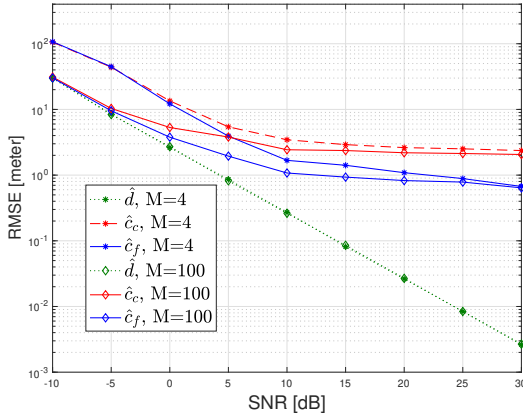


Figure 5.10: RMSE of the distance and coordinates as a function of SNR for numbers of antennas  $M = 4$  and  $M = 100$ .

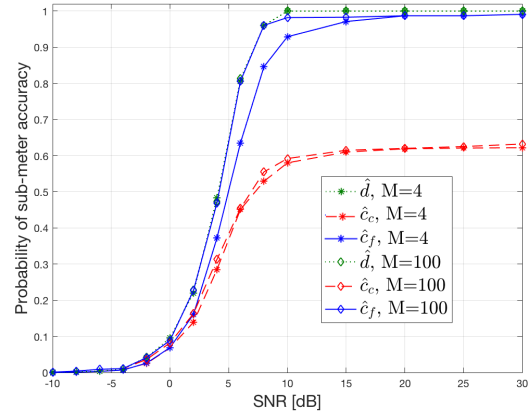


Figure 5.11: Probability of sub-meter precision as a function of the SNR for numbers of antennas  $M = 4$  and  $M = 100$

Thanks to the AoA estimation precision enhancement through the two stages, comparing coarse position estimate (resp. coarse probability of sub-meter accuracy) for  $M = 4$  and fine position estimate (resp. fine probability of sub-meter accuracy) for  $M = 100$  shows the gain by both changing antenna size and AoA search step between coarse and fine stages.

To assess the impact of the number of antennas at the BS side on the performance of the proposed method, we depict in fig. 5.12 and fig. 5.11 the distance and coordinates estimation RMSE and probability of sub-meter precision as a function of used antennas and compare between the coarse stage and the fine stage results. The antennas' number changes from 1 to 300 while the SNR is fixed to 5 dB. We note that increasing the number of antenna arrays vastly improves the performance. With reference to the previous results, we note that the probability to provide a sub-meter accuracy is 0.5 for  $M = 4$  can further be increased using higher  $M$  values. Indeed, due to the antenna arrays size increase, the angular resolution at the BS also improves.

We now focus on the efficiency and relevance of the proposed algorithm in a 5G context [40].

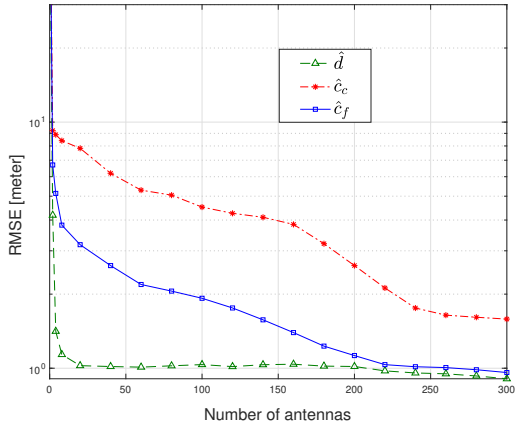


Figure 5.12: RMSE of distance and coordinates as a function of the number of antennas at the BS for SNR=5 dB.

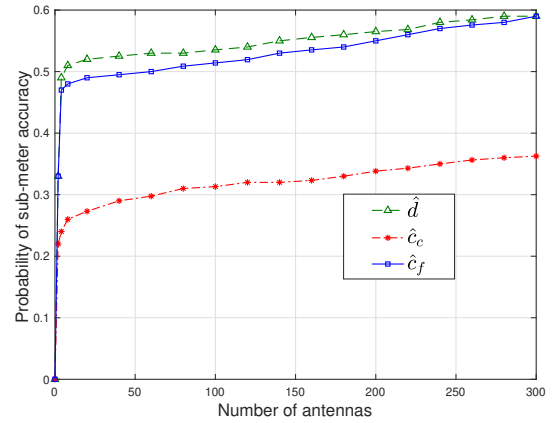


Figure 5.13: Probability of sub-meter precision as a function of the number of antennas at the BS for SNR=5 dB.

Differently from the previous assumptions, where channel response  $\Omega$  is assumed to be perfectly known, we here study the uncertainty on channel estimate by incorporating an error component modeled as Gaussian centered,  $\epsilon \rightarrow \mathcal{N}(0, \sigma_{CH}^2)$ , leading to an erroneous channel response  $\Omega' = \Omega + \epsilon$ . A stationary UE is randomly placed in the area. A total of  $10^4$  Monte Carlo realizations are evaluated under uncertain channel conditions in 30 GHz mm-waves.

#### 5.4.4.3 Impact of the wavelength

We start by examining the impact of the wavelength on localization precision. Particularly, we present the probability to achieve sub-meter accuracy in the estimation of the distance to the serving BS and the fine and coarse coordinates [40]. The results are presented in figure 5.14 for both 7 GHz and 30 GHz carrier frequencies, respectively corresponding to mm and cm waves. It is shown that for low SNR values, the accuracy obtained in the case of low frequency is higher than that obtained for high frequency. However, slightly better performance is shown in higher frequency when the SNR values increase. This behavior can be explained by the sensitivity of mm-waves to noise, which fosters their use for short-range communications.

Figure 5.15 depicts the RMSE of the AoA coarse and fine estimates  $\hat{\theta}_c$  and  $\hat{\theta}_f$ , and shows a low error even for very low SNR value where the RMSE is less than 0.1 at -10 dB. Consistently with the previous results, we note that mm-waves greatly reduce the error for high SNR values. Indeed, a 20 dB gain is achieved for the fine AoA estimate at an RMSE of about 0.003.

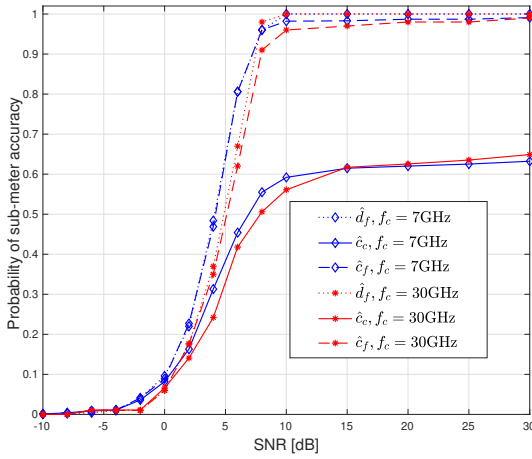


Figure 5.14: Probability of sub-meter precision of distance and coordinates estimates  $\hat{d}$ ,  $\hat{c}_c$ , and  $\hat{c}_f$  as a function of the SNR for carrier frequencies  $f_c = 7\text{GHz}$  and  $f_c = 30\text{GHz}$ .

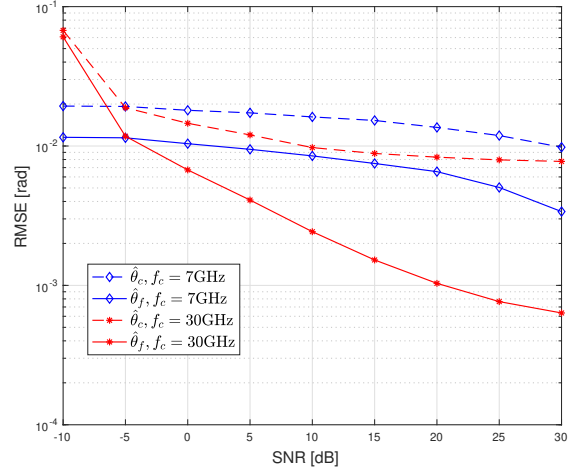


Figure 5.15: RMSE of the angle estimates  $\hat{\theta}_c$  and  $\hat{\theta}_f$  as a function of the SNR for carrier frequencies  $f_c = 7\text{GHz}$  and  $f_c = 30\text{GHz}$ .

#### 5.4.4.4 Impact of the channel error

Note that the above analysis assumes perfect channel knowledge ( $\Omega = \Omega'$ ), in what follows, we evaluate the effect of a channel error on the performance by presenting the probability of sub-meter accuracy as a function of the SNR in 3 different scenarios: 1) when the channel is perfectly known; 2) when the variance of the channel estimation error  $\sigma_{CH}^2$  is equal to  $10^{-1}$ ; and 3) when the channel estimation variance is equal to  $10^{-2}$  [40]. Indeed, channel error is incorporated as :  $\Omega' = \Omega + \epsilon$  where  $\epsilon$  is the Gaussian centered variable with variance  $\sigma_{CH}^2$ .

It can be clearly observed that the proposed method performs better when SNR value increases in the three scenarios, which is an expected result. We note that despite the satisfactory performance that exceeds 90% for fine coordinates estimation starting from an SNR value of 12 dB for an error variance  $\sigma_{CH}^2 = 10^{-2}$ , the error in the channel estimation still impacts localization accuracy as it is directly related to the estimation of  $d$ . Indeed, for the fine coordinate estimation, losses of about 2 dB and 4 dB are recorded when comparing the perfect channel case to the case of  $\sigma_{CH}^2 = 10^{-2}$  and  $\sigma_{CH}^2 = 10^{-1}$  respectively.

In figure 5.17, we present the RMSE of the fine and coarse AoA estimations as a function of the SNR under different channel conditions. It is natural that the perfect channel provides

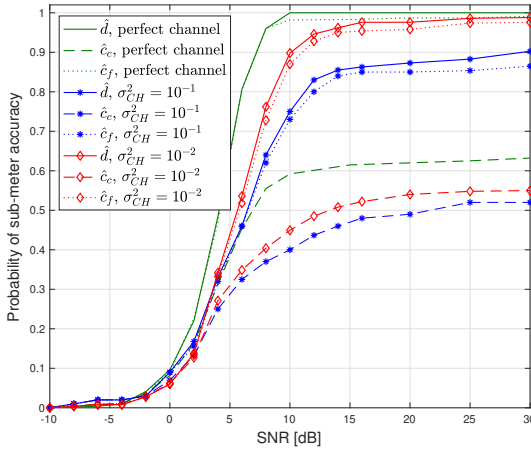


Figure 5.16: Probability of sub-meter precision of distance and coordinates estimates  $\hat{d}$ ,  $\hat{c}_c$ , and  $\hat{c}_f$  as a function of the SNR for channel estimation error variance  $\sigma_{CH}^2 = 10^{-1}$  and  $\sigma_{CH}^2 = 10^{-2}$  for carrier frequencies  $f_c = 7GHz$  and  $f_c = 30GHz$ .

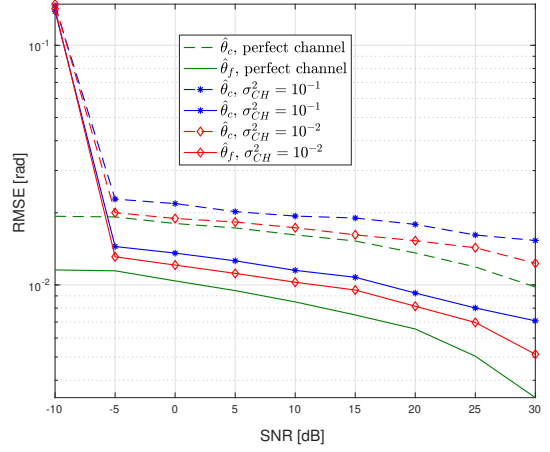


Figure 5.17: RMSE of the angle estimates  $\hat{\theta}_c$  and  $\hat{\theta}_f$  as a function of the SNR for perfect channel and erroneous channel estimation with error variance  $\sigma_{CH}^2 = 10^{-1}$  and  $\sigma_{CH}^2 = 10^{-2}$  for carrier frequencies  $f_c = 7GHz$  and  $f_c = 30GHz$ .

the lowest RMSE, while the error in the channel leads to a higher error especially for a very low SNR value (-10 dB). For medium and high SNR values, the gap between perfect channel and channel with estimation error variance  $\sigma_{CH}^2 = 10^{-2}$  is about 5 dB.

## 5.5 Conclusion

In this chapter, we studied the optimization of the height of a UAV relay node to provide a maximum coverage based on a) the SNR level of an edge user and on b) the average rate of ground users within a specific range. We exploited a physics-based channel model considering both deterministic large-scale path loss and random small-scale fading which we modeled by a Rician fading with an elevation angle-dependent  $K$  factor. By studying the maximum coverage radius based on the two criteria, we showed that there exists a unique optimum height at which the UAV should be located to maximize the deployment area. We also assessed the sensitivity of the optimal position to the surface characteristics.

Then, we tackled the problem of outdoor localization under Rician channel conditions. We proposed a multi-stage approach for the localization of a stationary UE in a massive MIMO

context. Once the UE is connected to a BS, this latter estimates the distance to the UE based on the reference signal power measurement. Sector ID identification at the UE side allows reducing AoA search space. A coarse AoA estimation is then performed throughout the sector identified. The second stage exploits the coarse AoA estimate to fine-tune the estimation around a very limited interval. The fine stage can also include an increased antenna size from the massive MIMO antenna compared to the first stage. Lastly, both distance and AoA estimates are used to find the UE coordinates. Simulations were performed and showed a localization accuracy that achieves an error lower than one meter. For more realistic evaluation, we considered channels affected by estimation errors and mm-waves. Comparing the obtained results to initial results, we noted that mm-waves provide better performance at high SNR values while cm-waves perform better at low SNR values. This behavior is justified by the sensitivity of mm-waves to noise. On the other hand, the studied localization scheme showed robustness to channel estimation errors. Extensions of this work consider neighbor-assisted approaches, which are presented in [37] and [38] for outdoor localization.

## Chapter 6

# Energy and MCS Allocation for Ultra-Reliable Communication

### 6.1 Introduction

ARQ is one of the main protocols which are adopted in wireless communication systems to ensure the quality of communications through re-transmission policies. Although re-transmissions offer time diversity and make communication links viable in front of the stringent requirements of URC, it greatly impacts the throughput efficiency and the energy budget. To reduce this impact, HARQ techniques use forward error correction coding.

This chapter studies a cross-layer approach, based on the Genetic Algorithms (GA), that aims to maximize the throughput efficiency of the HARQ protocol, while guaranteeing URC. The study combines Adaptive Modulation, and Coding (AMC) and Power Control (PC), at the physical layer, with ARQ and HARQ type I at the data link layer. The proposed optimization algorithm allows a judicious allocation of the available energy budget and a suitable Modulation and Coding Scheme (MCS) choice while keeping the same energy cost to maximize the throughput efficiency. Assuming partial CSI knowledge, the available energy budget is partitioned throughout the re-transmission attempts resulting in a vector of successively symbol energies, on which the throughput efficiency depends. Also, successive re-transmissions can use different MCS and symbol energies to maximize the throughput. Hence, for a given SNR, a vector of energy and an MCS are modeled as one individual from a population. The vector

elements correspond to the energy amounts allocated to each re-transmission trial. In a population, the individuals that provides the highest throughput efficiency are selected to be used in generating the next population through the crossover of the survivals and mutations. The processing repeats until stagnation of the throughput efficiency is observed. The individual that provides the highest throughput efficiency in the last population is selected as the solution offering the optimized parameters (symbol energy for each re-transmission attempt and MCS) used in the packet transmission at a specific SNR.

## 6.2 Related Works

In ARQ/HARQ techniques, a packet is retransmitted using the same energy level for all transmission attempts, which might not be the most efficient energy allotment procedure. To improve the performance of HARQ, in [141], HARQ was considered in Rayleigh block-fading channels where the transmitter only has knowledge of channel statistics, and, consistent with contemporary wireless systems, rate adaptation is performed such that a target outage probability (after a maximum number of H-ARQ rounds) is maintained. Then, in [142], power, as well as transmission rate are optimally adapted by the transmitter based on channel state information (CSI) obtained through feedback, while guaranteeing QoS constraints such as average throughput or average delay. The work in [143] proposes a framework in which a user selects an optimal amount of redundancy bits used for re-transmissions, an optimal packet error rate, and an optimal mapping of signal-to-interference-noise ratios (SINR) into modulation and coding scheme (MCS) such that the user throughput would be maximized.

Contrarily to [142] and [143], where HARQ mechanisms have been mainly studied as techniques to improve the throughput only, recent literature flags an increasing interest in energy efficiency. The author of [144] considered link adaptation with complete CSI knowledge for which the instantaneous SNR is known and with incomplete CSI for which only the average SNR is known. The work evaluated the packet loss probability and the throughput for both for a slow-varying and a fast-varying channel. In [145] and [146], based on the Lagrange multipliers, an optimized throughput was studied in an energy-constrained context. In [145], the optimal power level and the appropriate MCS are jointly determined, as a function of the fading channel conditions, to achieve the highest average throughput efficiency, for a fixed average transmit power constraint in AQR. Then, in [146], they developed an energy efficient

design which optimally combines AMC and PC with type-I (HARQ-I) protocol to maximize the average throughput efficiency under a prescribed average transmit power constraint.

In [147], the authors developed an energy consumption model that focuses on both simple HARQ and chase combining HARQ transmissions, which are studied under fast-fading and block-fading scenarios with Nakagami-m fading. Analytical expressions for the expected number of transmission trials were derived based on the statistic of re-transmissions. Later, the work in [148] investigated the trade-off between reliability and energy efficiency and proposed adaptive FEC/FWD and FEC/ARQ coding frameworks for clustered wireless sensor networks. The schemes considered channel condition and inter-node distance to decide the adequate channel coding usage. The work is energy efficient compared to ARQ schemes and FEC schemes, and suitable to prolong the clustered network lifespan as well as improve the reliability.

To improve energy efficiency, the works in [149] and [150] also optimized the power allocation considering truncated simple ARQ and HARQ. The optimization problem is solved in closed-form using the Karush-Kuhn-Tucker conditions and shows that power allocation in HARQ is a good strategy to improve the system energy efficiency. This work was extended in [151] to allow ultra reliable operation for HARQ with minimum power consumption in the finite blocklength regime. The results show that, contrarily to classical approaches, where it is optimal to allocate equal power with each transmission, the optimal strategy suggests transmission with incremental power in each round for operation in the ultra reliable regime. Meticulous energy distribution over re-transmissions is studied in [141] for a specific range of Signal to Noise Ratio (SNR) to increase the possibility to succeed packet transmission from the first attempt through boosting the energy during the first transmission. The work minimizes the average transmission energy while keeping a steady-state average probability of successful transmission. In [152], the authors aimed to minimize the average transmission energy while keeping a steady-state average probability of successful transmission.

### 6.3 Performance of ARQ/HARQ

In this section, we describe the operation of the ARQ retransmission protocol and the criteria for its evaluation. We consider the truncated version of ARQ which is well adapted for real time flows such as cloud gaming, voice over IP, and streaming system.

### 6.3.1 Presentation of the ARQ Protocol

The idea behind the ARQ, was to design a system that allows to detect the error burst, discard the affected packet, and request a re-transmission of the erroneous packet. The message sequence is broken up into packets of length  $k$ . Each of these packets is encoded using a rate binary error detecting code with length  $k_c$  to generate a coded packet of total size  $n = k + k_c$  [16]. Consequently, the ARQ protocol allows enhancing communication performance through re-transmission of erroneously received data packets.

As demonstrated in figure 6.1, it uses acknowledgment (positive and negative) and timeout to initiate a re-transmission in the case of detection of flawed data or to confirm that data is received correctly [158]. The protocol is used at the data link layer and exploits a  $k_c$ -bit Error Correction Code (ECC) to encode a packet of  $k$  useful bits and generate a coded packet of total size  $k + k_c$ .

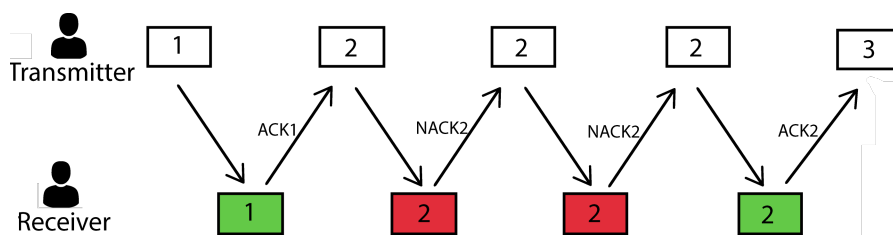


Figure 6.1: Setup for ARQ protocol. The transmitter sends the first packet and waits for the ACK from the receiver. Once ACK1 is received, the transmitter sends packet 2. If the receiver can not decode the packet, it discards the packet and sends back a NACK to the transmitter to ask for packet re-transmission.

The re-transmission process of ARQ can be done using one of three different strategies: 1) Stop-and-Wait, in which the transmitter sends one packet at a time and wait for the reception of either a positive acknowledgment (ACK) or a negative acknowledgment (NACK) to either transmit the next packet or repeat the transmission of the same packet, 2) Go-Back-N, in which the transmitter sends packets in a continuous stream until an erroneous packet is received, which blocks the acceptance of all following packets until a correct copy of it is received, and 3) Selective Repeat, which provides buffers in both the receiver and the transmitter to allow exclusive re-transmission of the erroneous packet only. To overcome the inefficiency due to re-transmission operations, Hybrid variants of ARQ incorporating FEC are used. The addition of FEC helps to maintain a significant throughput even in poor channel conditions and can also offer an increase in the throughput efficiency thanks to its ability to reduce the re-transmissions

by correcting the commonly occurred patterns as depicted in figure 6.2. The initial ARQ scheme is unable to provide that kind of efficiency because according to that scheme, defective packets must be re-transmitted.

The combination of ARQ and FEC produced three Hybrid types: HARQ type I, HARQ type II, and HARQ type III [159], [160], [161, 162]. Type I uses a fixed rate code designed for error correction, and a re-transmission remains necessary if the correction operation fails. The type II HARQ, however, adds memory and processing at the receiver to combine the multiple packets received within each ARQ transmission attempt, which allows increasing the correction capability of the code. Two common combining strategies exist in the literature: 1) incremental redundancy in which the redundancy is sent piece-wise upon error detection, and 2) the chase combining where the same information is combined (the re-transmission is an identical copy of the original packet). Contrarily to type II, where the decoder relies on both the initially transmitted packet and the additional incremental coded bits, in HARQ type III, incremental coded bits are self decodable which is suitable in the situation where a packet is lost or damaged.

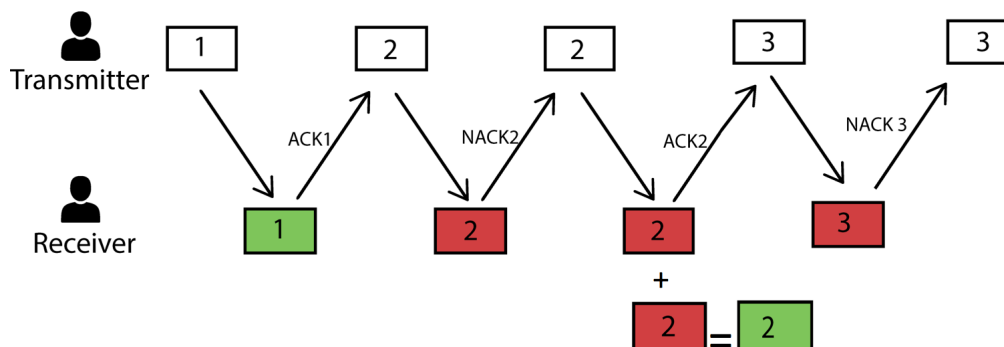


Figure 6.2: The setup for HARQ protocol. The transmitter sends first packet 1 and waits for the ACK from the receiver. Then it sends packet 2. If the receiver can not decode the packet, it buffers the packet and asks for re-transmission. Then, when it receives packet 2 once more, it combines it with the buffered packet to extract the information.

Consider a point-to-point communication link with a reliable feedback path between the receiver and the transmitter. The CSI is acquired at the receiver and then fed back to the transmitter with incomplete CSI for which only the SNR is known. According to the current CSI the transmitter selects the most appropriate transmit parameters to be used for the next transmission. The packets to be transmitted are first queued in a buffer of infinite size buffer, then transmitted on a packet-by-packet basis over the wireless channel. At the data link layer,

the selective repeat (SR) HARQ type I protocol is implemented. Due to latency constraints, we consider truncated HARQ, limiting the number of re-transmission attempts in equation (6.1) to a maximum of  $N$  trials. Each transmitted packet is encoded for both error detection and correction.

In what follows, we review the performance of ARQ/HARQ protocols for BPSK and M-ary modulations to determine the expressions of the throughput efficiency.

### 6.3.2 ARQ Performance for BPSK Modulation

The throughput, which we denote by  $\eta$  can be defined as the average number of encoded data packets accepted by the receiver (error-free packets) in the time it takes the transmitter to send a single  $k$ -bit data packet [16]. In an FEC system, the throughput is equal to the code rate  $R = k/n$ , where  $k$  is the useful data size and  $n$  is the total packet size (in bit). In a retransmission system, the throughput is a function of the number of times a packet has to be (re)transmitted before it is accepted by the receiver. Based on whether retransmission of an erroneous packet is carried out until an error-free reception is attained or not, we distinguish two types of ARQ : 1) truncated ARQ in which a fixed number of retransmissions attempts is set, over which a packet is thrown if it is not received correctly, and 2) non truncated ARQ in which an infinity retransmission attempts is allowed. We here consider the case of truncated ARQ, in which a packet is totally rejected after  $N$  erroneous trials. The average number of retransmission attempts, assuming independent and identically distributed (i.i.d) retransmissions, is then evaluated as

$$T_r = \sum_{i=0}^{+\infty} (P_r)^i = \frac{1}{1 - P_r}, \quad (6.1)$$

where  $P_r$  stands for the probability to generate a retransmission request (a packet is received with error). Given that the binary error probability  $p$  is known,  $P_r$  can be expressed as

$$P_r = 1 - (1 - P_e)^n. \quad (6.2)$$

The modulation used for the evaluation is Binary Phase Shift Keying (BPSK). In this case, the binary error probability  $P_e$  used in the packet error probability expressed in equation (6.2)

is equal to

$$P_e = \frac{1}{2} \operatorname{erfc}\left(\sqrt{\frac{E}{N_0}}\right), \quad (6.3)$$

where  $\operatorname{erfc}(\cdot)$  is the complementary error function [163] defined as

$$\operatorname{erfc}(x) = \frac{2}{\sqrt{\pi}} \int_x^{\infty} e^{-t^2} dt. \quad (6.4)$$

We here introduce another performance measurement criterion, which is the packet erasure probability  $P_{\text{loss}}$  defined as the probability that a packet is not received correctly even at the last retransmission attempt and is then thrown. Assuming a maximum number of  $N$  i.i.d retransmission attempts,  $P_{\text{loss}}$  can then be evaluated as the product of all retransmission attempts' packet error probabilities expressed below

$$P_{\text{loss}} = \prod_{i=1}^N P_{r,i} = \left(P_r\right)^N, \quad (6.5)$$

where  $P_{r,i}$  refers to the probability to generate a retransmission request at the  $i^{\text{th}}$  retransmission attempt. In addition to the number of transmission attempts, the throughput performance of the ARQ system depends strongly of how retransmission requests are handled by the transmitter and the receiver. Assuming a SR-ARQ protocol and the truncated scheme, the throughput expression that we consider in our work is given by the following equation

$$\eta = \frac{1}{T_r} \frac{k}{n} (1 - P_{\text{loss}}). \quad (6.6)$$

### 6.3.3 ARQ/HARQ Performance for M-ary Modulation

At the physical layer, a set of MCS is assumed to be supported and denoted as  $\vartheta$ . A given MSC  $\theta$  consists of a specific M-ary Quadrature Amplitude Modulation (QAM), a rate  $R_\theta$  FEC code and a packet size of  $Q$  symbols. At the transmitter side, an optimal transmit energy level  $E$  (or equivalently a transmit SNR  $\gamma$ ) and a convenient MSC  $\theta$  are selected as a function of the available CSI. The transmit SNR  $\gamma$  is defined as the ratio between the average transmit symbol energy  $E$  and the one-sided noise power spectral density  $N_0$ ,  $\gamma = \frac{E}{N_0}$ . Each packet corresponds to  $k$  bits of information which are first encoded with a detection code with  $k_c$  bits to issue a  $k + k_c$  codeword. Furthermore,  $m$  bits are appended to the generated codeword to complete the convolutional code trellis. Using an FEC of rate  $R$ , a final number

of  $(k + k_c + m)/R$  coded bits is obtained. For an M-ary QAM modulation, the coded bits are mapped to  $n = (k + k_c + m)/(\log_2(M)R)$  symbols.

We consider the throughput expression for hybrid type-I ARQ protocol and a given modulation and coding scheme  $\theta$  selected from the set of possible MCS  $\vartheta$ , with a modulation order  $M_\theta$  and rate, that is expressed as

$$\eta_\theta = \log_2(M_\theta) \frac{k}{k + k_c + m} \frac{1}{T_r}, \quad (6.7)$$

where  $T_r$  is the average number of re-transmission attempts expressed in equation (6.1), and  $P_r$  is the probability to generate a re-transmission request (a packet is received with an error that could not be corrected), tightly upper-bounded by

$$P_r(\gamma) \leq 1 - (1 - P_E(\gamma))^{k+k_c}, \quad (6.8)$$

for a specific SNR  $\gamma$ , where  $P_E(\gamma)$  stands for the error event probability of the Viterbi algorithm that can be expressed as

$$P_E(\gamma) = \min\left(1, \sum_{d=df}^{+\infty} a_d Q(\sqrt{2d\gamma})\right) \quad (6.9)$$

for a soft decision decoding. In the above equation (6.9),  $d_f$  and  $d_s$  are respectively the free distance and distance spectra of the code, and the  $Q(\cdot)$  is the Marcum function defined as

$$Q(x) = \frac{1}{\sqrt{2\pi}} \int_x^{+\infty} e^{-\frac{u^2}{2}} du \quad (6.10)$$

In addition to the throughput efficiency, we here introduce another performance measurement criterion, which is the packet erasure probability  $P_{\text{loss}}$  defined as the probability that a packet is not received correctly even at the last re-transmission attempt and is then thrown. Assuming a maximum number of  $N$  i.i.d re-transmission attempts,  $P_{\text{loss}}$  can then be evaluated as the product of all re-transmission attempts' packet error probabilities expressed below

$$P_{\text{loss}} = \prod_{i=1}^N P_{r,i}(\gamma) = \left(P_r(\gamma)\right)^N, \quad (6.11)$$

where  $P_{r,i}(\gamma)$  refers to the probability to generate a re-transmission request at the  $i^{\text{th}}$  re-transmission attempt.

For a given MCS  $\theta$ , when considering a packet size of  $Q$  symbols and assuming that  $k_c$  and  $m$  are  $\ll$  compared to  $Q$ , the packet error probability in (6.8) then turns into

$$P_r(\gamma) = 1 - (1 - Pe^{M_\theta}(\gamma))^{2Q}, \quad (6.12)$$

where  $Pe^{M_\theta}(\gamma)$  is the probability that the inphase/quadrature phase component of the  $M_\theta$ -QAM symbol be erroneously received, given by

$$Pe^{M_\theta}(\gamma) = \frac{\sqrt{M_\theta} - 1}{\sqrt{M_\theta}} \operatorname{erfc} \left( \sqrt{\frac{3}{2(M_\theta - 1)} \gamma} \right), \quad (6.13)$$

where  $\operatorname{erfc}(\cdot)$  is the complementary error function. Now combining the equations (6.1), (6.12) and (6.13), we can express the throughput efficiency as

$$\eta_{M_\theta}(\gamma) = \log_2(M_\theta) \left( 1 - \frac{\sqrt{M_\theta} - 1}{\sqrt{M_\theta}} \operatorname{erfc} \left( \sqrt{\frac{3}{2(M_\theta - 1)} \gamma} \right) \right)^{2Q}. \quad (6.14)$$

In this case, the throughput expression in (6.7), can further be rewritten as

$$\eta_{M_\theta} = \log_2(M_\theta) \times (1 - Pe^{M_\theta}(\gamma))^{2Q}. \quad (6.15)$$

## 6.4 Impact of PC and AMC on ARQ Performance

In this section, we study the impact of both energy and MCS on the throughput efficiency of packet transmissions adopting the ARQ protocol. We first present the impact in the case of BPSK modulation, where only energy is highlighted. Then, we generalize the study to both PC and AMC strategies.

### 6.4.1 Energy Allocation for BPSK modulation

For more significant evaluation, we are going to study the throughput efficiency as a function of the average energy cost due to packet transmission attempts, which is given by the following expectation

$$E_{\text{avg}} = E \times \sum_{i=1}^N (P_r)^i = E \times T_r. \quad (6.16)$$

To highlight the connection of the throughput  $\eta$  expressed in (6.6) to  $\gamma_{\text{avg}} = E_{\text{avg}}/N_0$ , we depict its curve in figure 6.3. We note that for several instances (e.g.  $\gamma_{\text{avg}} = 7$  dB), the same average SNR  $\gamma_{\text{avg}}$  leads to different throughput values, while only one of them leads to the maximum throughput. Thus, only the upper envelope of the throughput curve should be considered for an energy efficient system.

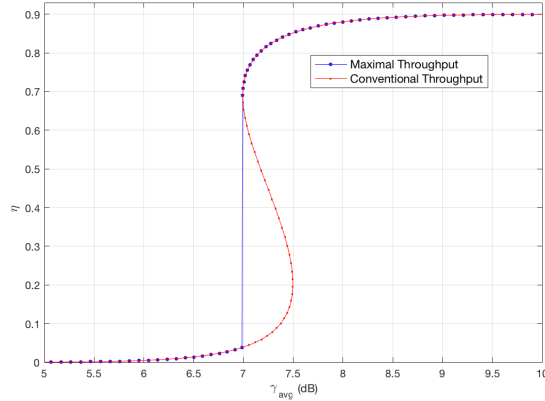


Figure 6.3: Throughput efficiency as a function of the average SNR for conventional ARQ (initial and upper envelope).  $N = 3, k = 90, n = 100$ .

#### 6.4.2 Energy Allocation and MCS Selection for M-ary Modulation

Figure 6.4 presents the throughput efficiency, expressed in equation (6.15) as a function of the SNR consumed per symbol for uncoded modulation and different MCS showing the impact of the MCS and energy selection and on the throughput efficiency. Using a single modulation technique for every transmission will not ensure the best data transmission at a given time, thus, the QoS will be affected. Also, having a single modulation scheme could cause an energy loss, for example taking the case of QPSK, the throughput stagnation start approximately at 12 dB, this means that any higher energy value will not affect on the throughput efficiency [41]. To ensure a reliable setting of the communication, we suggest to dynamically switch the MCS according to the SNR value, i.e. the appropriate MCS scheme is selected by comparing the received SNR to preset thresholds indicated by the crossing between curves [42].

To highlight the effect of allocating the available energy budget on the throughput, we illustrate the throughput efficiency in equation (6.15) as a function of the average SNR defined as  $\gamma_{\text{avg}} = E_{\text{avg}}/N_0$ , as expressed in equation (6.16). The throughput efficiency is drawn in figure

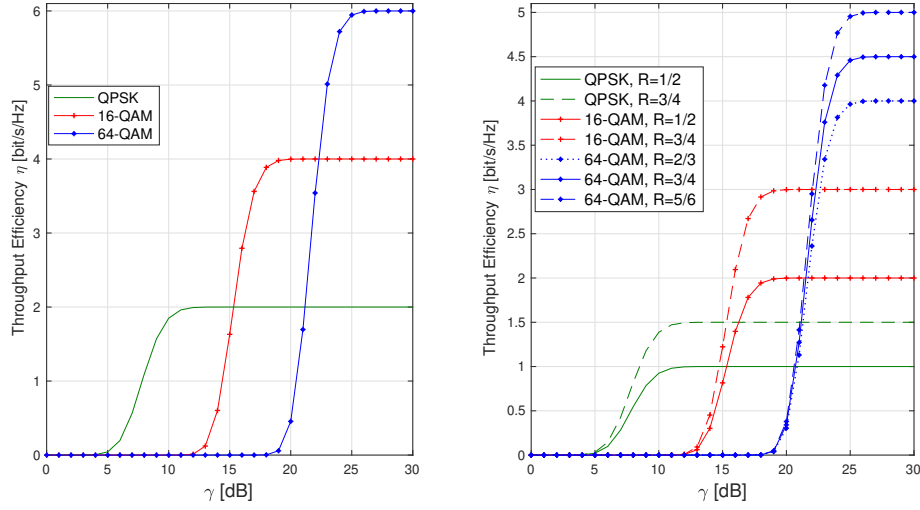


Figure 6.4: Throughput efficiency as a function of the SNR  $\gamma$  for conventional ARQ with different modulation and coding schemes.

6.5 in two cases: 1) case of conventional allocation with equal energy for all re-transmission attempts, and 2) upper envelope showing maximal throughput values only. It is notable that the same average SNR per symbol, with different values of the energy per symbol, can exhibit different throughput efficiency values at the same time. Thus, the upper envelope of the throughput curve should be considered for energy efficiency and optimized performance. It is ought to be noted that the average energy can still give a better performance and a higher throughput if the energy budget is distributed in a judicious manner all along the different  $N$  re-transmissions attempts [42]. Consequently, to enhance the throughput efficiency, we suggest the allocation of a different energy cost for each transmission, in addition to a suitable modulation and coding scheme.

As one of the aims of this work is to optimize the amount of energy allocated during each re-transmission attempt, we use a new total energy formula in the remaining of this chapter, which is expressed as

$$E_{\text{avg}} = E_1 + E_2 P_{r1} + E_3 P_{r1} P_{r2} + \dots + E_N P_{r(N-1)} P_{r(N-2)} \dots P_{r1}, \quad (6.17)$$

where  $P_{ri}$  stands for the probability to generate an  $i^{\text{th}}$  re-transmission request. Using the new

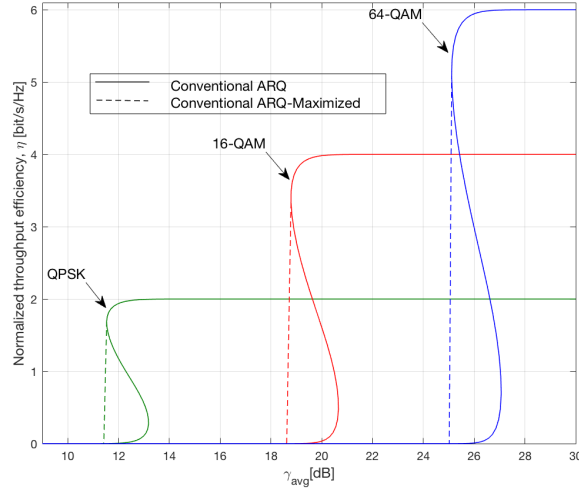


Figure 6.5: ARQ throughput efficiency as a function of the average SNR for QPSK, 16-QAM and 64-QAM modulations,  $N=3$ ,  $Q=120$  symbols.

expression the average energy, the re-transmission number becomes

$$Tr = 1 + P_{r1} + P_{r1}P_{r2} + \dots + P_{r(N-1)}P_{r(N-2)}\dots P_{r1}, \quad (6.18)$$

## 6.5 Optimized Performance through PC

### 6.5.1 Problem Formulation

The curves presented in figure 6.3 correspond to the case where the energy  $E$  spent per packet transmission remains the same for all transmission attempts. To enhance energy efficiency, we here suggest optimizing the allocation of the energy to be consumed for each transmission attempt [41], while keeping the same average energy  $E_{\text{avg}}$ . The main objective behind optimized energy allotment is to maximize the throughput efficiency, subject to the constraint of total target energy cost per all transmission attempts  $E_{\text{avg}} \leq E_{\text{target}}$ . For each SNR  $\gamma_{\text{avg}}$ , the

optimization problem can then be mathematically formulated as follows [42]

$$\begin{aligned}
& \underset{(\Upsilon)^{(\gamma_{avg})}}{\text{Maximize}} : & \eta &= \frac{1}{T_r} \frac{k}{n} (1 - P_e) \\
& \text{Subject to} : C_1 & E_{avg} &\leq E_{target}, \\
& & C_2 & N \geq 1,
\end{aligned} \tag{6.19}$$

where the optimization variable  $\Upsilon^{(\gamma_{avg})}$  introduced here stands for the vector of energy-per-packet allocated to each transmission attempt  $\Upsilon = [E_1, E_2, \dots, E_N]$ , for a fixed average SNR  $\gamma_{avg}$ . To solve our optimization problem, we opt for a GA based approach. The choice is justified by GA capabilities to check partially ordered search space for various tradeoffs as demonstrated in [154].

### 6.5.2 GA-based Solution

The Genetic Algorithm is a processing that transforms a set of individual objects, known as population, into a new generation through reproduction from the set of survivals selected based on their fitness values. Selection is achieved by evaluating fitness values and picking up a proportion  $N_s$  of the fittest individuals that will be involved in the next generation [42]. Reproduction consists of crossover and mutation by which new individuals are generated. The crossover is a recombination operation that creates variation in the population  $g + 1$  by producing offsprings combining traits from two parents (selected individuals from generation  $g$ ). To prevent convergence to a local optimum solution, mutation is applied to randomly change some individuals into the new population. The processing hence attempts to find the best (or near best) solution to the problem by genetically breeding the population of individuals over a series of generations, where each individual in the population represents a possible solution to a given problem. GA search has been used in different application fields of communication engineering like cooperative communication, sequence generation, and PAPR reduction [155,157]. The process of the proposed GA-based search described hereafter, includes the definition of the encoding rule, selection of potential solutions, and crossing and mutation operations.

1. **Encoding:** before applying the genetic algorithm to our problem, we need to design artificial chromosomes and define a mapping between the search space of the problem

and instances of the artificial chromosome. In our optimization problem, each individual represents a vector of  $N$  chromosomes represented by the energies allocated to each transmission attempts. Referring to the problem formulation in (6.20) of the section 6.5.1, an individual is presented by a vector of energies  $\Upsilon$  while the chromosomes of an individual are the elementary energies  $E_1, E_2, \dots, E_N$ .

2. **Population initialization:** the initial population is composed of  $N_p$  individuals ( $\Upsilon_j$ ,  $j = 1, 2, \dots, N_p$ ) whose chromosomes are randomly generated to form the population, which is an  $(N_p, N)$  matrix with lines corresponding to individuals set in such a way to satisfy the constraint  $C_1$ . The population size  $N_p$  must be parameterized sufficiently high to offer the maximum of diversity in combining energies  $E_i, i = 1, 2, \dots, N$  for each individual.
3. **Selection:** selecting the fittest individuals is based on evaluating the throughput efficiency expressed in (6.6). Within each generation  $g$ , the objective function  $\eta$  is first calculated for each vector or individual  $\Upsilon_{g,j}$ . The first  $N_s$  candidates with the highest throughput present the survival fittest ones. In this case, the vectors of the  $g^{\text{th}}$  generation  $\Upsilon_{g,j}, j = 1, 2, \dots, N_s$  that provide the highest throughput will survive to create offsprings of the next population.
4. **Crossover:** we here choose the one-point crossover due to the limited number of retransmission attempts  $N$  in practical truncated ARQ. In each iteration, one crossover point is chosen randomly to combine parents  $\Upsilon_{g,m}$  and  $\Upsilon_{g,n}$  to generate the new individuals  $\Upsilon_{g+1,m}$  and  $\Upsilon_{g+1,n}$ .
5. **Mutation:** to avoid sub-optimal solutions, the newly created population (using crossover) will further experience mutation with a small probability  $P_m$  and replaces the chosen elements with randomly generated ones.

Steps 3, 4 and 5 are repeated until either stagnation of the maximum value of throughput efficiency or a specified number of iterations is reached. At the end of processing, the individual with the highest throughput is selected to be applied for energy allocation during packet transmission attempts.

### 6.5.3 Performance Evaluation

In this section, numerical results are provided to assess the performance of optimized ARQ and compare it to the heuristic optimization introduced in [153]. We consider a truncated ARQ with  $N = 3$  maximum allowed transmission attempts,  $k = 90$  useful bits per packet and  $n = 100$  bits.

We recall that respecting the proposed GA based solution, for each average SNR  $\gamma_{avg}$ , we evaluate the objective function in (6.20) to select the best set of energy vectors in the  $g^{\text{th}}$  generation  $\Upsilon_{g,j}(j = 1, 2, \dots, N_g - N_s)$  that maximizes the throughput, carry out the genetic processing (crossover, mutation) to establish the new population ( $g + 1$ ) of energy sets more adapted. The stop condition of the research processing is here set to 50 iterations, which was experimentally shown to be sufficient to lead to convergence.

Figure 6.6 illustrates the comparison of ARQ throughput efficiency of the proposed GA-based solution, the dichotomy search-based solution, and the conventional non-optimized one. It is clearly shown that the optimal power allocation significantly improves the performances of the ARQ protocol especially for low and medium SNRs in both proposed and considered benchmark [153] allocation strategies. We can record a gain of about 0.3 dB and 3 dB for a throughput efficiency equal to 0.1 compared with the dichotomous search optimization and the conventional non-optimized allocation, respectively. From an average SNR value  $\gamma_{avg} = 9$  dB, all energy allocation procedures provide the absolute maximum of throughput efficiency.

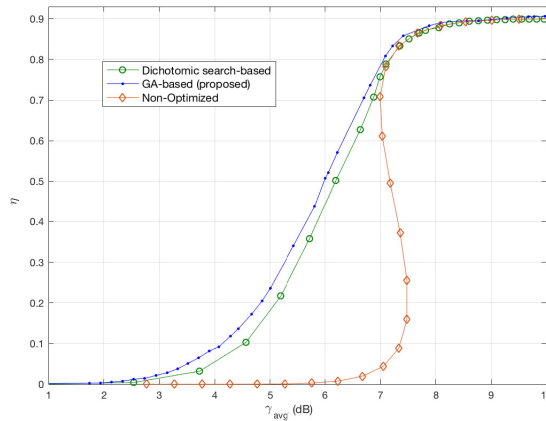


Figure 6.6: Throughput efficiency as a function of the average SNR for the optimized ARQ.  $N = 3, k = 90, n = 100$ .

For more significant assessment, we depict in figure 6.7 the number retransmission attempts in three scenarios : 1) non optimized energy allocation 2) GA-based energy allocation with maximized throughput as formulated in (6.20), and 3) GA-based energy allocation with minimized number of retransmission attempts and no constraint is set for the throughput efficiency. In the latter scenario, the objective function aims to minimize the number of retransmissions  $T_r$  given in (6.18) respecting the same constraints of energy allocation  $C_1$  and  $C_2$  set in (6.20). Consistently with the previous results, the optimized algorithm requires a much lower number of retransmissions to ensure error-free packet reception. It is worth here to note that the number of required retransmission attempts  $T_r$  is steady for both scenarios 1 and 2. This result highlights the efficiency of the proposed energy allocation solution in terms of minimizing the number of retransmission attempts while keeping an optimum throughput efficiency.

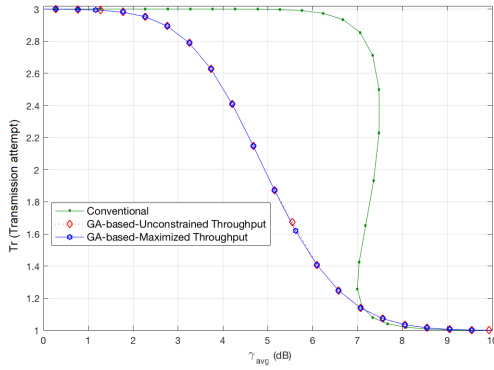


Figure 6.7: Number of retransmission attempts,  $N = 3, k = 90, n = 100$ .

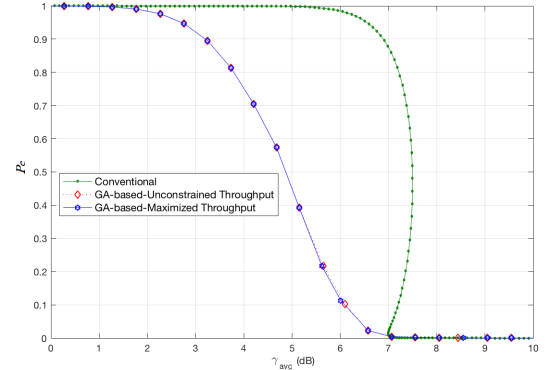


Figure 6.8: Probability of packet erasure,  $N = 3, k = 90, n = 100$ .

We present in figure 6.8 the probability of packet erasure expressed in equation (6.5) considering the three previous scenarios. This adds value to the performance evaluation by giving an idea about the loss in terms of data. We notice a strong connection between the re-transmission attempts' number  $T_r$  and the probability of erasure  $P_e$ , which is naturally due to their dependency to packets rejection. As the average SNR value increases, error-free packet reception becomes higher from the beginning of the transmission (first or second transmission attempts) and hence the probability that a packet is thrown after  $N$  transmission trials is decreased. We notice a gain of about 3 dB for a target erasure probability of 0.7 achieved through the proposed allocation energy strategy when compared to the uniform energy allocation used in conventional ARQ.

The work presented here studies efficient energy allocation to maximize the throughput for

ARQ with BPSK modulation using Genetic Algorithm (GA) based optimization. The available energy budget is allocated along transmission attempts (first transmission and potential re-transmission) while the total energy cost is kept steady for each packet. The results demonstrate the efficiency of the allocation strategy in terms of maximizing the average throughput efficiency and accordingly reveal the improvement in reducing the probability of packet erasure as well as the number of required transmissions to achieve high throughput. This work only considered Binary Phase Shift Keying (BPSK).

## 6.6 Optimized Performance through PC and AMC

### 6.6.1 Problem Formulation

Figures 6.4 and fig. 6.5 emphasize the impact of both energy allocation and MCS selection on the system performance, which motivates the work on optimizing these two parameters to maximize the throughput efficiency. Hence, we propose an optimization that consists in searching the most appropriate energy per symbol to spend at each packet transmission attempt to maximize the throughput for a total energy cost per symbol  $E_{\text{avg}}$  not exceeding the total target energy cost  $E_{\text{target}}$  ( $E_{\text{avg}} \leq E_{\text{target}}$ ). Besides, a judiciously chosen MCS  $\theta$  is selected among a set of available MCSs for each packet transmission that is adapted to the SNR value. Consequently, the throughput maximization problem can be mathematically formulated as

$$\begin{aligned}
 \text{Maximize : } & \quad \eta = \log_2(M_\theta) \frac{1}{Tr} \frac{k}{k + k_c + m} \\
 \text{Subject to : } & \quad C_1 \quad E_{\text{avg}} \leq E_{\text{target}}, \\
 & \quad C_2 \quad N \geq 1, \\
 & \quad C_3 \quad \theta \in \vartheta.
 \end{aligned} \tag{6.20}$$

The optimization variables of the problem are : 1)  $\Upsilon$  that stands for the vector of energy-per-packet allocated to each transmission attempt  $\Upsilon = [E_1, E_2, E_3, \dots, E_N]$ , for a fixed average SNR  $\gamma_{\text{avg}}$ , and 2)  $\theta$  that stands for the MCS chosen for the same SNR and which is selected from the set of MCSs  $\vartheta$  (QPSK, 16-QAM, and 64-QAM, with different coding rates). The optimization problem has been set to work under three different constraints: 1)  $C_1$  is set to

manage the available average energy budget  $E_{\text{avg}}$ , which should not surpass the fixed target energy  $E_{\text{target}}$  for the  $N$  packet (re)-transmission attempts, 2)  $C_2$  is the condition that guarantees the transmission of a packet for at least one time and at most  $N$  allowed re-transmissions number, and 3)  $C_3$  is defined to limit the MCS to be selected among the set of possible MSCs  $\vartheta$ . Due to the non-linearity and complexity of the studied optimization problem, we resort to a numerical Genetic Algorithm based search to approach the couple  $(\Upsilon, \theta)$  leading to a maximized throughput.

### 6.6.2 GA-based Solution

In this section, the GA is also used to search for the optimal combination of the vector of energy values allocated to each transmission attempt  $\Upsilon$  and the MCS  $\theta$ . To this aim, we model this couple as the two chromosomes composing an individual that belongs to a population. Each individual hence presents a potential solution of the optimization problem. Respecting the GA reproduction principle, the individuals of a population  $p$  are used in the generation of the following population  $p + 1$ . Given the fixed size of populations, only a selected set of individuals contributes to the reproduction process. These individuals are chosen based on their fitness function values, which is fixed as the throughput efficiency. To explain the proposed solution, we detail the processing through the flowchart in figure 6.9 and describe the steps in the following.

1. **Initialization:** the algorithm starts with an initial population of  $N_p$  randomly generated couples of energy vector and an MCS  $(\Upsilon, \theta)$  to form the individuals. We note each individual as  $I \leftarrow (\Upsilon, \theta)$ .
2. **Fitness calculation:** the fitness function is the evaluation metric of the individuals in a specific population. In our algorithm, the throughput expression in equation (6.7) is used as a fitness function to decide the surviving individuals in a population  $p$  that presents the parents in the population  $p + 1$ .
3. **Selection:** once the fitness functions of all individuals are calculated, the algorithm sorts them based on the highest values to determine the fittest ones. Then, the first  $N_s$  individuals are chosen to contribute in the population  $p + 1$ . The selected parents are put into a mating set to continue the genetic operations.

4. **Crossover:** according to a fixed crossover point number  $P_c$ , two parent individuals  $I_{P1}$  and  $I_{P2}$  are picked from the mating set are crossed to generate two new offspring individuals. In other words, our algorithm exploits the values of elements in the energy vectors of the parents to form new energy vectors  $\Upsilon_1$  and  $\Upsilon_2$  that present the first chromosomes of the two offsprings. Moreover, modulation orders and coding rates of the parents are recombined to create the second chromosomes of the two offsprings  $\theta_1$  and  $\theta_2$ . The results consist on two new individuals  $I_{O1} \leftarrow (\Upsilon_1, \theta_1)$  and  $I_{O2} \leftarrow (\Upsilon_2, \theta_2)$ .
5. **Mutation:** for a defined mutation probability  $P_m$ , the chromosomes in one or multiple individuals will be randomly changed with this probability. This means that the allocation of the energy vector and the selection of the MSC are randomly selected with the probability of  $P_m$  in each population to avoid sub-optimal solutions and add diversity.

After crossover and mutation operations are applied to the survivals, the resulting offsprings and their parents are all grouped to compose the new population. These steps are repeated until either stagnation of the maximum value of throughput efficiency or a specified number of iterations is reached. The GA processing is expected to ameliorate the performance provided by individuals from a population to its subsequent as only individuals with efficient genes participate in the generation of the following populations. At the end of the processing, the individual with the highest throughput is selected to be applied later during packet transmission attempts, depending on both the average energy  $E_{avg}$ .

A summary of the proposed solution is depicted in algorithm 1, which defines the inputs, outputs, and different steps. The algorithm is executed for each SNR value, assuming that this parameter is known. The population size is set to  $N_p$ , the mating set is fixed to  $N_s$ , the probabilities of crossover and mutation are set to  $P_c$  and  $P_m$  respectively. For each SNR value, as long as the difference between the throughput efficiency values at the iterations  $i$  and  $i - 1$  is high, the genetic processing is performed to produce better individuals. As detailed in the previous paragraph, this processing consists on evaluating the throughput efficiency to select the portion of  $N_s$  fittest individuals. These latter undergo crossover to generate the offsprings, a few of them change randomly with the mutation probability  $P_m$ . Once the genetic processing is finished, a new population is produced and individuals are evaluated again for reproduction. The stop condition is reached at the stagnation of the throughput efficiency value. The best individual of the last population is selected as a solution of the optimization problem that provides the optimal performance using the couple  $(\Upsilon_{opt}, \theta_{opt})$ .

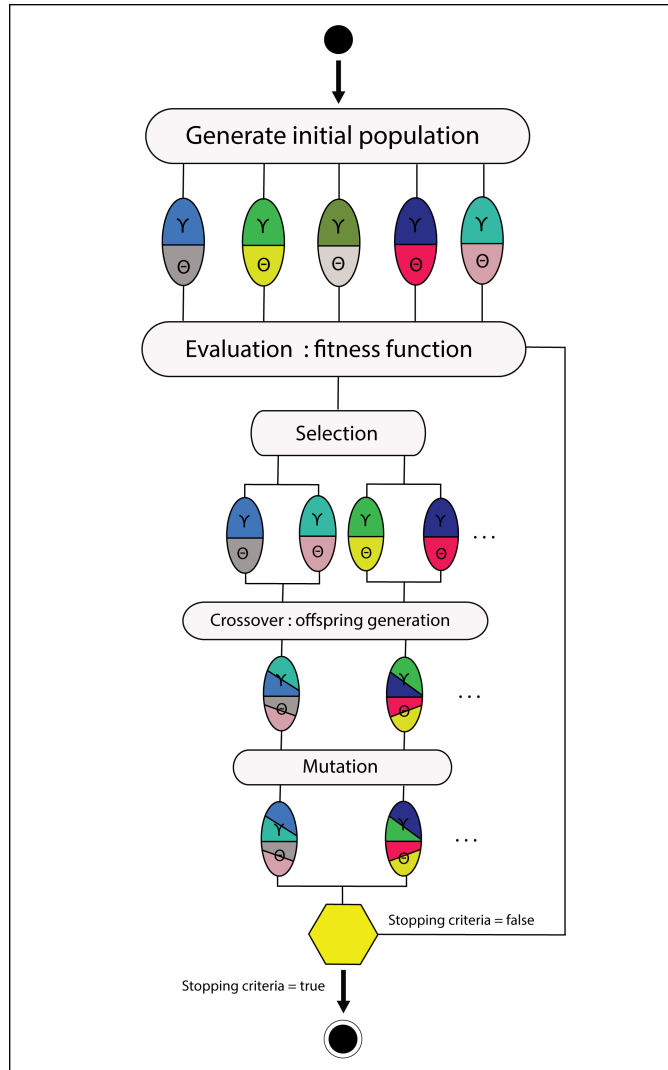


Figure 6.9: Genetic Algorithm Based Diagram

**Inputs:**

Population size:  $N_p$

Mating set size:  $N_s$

Crossover probability:  $P_c$

Mutation probability:  $P_m$

Number of re-transmissions:  $N$

Set of MCS:  $\vartheta = [\theta_1, \theta_2, \theta_3, \dots]$

Energy target value:  $E_{\text{target}}$

Average energy:  $E_{\text{avg}}$

One-sided noise power:  $N_0$

Throughput efficiency variance  $\epsilon \leftarrow 0$

---

**Outputs :**

Optimal energy vector:  $\Upsilon_{\text{opt}} = [E_1, E_2, \dots, E_N]I$

Optimal MSC:  $\theta_{\text{opt}}$

---

**begin**

**1 :** set parameters

**2 :** create an initial random population of  $N_p$  individuals

**while**  $\epsilon = (\eta_{\text{max}}^i - \eta_{\text{max}}^{(i-1)}) \gg$

**3 :** compute fitness functions of all  $I \in P$  as in eq. (1)

**4 :** sort individuals by highest fitness value

**5 :** select most fittest individuals in the mating set  $S$

**for**  $j=1$  **to**  $N_s/2$

**6 :** pick  $I_{Pj}$  and  $I_{P(j+1)}$  from  $S$  and perform crossover

**7 :** generate offsprings  $I_{Oj} \leftarrow (\Upsilon_1, \theta_1)$ ,  $I_{O(j+1)} \leftarrow (\Upsilon_2, \theta_2)$

**end for**

**8 :** mutate  $P_m$  random individuals

**9 :** increment  $i$

**end while**

**10 :** perform steps **3** and **4**

**11 :** select the best individual with highest  $\eta$  value

**10 :** return  $I_{\text{opt}} \leftarrow (\Upsilon_{\text{opt}}, \theta_{\text{opt}})$

**end**

---

It is worth noting that GA-based solutions are known for their high computational complexity due to the multiple iterations required for the algorithm to converge. In our case, however, the processing is carried out offline and the optimal solutions are saved to be used directly during transmission attempts depending on the channel conditions.

### 6.6.3 Performance Evaluation

In this section, we evaluate the performance of the proposed GA-based optimization approach [42] and compare it to the benchmarks in [145] and [146], which both use the technique of Lagrange multipliers. Particularly, We present the maximized throughput efficiency  $\eta$  resulting from the use of optimized energy and MCS for ARQ and HARQ-I in the case of both static and fading channels. Further, we depict the probability of packet erasure to highlight the capability of the proposed approach to offer an ultra reliable regime.

#### 6.6.3.1 Simulation parameters

The size of the initial population  $N_p$  is set to 100 individuals, from which the 50% fittest individuals are selected during each iteration to be used in the next population.  $N_s$  is then equal to 50 individuals. As the maximum allowed re-transmission attempt  $N$  is set to 3 leading to an energy vector of 3 elements, a one-point crossover is suitable and a mutation probability  $P_m = 0.02$  of the total population size. The total packet size is  $Q = 120$  symbols which are FEC coded and we use 7 MCS levels as presented in table I. For the fading channel, we consider a normalized Doppler frequency  $D_f T_s = 0.1$ .

Table 6.1: Convolutionally Coded Modulation

Modulation	QPSK		16-QAM		64-QAM		
Coding Rate	1/2	3/4	1/2	3/4	2/3	3/4	5/6

#### 6.6.3.2 Simulation Results

The performance of the proposed optimization solution is presented in terms of throughput efficiency and the probability of packet erasure to assessed its reliability. Furthermore, the energy allocation strategy resulting from our algorithm to maximize the throughput is for different SNR levels.

We compare in figure 6.10 our results to those obtained in [145] based on the Lagrange multipliers for simple ARQ protocol. It is clearly shown that the proposed GA-based optimization approach outperforms the Lagrange-based one at almost the whole considered SNR

range starting from 3dB and 6dB in the static channel and fading channel, respectively, realizing a gain that reaches 5dB at high SNR values. Below these SNR values, the benchmark realizes a slight gain of about 1dB in both channels. We also note that the static channel reaches the possible highest efficiency, while in the fading channel the curves stagnate at a lower value due to the higher channel power that further weakens the SNR level.

In figure 6.11, we depict the results in the case of HARQ-I compared to the results presented in [146]. Consistently with the previous figure, we observe that the proposed GA-based solution provides higher throughput efficiency starting from an SNR value of 5dB, yet with a lower gain compared to the results in figure 6.10. The proposed solution achieves a gain of about 2dB and 5dB in the static and fading channels, respectively.

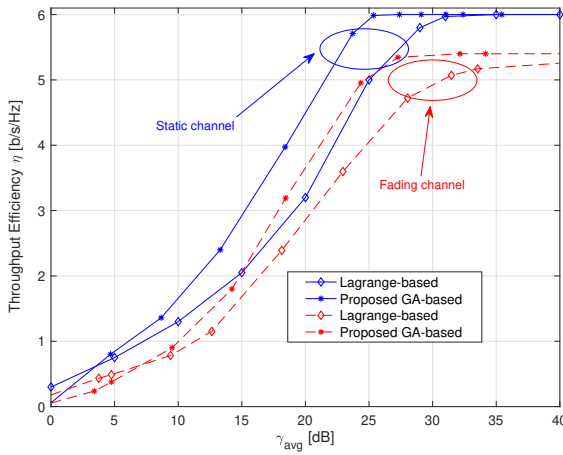


Figure 6.10: Average Throughput Efficiency for PC-AMC-ARQ of the proposed GA-based and the Lagrange-based [145] approaches,  $Q=120$ , static and fading channels  $N = 3$ .

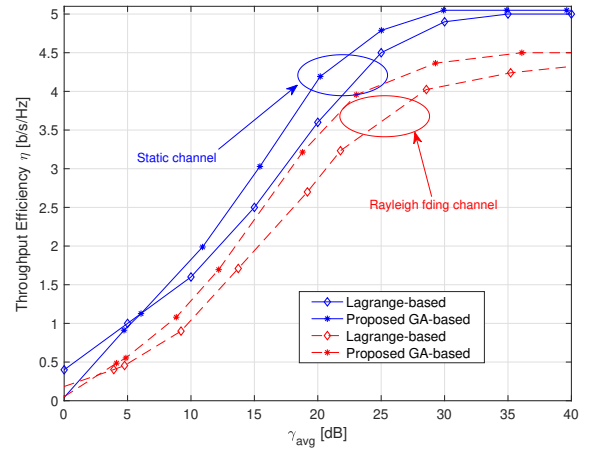


Figure 6.11: Average Throughput Efficiency for PC-AMC-HARQ type I of the proposed GA-based and the Lagrange-based [146] approaches,  $Q=120$ , static and fading channels,  $N = 3$ .

In both the proposed solution and the considered benchmark, we observe that the performance of HARQ is better than those of simple ARQ for low and moderate SNR ( $\gamma_{\text{avg}} < 10\text{dB}$ ) because the standard deviation of the SNR is higher. On the other hand, for higher SNR values ( $\gamma_{\text{avg}} > 10\text{dB}$ ), we note that simple ARQ provides higher throughput efficiency, and the difference compared with HARQ is smaller for fading channel because the average energy  $E_{\text{avg}}$  available to be allocated is high and judiciously partitioned.

To assess the performance of our approach in terms of packet loss, we depict in figure 6.12 the probability of packet erasure as defined in equation (6.11) in the two considered channels.

This adds value to the performance evaluation by giving an idea about the loss in terms of data. It can be seen that as the average SNR value  $\gamma_{avg}$  increases, error-free packet reception becomes higher, and hence the probability that a packet is thrown after  $N$  transmission trials is decreased. The URR operation, for which  $P_{loss} < 10^{-5}$ , starts from SNR values of 7dB and 13dB in static and fading channels, respectively.

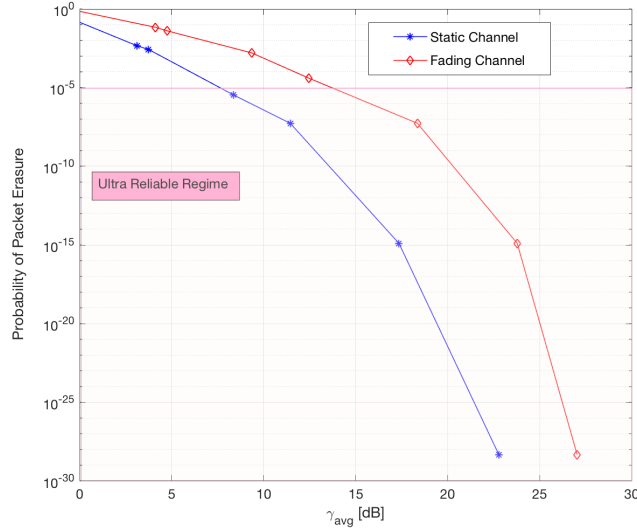


Figure 6.12: Probability of packer erasure for PC-AMC-HARQ type I of the proposed GA-based approach,  $Q=120$ , static and fading channels,  $N = 3$ .

Figure 6.13 presents an optimal distribution of the available energy budget among all allowed transmission attempts determined using the proposed GA-based optimization algorithm. The figure depicts three scenario corresponding to a) low average SNR ( $\gamma_{avg} = 0$ ), b) medium average SNR ( $\gamma_{avg} = 10$ ), and c) high average SNR ( $\gamma_{avg} = 20$ ). At low SNR, we note that most of the energy budget is allocated to the first transmission. This will increase the probability to succeed packet transmission from the first transmission as the energy budget to allocate to subsequent transmissions is limited. Usually, if the first attempt is unsuccessful, although it has been allocated the greatest portion of the energy budget, it is undoubtedly not necessary to go through other attempts with lower energy levels.

In figure 6.13.b) it is shown that for medium SNR values, the algorithm equally distributes the available energy budget throughout the three transmission attempts. Then in c), when having a high SNR, an optimal solution can provide a decent energy portion during the first transmission attempt without sacrificing the upcoming potential re-transmission attempts. In

the case of unsuccessful transmission, more energy is allocated in the next attempt while keeping the increase in total average energy cost moderate as re-transmissions probability is very unlikely. Overall, for a medium energy budget, the optimization results in an intermediate behavior between energy, which decreases per additional transmission attempt for low SNR, and energy increase per additional attempt for high SNR as re-transmissions are more and more unlikely.

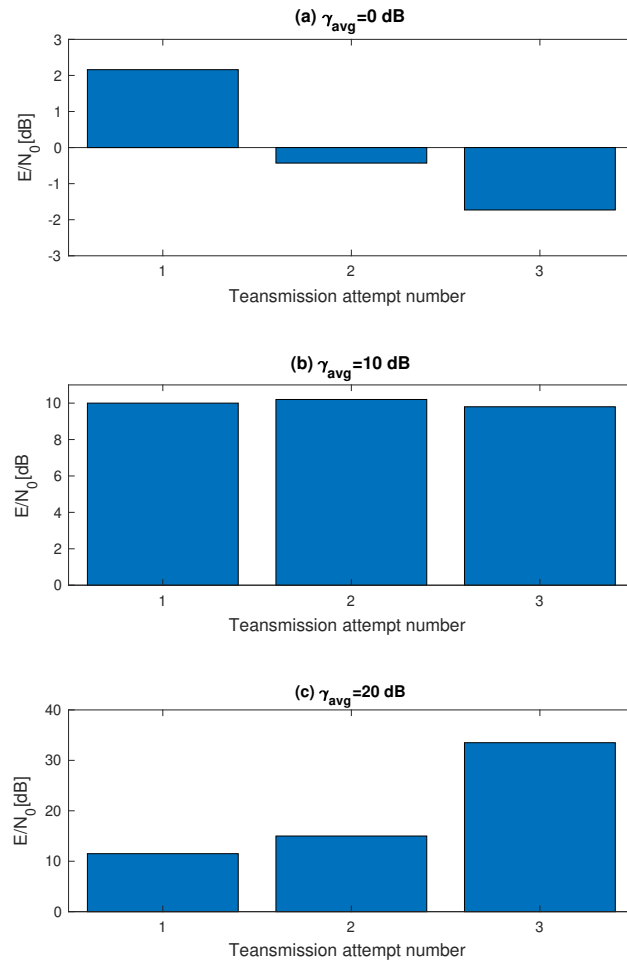


Figure 6.13: Examples of optimized energy budget allocation throughout (re)transmission attempts for different energy average in static channel.

## 6.7 Conclusion

In this chapter, we proposed a cross-layer algorithm to enhance the performance of the truncated ARQ/HARQ protocols. In particular, we investigated throughput maximization through an optimum combination of power control and adaptive modulation and coding under energy constraints. Initially, we studied the optimization through PC for BPSK modulation only. Then, we extended the study to cover both PC and AMC by involving more parameters in the optimization problem.

Unlike conventional truncated ARQ, where the energy budget is divided into equivalent partitions throughout all the transmission attempts, in our algorithm the total energy budget is wisely distributed among potential re-transmission attempts with different partitions. Furthermore, a specifically selected modulation order and code rate are used for each packet. These parameters are judiciously chosen to maximize the throughput efficiency and ensure reliability through genetic algorithm based processing. We presented numerical results in terms of throughput efficiency and the probability of packet loss. Our solution revealed a significant throughput improvement, especially for medium SNR, compared to the considered benchmark that used the Lagrange multipliers optimization for both ARQ and HARQ type I. We also considered the case of static channel and fading channel to cover a more realistic scenario assuming partial CSI knowledge, where only the SNR value is known.

## Chapter 7

# Resource Allocation in Energy Harvesting WBAN for E-Health Systems

### 7.1 Introduction

In e-Health platforms, the energy supply for sensor nodes is one of the major hurdles to offer sustainable services. In addition to harvesting energy from the environment, sophisticated processing and transmission techniques are required. To maximize the uninterrupted network lifetime, we here use dynamic time resource allocation based on the energy budget of each sensor node. We present two centralized solutions based on heuristic and game-theory strategies.

The first solution models the energy harvesting process at each sensor as a discrete-time Markov chain, and evaluate the net energy, defined as the gap between the consumed and harvested energies at each time slot. By minimizing this gap, a source node will maintain a sufficient energy level for a longer time after each packet transmission to the central node. The optimization problem is therefore formulated to minimize the total net energy of all connected nodes through packet transmission scheduling, subject to the requirement of energy availability. We then develop a heuristic algorithm to solve the optimization problem in a central manner based on the energy levels received at the Central Node (CN) [43].

A first price game theory Sealed-Bid Auction-Based (FPSBA) is also proposed to solve the same problem, yet contrarily to the first solution, it uses the frame structure of the IEEE 805.15.4 standard. The game model comprises a set of players, presented by the sensor nodes, which can act to either transmit data or harvest energy. The FPSBA is modeled by one auctioneer, which represents the CN and the set of players that compete for time slices. Only the players with the minimum required energy level are allowed to bid during an auction. Among them, the auctioneer chooses the bidder with the maximum instantaneous energy for data packet transmission [44].

## 7.2 Related Works

The purpose of a health monitoring system is to provide cost-effective health services to anyone, anywhere, and at any time. At the end user side, low-power, high reliability, and energy efficiency are important aspects in health monitoring systems to ensure service sustainability [167, 174], and prevention and early detection of diseases [170], [171]. In [173], the authors studied steady-rate optimization to minimize the source rate fluctuation with respect to the average sustainable rate, to provide uninterrupted service. Later, in [179], the authors proposed the optimization of time slot allocation to minimize the packet loss due to energy run-out. The two works used the Markov chain for modeling the energy harvesting process and used an analytical resolution in [173] and a heuristic algorithm in [179]. The work in [169] presented an optimal packet scheduling problem in a single-user energy harvesting wireless communication scenario. The work adaptively changes the transmission rate according to the traffic load and available energy, such that the time by which all packets are delivered is minimized.

Game theory has been also used in communication protocol for a better payoff, for example throughput, latency, energy, etc. In [180] the authors survey the use of game theory to solve the problems of energy efficiency, security, and pursuit-evasion games in sensor networks. For example, a well-known equilibrium concept is the Nash equilibrium. A player will receive an optimal or fair payoff given other players' strategies if the equilibrium point is reached. The authors of [181] demonstrated the applications of game-theoretic models to study the radio resource allocation issues in the context of D2D communication and proved how game models can provide distributed solutions to the resource allocation problems. Further, the work in [182] investigates the suitability of using online auctions to allow sensors to acquire preferential

access to network resources. A framework is presented that allocates network priority to sensor devices based on their characteristics such as cost, precision, location, significant changes to readings, and amount of data collected. These characteristics are combined to form the value for a particular sensor's bid in an auction. The sensor with the highest bid wins preferential access to the network. Priority can be dynamically updated over time with regard to these characteristics, changing conditions for the phenomenon under observation, and also with input from a back-end environmental model.

### 7.3 Network Lifetime Maximization using Heuristic Algorithm

To ensure a sustainable service, we here use a heuristic algorithm, which is designed to solve a problem in a faster and more efficient fashion than traditional methods by sacrificing optimality, accuracy, precision, or completeness for speed [43].

#### 7.3.1 System Model

As shown in figure 7.1, we consider a WBSN with a star topology composed of one Central Node (CN) or Hub node and  $N$  sensors indexed by  $n \in \{1, 2, \dots, N\}$ . All sensor nodes transmit their data packets periodically to the CN, which will forward the assembled data to the back-end health care system. This work is predominantly focused on the former part that concerns the energy harvesting based WBSN.

The WBSN exploits Time Division Multiple Access (TDMA) in the same frequency channel, which allows all sensors to transmit at different time slots and avoid collision within each frame [175]. In the considered model, the time resource is organized in a superframe composed of  $N_f$  frames. During one frame, a sensor node is allowed to occupy only one time slot to send its packet, while it harvests energy during the other  $N - 1$  time slots of the frame [43].

We assume that the CN has sufficient energy, while each sensor node is equipped with a rechargeable battery and an associated energy harvesting device. The process of energy harvesting at a sensor node  $n$  can be modeled in a discrete time manner using a Markov chain presented by  $\{S_n, Q_n\}$ , where  $S_n$  is the set of states of the Markov chain and  $Q_n$  is the transition probability matrix of the Markov chain [20]. We use  $s_{n,t} \{s_{n,t} \in \{1..S_n\}\}$  to denote

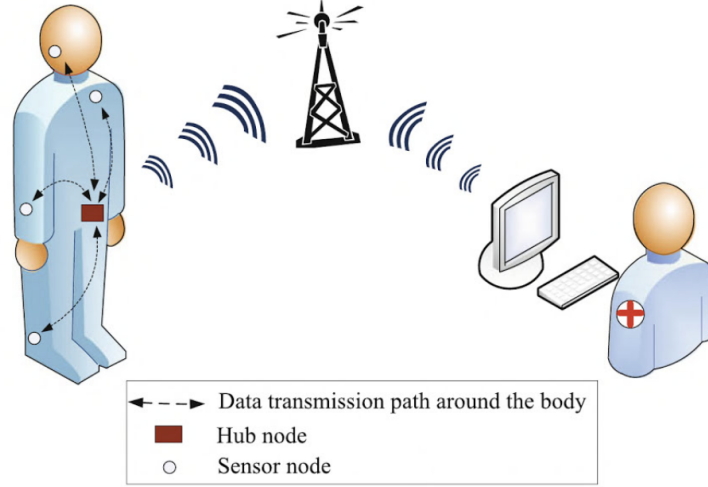


Figure 7.1: Body Sensor Network in pervasive health monitoring system [177]

the state of sensor  $n$  at the time slot  $t$ , during which the node  $n$  is harvesting energy at a constant recharging rate  $\beta_n^{(s_n,t)}$ . The states in  $S_n$  are organized in such an ascending order that  $\beta_n^{(1)} \leq \beta_n^{(2)} \dots \leq \beta_n^{(|S_n|)}$  where  $|S_n|$  is the number of the states in  $S_n$ . Furthermore, the sensor  $n$  transfers from the state  $s_{n,t}$  to the state  $s_{n,(t+1)}$  with the probability  $Q_{n(s_{n,t},s_{n,t+1})}$  in the next frame.

We denote the initial energy at the battery of each sensor node by  $E_n^{\text{init}}(0)$  and the instantaneous energy at time slot  $t$  by  $E_n^{\text{inst}}(t)$ , which is obtained as

$$E_n^{\text{inst}}(t) = E_n^{\text{init}}(0) + \sum_{i=1}^{t-1} E_n^H(i) - \sum_{i=1}^{t-1} E_n^C(i), \quad (7.1)$$

where the first summation term stands for all the energy, the sensor  $n$  harvests using energy harvesting device before transmission block  $t$  denoted as  $E_n^H$ , and the second summation term stands for all the energy consumed by the sensor  $n$ , before time slot  $t$ . At the time slot  $t$ ,  $E_n^C(t)$ , is defined as the energy amount composed from the sensing energy  $E_n^{\text{sens}}(t)$  and the transmission energy  $E_n^{\text{trans}}(t)$ . The sensing energy is proportional to the source rate  $r_n$  at sensor  $n$ . The transmission energy also depends on the source rate and on the path loss model of the wireless channel in body sensor networks, and it represents the largest portion of the energy consumed by a sensor node. The path loss in a WBSN can be modeled as [186]

$$PL(d_n) = PL(d_0) + 10m_p \log_{10}(d_n/d_0) + X_\sigma, \quad \forall n \in N, \quad (7.2)$$

where  $d_n$  stands for the distance between sensor  $n$  and the CN,  $PL(d_0)$  is the reference path loss at distance  $d_0$ ,  $m_p$  is the path loss exponent [172], and  $X_\sigma$  is a zero-mean Gaussian random variable. The total energy consumption at sensor node  $n$  is then given by

$$E_n^C(t) = E_n^{\text{sens}}(t) + E_n^{\text{trans}}(t) = \psi_n r_n + (\theta_n + \eta_n d_n^{m_p}) r_n, \quad (7.3)$$

where  $\psi_n$  stands for the sensing energy per bit,  $\theta_n$  is the energy cost of transmitting electronics of sensor  $n$ , and  $\eta_n$  is a coefficient term corresponding to the energy cost of transmit amplifier at node  $n$ . The source rate considered in this work is modeled respecting the analysis in [173] such to assign a fixed rate to each sensor depending on the type of gathered informations.

### 7.3.2 Problem Statement

The purpose of this work is to find the optimized scheduling for sensor nodes that maximizes the network lifetime and hence ensure service sustainability. The network lifetime is here defined as the duration of time before the earliest node depletes its battery and therefore, the duration of time before the first node in the network becomes unavailable due to its energy replenishment [166].

In order to maximize the network lifetime, a sufficient energy level has to be maintained at all sensor nodes, through the whole superframe. The idea of our work is to select nodes having the lowest gap between the consumed energy and the harvested energy to transmit their data packets first. This will help nodes with a high gap to reduce the difference between consumed and harvested energies during one superframe and hence increase their chances to transmit data at each frame to ensure service sustainability.

Let us introduce the net energy  $E_n^{\text{net}(t)}$  as the energy resulting from the difference between the energy consumed  $E_n^C(t)$  and energy harvested  $E_n^H(t)$  expressed as

$$E_n^{\text{net}}(t) = E_n^C(t) - E_n^H(t). \quad (7.4)$$

Note that reducing the net energy of nodes within each frame avoids the nodes from running out of energy and augments their lifetime. Maximizing network lifetime is then achieved by minimizing the sum of net energies at all sensor nodes. Therefore, the optimization problem

can be formulated as below

$$\min_v E_{\text{tot}}^{\text{net}}(t) = \sum_{n=1}^N E_n^C(t) - E_n^H(t) \quad (7.5)$$

S. T.

$$E_n^{\text{res}}(t-1) \geq E_n^C(t), \quad (7.6)$$

$$E_n^{\text{res}}(t) = E_n^{\text{inst}}(t) - E_n^W(t), \quad (7.7)$$

$$\sum_{i=1}^N v(i, j) = 1, \quad \forall j \in [1, \dots, N_f], \quad (7.8)$$

where  $v$  is the optimization variable, which we define by a bitmapping matrix of sensor nodes in rows and time slots in columns.

To avoid congestion and guarantee that only one sensor node occupies a time slot, the sum of each column must be equal to 1. This condition is expressed in the constraint (7.8) of the optimization problem. The energy values introduced  $E_n^{\text{res}}(t)$  and  $E_n^W(t)$  stand for the battery residual energy level at time slot  $t$  and the value of energy wasted due to battery overflow, respectively. The constraint (7.6) is set to ensure that the residual energy of sensor  $n$  at time slot  $t$  is greater than the energy to be consumed for data packet transmission. If this constraint is not satisfied, the data packet transmission of sensor  $n$  will be delayed so that the sensor node  $n$  harvests energy during time slot  $t$  and attempts to transmit during the next time slot.

### 7.3.3 Time Slot Allocation Algorithm

In this section, we present the heuristic algorithm proposed to find the optimal solution for maximizing network lifetime in the considered WBSN model. The proposed solution is referred to as Net-E approach. The main idea is to find the optimal scheduling of sensor nodes during each frame while minimizing the total net energy in order to avoid energy run out. This problem can be treated as separate sub-problems for each node apart to minimize the net energy at each sensor node.

At the beginning, all sensors have the same energy level. Based on the evaluation of net energy  $E_n^{\text{net}}$ , the CN will select the sensor node that will transmit first. While the selected sensor node is transmitting during time slot  $t$ , the other nodes, whose net energy is higher than the selected one, gather energy and hence reduce the gap between consumed energy and harvested energy for the current frame.

---

**Algorithm 1** Minimization of the net energy
 

---

```

1: input  $E^{\text{init}}, N, N_f, d, m_p, \theta, \delta, \psi, \eta, \mathbf{r}, \beta$ 
2: initialization  $E^{\text{res}} = E^{\text{init}}, E^{\text{inst}} = E^{\text{init}}$ ,
3: output  $v$ 
4: for  $frame = 1$  to  $N_f$  do
5:    $S\_Tab \leftarrow []$  /*table of nodes scheduled within the
   frame*/
6:   for  $timeslot = 1$  to  $N$  do
7:      $Used\_slot \leftarrow \text{false}$ 
8:      $Ev\_Tab \leftarrow []$  /*table of nodes whose energies are
   evaluated for possible transmission*/
9:     calculate  $E_n^C, E_n^H, E_n^{\text{net}}, \forall n \in N$ 
10:     $node \leftarrow \text{argmin}_n(E_n^{\text{net}}), \forall n \in N$ 
11:    while ( $Used\_slot = \text{false}$ ) && ( $node \notin S\_Tab$ )
    && ( $\text{length}(Ev\_Tab) < N$ ) do
12:      if  $E_{node}^{\text{res}}(timeslot) \geq E_{node}^C(timeslot)$  then
13:         $Used\_slot \leftarrow \text{true}$ 
14:        concatenate ( $S\_Tab, node$ )
15:        update  $E_{node}^{\text{res}}(timeslot)$ 
16:        update  $E_n^{\text{inst}}(timeslot), \forall n \notin Ev\_Tab$ 
17:      else
18:        update  $E_{node}^{\text{inst}}(timeslot)$ 
19:        concatenate ( $Ev\_Tab, node$ )
20:         $node \leftarrow \text{argmin}_n(E_n^{\text{net}}), \forall n \notin Ev\_Tab$ 
21:      end if
22:    end while
23:    update node states for all  $n \in N$  respecting the
    Markov chain
24:  end for
25: end for

```

---

We state our algorithm for the general scenario in Algorithm 1. As each sensor node is allowed to transmit one packet per frame, the proposed algorithm starts by computing the net energies of the  $N$  sensor nodes at the start of each frame among the  $N_f$  frames. The node with minimum net energy is selected for possible transmission. Then, the consumed energy  $E_n^C(t)$  is compared to the residual energy in the battery of the selected node. If the residual energy  $E_n^{\text{res}}(t-1)$  is higher than the required energy, the selected node is scheduled at time slot  $t$  and

the energy level is updated for all  $N$  nodes.

Otherwise, the node with minimum net energy among the  $N - 1$  remaining nodes will be selected as a candidate to occupy the time slot  $t$ . This processing is repeated among all nodes until a node satisfies the selection criteria (minimum net energy among all nodes and sufficient residual energy). If at a time slot  $t$  within a specific frame, none of the  $N$  nodes has sufficient energy, the channel will not be used during that time slot and all nodes will devote the time slot to harvest energy. At the end of the frame, the nodes with insufficient residual energy level will incur packet loss.

### 7.3.4 Performance Evaluation

In this section, we present simulation results to evaluate the performance of the proposed algorithm in terms of the probability of packet loss due to energy run. Simulations are carried out using MATLAB and are averaged over  $10^5$  trials [44]. We also evaluate the uninterrupted lifetime of each sensor and present a comparison of network lifetime with the work in [173] and present the residual energy level  $E_n^{\text{res}}(t)$ .

#### 7.3.4.1 Simulation Parameters

We deploy a five-sensors WBSN in health monitoring applications with typical sensors for body temperature, pulse oxygen, blood pressure, ECG, and EEG. Sensor nodes are located at distances uniformly distributed between 0.3 and 0.7m to the CN [186] and generates data at different source rates  $r_n, n \in \{1, \dots, N\}$  selected as determined in [173]. The initial energy of each sensor node is set to 0.1J, while the maximum battery capacity is 0.11J and the minimum energy required for each sensor node is 0.01J. In the considered WBSN, we assume that typical energy harvesting devices are vibration-based energy harvesters, which generate the power using human body motions during activities of daily living. Hence, we assume all sensor nodes are equipped with the same vibration-based energy harvesting device and model the processing by a two-state Markov chain, where the first state represents a non-actively recharging state and the second state represents an actively recharging state [20]. The transition probability from state 1 to state 2,  $Q_{n(1,2)}$ , is uniformly distributed between 0.6 and 0.8, and the transition probability from state 2 to state 1,  $Q_{n(2,1)}$ , is uniformly distributed between 0.2 and 0.4. In order to simulate the variations of transmission power consumption caused by the variations

Table 7.1: Uninterrupted lifetime

sensor	1,2,3 and 4	5
Steady rate	$\infty$	3395 s
Irregular rate	$\infty$	3075 s

of the distance and the direction, we change the transmission power consumption model at sensor  $n$  to  $E_n^{\text{trans}}(t) = \Omega E_n^{\text{trans}}(t)$ , where  $\omega$  is a Gaussian random variable with a variance of  $\sigma_\Omega^2 = 0.01$  and a mean of  $\mu_\Omega = 1$ .

As vibration-based energy harvesters generally remain at the same state for a time interval between 1 and 10s, we fix the time slot length to 5s. During a time slot, the energy recharging rate  $\beta$ , the distance, and the direction from a sensor node to the CN remain unchanged.

#### 7.3.4.2 Performance Evaluation

To assess the impact of source rate on the uninterrupted lifetime, we present the maximum uninterrupted lifetime of the proposed algorithm and compare it to the benchmark [173] in table 7.1 and table 7.4 respectively. We recall that the uninterrupted lifetime of a sensor is the duration from the start time of the sensor functioning to the time when its energy level reaches a value below the minimum energy required for it, which is set to 0.01 J in our network and 0 J in [173].

Table 7.1 depicts the maximum uninterrupted lifetime of all sensors for the considered network in the cases of steady and changing source rates. Each sensor  $n$  generates data with an irregular source rate higher than the steady source rate. We note that all sensors, except sensor 5, have an infinite lifetime respecting the considered scenarios for steady and changing source rates. However, the energy level of the battery of sensor 5, which generates a higher rate compared to the other sensors, reduces less than the threshold required to transmit. This leads to mean lifetime values equal to 3395 s and 3075 s for steady and irregular rates, respectively.

Table 7.2 presents the trade-off between the source rate  $r$  and the lifetime of one sensor node and shows the comparison of the proposed algorithm with the considered benchmark [173]. The table shows that, for the same parameters, the uninterrupted lifetime evaluated for sensor 3 is reduced as the source rate is increased for the considered benchmark, while it shows sustainability in the proposed algorithm. Indeed, when the source rate of sensor 3 is below 1574

bps, the uninterrupted lifetime has an infinity value for both algorithms. Beyond this rate value, the sensor runs out of energy at 13228 s in the algorithm of the considered benchmark [171]. In the proposed algorithm, the lifetime remains uninterrupted which ensures sustainability. Further assessment was carried out for sensor 3 using the highest rate in table 7.4 (1695 bps) for  $10^8$  seconds and has also shown an uninterrupted lifetime.

Table 7.2: Relationship between the source rate and the lifetime (in second) of one sensor

Source rate [bps]	847	1090	1332	1453	1574	1695
Benchmark [173]	$\infty$	$\infty$	$\infty$	$\infty$	13228	6614
Proposed NET-E	$\infty$	$\infty$	$\infty$	$\infty$	$\infty$	$\infty$

To examine the instantaneous residual energy, we set  $N_f = 100$  frames as a superframe length. We then present the variations of energy level at the batteries of sensors in Figures 7.9 and 7.3 for one realization and when averaged over  $10^5$  iterations, respectively. Consistently with the lifetime assessment, we note that the energy level at the battery of sensor 5, with the highest rate, decreases continuously, which explains the lifetime interruption presented in table 7.1 for this sensor.

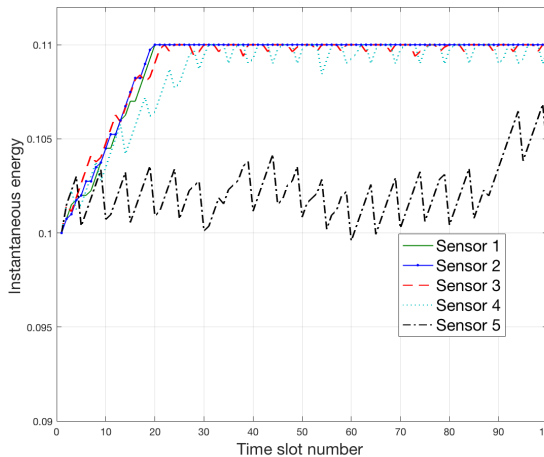


Figure 7.2: Instantaneous residual energy variations during 100 frames of 5 time slots each.

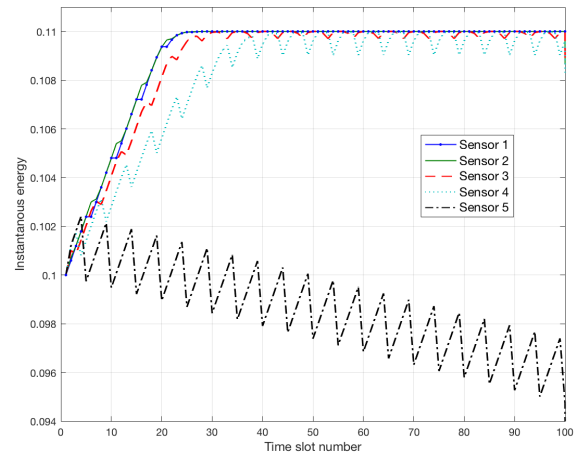


Figure 7.3: Averaged instantaneous residual energy level variations during 100 frames of 5 time slots each.

Ident that, if the net energy ( $E^{\text{net}}$ ) is positive, during one frame, the residual energy level at the battery is decreased as the consumed energy is higher than the harvested one. Otherwise, the residual energy level is increased as the consumed energy is smaller than the

harvested one. The variation of the energy level is bound by the maximum battery capacity 0.11 J, which may lead to energy waste if the battery energy level reaches its maximum while the node is harvesting energy. As shown in Figure 7.3, sensors 1,2,3, and 4 are overflowed, while sensor 5 whose rate is much higher leading to higher energy consumption does not exceed the maximum energy level.

Figure 7.4 presents the packet loss probability due to energy run out in the case of steady and irregular data rates for a superframe of length  $N_f = 200$  frames. It is worth noting that no packet loss is recorded until the frames of numbers 144 and 148 for the steady and irregular rates, respectively. At these frames, the packet loss probability has a value equal to  $2.10^{-6}$  and it increases in time as the energy level decreases to values below the amount of energy required to transmit a packet. The loss probability rises continuously to reach  $2.10^{-3}$  for irregular rate and  $3.10^{-4}$  for a steady rate and stagnates at these values. The loss probability is averaged over all sensors to show the whole network performance. However, only sensor 5 experiences the packet loss effect due to energy run out as shown in Table 7.1.

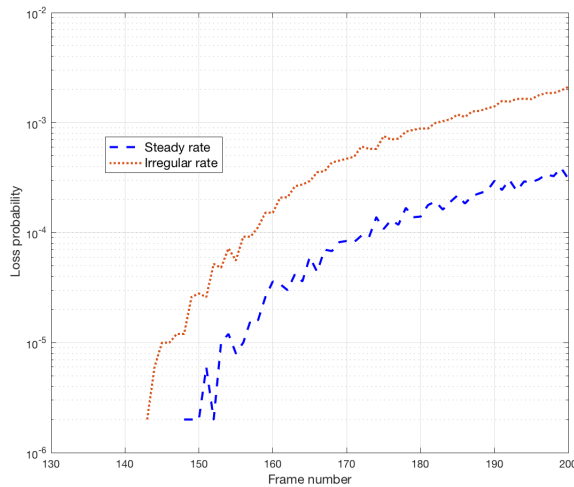


Figure 7.4: Probability of packet loss due to energy run out.

## 7.4 Network Lifetime Maximization using Game Theory

Game theory is a mathematical method to study the interactions between several decision-makers who have conflicts or common interest. A game theory model is carried out for better optimization when a group of players are involved in a game to select either cooperate or not

cooperative means to obtain better result with some specific strategy among the players [44].

In this section, we use the auction-based technique for energy harvesting in WBAN. Particularly, we exploit an auction-based algorithm to maximize network lifetime. Through First Price Sealed Bid Auction, the nodes entrust themselves to the central node to allocate the slices in an adequate way according to game rules. These rules will limit the packet loss as the results will be shown and the overlap of sending between the nodes and guarantee the maximum sufficient energy harvest possible to maintain a sustainable energy level.

### 7.4.1 System Model

Similarly to the first solution, we consider a WBAN with a star topology composed of CN and  $N$  sensors indexed by  $n \in \{1, 2, \dots, N\}$ . All sensor nodes transmit their data packets periodically to the CN, which will forward the collected data to the medical center. We assume that each sensor node  $n$  is equipped with a rechargeable battery and an associated energy harvesting device to replenish energy from the ambient environment. We opt for the same energy harvesting modeling as in section 7.3.1, while we adapt the herein presented solution to the standardized frame of the IEEE 802.15.4 network.

The IEEE 802.15.4 is the standard designed to support low data-rate and low energy applications in WBAN. IEEE 802.15.4 specifies Medium Access Control (MAC), Physical Layer, non-beacon-enabled mode, and beacon-enabled mode. In non-beacon-enabled mode, MAC is based Carrier Sense Multiple Access / Collision Avoidance (CSMA/CA). In beacon-enabled mode, the Central Node (CN) transmits beacons periodically to synchronize with sensor nodes. Since the beacon-enabled mode transmits well-timed data packets, we adopt this model in this work. The superframe of IEEE 802.15.4 is divided into an active period and an inactive period as shown in fig. 7.5. Each superframe is between two beacons generated by the CN. The superframe is divided into equal 16 slices [183]. During the active period, the sensor nodes request the CN for slices to transmit their data packets. In the inactive period, the sensor nodes harvest energy [44]. In the considered model, the time resource is organized in a superframe  $F$  divided into  $N_f$  slices, each has a duration of  $T$ . During one superframe, specifically on the active period, the CN allows a sensor node  $n$  to allocate  $S$  slices for its data packet transmission, while it harvests during the other  $N_f - S$  slices of the superframe.

In table 7.3, we depict an example of time resource allocation throughout the whole super-

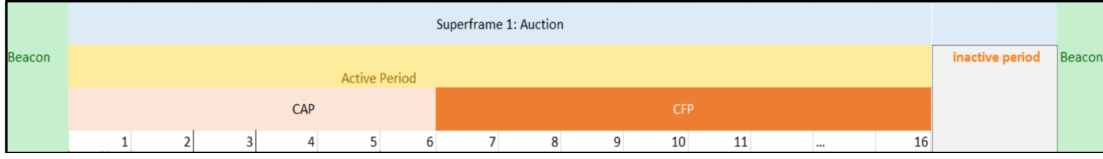


Figure 7.5: Frame structure of WBAN based on the standard IEEE 805.15.4.

frame for a WBAN composed of 4 sensors. To guarantee that each slice  $\tau$  is allocated by only one sensor node  $n$  and avoid congestion, the sum of each column is equal to 1. We denote  $\tau_n = S_n\tau$  as the time allocated for the  $n^{\text{th}}$  sensor that spans  $S_n$  slices.

Table 7.3: Example of time slot allocation.

Time slice	$\tau$	$2\tau$	$3\tau_3$	...	$N_f$
Sensor 1	0	0	1	...	0
Sensor 2	1	0	0	...	0
Sensor 3	0	0	0	...	1
Sensor 4	0	1	0	..	0
Column Sum	1	1	1	...	1

## 7.4.2 First Price Sealed-Bid Auction Modeling

In Health care systems, the major goal is to provide sustainable service for all patients via network lifetime maximization to continuously transmit all data packets to the medical center. The network lifetime is here defined as the duration until the energy level of the first sensor node becomes insufficient for packet transmission.

### 7.4.2.1 Game Model

A game model comprises a set of players, and an auction-based game theory model is represented by a set of players, a set of actions available for each player, a utility function corresponding to each combination of actions, and probability distributions associated with the types [187]. Generally, the players are the buyer(s) and the seller(s). The FPSBA is modeled by one Auctioneer, which represents the CN and  $N$  sensor nodes that are bidding for the same resource at the same slot  $\tau$  as illustrated in figure 7.6. Its principal idea is to allow the resource owner (i.e CN) to choose the bidder (i.e sensor node  $n$ ) with maximum instantaneous energy  $E_n^{\text{inst}}$  at a specific time of bidding and enter the auction for data packets transmission.



Figure 7.6: First price sealed-bid auction mechanism.

#### 7.4.2.2 Parameters Definition

The goal for sensor nodes is to reach the optimal allocation during each superframe. The bidders follow a non-dominant strategy and their valuations are random variables. Bidders are drawn from the continuous uniform distribution. Let us first recall some definitions and related structures associated with an FPSBA based game theory:

- *Players* : In our model, we assign a sensor node  $n$  as a *bidder* and CN as an *auctioneer* which owns the resource units (i.e slice  $\tau$ ) as shown in figure 7.6. We define  $N$  as a finite set of bidders,  $n = \{1, 2, \dots, N\}$ .
- *Strategy*: The set of *Actions* available for each bidder  $n$  (i.e sensor's state). It determines the activities of each sensor node during the auction. Each bidder  $n$  has two possible actions (transmission state  $T$  or harvesting state  $H$  as shown fig 7.7) at each auction. If it is in state H, it collects the energy to attain a sufficient energy level. Otherwise, in the T state, it will transfer the data packets to the medical center.

	1	2	3	4	5	6	...	$N_f$
Transmission	0	0	0	1	0	0	...	1
Harvesting	1	1	1	0	1	0	...	0

 Figure 7.7: Strategy matrix for one sensor during all  $N_f$  slices.

The actions number will be equal to  $2^{N_f}$ . We use  $s_{n,\tau}\{s_{n,\tau} \in \{1..S_n\}\}$  to denote the state of a bidder  $n$  at the slice  $\tau$ , which represents all the combination of  $H$  and  $T$  states for the  $N_f$  slices where  $S_n = 2^{N_f}$ . The bidder  $n$  is harvesting energy at a constant recharging rate  $\beta_n^{(s_{n,\tau})}$ . We define  $P_n$  as the state transition probability matrix of the sensor  $n$ . Based on the values on  $P_n$ , the bidder moves from the state  $s_{n,\tau}$  at the instant  $\tau$  to the state  $s_{n,(\tau+1)}$  at the slice  $\tau + 1$  with the probability  $P_{n(s_{n,\tau},s_{n,\tau+1})}$ . During each

time slot, one bidder  $n$  will win and be in the transmission state, while the other bidders will be in the harvesting state as shown in figure 7.8 for an example of two players and different transitions between the two possible states. Therefore, the equilibrium consists of choosing the best strategy depending on a given utility.

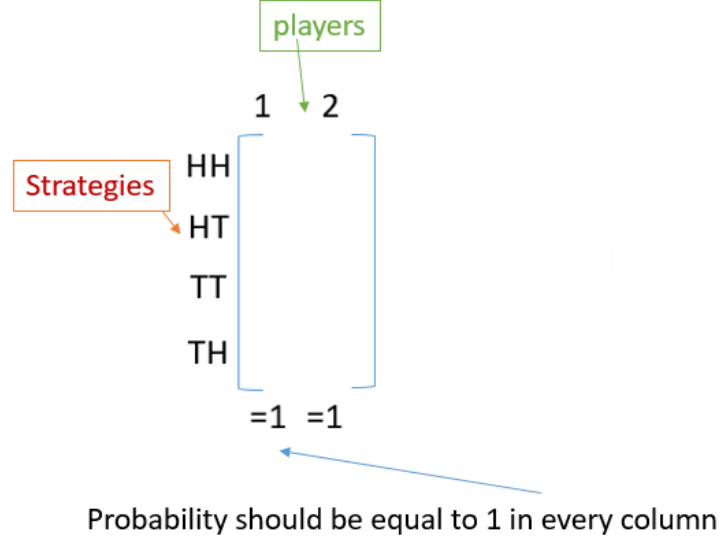


Figure 7.8: Example of the Matrix utility.

- *Utility* : The aim is to maximize the utility function  $U_n(s, \tau) = E_n^{\text{inst}}(\tau)$  defined in equation (7.7) to assist the CN to choose the sensor node with maximum instantaneous energy  $E_n^{\text{inst}}$ . The utility is then expressed as:

$$\begin{cases} U_n(s, \tau) = E_n^{\text{inst}}(\tau) & \text{if } U_n(s, \tau) \geq E_n^{\text{th}}, \\ U_n(s, \tau) \simeq 0 & \text{otherwise,} \\ \frac{E_m^{\text{res}}(s_n, \tau)}{E_n^{\text{res}}(s_n, \tau)} \simeq 1, & \forall m \in M, n \in N, \end{cases} \quad (7.9)$$

where  $E_n^{\text{th}}$  is the energy threshold that is already set up by the CN to fix the minimum energy level that the bidder must have to enter the auction. The parameter  $M$  stands for the number of of sensor nodes with sufficient energy to enter the auction for the slice bidding procedure. The eligibility criteria require bidders to have a sufficient energy level, i.e.  $\frac{E_m^{\text{res}}(s_n, \tau)}{E_n^{\text{res}}(s_n, \tau)} \simeq 1$  to ensure an energy level fairness within the bidders  $M$  and the rest of sensor nodes  $N$ . The fairness criterion is necessary to ensure a more or less equitable energy level for all the sensors who enter the auction or the others who are in a harvesting state. The sensors with high energy

level will affect the next auctions. This criterion ensures the energy level sufficiency for each bidder and avoid the energy run out.

### 7.4.3 Time Slot Allocation Algorithm

The auctions are held at a first price sealed-bid auction-based game theory. We here present the proposed algorithm, which is presented in Algorithm 1, in detail to describe the auction mechanism that enables a fair resource allocation while maximizing lifetime. In addition to the parameters introduced in section II, we define  $\delta$  as the optimization variable, which we define by a bitmapping matrix of sensor nodes in rows and slices in columns, similar to the one presented in table I [44]. To start the auction, the auctioneer CN announces the threshold  $E_n^{\text{th}}$  for all the bidders to avoid the energy run out of bidders with insufficient energy. Slices will be assigned to the  $N$  bidders with sufficient energy levels. Each bidder  $n$  knows only its own bid's valuation  $E_n^{\text{inst}}$  without the knowledge of other bidders. At the beginning of each auction among the superframe, the bidder  $n$  sends its energy information ( $E_n^{\text{H}}(\tau)$ ,  $E_n^{\text{C}}(\tau)$ ) to the CN for instantaneous energy evaluation. Indeed, if the bidder's residual energy is higher than its consumed energy ( $E_n^{\text{res}}(\tau) > E_n^{\text{C}}(\tau)$ ), and the instantaneous energy is greater than the threshold to insure the energy sufficiency ( $E_n^{\text{inst}} \geq E^{\text{th}}$ ), the bidder  $n$  submits its instantaneous energy  $E_n^{\text{inst}(\tau)}$  for the slice  $\tau$  as a bid. Therefore, the bidder  $n$  is moved to the set  $M$  and enters the auction with the other bidders satisfying the entrance criterion. The auctioneer CN determines for each slice  $\tau$  which bidder  $n$  should transmit first based on its bid valuation. The winner is the bidder  $n$  with maximum  $E_n^{\text{inst}}$ .

Once a bidder  $n$  is allocated the slice  $\tau$ , it transmits its data packets to the medical center in the active period [44]. Otherwise, the CN gives the bidder  $n$  with higher energy consumption  $E_n^{\text{res}}(\tau) < E_n^{\text{C}}(\tau)$  and insufficient energy level the chance to reduce the gap between the consumed and the harvested energy for the next data transmission by harvesting more energy in the inactive period. At the end of each superframe, if a bidder  $n$  with an insufficient energy level did not harvest the sufficient amount of energy, it will incur packet loss.

**Algorithm 2**: First Price Sealed-Bid Auction Resource Allocation

---

```

1: input  $E^{\text{init}}, N, N_f, d, m_p, \theta, \psi, \eta, \mathbf{r}, \beta$ 
2: initialization  $E^{\text{res}}=E^{\text{init}}, E^{\text{inst}}=E^{\text{init}}$ , the value  $E^{\text{th}}$  is the threshold value conditioned by CN for bidder  $n$ 
3: output  $\delta$ 
4: for  $\tau = 1$  to  $N_f$  do
5:    $\delta(\tau) \leftarrow []$ 
6:    $M \leftarrow []$ 
7:    $bidder\_Tab \leftarrow []$  /*table of bidders whose energies are evaluated for possible transmission*/
8:    $Auction\_Tab \leftarrow []$  /*table of bidders scheduled within the superframe during auctions*/
9:   for  $n = 1$  to  $N$  do
10:    calculate  $E_n^C, E_n^H, E_n^{\text{inst}}, E_n^{\text{res}} \quad \forall n \in [1..N]$ 
11:    if  $(E_n^{\text{inst}} \geq E_n^C) \ \&\& \ (E_n^{\text{inst}} \geq E^{\text{th}})$  then
12:      concatenate  $(n, M)$ 
13:       $bidder\_Tab(n) \leftarrow 1$ 
14:      for  $m = 1$  to  $M$  do
15:        calculate  $E_m^C, E_m^H, E_m^{\text{inst}}, E_m^{\text{res}} \quad \forall m \in [1..M]$ 
16:        while  $(\frac{E_m^{\text{res}}}{E_n^{\text{res}}} \simeq 1)$  do
17:           $Auction = \text{argmax}(E_m^{\text{inst}}), \quad \forall m \in [1..M]$ 
18:           $Auctions\_Tab(Auction) \leftarrow 1$ 
19:        end while
20:      end for
21:       $\delta(\tau) \leftarrow Auctions\_Tab$ 
22:    else
23:       $S_{n,\tau} \leftarrow H$ 
24:       $\delta(\tau) \leftarrow 0$ 
25:    end if
26:  end for
27: end for

```

---

#### 7.4.4 Performance Evaluation

In this section, we present simulation results to evaluate the performance of the proposed algorithm in terms of the uninterrupted lifetime of each sensor and present a comparison of network lifetime with the heuristic solution presented in the previous section and [173].

We deploy a five-sensors WBSN in health monitoring applications with typical sensors for body temperature, pulse oxygen, blood pressure, ECG, and EEG. Sensor nodes are located at distances uniformly distributed between 0.3 and 0.7m to the CN [186] and generates data at different source rates  $r$  selected as determined in [173]. The initial energy of each sensor node is set to 0.1 J, while the maximum battery capacity 0.11 J, and the minimum energy required for each sensor node is 0.01 J. We assume that each sensor node is equipped with the same vibration-based energy harvesting device and model the processing by a two-state, where the first state represents a non-actively recharging state and the second state represents an actively recharging state. The transition probability from state 1 to state 2 is uniformly distributed

between 0.6 and 0.8, and the transition probability from state 2 to state 1 is uniformly distributed between 0.2 and 0.4. To simulate the variations of transmission power consumption caused by the variations of the distance and the direction, we change the transmission power consumption model at sensor  $n$  to  $E_n^{\text{trans}}(\tau) = \Omega E_n^{\text{trans}}(\tau)$ , where  $\omega$  is a Gaussian random variable with a variance of  $\sigma_\Omega^2 = 0.01$  and a mean of  $\mu_\Omega = 1$ .

As vibration-based energy harvesters generally remain at the same state for a time interval between 1 and 10 s, we fix the time slot length to 5 s. During a time slot, the energy recharging rate  $\beta$ , the distance, and the direction from a sensor node to the CN remain unchanged.

Table 7.4 presents the trade-off between the source rate  $r$  and the lifetime of a sensor node and shows the comparison of the proposed algorithm with the considered benchmarks. The table shows that, for the same parameters, the uninterrupted lifetime evaluated for sensor 3 is reduced as the source rate is increased for the considered benchmarks, while it shows sustainability in the proposed algorithm. Indeed, when the source rate of sensor 3 is below 1574 bps, the uninterrupted lifetime is of an infinity value for the three algorithms. Beyond this value, the sensor runs out of energy at 13228 s and at 18676 s in [173] and the heuristic solution, respectively. In the proposed algorithm, the lifetime remains uninterrupted which ensures sustainability.

Table 7.4: Relationship between the source rate and the lifetime (in second) of one sensor

Rate [bps]	847	1090	1332	1453	1574	1695	1816
[173]	$\infty$	$\infty$	$\infty$	$\infty$	13228	6614	58
Proposed NET-E	$\infty$	$\infty$	$\infty$	$\infty$	$\infty$	$\infty$	18676
Proposed FPSBA	$\infty$						

To examine the instantaneous residual energy, the mean variations of energy level at the sensors' batteries for a time interval of length  $N_f = 100$  frames is presented in figure 7.9 averaged over  $10^5$  iterations. Consistently with the lifetime assessment, we note that the mean energy level of the sensors in approach [173] decreases continuously, which explain the lifetime interruption presented in table 7.4. The approach we proposed in the first section exhibits a higher mean energy level that decreases slower than that approach in [173], yet it is faster than the proposed auction-based approach. This latter seems to have a constant pattern that always keeps the mean energy level high and hence guarantee service sustainability. The variation of the energy level is bounded by the maximum battery capacity 0.11 J, which may lead to energy

waste if the battery energy level reaches its maximum while the node is harvesting energy.

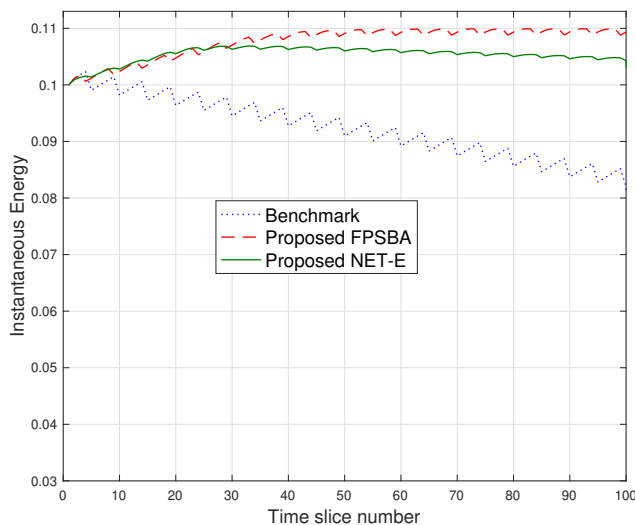


Figure 7.9: Variations of the mean instantaneous energy during 100 time slices.

## 7.5 Conclusion

In this chapter, we investigated network lifetime maximization with energy harvesting for WBAN to provide sustainable health monitoring services. For this purpose, we proposed an optimized time slots allocation schemes that allow to prioritize sensors with specific energy qualification such as to allow sensors with insufficient energy level to harvest more energy during one frame.

In particular, a first solution exploited a heuristic algorithm to allow sensor nodes whose net energy is the lowest among all nodes. The net energy was defined as the difference between the consumed energy and the harvested energy, which decreases in time as the node gathers energy. Hence delaying the transmission of packets belonging to nodes with low net energy would allow these nodes to provide sufficient energy to transmit during each frame. The second proposed solution was based on game theory and it prioritized the sensor nodes having the lowest instantaneous energy among all nodes by First price sealed-bid auction-based. Through simulations, we demonstrated that optimal resource allocation improves the system performances in terms of sustainability.

The performance was presented in terms of uninterrupted lifetime and packet loss probability due to energy run out for the first solution. Compared to the considered benchmark, the two proposed algorithms provided a longer uninterrupted lifetime. On the other hand, the second solution provided a longer lifetime and a higher instantaneous energy level. Also, in the NET-E solution, the longer uninterrupted lifetime was depicted in the packet loss probability of very low values appearing after a relatively long period of operating.

## Chapter 8

# Conclusion and Future Work

### 8.1 Conclusion

Introducing a revolutionary air interface that improves spectral efficiency and delivers mobile communication with massive connections, high reliability, and low latency has intensively driven research efforts on improving existing techniques and developing new ones to fit the requirements of the 5G system. In this context, the contributions presented in the previous chapters tackled sophisticated techniques to enable the deployment of IoT services, mMTC, and URLLC.

Respecting the standardized LTE signal structure defined in Rel. 12, 13, 14, and 15, we investigated synchronization, sector search, and neighbor discovery through theory and simulation. All considered methods respect the standard specifications and do not require any additional resources to achieve the task. The presented synchronization issues concern previously proposed methods, yet new aspects are studied. First, we studied synchronization exploiting the IEEE 802.11n standard, to which the reduced-complexity two-stage approach is applied exploiting the repetitive structure of its preamble. The approach that provided satisfactory performance in generalized OFDM systems, also showed its effectiveness in exploring the potential of MIMO diversity in the IEEE 802.11n standards. Then, the performance evaluation of the simply-differential and doubly-differential approaches was investigated to assess the impact of a frequency offset on synchronization accuracy through both theory and simulation in the LTE network. Further, multiple antenna configuration in the case of standardized EPA

and ETU channel models is assessed and it showed the robustness of the approaches even at very low SNR values. We also investigated the application of the simply-differential approach to MTC to jointly provide time synchronization and sector identifier. The performance evaluated through theoretical correct detection probability derived in its closed form, and compared to the experimental probability showed that, when applied to the LTE signal specified for MTC, the studied approach provided good detection accuracy with a perfect match between simulation and theory.

Neighbor discovery for ProSe and V2X communications underlying cellular networks was investigated by utilizing physical and MAC features of the newly introduced SideLink. A theoretical study of single-round discoveries was presented in terms of discovery probability under a simple cross-correlation and power-normalized-correlation applied on SRS and DMRS sequences, respectively. The obtained results demonstrate that, when applied to the LTE signal, the simulated probability agrees perfectly with the theoretical one, validating the analysis carried out and the approximated closed-form for any functional parameters. Also, the multiple-round discovery was then considered to assess the performance of distributed and network-assisted discovery strategies. In the distributed strategy, users continue to transmit their discovery messages, which results in a high collision rate that delays the completion of the discovery process of all users in the vicinity. In the network-assisted strategy, however, discovered users are notified to cease sending their discovery messages, which leads to enhanced performance. To present a realistic assessment of collision, we opted for a physical model in addition to the typical legacy MAC model. Throughout the performance evaluation, both low and high-mobility channel models were considered to cover both ProSe and vehicular use case applications. Simulation results showed a noticeable improvement in the physical collision model in all the considered scenarios.

Positioning and localization were also studied to improve system performance under Rice channel models. First, we studied the maximization of coverage radius optimized through UAV height based on a) the SNR level of an edge user and on b) the average rate of ground users within a specific range. We showed that there exists a unique optimum height at which the UAV should be located to maximize the deployment area. We also assessed the sensitivity of the optimal position to the surface characteristics. Then, we considered the localization of a stationary UE in a massive MIMO and mm-wave 5G system. A reduced-complexity processing based on distance and AoA measurements was used to estimate the exact UE coordinates. We showed that mm-waves provide better performance at high SNR values while cm-waves

perform better at low SNR values. This behavior is justified by the sensitivity of mm-waves to noise. On the other hand, the studied localization scheme showed robustness to channel estimation errors.

We also proposed energy optimization and MCS selection solution for truncated ARQ/HARQ protocols. The optimization aims to maximize the throughput efficiency by meticulously distributing the prescribed energy budget among all (re)-transmission attempts, while maintaining a fixed total energy-per-packet cost. Furthermore, a specifically selected modulation order and code rate are selected for each packet. These parameters are judiciously chosen to maximize the throughput efficiency and ensure reliability through a genetic algorithm based processing. We also considered the case of static channel and fading channel to cover a more realistic scenario. Our solution revealed a significant throughput improvement for both throughput efficiency and packet erasure probability, especially for low and medium SNRs, relatively to the uniform energy allocation used in the conventional ARQ protocol. Initially, we studied the optimization through PC for BPSK modulation only. Then, we extended the study to cover both PC and AMC by involving more parameters in the optimization problem.

Finally, we investigated network lifetime maximization with energy harvesting for WBAN to provide sustainable health monitoring services. For this purpose, we proposed an optimized time slots allocation that allows to prioritize sensors with specific energy qualification such to allow sensors with insufficient energy level to harvest more energy during one frame. In particular, a first solution exploited a heuristic algorithm to allow sensor nodes whose net energy is the lowest among all nodes. Then, a second solution that gives the priority to the sensor having the lowest instantaneous energy among all nodes by First price sealed-bid auction-based. The overall performance was presented in terms of uninterrupted lifetime and packet loss probability due to energy run out for the first solution. The proposed algorithms provided a longer uninterrupted lifetime, which is depicted in the packet loss probability of very low values appearing after a relatively long period of operating.

## 8.2 Ongoing and Future Works

This manuscript covered several aspects in enabling techniques that hit the design and evaluation of 5G systems performance, yet further investigation would add values to the achieved results.

Almost all the investigations concerning neighbor discovery considered perfect synchronization, so extending the study to the case of unsynchronized neighbors UEs will provide a complete and more realistic insight on the performance of the proposed approaches.

Also, localization was assessed assuming the presence of a LOS path in addition to scattering multipath modeled by Rician channel. Ongoing works consider harsh channel conditions, where only multipath Rayleigh propagation is available. To achieve accurate coordinates' estimation of obstructed UEs, we suggest a process that involves a minimum of two neighboring UEs who are assumed to have sufficiently high received signal power allowing their localization based on the RSSI measurement followed by AoA estimation beamforming processing as in [36]. Two approaches are proposed for neighbor-assisted localization and are presented in [37] and [38]. Furthermore, localization in the context of UAV-assisted network is envisaged as the use of flying platforms is increasing to offer an on-demand connectivity.

Aligned with the previous work in UAV positioning, we propose to study the optimization for a more generalized environment, which respects a probabilistic propagation model that includes rural and urban scenario, each with a specific probability. Then, the navigation trajectory of a flying UAV will be considered for optimization. We envisage considering real cities' maps. These works are planned to be elaborated during a master project and extended to a PhD. Finally, new research tracks have just been started. Particularly, the use of Blockchain for IoT health applications to ensure secured resource allocation, in the context of the ongoing PhD entitled "Resource Allocation for IoT Health Monitoring Applications with Energy Harvesting" [188].

Further ideas in the previously mentioned research topics are either under investigation or planned for the forthcoming period. In particular, social awareness in localization and discovery procedures, Artificial Intelligence (AI) and Machine Learning (ML) in resources allocation, beamforming and positioning. Ultimately, the research findings will be disseminated through a variety of scientific publications in renowned journals/conferences.

Longer-term research agenda expands my central substantive area to more thoroughly investigate emerging technologies for the 6G system, including AI/ML for communications, unmanned platforms, network automation, and autonomous electric vehicles. In keeping with my past and current research experiences, I intend to initiate further collaborations and to develop proposals for securing grants and funds from the transdisciplinary research efforts.

# Bibliography

- [1] Cisco, “Cisco Annual Internet Report (2018-2023) White Paper”, Mar. 2020.
- [2] R. Ratasuk, N. Mangalvedhe, and A. Ghosh, “Overview of LTE Enhancements for Cellular IoT”, *IEEE PIMRC*, pp. 2293-2297, Sep. 2015.
- [3] J. Gozalvez, “New 3GPP Standard for IoT”, *IEEE vehicular technology magazine*, vol. 11, pp. 14-20, Mar. 2016.
- [4] A. Asadi, Q. Wang, and V. Mancuso, “A survey on device-to-device communication in cellular networks”, *IEEE Communications Surveys and Tutorials*, vol. 16, n. 4, pp. 1801-1819, Apr. 2014.
- [5] 3GPP, TR 22.803 ver.12.2.0, “Feasibility Study for Proximity Services (ProSe)”, Jun. 2013.
- [6] G. Baldini, S. Karanasios, D. Allen, and F. Vergari, “Survey of wireless communication technologies for public safety”, *IEEE Communications Surveys Tutorials*, vol. 16, no. 2, pp. 619-641, 2014.
- [7] R. Chavez-Santiago, M. Szydelko, A. Kliks, F. Foukalas, Y. Haddad, K. E. Nolan, M. Y. Kelly, M. T. Masonta, and I. Balasingham, “5G: The Convergence of Wireless Communications”, *Wireless Personal Commun.*, vol 83, pp. 1617-1642, Mar. 2015.
- [8] J. Rodriguez, *Fundamentals of 5G Mobile Networks*, John Wiley & Sons, Ltd., 2015.
- [9] P. Popovski, *et al.*, “Deliverable d6.3 intermediate system evaluation results”, ICT-317669-METIS/D6.3, Aug. 2014.
- [10] G. Durisi, T. Koch, and P. Popovski, “Toward massive, ultra reliable, and low-latency wireless communication with short packets”, in *Proc. IEEE*, vol. 104, no. 9, pp. 1711-1726, Sep. 2016.

- [11] K. P. Valavanis and G. J. Vachtsevanos, *Handbook of unmanned aerial vehicles*, Springer Publishing Company, Incorporated, 2014.
- [12] R. Austin, *Unmanned aircraft systems: UAVS design, development and deployment*, John Wiley & Sons, vol. 54, 2011.
- [13] A. Puri, "A survey of unmanned aerial vehicles (UAV) for traffic surveillance", *Department of computer science and engineering*, University of South Florida, 2005.
- [14] M. Mozaffari, W. Saad, M. Bennis, and M. Debbah, "Unmanned aerial vehicle with underlaid device-to-device communications: Performance and tradeoffs", *IEEE Transactions on Wireless Communications*, vol. 15, no. 6, pp. 3949-3963, Jun. 2016.
- [15] M. Mozaffari, W. Saad, M. Bennis, Y.-H. Nam, and M. Debbah, "A Tutorial on UAVs for Wireless Networks: Applications, Challenges, and Open Problems", *IEEE Communications Surveys and Tutorials*, arXiv:1803.00680v2, Mar. 2019.
- [16] S.B. Wicker, *Error Control Systems for Digital Communication and Storage*, Prentice Hall, 1995.
- [17] 3GPP, *5G; Study on New Radio (NR) access technology*, TR 38.912 (Rel. 14), ESTI, Sophia Antipolis, France, May 2017.
- [18] L. Nasraoui, L. Najjar Atallah, and M. Siala, "A Very Efficient Time and Frequency Synchronization Method for OFDM Systems Operating in AWGN Channels," in *Proc. ComNet*, pp. 1-5, Nov. 2010.
- [19] L. Nasraoui, L. Najjar Atallah, and M. Siala, "An Efficient Synchronization Method for OFDM Systems in Multipath Channels," in *Proc. ICECS*, pp. 1152-1155, Dec. 2010.
- [20] A. Seyedi and B. Sikdar, "Modeling and analysis of energy harvesting nodes in body sensor networks," in *Proc. Inter. Summer School and Symposium on Medical Devices and Biosensors*, pp.175-178, Aug. 2008.
- [21] L. Nasraoui, *Advanced Synchronization Techniques for OFDM Systems*, Thesis dissertation, University of Carthage, Apr. 2015.
- [22] L. Nasraoui, L. Najjar Atallah, and M. Siala, "An Efficient Reduced-Complexity Two-Stage Differential Sliding Correlation Approach for OFDM Synchronization in the AWGN Channel", in *Proc. IEEE VTC-Fall*, pp. 1-5, Sept. 2011.

- [23] L. Nasraoui, L. Najjar Atallah, and M. Siala, "Analytical Performance Evaluation of an Efficient Reduced-Complexity Time Synchronization Approach for OFDM Systems", in *Proc. IEEE VTC-Fall*, pp. 1-5, Sept. 2012.
- [24] L. Nasraoui, L. Najjar, and M. Siala, "An Efficient Reduced-Complexity Two-Stage Differential Sliding Correlation Approach for OFDM Synchronization in the Multipath Channel", in *Proc. IEEE WCNC*, pp. 2059-2063, Apr. 2012.
- [25] L. Nasraoui, L. Najjar, and M. Siala, "Robust Synchronization Approach for MIMO-OFDM Systems with Space-Time Diversity", in *Proc. IEEE VTC-Spring*, pp. 1-5, May 2015.
- [26] L. Nasraoui, L. Najjar, M. Siala, "Robust doubly-differential primary synchronization approach for 3GPP LTE systems", in *Proc. International Wireless Communications and Mobile Computing Conference (IWCMC)*, pp. 1069-1074, Aug. 2014.
- [27] L. Nasraoui, L. Najjar, and M. Siala, "A Simply-Differential Low-Complexity Primary Synchronization Scheme for 3GPP LTE Systems", in *Proc. EUSIPCO*, pp. 411-415, Sep. 2014.
- [28] L. Nasraoui, L. Najjar, and M. Siala, "Synchronization technique for MIMO-OFDM WLAN systems with space time diversity", in *Proc. International Wireless Communications and Mobile Computing Conference*, pp. 250-255, Aug. 2015.
- [29] L. Nasraoui, L. Najjar, and M. Siala, "Reduced-Complexity synchronization technique for MIMO-OFDM WLAN systems", in *Proc. International Conference on Communications and Networking (COMNET)*, pp. 1-5, Nov. 2015.
- [30] L. Nasraoui, L. Najjar, and M. Siala, "Reduced-complexity simply/doubly differential primary synchronization for LTE systems", *Transactions on Emerging Telecommunications Technologies*, vol. 83, no. 8., Feb. 2017.
- [31] L. Nasraoui and L. Najjar, "SRS-Based D2D Neighbor Discovery Scheme for LTE Cellular Networks", in *Proc. IEEE Inter. Sym. on Personal, Indoor and Mob. Rad. Comm. (PIMRC)*, pp. 1-5, Oct. 2017.
- [32] L. Nasraoui and S. Ikki, "Robust D2D Neighbor Discovery through SideLink Demodulation Reference Signal for LTE Network", in *Proc. IEEE Inter. Sym. on Personal, Indoor and Mob. Rad. Comm. (PIMRC)*, pp. 1-5, Sep. 2019.

- [33] L. Nasraoui and S. Ikki, "Neighbor Discovery for ProSe and V2X Communications", *IEEE Internet of Thing Journal*, Nov. 2020.
- [34] L. Nasraoui, "On the Probability of Discovery for Proximity Services and Vehicular Communications", *IEEE Sensors Letters*, vol.5, n. 12, pp. 1-4.
- [35] L. Nasraoui, "Partial Contention-Free D2D Discovery for Proximity-Based Services in Cellular Networks", in *Proc. Inter. Conf. on Smart Comm. in Net. Tech. (SaCoNeT)*, pp. 177-182, Oct. 2018.
- [36] A. Sellami, L. Nasraoui, and L. Najjar, "Multi-Stage Localization for Massive MIMO 5G Systems," *IEEE Vehicular Technology Conference (VTC2020-Spring)*, pp. 1-6, Jun. 2020.
- [37] A. Sellami, L. Nasraoui, and L. Najjar, "Neighbor-Assisted Localization for Massive MIMO 5G Systems," *International Multi-Conference on Systems, Signals & Devices (SSD)*, pp. 1-6, Mar. 2021.
- [38] A. Sellami, L. Nasraoui, and L. Najjar, "Outdoor Neighbor-Assisted Localization Algorithm for Massive MIMO Systems," *IEEE Vehicular Technology Conference (VTC2021-Fall)*, pp. 1-5, Sep. 2021.
- [39] L. Nasraoui and S. Roy, "Optimal uav positioning for terrestrial users," *IEEE Vehicular Technology Conference (VTC2020-Spring)*, pp. 1-6, Jun. 2020.
- [40] A. Sellami, L. Nasraoui, and L. Najjar, "Analysis of Localization Performance in Mm-Wave 5G Network under Channel Uncertainties", Early access, in *IEEE Internet of Things Journal*, 2022, doi:10.1109/JIOT.2022.3218370.
- [41] L. Nasraoui, L. Najjar, and M. Siala, "Throughput Maximization with Optimum Energy Allocation for ARQ re-transmission Protocol", in *Proc. International Conference on Communications and Networking (ComNet)*, pp. 1-5, Nov. 2018.
- [42] A. Dabbar, L. Nasraoui, and M. Siala, "Energy and MCS Optimization in HARQ Protocol for Ultra-Reliable Regime with Maximized Throughput", *IEEE Systems Journals*, in press.
- [43] N. Badri, L. Nasraoui, L. Azouz Saidane, and S. Ikki, "Maximizing Lifetime in Energy-Harvesting WBSN for Health Monitoring Systems Through Dynamic Slots Allocation", in *Proc. International Wireless Communications and Mobile Computing Conference (IWCMC)*, pp. 325-329, Jun. 2019.

- [44] N. Badri, L. Nasraoui, L. Azouz Saidane, and N. Brinis, "Auction-based Time Resource Allocation for Energy Harvesting WBAN", in *Proc. International Wireless Communications and Mobile Computing Conference (IWCMC)*, pp. 764-769, Jun. 2020.
- [45] L. Nasraoui, A. Cabani, and H. Trimech, "Implementing Lightweight Key Exchange Solutions for WSN with LoRa Connectivity", *International Journal of Sensor Networks (IJS-NET)*, vol. 39, n. 3, pp. 192-204, Jan. 2022.
- [46] E. Dahlman, S. Parkvall, and J. Skold, *4G LTE/LTE-Advanced for Mobile Broadband*, Academic Press, 2011.
- [47] R. Prasad, *OFDM for wireless communications systems*, Artech House, 2004.
- [48] R. D. Murch and K. B. Letaief, "Antenna Systems for Broadband Wireless Access", *IEEE Commun. Magazine*, vol. 40, no. 4, pp. 76-83, Apr. 2002.
- [49] W. Zhang, X.-G. Xia, and K. B. Letaief, "Space-Time/Frequency Coding for MIMO-OFDM in Next Generation Broadband Wireless Systems", *IEEE Wireless Commun.*, vol. 14, no. 3, pp. 32-43, Jun. 2007.
- [50] V. Tarokh, H. Jafarkhani, and A. R. Calderbank, "Space-Time Block Codes from Orthogonal Designs", *IEEE Trans. Inform. Theory*, vol. 45, no. 5, pp. 1456-1467, Jul. 1999.
- [51] L. Nasraoui, L. Najjar Atallah, and M. Siala, "Encoding Sequence Design for a Reduced Complexity Time Synchronization Technique for OFDM Systems", in *Proc. IEEE ICECS*, pp. 913-916, Dec. 2012.
- [52] V. Tarokh and H. Jafarkhani, "A differential detection scheme for transmit diversity", *IEEE J. Select. Areas Commun.*, vol. 18, no. 7, pp. 1169-1174, Jul. 2000.
- [53] S. M. Alamouti, "A Simple Transmit Diversity Technique for Wireless Communications", *IEEE J. Select. Areas Commun.*, vol. 16, no. 8, pp. 1451-1458, Oct. 1998.
- [54] S. N. Diggavi, N. Al-Dhahir, A. Stamoulis, A. R. Calderbank, "Differential Space-Time Coding for Frequency-Selective Channels", *IEEE Commun. Letters*, vol. 6, no. 6, pp. 253-255, Jun. 2002.
- [55] T. Aoki and D. Takeda, "Backward compatibility of CDD preambles, IEEE 802.11-05/0006r0", Jan. 2005.

- [56] L. Nasraoui, L. Najjar Atallah, and M. Siala, "Performance Study of a Reduced Complexity Time Synchronization Approach for OFDM Systems," in *Proc. ComNet*, pp. 1-5, March 2012.
- [57] L. Nasraoui, L. Najjar Atallah, and M. Siala, "Performance Evaluation of an Efficient Reduced Complexity Time Synchronization Approach for OFDM Systems", *Annals of Telecommunications*, vol. 69, pp 321-330, May 2013.
- [58] J. V. Beek, M. Sandell, and P. Börjesson, "ML Estimation of Timing and Frequency Offset in OFDM Systems", *IEEE Trans. Signal Processing*, vol. 45, pp. 1800-1805, Jul. 1997.
- [59] W. L. Chin and S. G. Chen, "A Blind Synchronizer for OFDM Systems Based on SINR Maximization in Multipath Fading Channels", *IEEE Trans. Veh. Technol.*, vol. 58, pp. 625-635, Feb. 2009.
- [60] Y. El Hajj Shehadeh, S. Bamgartner, and G. Hirtz, "A Robust Blind Time Synchronization Method in OFDM Systems over Multipath Fading Channels", in *Proc. European Wireless Conference*, pp. 16, May 2015.
- [61] T.M. Schmidl and D. Cox, "Robust frequency and timing synchronization in OFDM", *IEEE Trans. on Comm.*, vol. 45, pp. 1613-1621, Dec. 1997.
- [62] P.K. Singya and A.S. Gandhi, "A data-aided timing offset estimator for OFDM synchronization", in *Proc. IEEE SPICES*, pp. 1-5, Feb. 2015.
- [63] A. N. Mody and G. L. Stüber, "Synchronization for MIMO OFDM systems", in *Proc. IEEE Globecom*, vol. 1, pp. 509-513, Nov. 2001.
- [64] D. Wang and J. Zhang, "Timing Synchronization for MIMO-OFDM WLAN systems", in *Proc. IEEE WCNC*, pp. 1178-1182, Mar. 2007.
- [65] A. Ali, W. Mahmood, I. Javed and I. Ur Rehman, "IEEE802.11n Time Synchronization for MIMO OFDM WLAN", in *International Journal of Computer and Communication Engineering*, vol. 2, no. 5, pp. 576-579, Sep.. 2013.
- [66] Y. Tsai and G. Zhang, "Time and Frequency Synchronization for 3GPP LTE Long Term Evolution Systems", in *Proc. IEEE VTC-Spring*, pp.1727-1731, Apr. 2007.
- [67] Tsai Y, Zhang G, Grieco D, Ozluturk F. Cell Search in 3GPP Long Term Evolution Systems. *IEEE Vehicular Technology Magazine* 2007; **2**(2): 23-27.

- [68] L. Nasraoui, L. Najjar Atallah, and M. Siala, "Robust Brute Force and Reduced Complexity Approaches for Timing Synchronization in IEEE 802.11a/g WLANs", in *Proc IWCMC*, pp. 1365-1369, July 2013.
- [69] Elsherif AR, Khairy MM. Adaptive Primary Synchronization Signal Detection for 3GPP Long Term Evolution. In *International Wireless Communications & Mobile Computing Conference*, pp. 1716-1721, Jul. 2013.
- [70] Manolakis K, Estevez D, Jungnickel V, Xu W, Drewes C. A Closed Concept for Synchronization and Cell Search in 3GPP LTE Systems. In *IEEE Wireless Communications and Networking Conference*, pp. 1-6, Apr. 2009.
- [71] Xu W, Manolakis K. Robust Synchronization for 3GPP LTE Systems. In *IEEE Global Telecommunications Conference*, pp. 1-5, Dec. 2010.
- [72] IEEE 802.11n D9.0: *Wireless LAN medium access control (MAC) and physical layer (PHY) specifications: Further Higher Data Rate Extension in the 2.4 GHz Band*, Mar. 2003.
- [73] G. J. Foschini, "Layered Space-Time Architecture for Wireless Communication in a Fading Environment When Using Multi-Element Antennas", *Bell Labs Tech. J.*, vol. 1, no. 2, pp. 41-59, 1996.
- [74] S. Wittneben, "A new bandwidth efficient transmit antenna modulation diversity scheme for linear digital modulation", in *Proc. IEEE Int. Conf. on Communications*, pp. 1630-1634, May 1993.
- [75] IEEE standard 802.11a: *Wireless LAN medium access control (MAC) and physical layer (PHY) specifications: high-speed physical layer in the 5 GHz band*, Dec. 1999.
- [76] IEEE Std 802.11n: *Wireless LAN Medium Access Control (MAC) and Physical Layer (PHY) Specifications, Amendment 5: Enhancement for Higher Throughput*, Oct. 2009.
- [77] IEEE P802.11 Wireless LANs Std., *TGn Channel Models*, IEEE 802.11-03/940r4, May 2004.
- [78] D. Astély, E. Dahlman, A. Furuskär, Y. Jading, M. Lindstrom, and S. Parkvall, "LTE: The Evolution of Mobile Broadband", *IEEE Commun. Magazine*, vol. 47, no. 4, pp. 44-51, Apr. 2009.
- [79] 3 GPP (TS 36.211 V8.7.0), *Physical Channels and Modulation*, May 2009.

- [80] G. Fodor, E. Dahlman, G. Mildh, S. Parkvall, N. Reider, G. Miklós, and Z. Turányi, “Design Aspects of Network Assisted Device-to-Device Communications”, *IEEE Communications Magazine*, vol. 50, n. 3, pp. 170-177, Mar. 2012.
- [81] 3GPP TR 23.887: “Study on Machine-Type Communications (MTC) and Other Mobile Data Applications Communications Enhancements”, Dec. 2013.
- [82] 3GPP TS 36.213: “Evolved Universal Terrestrial Radio Access (E-UTRA); Physical layer procedures”, Mar. 2015.
- [83] D. C. Chu, “Polyphase Codes with Good Periodic Correlation Properties”, *IEEE Trans. on Inf. Theory*, vol. IT-18, pp. 531-532, Jul. 1972.
- [84] D. V. Sarwate, “Bounds on crosscorrelation and autocorrelation of sequences”, *IEEE Trans. on Inf. Theory*, vol. IT-25, pp. 720-724, Nov. 1979.
- [85] R. E. Walpole, R. H. Myers, S. L. Myers, and K. Ye, *Probability and Statistics for Engineers and Scientists*, 8<sup>th</sup> Ed., Pearson Prentice Hall, 2007.
- [86] 3<sup>rd</sup> Generation Partnership Project TR 25.913 V9.0.0. Requirements for Evolved UTRA (E-UTRA) and Evolved UTRAN (E-UTRAN), Dec. 2009.
- [87] Perez A. 2015. *LTE and LTE Advanced*, John Wiley & Sons.
- [88] Sorensen T, Mogensen P, Frederiksen F. Extension of the ITU Channel Models for Wideband (OFDM) Systems. In *IEEE Vehicular Technology Conference-Fall*, Sep. 2005; **1**: 392-396.
- [89] 3<sup>rd</sup> Generation Partnership Project TS 36.101. User Equipment (UE) Radio Transmission and Reception, Jul. 2010.
- [90] 3<sup>rd</sup> Generation Partnership Project TS 36.104. Base Station (BS) Radio Transmission and Reception, Jul. 2010.
- [91] J. Lin, W. Yu, N. Zhang, X. Yang, H. Zhang, and W. Zhao, “A survey on Internet of Things: Architecture, enabling technologies, security and privacy, and applications”, *IEEE Internet of Things J.*, vol. 4, no. 5, pp. 1125-1142, Oct. 2017.
- [92] L. Davoli, L. Belli, A. Cilfone, and G. Ferrari, “From Micro to Macro IoT: Challenges and Solutions in the Integration of IEEE 802.15.4/802.11 and Sub-GHz Technologies”, *IEEE Internet of Things J.*, vol. 5, no. 2, pp. 784-793, Apr. 2018.

- [93] S. Gezici, "A survey on wireless position estimation", *Wireless Personal Communications*, vol. 44, no. 3, pp. 263-282, Oct. 2007.
- [94] D. Tsolkas, N. Passas, and L. Merakos, "Device discovery in LTE networks: A radio access perspective", *Computer Networks Journal*, vol. 106, pp. 245-259, Sep. 2016.
- [95] X. Wu, S. Tavildar, S. Shakkottai, T. Richardson, J. Li, R. Laroia, and A. Jovicic, "Flash-LinQ: A Synchronous Distributed Scheduler for Peer-to-Peer Ad Hoc Networks", *IEEE 48th Annual Allerton Conf. on Commun., Control, and Computing*, Sep. 2010.
- [96] F. Baccelli, N. Khude, R. Laroia, Li Junyi, T. Richardson, S. Shakkottai, S. Tavildar, and W. Xinzhou, "On the design of device-to-device autonomous discovery", in *Proc. COM-SNETS*, pp. 1-9, Jan. 2012.
- [97] M. Wang and C. Jiang, "Discovery Signal Design and Its Application to Peer-to-Peer Communications in OFDMA Cellular Networks", *IEEE Trans. on Wireless Commun.*, pp. 3995-4009, Jul. 2013.
- [98] W. Lee, J. Kim, and S.W. Choi, "New D2D Peer Discovery Scheme based on Spatial Correlation of Wireless Channel", *IEEE Trans. on Veh. Tech.*, vol. 65, pp. 10120-10125, Feb. 2016.
- [99] K.W. Choi and Z. Han, "Device-to-Device Discovery for Proximity-Based Service in LTE-Advanced System", *IEEE Journal on Selected Areas in Commun.*, vol. 33, pp. 55-66, Jan. 2015.
- [100] K. Doppler, C. B. Ribeiro, and J. Knecht, "Advances in D2D communications: Energy efficient service and device discovery radio", in *Proc. Wireless VITAE*, Feb. 2011.
- [101] K. W. Choi and Z. Han "Device-to-Device Discovery for Proximity-Based Service in LTE-Advanced System", *EEE Journal on Seleted Areas in Commun.*, vol. 33, pp. 55-66, Jan. 2015.
- [102] H. Tang, Z. Ding, and B.C. Levy, "Enabling D2D Communications Through Neighbor Discovery in LTE Cellular Networks", *IEEE Trans. on Signal Processing*, vol. 62, pp. 5157-5170, Oct. 2014.
- [103] H. Tang, Z. Ding, and B.C. Levy, "D2D Neighbor Discovery and Resource Scheduling Through Demodulation Reference Signal", *IEEE VTC-Fall*, pp. 1-6, Sep. 2016.

- [104] D. Camara and N Nikaein, *Wireless Public Safety Networks 1*, Ed. 1, Elsevier, Nov. 2015.
- [105] J. Schlien and A. Roessler, *Device to Device Communication in LTE*, White paper, Rohde & Schwarz.
- [106] 3GPP TS 36.101 V14.0.0, “Evolved Universal Terrestrial Radio Access (E-UTRA); User Equipment (UE) Radio Transmission and Reception”, Jul. 2016.
- [107] G. H. Golub and C. F. Van Loan, *Matrix Computations*, Ed. 3, The Johns Hopkins University Press, 1996.
- [108] 3GPP, “LTE; Service requirements for V2X services”, TS22.185 V14.3.0, Mar. 2017.
- [109] 3GPP, “Study on enhancement of 3GPP Support for 5G V2X Services”, TR22.886 V15.1.0, Mar. 2017.
- [110] 3GPP, “Evolved Universal Terrestrial Radio Access (E-UTRA); User Equipment (UE) Radio Transmission and Reception”, TS 36.101 V12.5.0 Rel. 12, Nov. 2014.
- [111] 3GPP, “Evolved Universal Terrestrial Radio Access (E-UTRA); User Equipment (UE) radio transmission and reception”, TS 36.101 V14.3.0 Rel. 14, Apr. 2017.
- [112] 3GPP, “Evolved Universal Terrestrial Radio Access (E-UTRA): Physical layer procedures”, TS 36.312 V15.4.0 Rel. 15, Jan. 2019.
- [113] G. Xiong, D. Chatterjee, and H. Niu, “Demodulation reference signal (DMRS) sequence design for device-to-device (D2D) discovery”, US Patent 20150326362A1, Oct. 2015.
- [114] W. Zeng, X. Chen, A. Russell, S. Vasudevan, B. Wang, and W. Wei, “Neighbor Discovery in Wireless Networks with Multipacket Reception”, *IEEE Trans. on Parallel and Distributed Sys.*, vol. 26, no. 7, pp. 1984-1998, Jul. 2015.
- [115] Z. Gao, C. Zhang, Z. Wang, “Robust Preamble Design for Synchronization, Signaling Transmission and Channel Estimation”, *IEEE Trans. on Broadcasting*, vol. 61, no. 1, pp. 98-104, Mar. 2015.
- [116] T. Rappaport, *Wireless Communications: Principles and Practice*, Englewood Cliffs, NJ: Prentice-Hall, 1996.
- [117] F. Frishman, “On the Arithmetic Means and Variances of Products and Ratios of Random Variables”, *Nat. Tech. Inf. Ser.*, pp. 331-345, 1971.

- [118] J. Wang and R. Rouil, “BLER performance evaluation of LTE device- to-device communications”, NISTIR8157, US Department of Commerce, Nov. 2016.
- [119] T. Blazek, M. Ashury, C. F. Mecklenbrauker, D. Smely, and G. Ghiaasi, “Vehicular Channel Models: A System Level Performance Analysis of Tapped Delay Line Models”, in *Proc. Inter. Conf. on ITS Telecomm. (ITST)*, pp. 1-8, May 2017.
- [120] A. Hourani, S. Kandeepan, and A. Jamalipour, “Modeling air-to-ground path loss for low altitude platforms in urban environments”, in *Proc. IEEE Global Telecommunications Conference (GLOBECOM)*, pp. 2898-2904, Dec. 2014.
- [121] Y. Zeng, R. Zhang, and T. J. Lim, “Wireless communications with unmanned aerial vehicles: opportunities and challenges”, *IEEE Communications Magazine*, vol. 54, no. 5, pp. 36-42, May 2016.
- [122] M. Mozaffari, W. Saad, M. Bennis, Y.-H. Nam, and M. Debbah, “A Tutorial on UAVs for Wireless Networks: Applications, Challenges, and Open Problems”, *Information Theory*, Cornell University Library, 2018.
- [123] A. Al-Hourani, S. Kandeepan and A. Jamalipour, “Modeling Air-to-Ground Path Loss for Low Altitude Platforms in Urban Environments”, in *Proc. GLOBECOM Symposium on Selected Areas in Communications: GC14 SAC Satellite & Space Communication*, pp. 2898-2904, Dec. 2014.
- [124] P. Landosz, H. Oh and W-H. Chen, “Optimal positioning of communication relay unmanned aerial vehicles in urban environments”, in *Proc. Internat. Conf. on Unmanned Aircraft Systems*, pp. 1140-1147, Jun. 2016.
- [125] M. Alzenad, A. El-Keyi, F. Lagum and H. Yanikomeroğlu, “3-D placement of an Unmanned Aerial Vehicle Base Station (UAV-BS) for Energy-Efficient Maximal Coverage”, *IEEE Wireless Commun. Letters*, vol. 6, no. 4, pp. 434-437, Aug. 2017.
- [126] A. Al-Hourani, S. Kandeepan and S. Lardener, “Optimal LAP Altitude for Maximum Coverage”, *IEEE Wireless Comm. Letters*, vol. 3, no.6, pp. 569-572, Dec. 2014.
- [127] M.M. Azari, F. Rosas, K-C. Chen and S. Pollin, “Ultra Reliable UAV Communication Using Altitude and Cooperation Diversity”, *IEEE Trans. on Comm.*, vol. 33, no. 1, pp. 330-344, Jan. 2018.

- [128] M.M. Azari, F. Rosas, K-C. Chen and S. Pollin, "Optimal UAV Positioning for Terrestrial-Aerial Communication in Presence of Fading", in *Proc. IEEE GLOBECOM*, pp.1-7, Dec. 2016.
- [129] A. Cernigliaro, S. Valloreia, L. Galleani, and P. Tavella, "GNSS space clocks: Performance analysis", in *Proc. International Conference on Localization and GNSS (ICL-GNSS)*, pp.1-5, Jun. 2013.
- [130] B. Chitambira, S. Armour, S. Wales, and M. Beach, "Direct Localisation using Ray-tracing and Least-Squares Support Vector Machines", in *Proc. International Conference on Localization and GNSS (ICL-GNSS)*, no. 4, Jun. 2018.
- [131] H. Du, C. Zhang, Q. Ye, W. Xu, P. L. Kibenge, and K. Yao, "A hybrid outdoor localization scheme with high-position accuracy and low-power consumption", *EURASIP Journal on Wireless Communication and Networking*, no. 4, Jan. 2018.
- [132] N. Garcia, H. Wymeersch, E. G. Larsson, A. M. Haimovich, and M. Coulon, "Direct localization for massive MIMO", *IEEE Transactions on Signal Process*, vol. 65, no. 10, pp. 2475-2487, May 2017.
- [133] E. Rastorgueva-Foi, M. Costa, M. Koivisto, K. Leppanen, and M. Valkama, "User positioning in mmW 5G networks using beam RSRP measurements and Kalman filtering", in *Proc. International Conference on Information Fusion*, pp. 1-7, Jul. 2018.
- [134] M. K. Simon and M-S. Alouini, *Digital communication over fading channels*. John Wiley & Sons, 2000.
- [135] A. Spizzichino and P. Beckmann, *Scattering of electromagnetic waves from rough surfaces*, Inter. series of monographs on Electromagnetic Waves, The MacMillan Company, 1963.
- [136] P. ZHANG, J. Lu, Y. Wang, and Q. Wang, "Cooperative localization in 5G networks: A survey", *ICT Express*, vol. 3, no. 1, pp. 27-32, Mar. 2017.
- [137] S. M.R., S. Dama, and K. Kuchi, ",A complete cell search and synchronization in LTE, *EURASIP J. Wirel. Commun. Netw.*, 101 (2017), May 2017.
- [138] M. Malekzadeh and A. A. Abdul Ghani, "3-Sector Cell vs. Omnicell: Cell Sectorization Impact on the Performance of Side-by-Side Unlicensed LTE and 802.11ac Air Interfaces," in *IEEE Access*, vol. 7, pp. 122315-122329, Sep. 2019.

- [139] L. Nasraoui, L. Najjar, and M. Siala, "Performance Analysis of Low-Complexity Simply-Differential Time Synchronization Approach for MTC over LTE Systems", in *Proc. IEEE Veh. Tech. Conf. (VTC-Fall)*, pp. 1-5, sep. 2016.
- [140] B. Yang, Z. Yu, J. LAN, R. Zhang, J. Zhou, and W. Hong, "Digital beamforming-based massive MIMO transceiver for 5G millimeter-wave communications", *IEEE Transactions on Microwave Theory and Techniques*, vol. 66, no 7, pp. 3403-3418, May 2018.
- [141] P. Wu and N. Jindal, "Performance of hybrid-ARQ in block-fading channels: A fixed outage probability analysis", *IEEE Trans. Commun.* vol. 58, no. 4, pp. 1129",1141, Apr. 2010.
- [142] N. Arulselvan and R. Berry, "Efficient energy allocations in wireless ARQ protocols", *Inter. Symp. on Wireless Personal Multimedia Commun.* vol. 3, pp. 976-980, Nov. 2002.
- [143] J.-W. Cho, Y. Chang, Y. Kim, and J. Chon, "WLC10-2: Analytic optimization of hybrid ARQ performance in wireless packet data systems", in *Proc. IEEE GLOBECOM*,pp. 1-6, Nov. 2006.
- [144] X. Lagrange, "Performance analysis of HARQ protocols with link adaptation on fading channels", *Annals of Telecommunication*, no. 66, 695",705, Mar. 2011.
- [145] A. Selmi, M. Siala, and H. Boujemaa, "Optimum joint Adaptive Modulation and Coding and Power Control for packet transmission over fading channels using the ARQ protocol," in *Information Science, Signal Processing and their Applications*, pp. 573-577, Jul. 2012.
- [146] A. Selmi, M. Siala, and H. Boujemaa, "Efficient combination of hybrid ARQ with Adaptive Modulation and Coding and Power Control operating in tracking mode", in *Proc. IEEE International Symposium on Personal, Indoor, and Mobile Radio Communications (PIMRC)*, pp. 1507-1512, Sep. 2013.
- [147] F. Rosas, R. D. Souza, M. E. Pellenz, C. Oberli, G. Brante, M. Verhelst, and S. Pollin, "Optimizing the Code Rate of Energy-Constrained Wireless Communications With HARQ", *IEEE Trans. on Wireless Commun.* vol. 15, no. 1, pp. 191-205, Jan. 2016.
- [148] I. Ezz-azi, M. Arioua, A. El Oualkadi, and P. Lorenz, "On the performance of adaptive coding schemes for energy efficient and reliable clustered wireless sensor networks", *Ad Hoc Networks*, vol. 64, pp. 99-111, Jul. 2017.

- [149] E. Dosti, U. L. Wijewardhana, H. Alves, and M. Latva-Aho, "Ultra reliable communication via optimum power allocation for type-I ARQ in finite block-length", in *Proc. IEEE Int. Conf. Commun. (ICC)* pp. 1-6, May 2017.
- [150] E. Dosti, M. Shehab, H. Alves, and M. Latva-Aho, "Ultra reliable communication via CC-HARQ in finite block-length", in *Proc. Eur. Conf. Netw. Commun. (EuCNC)* pp. 1-5, Jun. 2017.
- [151] E. Dosti, M. Shehab, H. Alves, and M. Latva-Aho, "Ultra Reliable Communication via Optimum Power Allocation for HARQ re-transmission Schemes, *IEEE Access*, vol. 8, pp. 89768-89781, May. 2020.
- [152] N. Arulselman and R. Berry, "Efficient power allocations in wireless ARQ protocols", *Inter. Symp. on Wireless Personal Multimedia Commun.*, vol. 3, pp. 976-980, Nov. 2002.
- [153] B. Kaddour, M. Siala, and H. Boujemaa, "Improving the Performance of ARQ Protocols Over AWGN Channels Using an Optimized Energy Allocation", in *Proc. Int. Conf. on Commun. and Networking* pp. 1-6, Nov. 2010.
- [154] J. R. Koza, "Survey of Genetic Algorithms and Genetic Programming", in *Proc. Microelectron. Commun. Tech. Producing Quality Products Mobile Portable Power Emerg. Techn.*, pp. 589-594, Nov. 1995.
- [155] M. Lixia, M. Murrioni, and V. Popescu, "PAPR reduction in Multicarrier Modulations using Genetic Algorithms", in *Proc. OPTIM*, pp. 938-942, May 2010.
- [156] Z. Sihai, L. Yuan, Z. Ming, and Z. Wuyang, "Improved GA solution on LNC coefficient matrix for multi-user cooperative communication", in *Proc. IEEE Inter. Symp. on Personal, Indoor and Mobile Radio Commun.*, pp. 809-814, Sep. 2012.
- [157] L. Nasraoui, L. Najjar, and M. Siala "Genetic Algorithm Based Optimization of Encoding Sequence for a Reduced Complexity OFDM Time Synchronization Technique", in *Proc. IEEE Vehicular Technology Conf. Fall*, pp. 1-5, Sep. 2013.
- [158] S.B. Wicker, *Error Control Systems for Digital Communication and Storage*, Prentice Hall, 1995.
- [159] M. W. El Bahri, H. Boujerna and M. Siala, "Performance comparison of type I, II and III hybrid ARQ schemes over AWGN channels", in *Proc. IEEE International Conference on Industrial Technology (IEEE ICIT)*, vol. 3, pp. 1417-1421, Dec. 2004.

- [160] S. Kallel, "Analysis of a type II hybrid ARQ scheme with code combining," in *IEEE Transactions on Communications*, vol. 38, no. 8, pp. 1133-1137, Aug. 1990.
- [161] E. Malkamaki, H. Leib, "Performance of truncated type-II hybrid ARQ schemes with noisy feedback over block fading channels", *IEEE Trans. on Commun.*, vol. 48, no. 9, pp. 1477-1487, Sep. 2000.
- [162] S. Kallel, "Analysis of a type II hybrid ARQ schemes with code combining", *IEEE Trans. on Commun.*, vol. 38, pp. 1133-1137, Aug. 1990.
- [163] M. Abramowitz, and I.A. Stegun, *Handbook of Mathematical Functions*, Dover, New York, 1965.
- [164] F. Mansourkiaie, L. S. Ismail, T. M. Elfouly, and M. H. Ahmed, "Maximizing Lifetime in Wireless Sensor Network for Structural Health Monitoring With and Without Energy Harvesting", *IEEE Access*, vol.5, pp. 2383-2395, 2017.
- [165] T. Shu, M. Krunz, and S. B. K. Vrudhula, "Joint Optimization of Transmit Power-Time and Bit Energy Efficiency in CDMA Wireless Sensor Networks", *IEEE Transactions on Wireless Communications*, vol.5, no.11, pp. 3109-3118, Nov. 2006.
- [166] J.Jung, W. Woo, and A.Mary, "On using cooperative routing for lifetime optimization of multi-hop wireless sensor networks: Analysis and guidelines," *IEEE Transactions on Communications*, vol.61, no.8, pp.3413-3423, 2013.
- [167] F.Nasri and A.Mtibaa, "IoT Platform for Healthcare System: Protocols Interoperability," *International Journal of Applied Engineering Research*, vol.12, no.22, pp. 12510-12518, 2017.
- [168] S.Xiao, A.Dhamdhere, and V. Sivaraman, "Transmission power control in body area sensor networks for healthcare monitoring," *IEEE Journal on Selected Areas in Communications*, vol.27, no.1, pp. 37-48, 2009.
- [169] J.Yang and S.Ulukus, "Optimal packet scheduling in an energy harvesting communication system," *IEEE Transactions on Communications*, vol.60, no.1, pp.220-230, Jan. 2012.
- [170] D. Niyato, E. Hossain, and S.Camorlinga, "Remote patient monitoring service using heterogeneous wireless access networks: architecture and optimization," *IEEE Journal on Selected Areas in Communications*, vol.27, no.4, pp.412-423, 2009.

- [171] F. Chiti, R. Fantacci, F. Archetti, E. Messina, and D. Toscani, “An integrated communications framework for context aware continuous monitoring with body sensor networks,” *IEEE Journal on selected Areas in Communications*, vol.27, no.4, pp.379-386, 2009.
- [172] Rappaport, S.Theodore, “Wireless Communications–Principles and Practice,” *Microwave Journal*, vol.45, no.12, pp.128-129, Jul. 2002.
- [173] Y.He, W.Zhu, L.Guan, “Optimal resource allocation for pervasive health monitoring systems with body sensor networks,” *IEEE Transactions on Mobile Computing*, vol.10, no.11, pp.1558-1575, Nov. 2011.
- [174] S. Moad, *Energy consumption in wireless sensor networks*, Master dissertation, IFSIC-Rennes, 2007/2008.
- [175] A.Astrin, *Standard for Local and metropolitan area networks part 15.6: Wireless Body Area Networks*, IEEE Std 802.15. 6, Feb. 2012.
- [176] D.J.Goodman and R.D.Yates, *Probability and stochastic processes: a friendly introduction for electrical and computer engineers*, John Wiley & Sons, 2014.
- [177] M.H.Seyedi and D.Lai, *A novel intrabody communication transceiver for biomedical applications*, Springer, 2017.
- [178] A. Olivares, G. Olivares, P. Gloesekoetter, J.M. Gorriz, and J. Ramirez, “A study of vibration-based energy harvesting in activities of daily living”, *Proc. International Conference on Pervasive Computing Technologies for Healthcare (Pervasive Health)*, pp.1-4, Mar. 2010.
- [179] B. Liu, S. Yu and C.W. Chenz, “ Optimal resource allocation in energy harvesting-powered body sensor networks, “ in *2nd International Symposium on Future Information and Communication Technologies for Ubiquitous HealthCare (Ubi-HealthTech)*, pp.1-5, 2015.
- [180] E. Altman, T. Boulogne, R. El-Azouzi, T. Jiménez, Tania, and L. Wynter, “A survey on networking games in telecommunications”, *Computers & Operations Research*, vol. 33. no. 2, pp. 286-311, 2006.
- [181] L. Song, D. Niyato, Z. Han, and E. Hossain, “Game-theoretic resource allocation methods for device-to-device communication, ” *IEEE Wireless Communications*, vol. 21. no. 3, pp. 136-144, Apr. 2014.

- [182] J. Trevathan, L. Hamilton, and W. Read, "Allocating sensor network resources using an auction-based protocol", *Journal of theoretical and applied electronic commerce research*, vol. 11. no. 2, pp. 41-63, 2016.
- [183] A. Koubaa, M. Alves, and E. Tovar, Eduardo "GTS allocation analysis in IEEE 802.15.4 for real-time wireless sensor networks", in *Proc. Proceedings 20th IEEE Inter. Parallel & Distributed Process. Symp.*, pp. 8-35, Apr. 2006.
- [184] K.Routh and T.Pal, "A survey on technological, business and societal aspects of Internet of Things by Q3, 2017", in *Proc. Inter. Conf.On IoT: Smart Innovation and Usages (IoT-SIU)*, pp.1-4, Feb. 2018.
- [185] L. Nasraoui, "Channel Modeling for UAV-Enabled Cellular Networks: A Survey", *International Journal for Research in Applied Science & Engineering Technology (IJRASET)*, vol. 8, no. V, pp. 2834-2841, May 2020.
- [186] Y. Zhao, A. Sani, H. Andrea, L.Yang, Y.Su-Lin, and Z. Guang, "A simulation environment for subject-specific radio channel modeling in wireless body sensor networks", in *Proc. Inter. Workshop on Wearable and Implantable Body Sensor Networks*, pp.23-28, Jun. 2009.
- [187] K. Akkarajitsakul, E. Hossain, and D. Niyato, Dusit, "Distributed resource allocation in wireless networks under uncertainty and application of Bayesian game", *IEEE Communications Magazine*, vol. 49, no. 8, pp. pp. 120-127, 2011.
- [188] N. Badri, L. Nasraoui, L. Azouz Saidane, and N. Brinis, "Blockchain for WSN and IoT Applications", in *Proc. IEEE International Conference on Sciences of Electronics, Technologies of Information and Telecommunications (SETIT)*, pp. 543-548, May 2022.